

EUR 12 385



COMMISSION OF THE EUROPEAN COMMUNITIES

Joint Research Centre

INSTITUTE
FOR TRANSURANIUM ELEMENTS
KARLSRUHE

Annual Report 1988

TUAR-88

1989

EUR 12385 EN

COMMISSION OF THE EUROPEAN COMMUNITIES

Joint Research Centre

**INSTITUTE
FOR TRANSURANIUM ELEMENTS
KARLSRUHE**

Annual Report 1988

TUAR-88

1989

PAP. EUR
C /
CL EUR 12385 EN

Published by the
COMMISSION OF THE EUROPEAN COMMUNITIES
Directorate-General
Telecommunications, Information Industries and Innovation
Bâtiment Jean Monnet
LUXEMBOURG

LEGAL NOTICE

Neither the Commission of the European Communities nor any person acting on behalf of the Commission is responsible for the use which might be made of the following information

Luxembourg: Office for Official Publications of the European Communities, 1989

Catalogue number: CD-NA-12385-EN-C
ECSC-EEC-EAEC, Brussels Luxembourg, 1989
Printed in the Federal Republic of Germany

Abstract

In the context of studies of **Oxide Fuel Transients**, a comprehensive data base on observations with transient-tested LWR fuel was further extended. - Hot cell anneals of high burn-up UO_2 were carried out up to the melting point to study fission gas migration and release. This research were accompanied by investigations on unirradiated uranium oxide with additives simulating the presence of fission products at high burn-up. - Debris originating from the molten core and from the outer crust of the Three Mile Island reactor, together with pieces of structural material like control rods, were examined with the aim to analyse the microstructure of the debris and to determine its content in volatile fission products as well as the maximum temperatures to which the material was exposed.

Work in the field of **High Burn-Up Chemistry** could not be kept on schedule due to external circumstances. Progress of work in the field made in 1988 will be described in the 1989 report.

Within the frame of the project on the **Optimisation of Dense Fuels**, two He-bonded nitride pins and two carbide pins were produced for the irradiation experiment NIMPHE 2 in the PHENIX reactor in Marcoule. - Two short-term irradiations, which had been carried out in HFR Petten with nitride fuels prepared by three different fabrication routes were analysed in order to identify an optimum procedure for the fabrication of a fuel which can be safely operated up to high burn-up. - As a support to these activities, basic data on the self-diffusion and on lattice defects in sintered UN samples and UN single crystals were determined.

In the field of **High-Temperature Properties of Nuclear Materials**, previous observations, that the thermal conductivity of molten UO_2 is lower than that in the solid phase near the melting temperature, were confirmed. - Radiative properties of uranium oxide have been measured up to 4000K. The spectral emissivity of UO_2 was found to increase with temperature but showed a pronounced minimum around the melting point. - Construction of equipment to measure thermal diffusivity and vapour pressure of irradiated fuel samples was started.

Studies of the **Formation of Actinides** were continued and the impact of recycling minor actinides assessed by assuming the transmutation in fast reactors or in special minor actinide burners. - The SUPERFACT experiment, designed to test the irradiation behaviour of minor actinide containing fuel in a fast flux, was terminated as planned. The fuel will undergo post-irradiation examination in 1989.

Methods for the **Safe Handling of Nuclear Materials** involved the execution of large-scale fire experiments with burning of glove-box size pieces of plexiglass "contaminated" with radioactive simulants. The results of these tests were compared with those performed with plutonium oxide powder on plexiglass chips in a glove box. - In a second series of experiments, other substrates were used: polyethylene, polycarbonate, neoprene, hypalon, cardboard, and polyvinylchloride. Resuspension was found to be greatest from plexiglass and not measurable from polyethylene. Only maximum 2% of the contaminant particles were sufficiently stable to reach the outlet duct.

Key problems in **Reprocessing of Nuclear Fuels** were dealt with by performing tests on the destruction of ammonium ions (which may give rise to safety problems during reprocessing) in solutions of dissolved nitride fuels and by studying the extraction of actinides from waste actinide mixtures and their purification.

The goal of **Actinide Research**, is the understanding of the properties of actinide-containing solids in terms of the electronic structure of their constituents and of the contribution of 5f electrons to the chemical bond. - During the reporting period, search for new materials with interesting magnetic properties was directed towards ternary compounds containing Rh, Ru, or Tc, together with Np and Si. - In high-pressure research, X-ray experiments on the monochalcogenides and monpnictides were completed. - Photoelectron spectroscopy has been used in search for localization-delocalization effects in Pu-Al alloys. - Following the predictions of band structure studies, a neutron diffraction experiment illustrated the cancellation of spin and orbital magnetic moments in UFe_2 . - In 1988, more than 20 laboratories in Europe and in the US carried out experiments with samples prepared at the Karlsruhe laboratories.

Work on **Fuel Behaviour under Accident Conditions** concerned mainly a) the development of laboratory equipment for analysing fission products released from irradiated fuel to be used for the collaboration in the PHEBUS PF project and b) the development and improvement of the TRANSURANUS fuel pin computer code system.

Measurements on a round robin glass have been carried out within the frame of our efforts on the **Characterisation of Nuclear Waste Forms** for the EC Repository Simulation Test programme. The results are now under evaluation. - After completion of the verification of the OXAL process on intermediate level waste, resulting alpha-free solutions were isolated in a cement matrix and the properties (compressive strength, porosity, leaching) of this waste form are under study. - The characterisation of active (up to 287 Ci/kg) borosilicate glass samples containing 15 to 30% fission products has been essentially completed with the scanning electron microscopic examination of polished and fractured surfaces. - As a result of leaching studies, the leaching process was shown to proceed from the surface by formation of channels enriched in selected elements (Fe especially) and depleted in others, such as Si. - The studies of the long-term irradiation on ^{244}Cm -doped glasses have been completed and will be evaluated in a final report.

Research and Development Work in Destructive Analysis of Fissile Materials centered on the development of an expert system which will define and initiate automatic analyses to be performed at the Laboratory. In its present state the system automatically receives on-line from Luxembourg the sample characteristics.

Work as a **Support to Community Policies** was continued by performing a large number of analyses on samples taken by EURATOM safeguards inspectors at nuclear facilities all over Europe.

Prospective Studies dealt with aerosol agglomeration studies in experimental chambers with volumes of 5, 15, and 170 m³, using electro-acoustic transducers which operate at a frequency of 21 kHz. Test aerosols included carbon black (soot), produced by burning rubber, and a white chemical fog. A method for large-scale scavenging of hazardous aerosols, based on these experimental results, has been worked out. - Other prospective studies concerned structural investigations on YBa_2CuO_7 and La_2NiO_4 in an effort to understand the physics of high T_c superconduction.

A method for the on-line determination of the plutonium enrichment in MOX-fuel , using energy-dispersive X-ray fluorescence, was studied under contract as **Work for Third Parties**.

Commission of the European Communities
Joint Research Centre

TUAR 88

Institute
for Transuranium Elements
Annual Report

January - December 1988

Table of Contents

I. Foreword	7
II. Executive Summary	13
III. Scientific-Technical Achievements	27
1 Oxide Fuel Transients	29
Introduction	29
Irradiation Experiment VOLEX	29
Irradiation Experiment BUMMEL	29
EPMA of an As-Fabricated MOX Fuel Pellet	29
Behaviour of UO ₂ Fuel during a Temperature Transient	32
TMI-2 Reactor Core Sample Examination	34
Fission Product Behaviour and Microkinetics	40
Electron Microscopy Studies of SIMFUEL Samples	42
Transuranus Code - Development and Applications	45
Program FUTURE - Fuel Transient Ultimate Response	50
Comparison of FUTURE with Recent Transient Fission Gas Release Data	53
2 High Burn-Up Chemistry	57
3 Optimisation of Dense Fuels	59
Introduction	59
Fuel Fabrication, Characterisation, and Irradiation	59
Irradiation Experiments	72
Basic Studies on Uranium Nitride	73

4 High-Temperature Properties of Nuclear Materials	79
Introduction	79
Thermal Conductivity of Liquid UO ₂	80
Measurement of Specific Heat with Pulsed Lasers	92
Deduction of C _p in Pulse Heated Samples under Slow Heat Transport Conditions	94
Measurement of Melting Point and Spectral Emissivity of Refractory Metals	96
Radiative Properties of UO ₂ in Liquid and Solid Phases	102
Measurement of Thermal Diffusivity by Laser Flash	103
Pyrometry	104
Thermodynamic Calculations	104
5 Formation of Actinides	107
Status of the SUPERFACT Irradiation	107
Status of Analysis of KNK IIb Samples	107
Minor Actinide Recycling Scenario in Europe	108
Extraction of Actinides from Highly Active Waste	113
The Potential of Estimating Nuclear Fuel Parameters from Measurements of Rare-Earth Fission Products using ICP-MS	115
6 Safe Handling of Nuclear Materials	115
The Resuspension of Uranium-Plutonium Oxide Particles from Burning Substrates	115
Fire Experiments under Realistic Laboratory Conditions	116
7 Reprocessing of Nuclear Fuels	119
Introduction	119
Fuel Dissolution Studies	119
Absorption Spectroscopy of Neptunium	119
Colloidal Plutonium	120
Actinide Separation and Recovery	121

8 Actinide Research	125
Introduction	125
Objectives	125
Preparation and Characterisation of Actinides and Actinide Compounds	125
Electronic Structure Studies on Actinide Systems	132
Actinide Studies at Large Central Facilities	137
Collaborative Research	139
High-Pressure Studies on Actinide Systems	142
Collaborations with External Organisations	143
9 Fuel Behaviour under Accident Conditions	145
Introduction	145
Study of Fuel Behaviour under Accident Conditions using the TRANSURANUS Code	145
Ultrasonic Thermometry	150
10 Characterisation of Nuclear Waste Forms	151
Radioactive Waste Management and the Fuel Cycle	151
European Community Repository Systems Simulation Test	155
Radiation Damage Studies	163
Leaching Study of SYNROC	164
Comparison of Vickers Indentation and Short Rod Fractometry to Determine Fracture Toughness of Waste Glasses	169
Characterisation of Highly Active Glasses	173
Spent Fuel Direct Storage	179
11 R&D in Destructive Analysis of Fissile Materials	183
Conceptual Design of an On-Site Laboratory for Nuclear Materials Safeguards	183

12 Support to Community Policies	185
IAEA Support Programme	185
Transmission of Data to a Laboratory Computer and Incorporation of a Bar Code Reader in the Analytical Robot System	185
Establishment of Electronic Mail Service between DCS Luxembourg and the Institute	188
Software and Hardware Updates for the Laboratory Robot	189
13 Prospective Studies	191
Acoustic Scavenging of Hazardous Aerosol and Gas	191
Acoustically Enhanced Toxic Gas Absorption	196
High-Tc Materials Studies	199
14 Work for Third Parties	201
On-Line Determination of the Pu-Enrichment of MOX Fuel by Energy Dispersive X-Ray Fluorescence	201
IV. List of Publications	203
V. Glossary	225
List of Authors	231
Previous Programme Progress Reports	233

I. Foreword

The present report summarizes the results of the work which has been performed in 1988 at the Institute for Transuranium Elements of the Joint Research Centre of the Commission of the European Communities. While, as in the past, major efforts were devoted to the Programme on Nuclear Fuels and Actinide Research, important contributions were made to other JRC Specific Programmes, i.e. Reactor Safety, Radioactive Waste Management, and Safeguards and Fissile Materials Control. In addition, The Institute has carried out analytical work for the EURATOM Safeguards Directorate and executed research tasks in the safeguards context, both, for the Commission of the European Communities and for the International Atomic Energy Agency in Vienna. Exploratory Research, finally, dealt with an investigation of possibilities of acoustic aerosol scavenging.

A memorable event in the history of the Institute was the celebration of its 25th anniversary with a Symposium on "Transuranium Elements Today and Tomorrow - Prospects, Properties, Problems" on October 26 and 27. The state of the art in research on transuranium elements was summarized in three sessions: (I) Basic Research on Transuranium Elements, (II) Transuranium Elements as Nuclear Fuels, and (III) Transuranium Elements and the Environment. More than 50 invited and contributed papers and posters were presented to the 250 scientists from Europe and overseas who attended the meeting.

The Symposium was followed by an official ceremony on October 28, with an historic account "Pioneering the Nuclear Age" given by G.T.Seaborg, who received the Nobel prize in 1951 for his discovery of the first transuranium elements.

Another important event in 1988 was the signing of a research contract with the Central Research Institute of the Electric Power Industry of Japan on March 7 in Brussels concerning the study of minor actinide alloys with possible use as fuel for an actinide burner, to be carried out at the Institute.

Among the meetings and conferences, organized by and held at the Institute in 1988 were also

- the Spring Session of the 'Arbeitskreis Thermophysik, Deutsche Keramische Gesellschaft', on May 16 and 17,
- an IAEA Seminar on Burn-up Determination in LWR Fuel, on June 13 - 16,
- a Workshop on Spent Fuel as Nuclear Waste Form, on October 5-6,
- a meeting of the JRC Board of Governors on October 27,
- a meeting of the JRC Advisory Committee on Nuclear Fuel Cycle Research (CGC-6), on November 3.

and

- a Workshop on Advanced Techniques in Radiochemical Analysis, on November 8 and 9.

An important step towards streamlining the internal structure of the Institute was made in November 1988, when the existing laboratories were grouped into five specialized Services, Technical Physics, Applied Physics, Nuclear Technology, Nuclear Chemistry, and Actinide Research, with the new structure providing for more flexibility and corresponding better to the requirements of the New Orientations of the Joint Research Centre.

By stepping up efforts in 1988 in the field of radioactive waste management (under special consideration of the direct disposal of spent fuel), in radioactive aerosol research, and in the context of minor actinide recycling, the Institute has again increased its capabilities in the overall support of nuclear safety.

Karlsruhe, August 1989


J. Van Geel
Director



Signing of a research contract on the development of minor actinide alloys with the Central Research Institute of the Electric Power Industry of Japan (CRIEPI) on March 7, in Brussels - from left to right: Dr.T.Nakajima, Vice-President CRIEPI, J.-P.Contzen, Director-General JRC; J. van Geel, Director ITU.



25th Anniversary of the Institute, October 26-28,- Welcome to Professor Glenn T. Seaborg at the entrance to the Institute (first row, from left to right: J. Fuger (ITU), H.Blank (ITU), G.T. Seaborg, J. van Geel (ITU)).



25th Anniversary of the Institute, October 26-28,- Official ceremony at the Schule für Kerntechnik, Nuclear Research Centre, Karlsruhe. Listening in the front row (from left to right): Sir John Kendrew, Chairman of the JRC Board of Governors; Prof. W. Odersky, President of the Federal Supreme Court, Karlsruhe; Prof. H. Böhm, Chairman of the Board of the Kernforschungszentrum Karlsruhe; J.-P. Contzen, Director-General of the Joint Research Centre; Dr. J. Rembser, Federal Ministry of Research, Bonn; Dr. G. Lehr, JRC Board of Governors, Dr. G. Schuster, former Director General, DGXII.



25th Anniversary of the Institute, October 26-28,- Dr. K.H. Narjes, Vice-President of the Commission of the European Communities, delivering his address at the official ceremony

II. Executive Summary

1. Programmes

NUCLEAR FUELS AND ACTINIDE RESEARCH

The Programme is structured in four Projects:

- Safety of Fuel Applications,
- Safety of the Fuel Cycle and its Effect on the Environment,
- Actinides Research,
- Actinides Information Centre.

The Project on the **Safety of Fuel Applications** is concerned with the study of mechanisms and properties determining the behaviour of fuel and fission products during base irradiation and under off-normal operating conditions in both advanced and light water reactor fuels.

In this context, a comprehensive data base on observations with transient-tested LWR fuel was further extended, in particular by careful electron microprobe analysis of a porous outer ring which forms in UO_2 at high burn-up. Hot cell anneals of high burn-up UO_2 were carried out up to the melting point to investigate fission gas migration and release. The studies were accompanied by investigations on unirradiated uranium oxide with additives simulating the presence of fission products at high burn-up.

Due to difficulties in transporting irradiated fuel, encountered in 1988 in the Federal Republic, it was not possible to stay on schedule with the analysis of fuel samples which had been subjected to transients by KWU (MOX) and in the frame of the international Riso III fission gas release project.

Modelling activities, on the contrary, proceeded as planned. The **FUTURE** code was used to analyse all available experimental data, and the **TRANSURANUS** code was validated by comparison of predictions with experimental findings. The **TRANSURANUS** code was transferred to several national licensing authorities and a revised version was incorporated into the European Accident Code EAC developed at JRC Ispra.

Debris originating from the molten core and from the outer crust of the Three Mile Island reactor, together with pieces of structural material like control rods, were

investigated in our hot cells with the aim to analyse the microstructure of the debris and to determine its content in volatile fission products and the maximum temperatures to which the material was exposed.

Most of the equipment needed for analysing the chemical state of high burn-up LWR fuel in the context of an international cooperation (HBC, High Burn-Up Chemistry) became operational. First samples originating from ASEA (Sweden) and CEN Mol are expected to arrive in March `89.

In a joint effort with CEN Cadarache to investigate the behaviour of advanced fuels under irradiation, two carbide and two nitride fuel pins were fabricated for the irradiation experiment NIMPHE 2, and are presently undergoing irradiation in the PHENIX reactor.

Three other nitride pins had been irradiated in the Petten high-flux reactor. Detailed post-irradiation analysis of these pins revealed marked structural differences due to differences in fabrication procedure. This opens up possibilities for preparing fuel pellets with a "tailored" structure.

Efforts to investigate fuel properties under accident conditions, i.e. at extremely high temperatures, were continued. Previous observations that the thermal conductivity of molten UO_2 is lower than that in the solid phase near the melting temperature, were confirmed. Radiative properties of uranium oxide have been measured up to 4000K. The spectral emissivity of UO_2 was found to increase with temperature but showed a pronounced minimum around the melting point. Construction of equipment to measure thermal diffusivity and vapour pressure of irradiated fuel samples was started.

Studies on the Safety of the Fuel Cycle and its Effect on the Environment dealt with a continuation of studies of in-pile actinide formation. In order to assess the accumulation of minor actinides (i.e. Np, Am, Cm) in the Community, two scenarios were considered: The transition from LWRs to fast reactors and the recycling of plutonium in light water reactors. The impact of recycling minor actinides was assessed by assuming the transmutation in fast reactors or in special minor actinide burners.

The SUPERFACT experiment, designed to test the irradiation behaviour of minor actinide containing fuel in a fast flux, was finished as planned. The fuel will be examined in our hot cells in 1989.

One of the means by which fuel cycle operations may affect the environment is via nuclear aerosols. This is why much emphasis is being put on the investigation of mechanisms of release and dispersion of radioactive dust particles. Particular attention was paid in 1988 to the release of aerosols in case of a fire in a nuclear facility. The results of large-scale fire experiments involving burning of glove-box size pieces of plexiglass "contaminated" with radioactive simulants were compared to those performed with plutonium oxide powder on plexiglass chips in a glove box. In a second series of tests, other substrates were used: polyethylene, polycarbonate, neoprene, hypalon, cardboard, and polyvinylchloride. Resuspension was found to be greatest from plexiglass and not measurable from polyethylene. Only maximum 2% of the contaminant particles were sufficiently stable to reach the outlet duct.

Work on key problems in fuel reprocessing dealt essentially with tests on the destruction of ammonium ions (which may give rise to safety problems during reprocessing) in solutions of dissolved nitride fuels and with the extraction of actinides from waste actinide mixtures and their purification.

Three different methods to separate plutonium at the 30 ppm level from highly enriched uranium were successfully tested.

In **Actinide Research** the effort in 1988 has focussed on the systematic preparation of single crystals of large families of isostructural actinide compounds and the preparation of new compounds with potentially interesting properties for both fundamental and applied materials science. The crystal structures of different actinide organometallic compounds and complexes containing cyclopentadienyl, indenyl, and nitrate ligands were established by x-ray diffraction.

Progress was made in the understanding of hybridisation which occurs when actinide elements are alloyed with transition metals. Band structure calculations including spin-orbit coupling have been made to account for many of the observed physical properties of these materials and predictions were made on their basis

about certain unusual neutron scattering features due to the cancellation of electronic spin and orbital moments. In a collaboration involving samples prepared at the Transuranium Institute and neutron scattering experiments at different European facilities, these effects were searched for and found in single crystals of UFe_2 and PuFe_2 . The confirmation of these band structure effects allows them to be used in the evaluation of other interesting materials, for example CeFe_2 .

In other successful collaborations electrical resistivity, magnetisation and neutron diffraction studies were carried out on the actinide chalcogenides UTe , NpTe , and PuTe . Photomission experiments have been used to search for similar effects in PuAm alloys.

Catalytic effects were studied in a correlation between electronic structure and chemical reactivity in the case of the ethane hydrogenolysis on UNi_2 , UO_2/Ni and, for comparison, Ni.

Studies of x-ray diffraction, x-ray absorption and optical reflectivity under extremely high pressures concentrated on the actinide monpnictides and monochalcogenides. Nearly all of them exhibit structural phase transitions under pressure. Pressure induced structural transitions in UC and UP were found to be accompanied by a 1 - 2 eV shift of the LIII x-ray absorption edge, which could be explained in terms of increasing delocalisation of 5f electrons.

Work to establish at JRC Karlsruhe an Actinides Information Centre was continued by implementing a retrieval system for computer-stored bibliographical references on actinides.

REACTOR SAFETY - Fuel Behaviour under Accident Conditions

Work for the Reactor Safety Programme in 1988 concerned mainly a) the development of laboratory equipment for analysing fission products released from irradiated fuel to be used for the collaboration in the PHEBUS PF project and b) the development and improvement of the TRANSURANUS fuel pin computer code system.

General improvements of the code dealt with

- a revision of the FBR version,
- reformulations of subroutines concerning central void formation, volume increase due to melting, and partial filling of the pore volume,
- development of a coupling programme to the MDYN (materials dynamic program) which calculates the fuel-coolant interaction and all material movements and freezing phenomena in the central void,
- further improvements of the coupling of TRANSURANUS with the in-pile fuel motion model CAMDYM, with the thermohydraulics model CFEM and with the German reference code BLOW.

MANAGEMENT OF NUCLEAR WASTE - Waste Characterisation

The characterisation on the active (up to 287 Ci/kg, containing 15 to 30% fission products) borosilicate glass samples from the ESTER experiment initiated in 1987, is essentially complete. Supplementing earlier work, characterisation after leaching tests (Soxhlets, H₂O, 100°C, 14 days) of one of the samples was done by optical microscopy and scanning electron microscopic examination of polished and fractured samples. The leaching process was shown to proceed from the surface by formation of channels enriched in selected elements (Fe especially) and depleted in others, such as Si.

The measurements on the Round Robin glass in the frame of the European Commission's Repository Simulation Test have been completed and are under evaluation in Brussels. The Institute has participated in this exercise, together with ten other laboratories, by performing tests under salt and granite repository conditions and carried out a series of optional analyses on the leachant, including anions, in addition to the determination of the compulsory elements (Si, B, Li, Mo); also surface analysis by Rutherford backscattering and electron microprobe investigation were carried out.

After completion of the verification of the OXAL process on intermediate level waste, resulting alpha-free solutions were isolated in a cement matrix and the characteristics (compressive strength, porosity, leaching properties ..) of this

waste form are under investigation, with emphasis on the effect of excess oxalic acid on the quality of the product.

The studies of the long-term irradiation on ^{244}Cm -doped glasses have been completed and will be evaluated in a final report.

In the context of the 1988 results and in preparation of coming activities (glass and spent fuel studies) development of new equipment has become very important:

- Soxhlets have been constructed, installed in hot cells and used for leaching tests;
- three cutting machines (mechanic, ultrasonic, and laser) are in various stages of modification to adapt them to remote control operation;
- a thermal diffusivity apparatus based on the laser flash method has been developed as a prototype for work with alpha emitters and is being modified for hot cell operation.

SAFEGUARDS AND FISSILE MATERIALS MANAGEMENT - Destructive Analysis

An expert system was developed which will define and initiate automatic analyses to be performed at the laboratory. In its present state the system (written in TURBO PROLOG) automatically receives on-line from Luxembourg the sample characteristics. The activities in 1988 have concentrated on testing the system, processing the analysis of the shipping data and determining, from filed experience, type and scope of sample conditioning and measurement.

A bar-code reader was installed to identify the samples for further processing.

The data link between Karlsruhe and DCS Luxembourg was improved, thus improving data transmission and quality control.

In order to speed up separation of U and Pu for the subsequent mass-spectrometric analyses, the tedious ion exchange separation hitherto used has been replaced by an extraction procedure based on TBP. Usually, ion exchange separations are preferred to extraction because of their easier implementation in glove boxes.

Using analytical robots, the situation has changed because the extraction procedure, although it involves more steps than ion exchange, can more readily be performed by a robot.

PROSPECTIVE STUDIES - Acoustic Aerosol Scavenging

Aerosol agglomeration studies have been performed in 1988 in experimental chambers with volumes of 5, 15, and 170 m³, using electro-acoustic transducers which operate at a frequency of 21 kHz. Test aerosols included carbon black (soot), produced by burning rubber, and a white chemical fog.

Quantitative determinations of the mass loading of the various aerosols versus time for different acoustic powers have been made.

A volume of 15 m³ could, for example, be cleared of a dense black aerosol in approximately 15 minutes, using 1 kW of acoustic power.

A method for large-scale scavenging of hazardous aerosols, based on these experimental results, has been proposed.

WORK IN SUPPORT OF COMMISSION SERVICES - DG XVII: Nuclear Safeguards - ECSAM

The analytical support to DG XVII, DCS, Luxembourg, was continued, involving more than 1000 samples.

In addition to performing analytical work, certain analytical techniques were further developed:

- a robotic installation was coupled to an expert system,
- procedures for separating U and Pu were set up which could more easily be incorporated into an on-site laboratory concept and adapted to the specific conditions of an inspected plant than the separation methods used previously.

The latter one involves the analysis of solid material found in a reprocessing plant, and the determination of U and Pu in highly active solid and liquid waste.

In order to speed up and ease the transfer of requests and analytical results, a data link to Luxembourg has been installed and the necessary software written; the design of a direct connection between the laboratory and the inspected facilities using portable computers was completed and the hardware was ordered.

WORK IN SUPPORT OF COMMISSION SERVICES - DG I - IAEA Support Programme

Due to the longer shut-down of the WAK reprocessing plant, the field test of the K-edge densitometer could not be brought to an end. Several samples have, however, been analysed by this technique and with the routine isotope dilution mass spectrometry (IDMS). But a comparison could not be made since the density measurements of the samples at the reprocessing plant were based on unfiltered solutions.

In discussions with the IAEA Safeguards Laboratory, the function and the design of a robot glove box was defined. In addition to the conditioning of reprocessing input samples for IDMS, as performed in the Karlsruhe laboratories, provisions are made for separation by ion exchange. This method was developed by the IAEA and will be installed by the Karlsruhe group. The components for the construction of the system have been ordered (by the IAEA).

It was not possible to select a reprocessing plant for the field test of on-site conditioning of reprocessing input samples. The plant foreseen for this purpose, in India, will not reprocess fuel under safeguards inspection in the near future. The search for other sites continues.

2. Operation of the Laboratory 1988

(Status December)

The Staff

Permanent staff

Total: 187

by activities

administration and S/T management:	26
radiation protection:	17
technical infrastructure:	44
* maintenance:	25
* hot cell operations:	9
* workshops:	10
research staff:	100

by training

university trained:	40
technicians, administrators:	145
skilled workers:	2

by nationality

- B:	21	(11.2%)
- D:	85	(45.5%)
- DK:	1	(0.5%)
- E:	3	(0.6%)
- F:	30	(16.0%)
- GB:	9	(4.8%)
- GR:	1	(0.5%)
- I:	16	(8.6%)
- IRL:	1	(0.5%)
- LUX:	7	(3.7%)
- NL:	13	(7.0%)

by age

- 23 to 27:	8
- 28 to 32:	13
- 33 to 37:	14
- 38 to 42:	15
- 43 to 47:	42
- 48 to 52:	43
- 53 to 57:	37
- 58 to 62:	13
- 63 to 65:	2

Local employees:

Total: 101

Scientific visitors and trainees

Total: 21 (from 7 countries), comprising 7 visiting scientists, 3 post-doctoral fellows and 11 post-graduate fellows

The Institute

Buildings

Total surface: 16 000 m²
 Total volume: 188 000 m³

Laboratories:

Number of alpha-Laboratories	30
Number of "cold" laboratories in the controlled area	16
Number of hot cells	14
Number of installed glove boxes provided with gloves or manipulators (6 of them shielded with lead or water)	420

The Budget (in kECU)

Year	1986	1987	1988
Staff and Infrastructure	18.220	17.390	17.190
Specific S/T Credits	2.030	2.640	2.801
- Lab. running cost	305	268	290
- Nucl. Fuels & Act. Res.	1.420	1.320	1.500
- Waste Management	192	208	208
- Reactor Safety	9	85	122
- Safeguards	0	57	31
- Support to DG XVII and I	103	708	650
Total	20.250	20.030	19.991

Installations and Consumption (in 1988)

Nitrogen purification plants

total throughput:	600 000 m ³ /h
+ hot cells:	2000 m ³ /h
+ glove boxes:	900 m ³ /h

Consumption

Electrical power:	11 GWh
Heating power:	71 000 GJ

The Radiation Protection Service:

Hand and foot monitors in continuous operation	42
Continuous air monitoring posts	42
Dust collecting filters measured	20 000
Dosimeters checked per year:	10 000
Specimens analysed for radiation	3 500
Smear tests evaluated	9 000
Area of laboratory floor under surveillance	150 000 m ²
Instructions on radiation protection matters given	250

Publications:

	1984	1985	1986	1987	1988
Contributions to journals	39	29	30	34	50
Books and monographs	4	10	3	5	3
Conference papers	45	69	70	56	104
Various reports	15	9	21	19	14
Total	103	117	124	114	172

Collaborations with External Organisations

Belgium: Belgonucléaire, CEN Mol, University of Liège, University of Namur, University of Antwerp.

Canada: Atomic Energy of Canada Ltd.

Czechoslovakia: University of Prague.

Federal Republic of Germany: ALKEM, Hanau; Battelle Institut, Frankfurt; DESY, Hamburg; Freie Universität Berlin; Hahn-Meitner-Institut, Berlin; KFA Jülich (Institut für Festkörperforschung, Institut für Chemische Technologie); KfK Karlsruhe (Institut für Heisse Chemie, Institut für Material- und Festkörperforschung, Institut für Nukleare Entsorgungstechnik, Institut für Neutronenphysik und Reaktortechnik, Institut für Genetik und Toxikologie der Spaltstoffe, Institut für Nukleare Festkörperphysik, Institut für Radiochemie, Projekt Schneller Brüter); Max-Planck-Institut für Chemie, Mainz; Max-Planck-Institut für Festkörperphysik, Stuttgart; Max-Planck-Institut für Metallforschung, Stuttgart; NUKEM, Hanau; Siemens-KWU, Erlangen; Technische Universität München; TÜV Baden; TÜV Bayern; TÜV Hamburg; Universität Erlangen. Universität Karlsruhe (Physikalisches Institut, Institut für Chemische Technik); Universität Paderborn, Universität Stuttgart.

France: CEA, CEN Cadarache; CEA, CEN Grenoble; CEA, CEN Saclay; CEA, CEN Fontenay-aux-Roses; CNRS Strasbourg; CNRS Orsay; CNRS Villetaneuse; ILL Grenoble; Institut Curie, Paris; LURE, Orsay; Péciney-Comhorhex, Paris; University of Strasbourg.

Greece: University of Patras

Italy: Entente Nazionale Energia Alternative, Casaccia; Istituto Nazionale Fisica Nucleare, Frascati; University of Bologna; LAMEL, Bologna; Lavoro e Ambiente, Bologna; Politecnico Milano; University of Padova; University of Parma.

Japan: CRIEPI; National Laboratory of Metrology.

Netherlands: AKZO, Arnhem; Philips Eindhoven; University of Amsterdam.

Portugal: ICEN-LNTI, Lisboa.

Spain: ENRESA, Madrid; Instituto de Acustica, CSIC, Madrid.

Switzerland: ETH Zürich; Paul Scherrer Institut, Würenlingen; University of Geneva.

United Kingdom: AERE Harwell; Birbeck College; Rutherford-Appleton Laboratory, Chilton, Didcot; University of Manchester (UMIST); University of Salford; University of Warwick, Coventry.

United States of America: Ames Laboratory and Iowa State University, Ames, IO; Argonne National Laboratory, Argonne, IL; Northwest University, Evanston, IL; Battelle Columbus, Columbus, OH; Battelle Northwest Laboratories, Richland, WA; Cornell University, Itahaca, NY; EG&G, Idaho Falls, ID; Florida State University, Talahassee, FL; Lawrence Livermore National Laboratory, Livermore, CA; Los Alamos National Laboratory, Los Alamos, NM; National Institute of Standards and Technology, GaithersburgMA; Oak Ridge National Laboratory, Oak Ridge, TE; Rockwell International, Rocky Flats, CO; University of Cincinnati, Cincinnati, OH; University of California, Berkeley, CA; University of California at Los Angeles, Los Anegels, CA; University of Connecticut, Storrs, CON; University of Florida, Gainesville, FL; University of Minnesota, Minneapolis, MIN; University of West Virginia, Morganton, VA.

International Organisations: CEC, DCS Luxembourg; JRC Ispra, Petten, Geel; IAEA Vienna; OECD Paris.

III. Scientific-Technical Achievements

1 Oxide Fuel Transients

Introduction

The OFT project was continued in 1988 in close cooperation with international projects and in collaboration with industry. Progress was achieved in the three main objectives of the project to better understand the behaviour of oxide fuel at intermediate and high burn-up under transient conditions. These three objectives are

- detailed analysis of commercial LWR oxide fuel irradiated to high burn-up in excess of 50 GWd/t after both steady state base irradiation and under transient testing, to understand the mechanisms operative in such fuels under these conditions, and to provide a quantitative description that can be extended to hypothetical accident conditions of severe fuel damage.
- to perform parallel basic laboratory work to further investigate fundamental mechanisms of diffusion, precipitation and release of volatile fission products at high temperatures, and to better understand fuel chemistry at high burn-up.
- to develop models for gas release and for fuel performance under normal and off-normal conditions with the aid of different fuel performance codes developed at the Institute.

A certain delay in the first of these objectives was unfortunately unavoidable since for most of the reporting period, the necessary fuel could not be transported to the Institute due to the known political difficulties of transporting fissile material in the FRG in 1988. This difficulty was only overcome in December 1988. In addition, a detailed study of fuel remnants and of reactor core debris from the Three Mile Island Reactor 2 (TMI-2) is included which fits into the scope of the project and which could be performed due to the delay in transport of transient tested high burn-up LWR fuel.

The main aims and results of the project were presented at two conferences within the reporting period [1,2] and the working philosophy followed to achieve the aims of the project as well as to successfully perform other fuel research was summarized [3] (refs. see end of Chapter 1)

Irradiation Experiment VOLEX (VOLume EXpansion)

The irradiation of the 8 VOLEX capsules was completed on February 29, 1988. The equivalent burn-ups of the capsules are in the range 0.205 to 81.78×10^{18} fission.cm⁻³.

Seven capsules are already back in the Institute and are waiting for post-irradiation examination.

Irradiation Experiment BUMMEL (BUbble Mobility MEasurement Level)

The irradiation of the two BUMMEL pins started on September 7, 1988. The irradiation device is performing satisfactorily and the base irradiation phase (goal burn up: 5000 MWj/t) will be achieved in February 1989.

The first stage of the second phase - out of pile annealing - is now in preparation.

EPMA of an As-Fabricated MOX Fuel Pellet

Background

TUAR 87 contains a report on the composition of MOX fuel after irradiation under normal and transient conditions (TUAR 87, 75 ff). Questions have been raised about the precision of the Pu concentrations given in this report. The Pu data are suspect for two reasons.

- 1) The concentration of Pu measured in the UO₂ matrix of the fuel segment irradiated under normal conditions was much higher than expected.
- 2) The Pu content of MOX agglomerates in the outer regions of both fuel segments investigated greatly exceeded the predicted value.

In order to check the precision of the Pu concentrations reported in TUAR 87, point analysis has been carried out on a MOX archive pellet of known composition. The pellet was taken from the production batch used in the fabrication of the base irradiated and transient tested fuel rods.

Results

- When EPMA is carried out with UO_2 and PuO_2 standards the mass concentrations of U and Pu in MOX fuel are equal to the measured k values (the quotient of the X-ray intensity from the fuel and the standard). The application of a ZAF correction procedure to the k data can introduce errors of several per cent.

This is clear from Tab. 1.1 which lists the concentrations of Pu and U in the MOX agglomerates obtained before (k value) and after the application of a standard ZAF correction. It can be seen that the U and Pu k values sum to about 88 wt% which corresponds to the concentration of metal in the actinide oxides.

- It is likely that the intensity of the $\text{Pu } M_\beta$ line emitted from highly porous MOX agglomerates in irradiated fuel is different from that obtained from dense material of the same composition. Weisweiler's model [1] for X-ray absorption in porous material predicts that porosity enhances the emitted X-ray intensity during point analysis (Fig. 1.1), whereas when line scanning is employed, porosity can either cause an enhancement or a decrease in the X-ray intensity depending on the pore size (Fig. 1.2).
- The porosity observed in MOX agglomerates during post-irradiation examination is created in the course of irradiation. At the beginning of

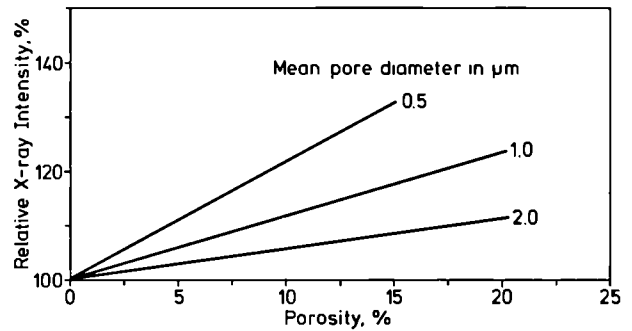


Fig. 1.1 Influence of the porosity in MOX agglomerates on the $\text{Pu } M_\beta$ X-ray intensity measured by point analysis as calculated with the Weisweiler Model [1].

life the MOX agglomerates are highly dense. Fig. 1.3 contains X-ray maps and electron absorption micrographs showing the distribution of MOX agglomerates at three positions on the cross-section of the as-fabricated fuel. The electron micrographs show that the MOX agglomerates are highly dense prior to irradiation.

- The Pu measured in the UO_2 matrix of irradiated MOX fuel results from processes that occur during the irradiation of the fuel (neutron capture in ^{238}U and the diffusion of Pu out of MOX agglomerates). In the UO_2 matrix of the

Tab. 1.1 EPMA Results for the MOX Agglomerates

determination number						
	k value ^{a)}			Concentration ^{b)} wt%		
	U	Pu	U+Pu	U	Pu	U+Pu
1	59.72	27.83	87.55	58.90	26.25	85.15
2	64.03	23.36	87.94	62.99	22.04	85.03
3	63.47	25.10	88.57	62.50	23.68	86.18
4	59.96	28.17	88.13	59.19	26.57	85.76
5	63.56	24.88	88.44	62.59	23.47	86.06

- a) $k = C_0(I/I_0)$ where C_0 is the concentration of the element in the standard, I is the X-ray intensity from the specimen and I_0 is the X-ray intensity from the standard.
- b) given by kF , where F is a standard ZAF correction factor.

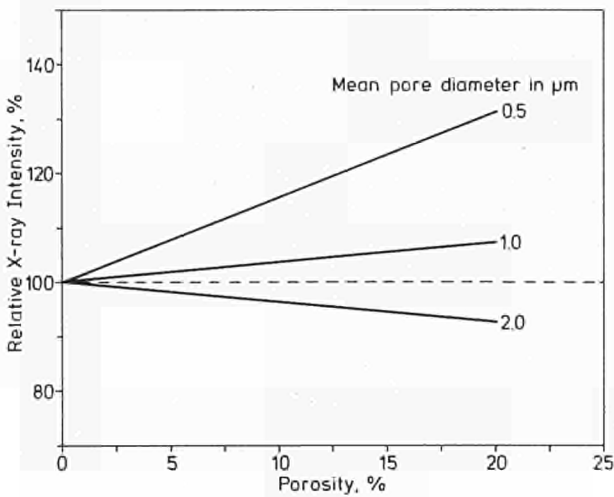


Fig. 1.2 Influence of the porosity in MOX agglomerates on the $Pu M_{\beta}$ X-ray intensity monitored during line scanning as calculated with the Weisweiler Model [1].

as-fabricated MOX fuel pellet the concentration of Pu did not exceed the limit of detection for the analysis of 0.23 wt%.

Conclusions

The plutonium concentrations given in the report on MOX fuel in TUAR 87 are in fact too high. One source of error has been unambiguously identified: that is the unnecessary use of a ZAF correction factor. This raised the Pu concentrations measured in the UO_2 matrix by about 7% relative to the true value. For the MOX agglomerates the high percentage of porosity represents a second and more serious source of error which may have increased the measured Pu concentrations by as much as 20%.

To obtain the true concentration of Pu in irradiated MOX agglomerates the measured X-ray intensity has to be corrected for the influence of the porosity. This requires an priori knowledge of the size and density of the pores in the MOX agglomerates. Thus, in future EPMA should be supplemented by detailed quantitative image analysis (QIA). The best solution would be to perform QIA on high magnification electron absorption images of the analyzed agglomerates. Once the pore characteristics are known a correction factor can be derived from the appropriate theoretical curve for the change in X-ray intensity with the volume fraction of pores calculated with the Weisweiler Model.

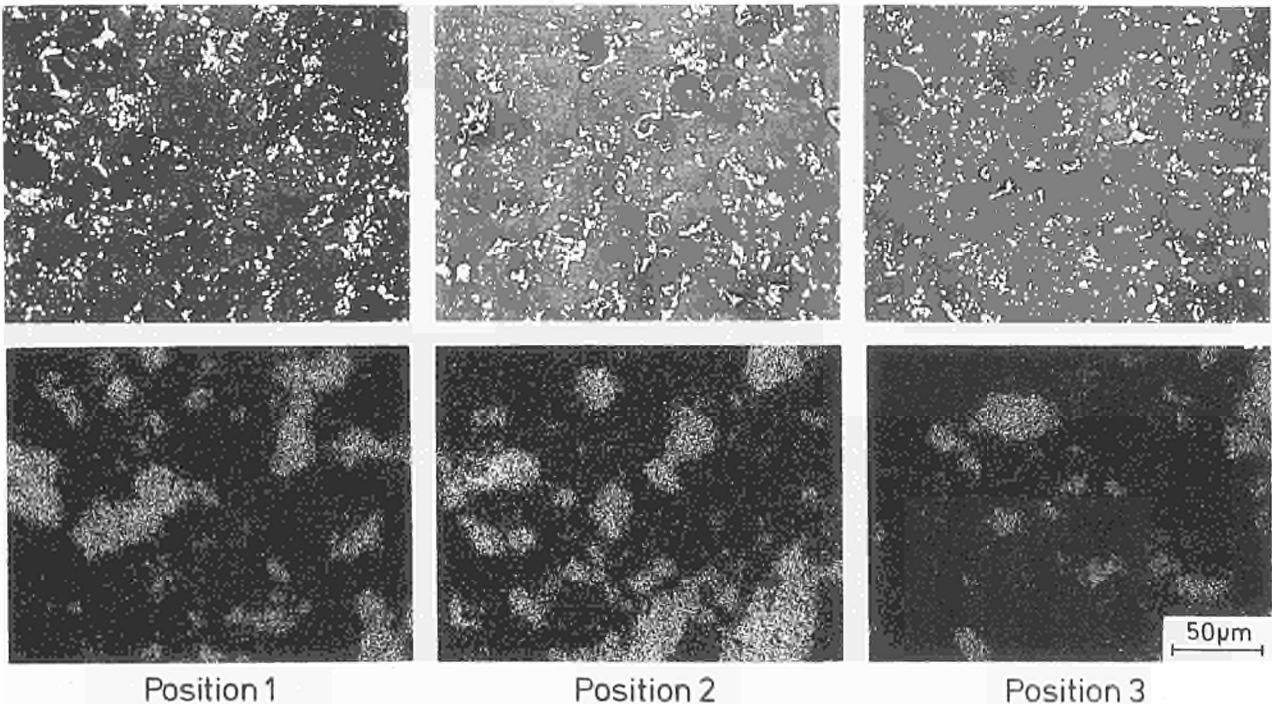


Fig. 1.3 $Pu M_{\beta}$ X-ray maps and electron absorption micrographs showing the distribution of MOX agglomerates at three positions in the fuel

Reference

- [1] W. Weisweiler, *Archiv Eisenhüttenw.* 42 (1971) 1.

Behaviour of UO_2 Fuel During a Temperature Transient

Work was completed on the GE fuel segment STR018 from the Second Risø Fission Gas Release Project and a paper reporting the findings has been published [1]. The Replica and EPMA investigations described in TUSR 38 and 39 have been supplemented by X-ray Fluorescence analysis which was carried out at the Risø National Laboratory and by a SEM investigation of the development of gas bubbles on the grain faces.

The study has shown that internal compressive stress in the fuel is important in determining the level of release under transient conditions. EPMA revealed a marked increase in "in grain" retention of fission gas in the central region of the fuel, while XRF showed that a substantial amount of gas had collected on the grain boundaries at intermediate radial positions (Fig.1.4). Both findings are ascribed to high compressive stress in the fuel.

For the first time, the pressure of the gas in bubbles and pores on grain boundaries has been

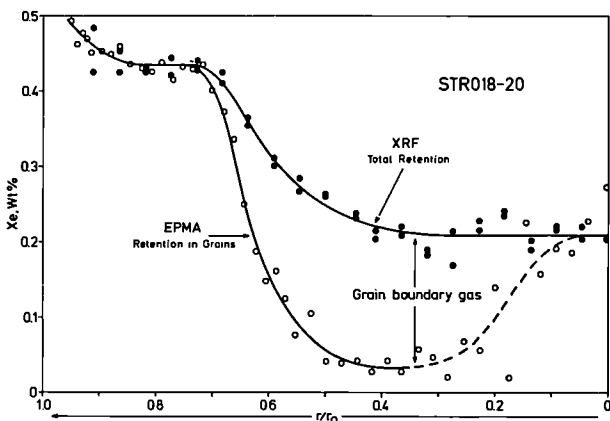


Fig. 1.4 Radial distribution of retained Xe in pin section STR018-20.

determined from experimental data. The instrumented tests on GE fuel revealed that 80% of the gas release occurred on termination of the transient test [2]. It was found that if all the gas released from the grains during the transient was held up in the grain boundary porosity, then the average pressure in the bubbles and pores was about equal to the mechanical restraint pressure (Fig. 1.5). This implies that the gas

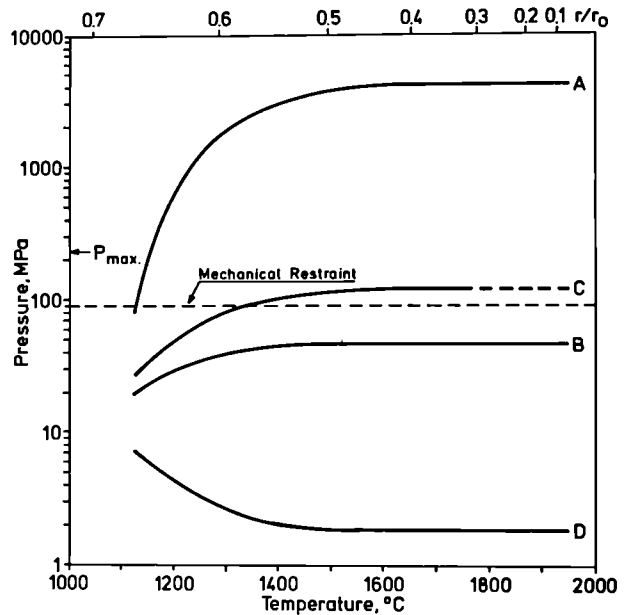


Fig. 1.5 Average pressure of the gas in bubbles and pores on the grain boundaries in STR018-20. $P_{max.}$ = maximum pressure sustainable by the fuel.

Curve A Assuming all the gas found on the grain boundaries was contained in the non-inter-linked grain face bubbles.

Curve B Assuming the gas found on the grain boundaries was distributed in the grain boundary porosity.

Curve C Assuming the grain boundary porosity had once contained all the gas released from the UO_2 .

Curve D The surface tension pressure, $2\gamma/r$.

pressure was determined by the mechanical state of the fuel!

The degree of interlinkage exhibited by the gas bubbles on the grain faces was small (Fig. 1.6).

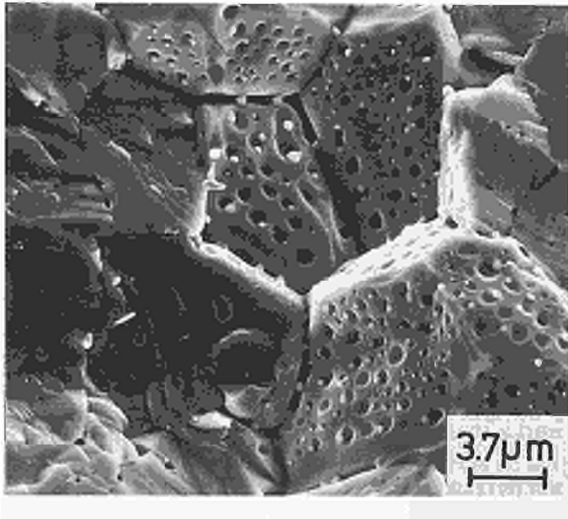


Fig. 1.6 Scanning electron micrograph of grain faces at $r/r_o = 0.55$ in STR018-20. Most of the gas bubbles present are not interlinked.

This is thought to be the main reason why appreciable gas release was delayed until the end of the transient test. It was found that non-interlinked bubbles coarsened with no change in the total pore volume (Fig. 1.7). This is taken as evidence that grain faces with non-interlinked bubbles were "passive" during the transient test. That is to say, they behaved as closed systems with little fission gas arriving from the grain interior or leaving for the grain edges. On these grain faces the gas bubbles probably grew by "Ostwald Ripening". This involves the dissolution of bubbles smaller than a critical size and the deposition of the resultant material on larger bubbles causing them to grow.

Two explanations have been put forward for the occurrence of grain faces that take no part in the gas release process. One is that the affected grain faces lie in regions where the local restraint pressure in the fuel is high. This would inhibit gas bubble interlinkage and hence impede the transport of gas to the grain edges. A second explanation could be that the fuel adjacent to these grain faces is depleted in fission gas. Many areas denuded in fission gas bubbles were found in fuel from STR018 (Fig. 1.8). EPMA revealed that where bubbles were absent, the

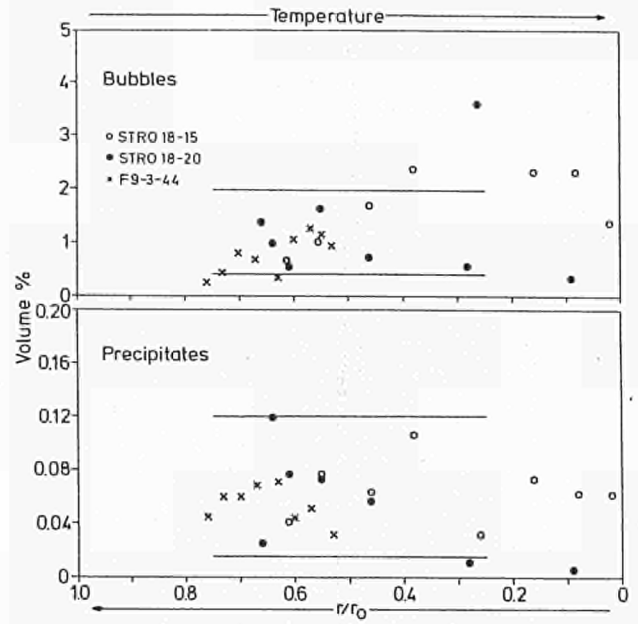


Fig. 1.7 Percentage by volume of non-interlinked gas bubbles and their metallic precipitates on grain faces in STR018-15 and STR018-20. Data for a Risø fuel, section F9-3-44 [3], are included for comparison. The thin horizontal lines mark the limits of the 1σ scatter bands.

fuel contained very low concentrations of xenon (usually < 0.05 wt%). The bubble denuded zones in STR018 were assumed to have formed at the beginning of the transient test.

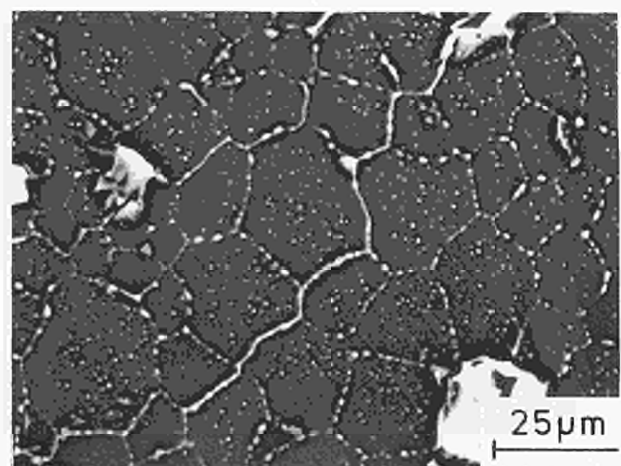


Fig. 1.8 Electron absorption micrograph showing bubble denuded zones along grain boundaries at $r/r_o = 0.60$ in STR018-20.

A further interesting result from the SEM study is the finding that metallic fission product precipitates appeared on the grain boundaries in advance of gas bubbles and apparently acted as nucleation sites for the bubbles (Fig. 1.9). In addition, the metallic precipitates also appear to have pinned the grain face bubbles and thus retarded their movement during growth.

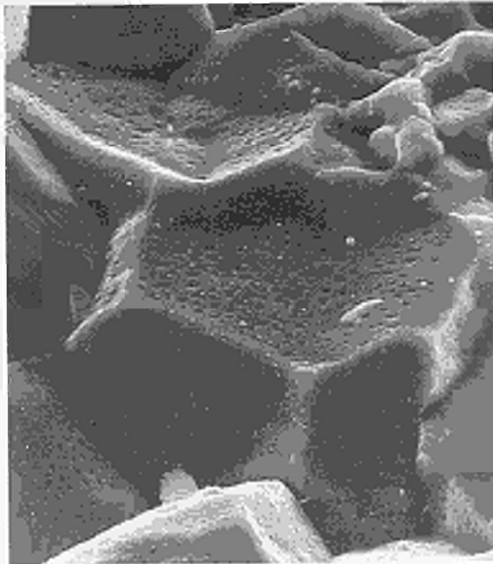


Fig. 1.9 Scanning electron micrograph of grain faces at $r/r_0 = 0.66$ in STR018-20 close to where gas release from the fuel grains began. Nearly all the gas bubbles contain a metallic fission product precipitate.

References

- [1] C.T. Walker, P. Knappik and M. Mogensen, *J. Nucl. Mater.* **160** (1988) 10.
- [2] P. Knudsen, C. Bagger, H. Carlsen, B.S. Johansen, M. Mogensen and I. Misfeld, in *Proc. ANS Topical Meeting on LWR Fuel Performance*, Williamsburg, 17-20 April 1988.
- [3] M. Mogensen, C.T. Walker, I.L.F. Ray and M. Coquerelle, *J. Nucl. Mater.* **131** (1985) 161.

TMI-2 Reactor Core Sample Examination

Introduction

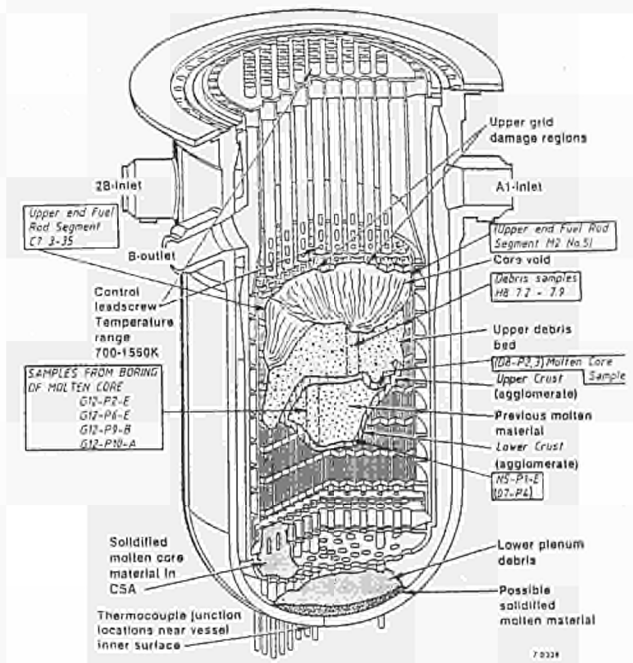
The Institute is participating in a programme of collaboration with the US Department of Energy's Accident Evaluation Programme into the Three Mile Island Reactor 2 incident (TMI-2) in March 1979. This is organised through the OECD Nuclear Energy Agency.

The samples of fuel rod remnants, fused ceramic materials (rocks), and reactor core debris received by ITU and their original location in the reactor are given in Fig. 1.10.

Examination of Specimen from the Molten Core

Microstructure analysis

The G12 specimens from the core, under the optical and electron microscopes, appeared to



n.b. samples shown in brackets have not yet been examined

Fig. 1.10 Location of specimens taken for analysis from TMI-2 in its end-state configuration.

have been in a molten state with a uniform, fine eutectic-type microstructure. Energy dispersive X-ray analysis (EDAX) revealed that these were phases rich in uranium and zirconium mixed with Fe, Cr, Al, and Ni-containing phases (Figs. 1.11a and 1.11c). These appear to have originated from the melted-down UO_2 fuel rods, zircalloy cladding, and stainless steel/Inconel structural components.

X-ray diffraction

X-ray powder diffraction analyses were performed on ground samples from the two G12 molten core ceramic specimens, as well as on a portion of fuel from a fuel rod segment from the reactor edge, and confirmed that the U-rich phase was UO_{2+x} . Lattice parameter (a) measurements indicated that the value of x had a maximum at 0.15, as the presence of ZrO_2 in solid solution in the UO_2 also influences this parameter. The measured values are given in Tab. 1.2.

Tab. 1.2 Lattice parameters (a) and O/M-ratios for three TMI fuel samples

Sample	a (Å)	O/M
C7 3-35 fuel	5.4682	2.04
G12-P9-B	5.4530	2.14
G12-P10-A	5.4519	2.14

Thermogravimetric analysis of G12-P9-B and G12-P10-A indicated a value of x between 0.06 and 0.11. The slightly lower values of x obtained by thermogravimetry (which are not affected by the presence of ZrO_2 , unlike the X-ray diffraction values) also imply that there is Zr in solid solution.

Microprobe and phase analysis

Microprobe analysis of G12-P9-B indicates that all three phases contain oxygen and has shown that both main phases (UO_{2+x} and ZrO_2) contain certain amounts of the other cation in solid solution (i.e. Zr in UO_2 and U in ZrO_2) at a level of between 2 and 15 w/o. There are also secondary precipitates of UO_2 in the ZrO_2 and of ZrO_2 in the UO_2 (Fig. 1.11b).

The UO_2 -rich phase was measured by optical phase analysis as having approximately 40% of the cross-sectional area, the ZrO_2 -rich phase as having approximately 45%, and the ferrous oxide (spinel) phase 13% for specimen G12-P9-B. Other G12 specimens showed varying proportions of ferrous spinel phases and variations in the size of the UO_2/ZrO_2 eutectic-type structure down to $1\mu\text{m}$ average width. This structure implies that the molten core cooled down rather than was quenched.

Gamma-spectrometry

Qualitative gamma spectroscopy confirmed the presence of the long-lived fission products in the G12 specimens. These include $^{134,137}\text{Cs}$, ^{125}Sb , ^{154}Eu , and ^{144}Ce (Tab. 1.3); Xe and Kr isotopes were not found, although ^{85}Kr was evident in the fuel from the fuel rod segments C7 3-35 from the reactor edge. The presence of the very volatile caesium nuclides was very surprising in view of the high temperatures it had been exposed to.

Examination of Fuel Rod Segment C7 3-35

A broken fuel rod segment (C7 3-35) from the outer edge of the reactor core was examined. The fuel exhibited a microstructure similar to that of the starting material with no evidence of grain growth (grain diameter 5 - 10 μm). The cladding showed an outer oxide layer of columnar grains, 30 μm thick, thought to be of $\alpha\text{-Zr(O)}$ (Fig. 1.12).

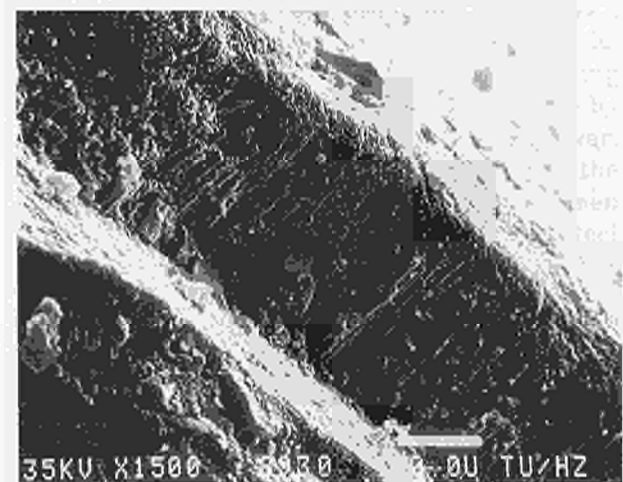
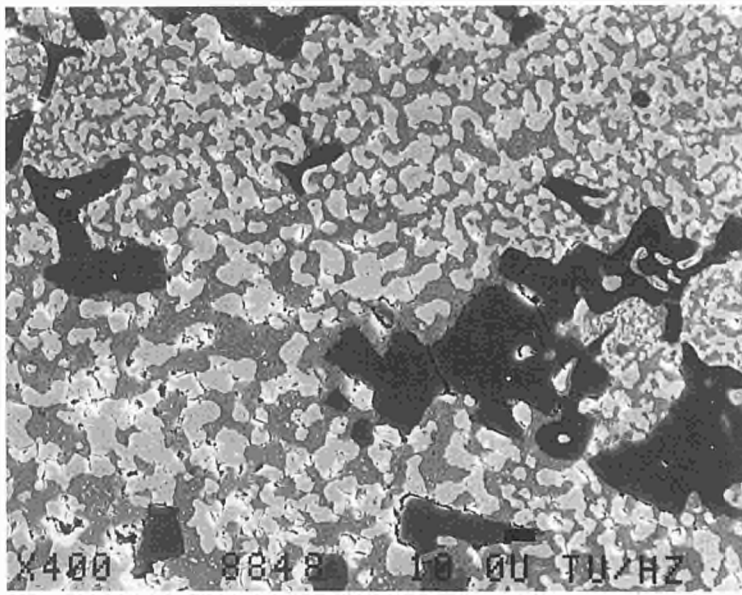
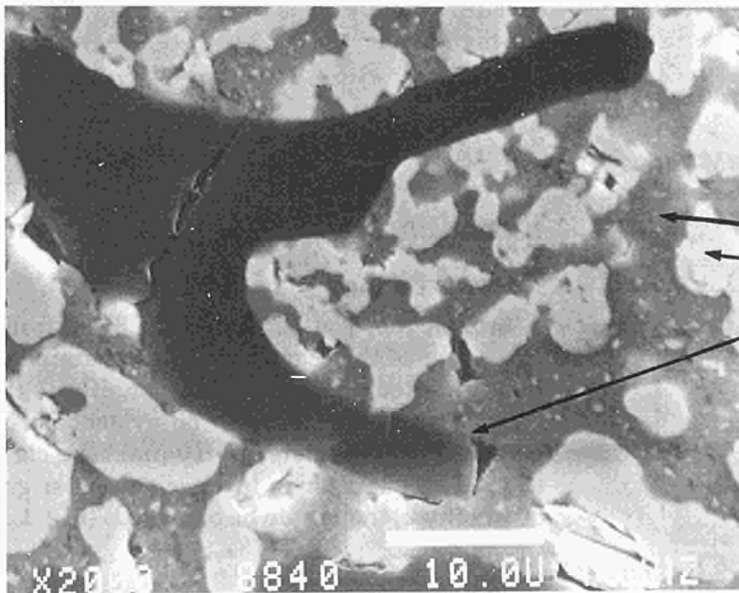


Fig. 1.12 Fuel rod segment C7 3-35, outer oxidation of cladding (1500 \times)



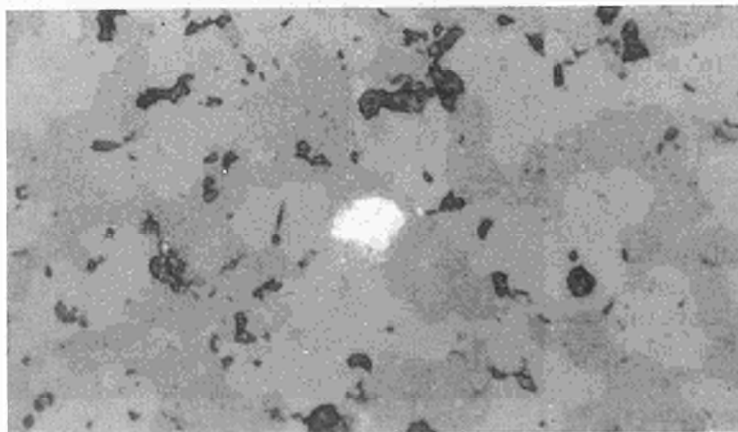
a) SEM Micrograph
(200 x)

Eutectic Phase
i) Zr-rich phase
ii) U-rich phase
Ferrous phase



b) SEM Micrograph
(2000x)

Eutectic:
Zr-rich phase
U-rich phase
Ferrous phase



c) Optical Micrograph
(1030 x)

Fig. 1.11 G12-P9-B microstructure.

Tab. 1.3 γ -Spectroscopy analysis of TMI-2 specimens

Radionuclide Main Peak (keV) SPECIMEN	Irradiation Products					Fission Products											
	1) Fuel		2) Steel			²⁴¹ Am	⁶⁰ Co	⁸⁵ Kr	⁸⁵ Nb	¹⁰⁶ Ru	¹⁰⁹ Cd	¹²⁵ Sb	¹³⁴ Cs	¹³⁷ Cs	¹⁴⁴ Pr	¹⁴⁴ Ce	¹⁵⁴ Eu
	60		1160	514	1085	511	88	463	569, 861	661	696	134	1600 1274				
G-12-P9-B	●		-	-	-	●	-	●	●	●	-	●	●	-	●	●	-
C7 3-35 (FUEL)	●		-	●	-	●	●	-	●	●	-	●	●	●	●	-	●
H8 DEBRIS 7.2 PIECE			●	-	●	●	-	●	●	●	●	●	●	●	-	●	●
III			-	-	-	●	-	●	●	●	●	●	●	●	-	●	●
IV			●	-	-	●	-	●	●	●	●	●	●	●	-	●	●
VIII			●	-	-	●	-	●	●	●	●	●	●	●	-	●	●
VII			●	-	-	●	-	●	●	●	●	●	●	●	-	●	●
CONDENSATE (x) FROM HEATED G12-P9-B SAMPLE			●	-	-	●	-	-	●	●	-	●	●	-	-	●	-

(x) Peaks of ¹²⁶Sn and ¹⁵²Eu were also detected in the spectrum

Note: No ¹²⁹I was detected in these samples. Peaks indicating the presence of ²²Na and ⁴⁰K were noted in some of the samples; the origin of these isotopes is unknown.

Little trace of fission products was found on the outer surface, although spherical deposits of Cr-rich or Fe-rich composition were observed (Fig.1.13). These may have been the result of condensation on the outer, cooler rods of the reactor core, or possibly droplets of liquified structural material and cladding that had splashed onto the rod and frozen in position.

Examination of Agglomerated Crust Specimen (N5-P1-E)

Specimen N5-P1-E was taken from the outer edge of the melted core region; the structures in such regions as well as in the debris found lying

on the top of the crust are more varied and heterogeneous and display remnants of the original component structure, indicating incomplete melting. The specimen was found by EDAX analysis to contain precipitates of silver, often with a nucleus of chromium, in the iron/nickel matrix (Fig.1.14). The specimen seemed to be the semi-fused 304 stainless steel cladding of a Ag-15In-5Cd control rod. The silver precipitates in the ferrous matrix were probably the result of diffusion into the cladding at elevated temperatures, followed by precipitation on cool-down.

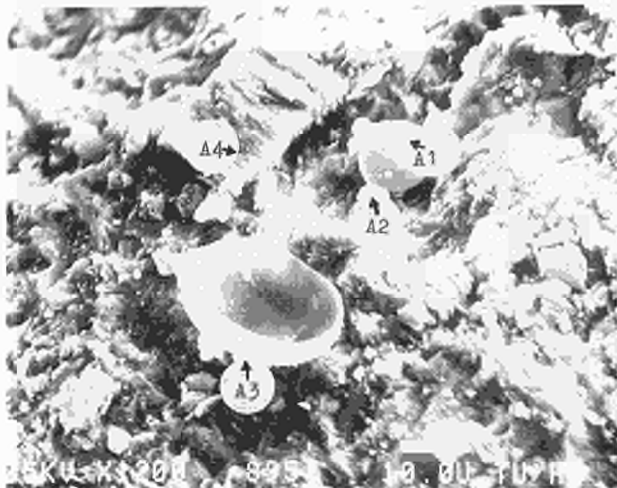


Fig. 1.13 Fuel rod segment C7 3-35, deposits on outer surface (1200 ×)

- A1 : Zr ≧ Al, Fe (Sn, Ni)
- A2 : Zr ≧ Al, Sn, Fe, Eu
- A3 : Zr ≧ Fe, Al (Sn, Eu)

Fission Product Release

The fission gas release study indicated that the caesium present in the fuel (with 0.5 a/o burn-up) from segment C7 3-35 was largely retained on heating in a He-2%H atmosphere up to 2000 °C and that it was necessary to heat up to 2500 °C to release the major part of the volatile fission products (e.g. Cs) and the noble gases (Fig. 1.15). This demonstrates, together with the gamma

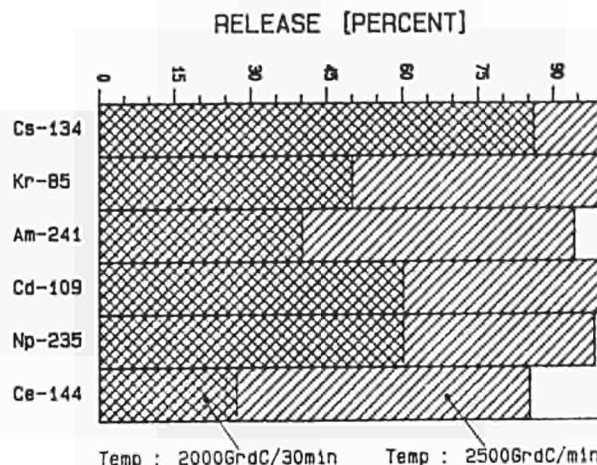


Fig. 1.15 Fuel rod segment C7 3-35, volatile product release under transient heated conditions measured as % release of γ -activity of nuclides (or β -activity of ⁸⁵Kr).

spectroscopy of the G12 specimens, that caesium is not as volatile as expected from its thermodynamic data. A likely retention mechanism or even a plausible explanation for its behaviour under the conditions of core meltdown has not yet been put forward.

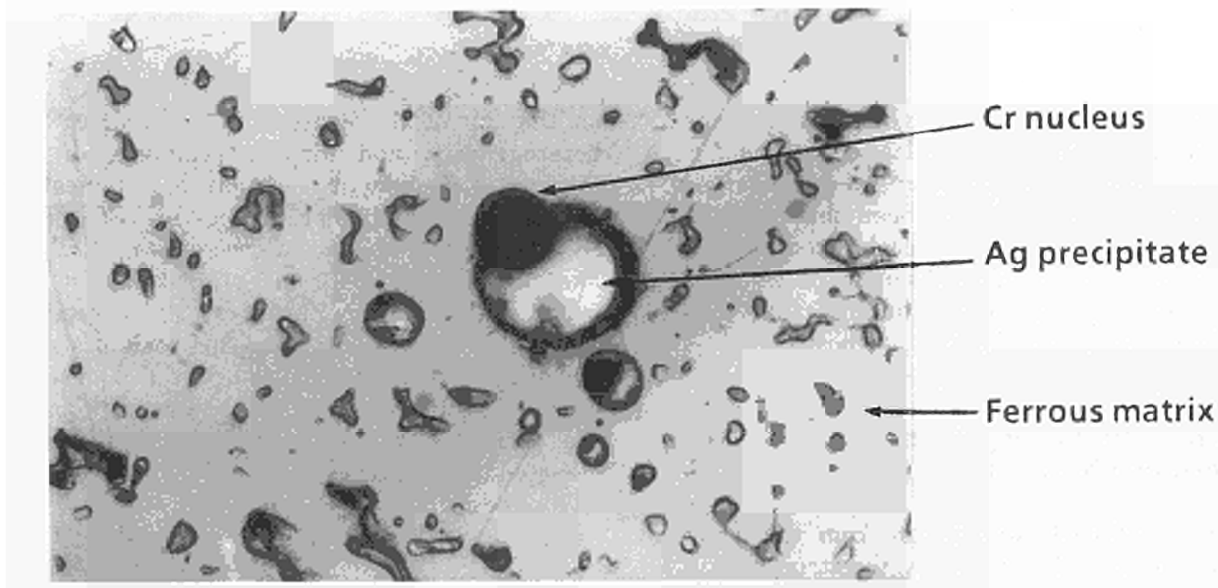


Fig. 1.14 Agglomerated crust N5-P1-E, optical micrograph (1033 ×)

Meltdown of Reactor Materials

From the analysis of the reactor samples, likely reactions between the original structural components and the products found in analysis have been compiled and are given in Tab. 1.4.

Temperature Estimates

Maximum temperatures attained by the molten core form an important part of the accident assessment. Estimates are obtained from the analysis of the fully molten core specimens and reference to the appropriate Zr(O)-UO₂ or ZrO₂-UO₂ phase diagrams [1,2]. The G12 specimens

indicate minimum temperatures in the range 1900 °C - 2500 °C, with the likelihood that they were in the upper half of the range if fully oxidising conditions were maintained in the completely molten core.

At the agglomerated crust and in some of the associated debris, maximum temperatures were clearly lower, in the range from 900 °C up to 1400 °C (*i.e. approaching the melting point of stainless steel*). The temperature gradients were also greater. The standing fuel rod segment from the edge of the reactor core showed little evidence of overheating. This demonstrates the wide span of temperatures which *may have occurred* during the accident.

Tab. 1.4 Summary of structural changes of the TMI-2 core materials during the accident

Component	Chemical Form before Accident	Chemical Form after Accident
Fuel	UO ₂	1) UO ₂ 2) ZrO ₂
Cladding	Zr - 2 % Sn (Zry-4)	3) UO ₂ -ZrO ₂ eutectic (O/M(UO ₂) = 2.03-2.13)
Control Rods Cladding End fittings Retainers	304 stainless steel	4) Ferrous phases i) Fe, Ni, Cr + Al Oxides ii) (Fe + Sn), (Fe + Ni) Eutectic
Control Rods	Ag - 15In - 5Cd	1) Ag spheres in UO ₂ -ZrO eutectic 2) Ag precipitates with a Cr nucleus in ferrous cladding
Burnable Poison Rods	Al ₂ O ₃ - B ₄ C	1) Al migrates to ferrous phases 2) B-not traced likely dissolved in water, or reacted with Cs
Spacer Grids	Inconel 718	1) (See above) grids dispersed in ZrO ₂ -UO ₂ melt as mixed Fe, Cr, Ni Oxides

* a separation of Cr from the Fe- and Ni-phases was sometimes observed, and also the separation of Ni from the Fe- and Cr-phases.

Conclusions and Future Work

Examination and analysis of the specimens has enabled their original composition and position in the reactor to be verified and the likely reactions that they have undergone to be described; this in turn made it possible to determine the temperatures which occurred in the various parts of the reactor, particularly the maximum temperatures which were reached in the fully molten core. This latter estimate is especially important in the assessment of the reactor damage and the mechanisms underlying this and the temperatures at which they were operative. The extent of retention of volatile fission products in the melted reactor core has been an unexpected result from this work.

Future efforts will concentrate on examining the remaining specimens as well as addressing specific questions such as

- what level of oxidation prevailed during the accident (i.e. ΔG_{O_2} versus time)?
- and what is the mechanism of Cs release and its retention?

References

- [1] P.Hoffmann (KfK), private communication, SFD Programme Meeting, Idaho Falls, ID, April 1985
- [2] A.Skokan, 'High-Temperature Phase Relations in the U-Zr-O-System', 5th Internat. Meeting on Thermal Nuclear Reactor Safety, Karlsruhe, FRG, August 1984

Fission Product Behaviour and Microkinetics

Diffusion and Precipitation of Fission Product Atoms in UO_2

Introduction

The technique of introducing interesting fission products into oxide fuels by controlled ion implantation was used to study the release behaviour of UO_2 with simulated burn-ups of 3 at.%. This so-called SIMFUEL was produced at AECL, Chalk River and contained the fission products Y, Zr, Mo, Ru, Ba, La, Ce and Nd in the concentrations corresponding to the simulated burn-up. Kr-85 was implanted into pre-annealed discs in the electromagnetic mass-separator of the Chalk River Nuclear Laboratories, either as tracer alone (1 to 4×10^{12} ions/cm²) or following a prebombardment with ^{84}Kr (1×10^{16} ions/cm²), to increase the gas concentration. Disturbing effects were found due to the formation of surface scales of fission products on the SIMFUEL since part of the implanted krypton was located in these scales and therefore showed release kinetics different from that in the fuel. The perovskite-type scales (rare earths containing bariumzirconates) release most of their gas between 700 to 900° C, similar to the behaviour of the similarly complex oxide Synroc [1]. The results obtained so far have therefore to be corrected for the presence of these scales. Fig. 1.16 shows a typical isochronal release curve for UO_2 with results for 3 % SIMFUEL as dashed curve. Obviously, there is no large effect on the Kr-release, in agreement with results for Kr, I and Rb and scale-free ThO_2 -based SIMFUEL (see Fig. 1.17 where the results for ThO_2 without added fission products are given as dashed curves).

A large number of similar release curves have been measured, both under reducing (Ar/H_2) and under oxidising conditions (CO/CO_2 mixture). The evaluations will be given in the next report. In no case was there any release at very low temperatures, as claimed in the literature [2].

The situation can best be illustrated in a figure from a recent review [3]. At very low gas concentrations, a constant diffusion coefficient is known to exist for rare gas diffusion in UO_2 [4, 5].

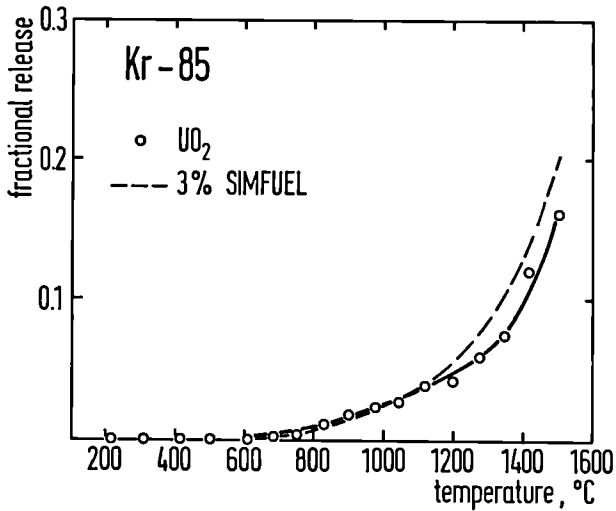


Fig. 1.16 Isochronal release of Kr-85 from UO_2 and from UO_2 -based SIMFUEL. The dashed curve is corrected for the presence of surface scales

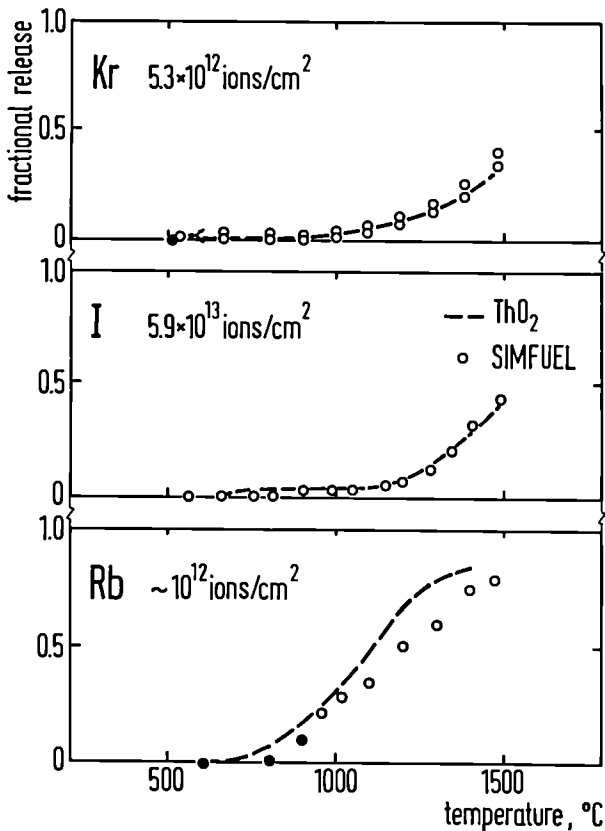


Fig. 1.17 Release of Rb, I, and Kr from ion-implanted ThO_2 -based SIMFUEL (3 at.% b.u.). ThO_2 is used to guarantee a constant O/M ratio

At higher gas (and damage) concentrations, trapping occurs leading to significantly reduced D-values. The lowest values measured by MacEwan and Stevens were previously regarded as saturation values, since ion bombardment data (full dots in Fig. 1.18) seemed to confirm the assumption of saturation up to very high gas concentrations. However, a recent careful study performed within the cooperation with AECL and using intermediate concentrations [6] indicated a much more complex picture (dotted curve in Fig. 1.18). This curve can be quantitatively interpreted as being due to a complex interplay of formation of gas-filled bubbles of different pressure causing much of the gas to stay in solution or be thermally dissolved in the lattice whenever the gas pressure approaches maximum values. Note that the previous "saturation value" for trapping was reached after a very short irradiation of a few days only, and that the indicated maximum at some fraction of an atom percent of gas corresponds to realistic burn-ups of interest in the OFT project. It helps also to explain why relatively high effective D-values have to be used in modelling for realistic burn-ups.

The new results for Kr in UO_2 and in SIMFUEL show that the presence of non-gaseous fission products does not significantly affect the behaviour of trapped fission gas. Data at intermediate gas concentration have still to be measured.

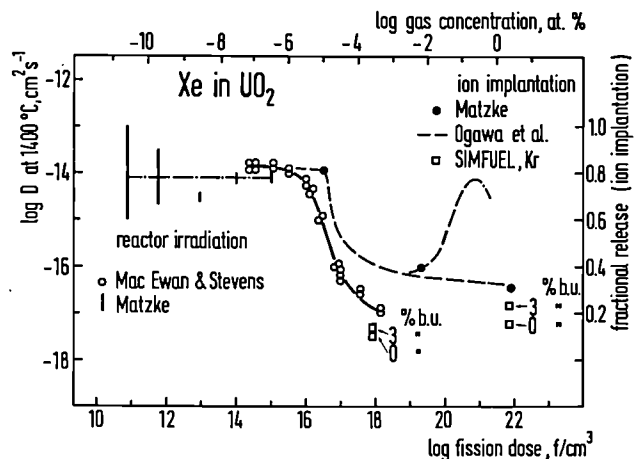


Fig. 1.18 Trapping of Xe in reactor irradiated and ion bombarded UO_2 [3-6]. (Most data from Ogawa et al. are for ThO_2). The new results for Kr, two gas concentrations and SIMFUEL (3 % b.u.) are shown as squares

References

- [1] Hj. Matzke, Nuclear Waste Materials, Chapter 12 in Ion Beam Modifications of Insulators, Eds. G. Arnold and P. Mazzoldi, Elsevier, Amsterdam (1987) 501
- [2] I. Misfeldt, J. Nucl. Mater. 135 (1985) 1
- [3] Hj. Matzke, Fission Gases in Nuclear Fuels, invited review for Ann. Chim., Science des Materiaux, Paris, in print
- [4] Hj. Matzke, Nucl. Applic. 2 (1966) 131
- [5] J.R. MacEwan and W.H. Stevens, J. Nucl. Mater. 11 (1964) 77
- [6] T. Ogawa, R.A. Verrall, D.M. Schreiter and O.W. Westcott, Canada Report AECL-9475 (1987) 543

Electron Microscopy Studies of SIMFUEL Samples.

Scanning Electron Microscopy (SEM) and Transmission Electron Microscopy (TEM) have been used to examine specimens of UO_2 SIMFUEL containing 3% and 6% simulated waste, and ion-bombarded with Kr or Xe. The composition of the samples is given in Tab. 1.5.

Tab. 1.5 Composition of SIMFUEL with 3 and 6 at% b.u. starting powders

Compound	3 at% SIMFUEL	6 at% SIMFUEL
UO_2	97.680	95.315
BaO	0.117	0.311 (BaCO ₃)*
CeO ₂	0.284	0.526
La ₂ O ₃	0.106	0.194
MoO ₃	0.359	0.730
SrO	0.072	0.110
Y ₂ O ₃	0.041	0.061
ZrO ₂	0.339	0.601
Rh ₂ O ₃	0.028	0.034
PdO	0.149	0.440
RuO ₂	0.363	0.764
Nd ₂ O ₃	0.460	0.912

* Barium for 6 at% SIMFUEL was added in the form BaCO₃. During heating, CO₂ is evolved; the concentration of BaO remaining is 0.242 wt%.

Scanning Electron Microscopy

It was possible to examine the samples directly without coating with gold. Fig. 1.19 shows the surface structure of the 6% SIMFUEL sample 159-1-1. This is characterised by very clearly defined grain boundaries and a high density of the large spherical precipitates. Fig. 1.20 is a higher magnification view of part of the same surface. The spherical precipitates represent the well known noble metal fission product inclusions. These were analysed by energy dispersive X-ray analysis, and found to contain principally molybdenum and ruthenium as expected. Iron was also present, probably from the ball milling process.

The energy dispersive X-ray spectrum for the precipitates shown in Fig. 1.20 is given in Fig. 1.21.

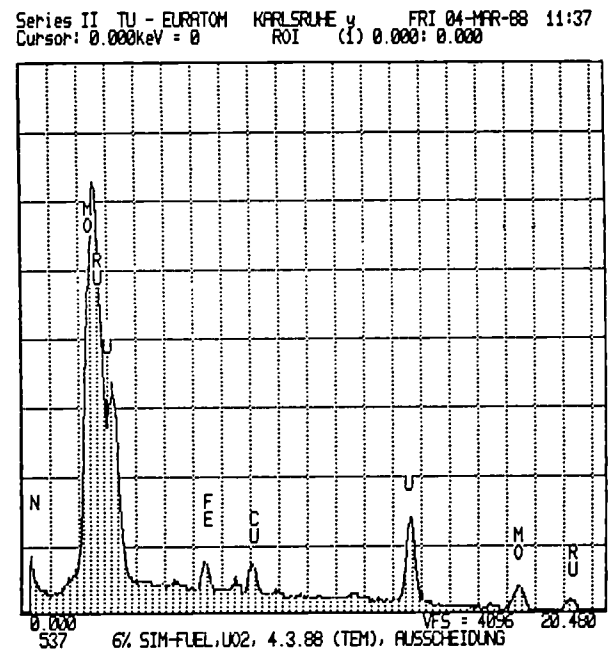


Fig. 1.21 Energy dispersive X-ray spectrum from the spherical precipitates imaged in Fig. 1.20.

In addition to this precipitation, another marked feature of the microstructure of SIMFUEL samples annealed at high temperatures (1500°C) is a dark scaling visible on some of the grain faces, as can be seen clearly in Fig. 1.22. Energy dispersive X-ray analysis showed this scale to be

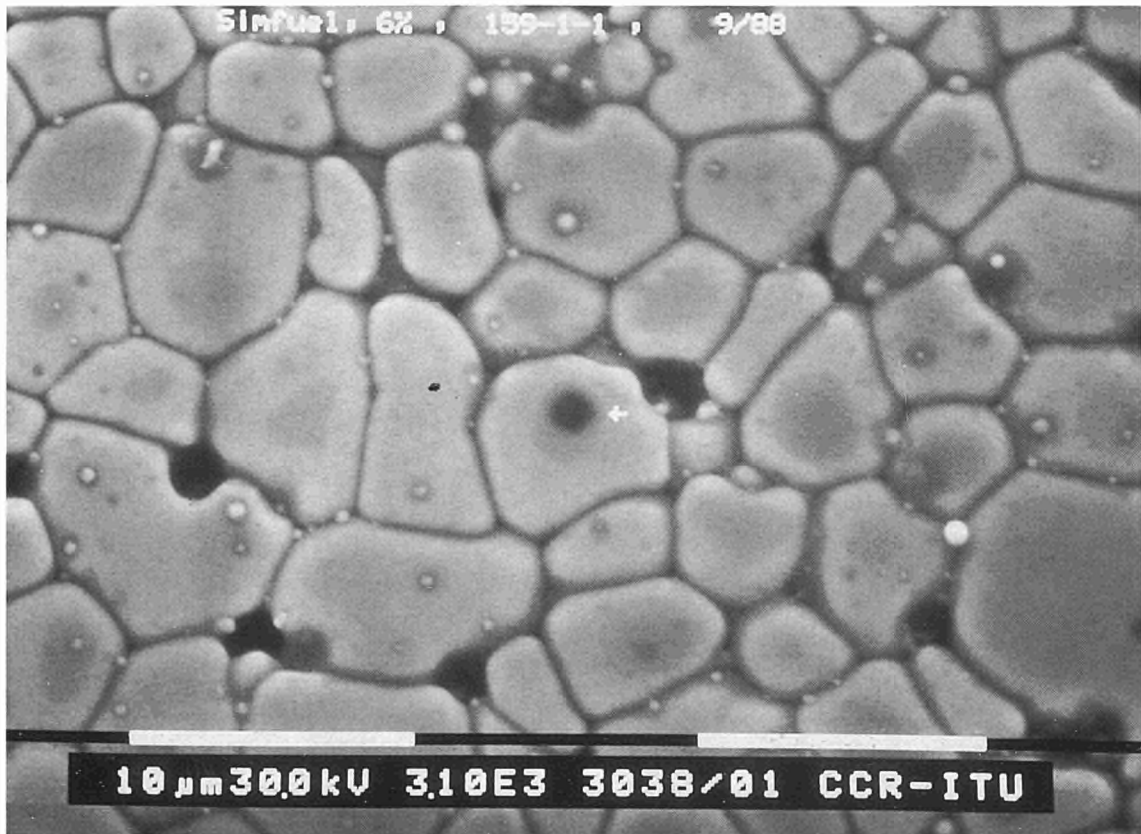


Fig. 1.19 SEM micrograph of the surface of 6% SIMFUEL sample 159-1-1 showing clearly defined grain boundaries.



Fig. 1.20 High magnification micrograph of part of the same area showing the spherical Mo/Ru precipitates.

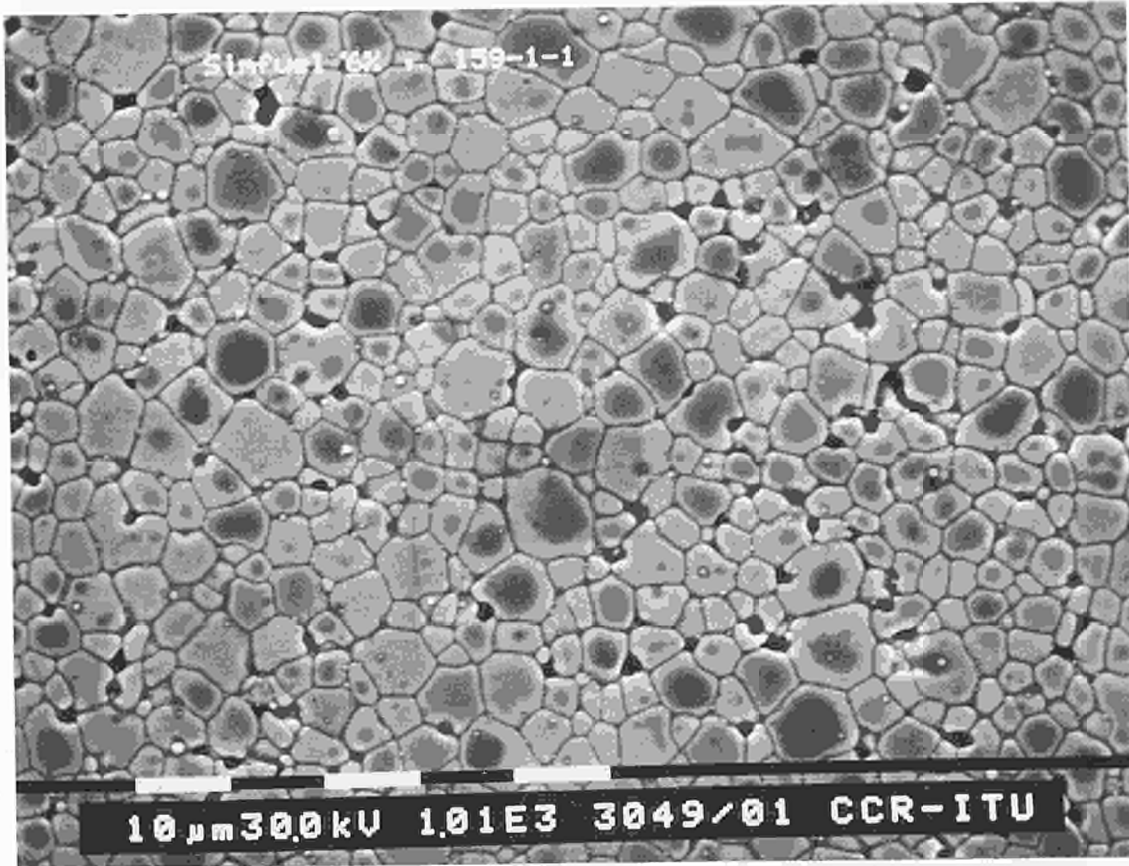


Fig. 1.22 SEM micrograph showing the dark surface scaling on the sample after annealing, found to be rich in Ba.

rich in barium. An example of the analysis is shown in Fig. 1.23.

An attempt was made to estimate the thickness of this scale by operating the microscope at progressively lower accelerating voltages down to about 5kV, and recording the energy

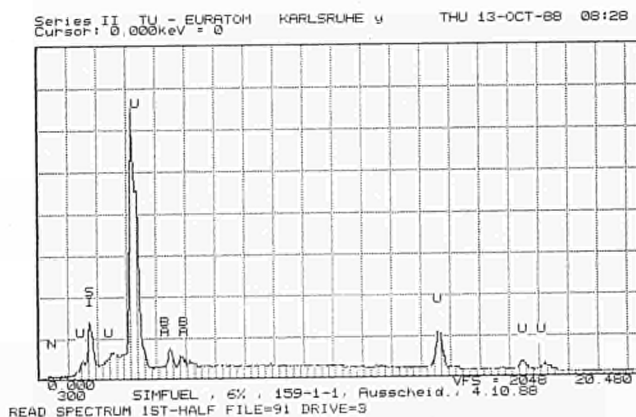


Fig. 1.23 Energy dispersive X-ray analysis of the surface scale.

dispersive X-ray spectra at each stage. The spectra were then semi-quantitatively analysed using a programme which compensates for the change in excitation probability with voltage, and it was found that the uranium signal from the UO_2 substrate had effectively disappeared by 5kV. From this it is estimated that the layer has a thickness greater than 75nm, and this can be taken into account in analysing the results from the Kr and Xe ion bombardment experiments.

Transmission Electron Microscopy

Specimens of the as-received non-ion-implanted SIMFUEL were prepared for the transmission electron microscope by electropolishing. Typical microstructures are shown in Fig. 1.24 and Fig. 1.25.

These transmission samples showed the formation of precipitates, particularly on the grain boundaries and triple points. Energy

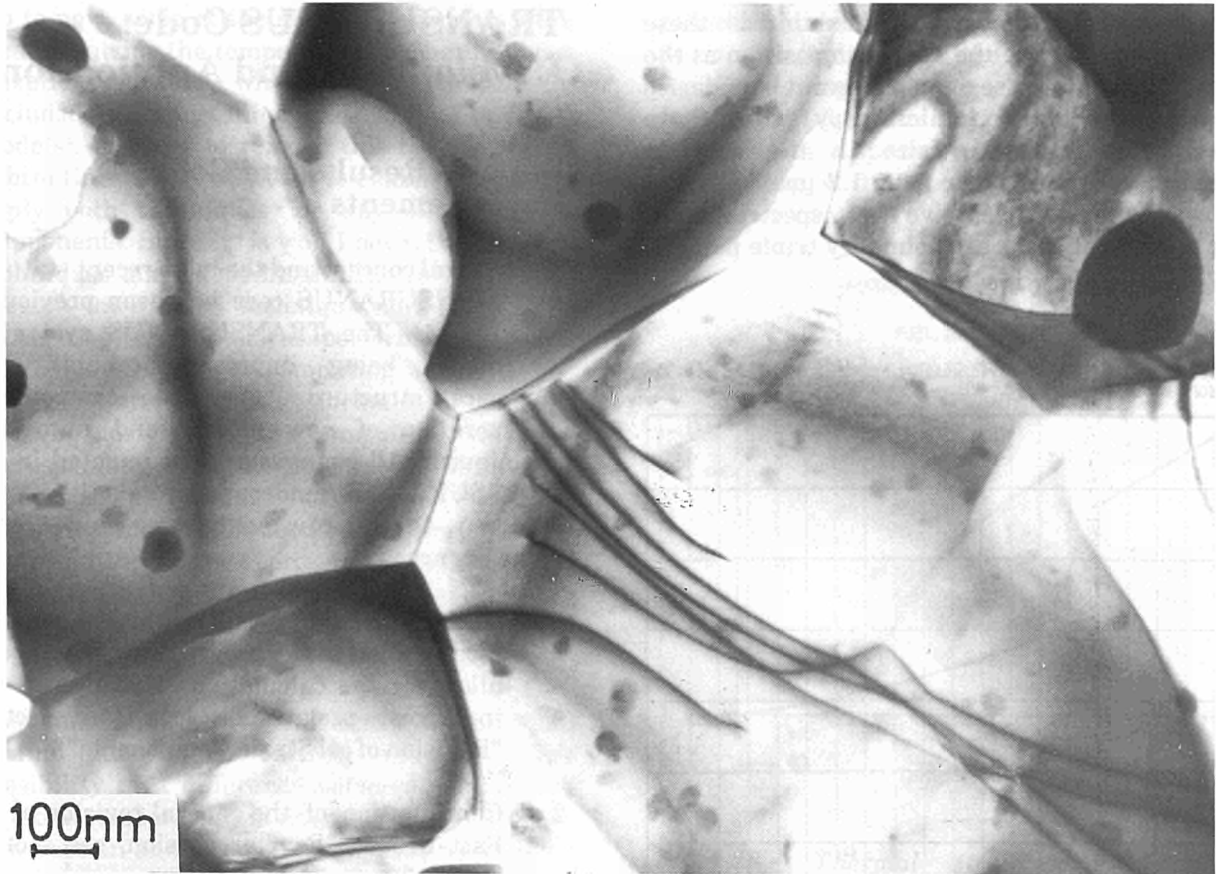


Fig. 1.24 TEM micrograph of the as-received material, before ion bombardment, showing a fine grain structure.

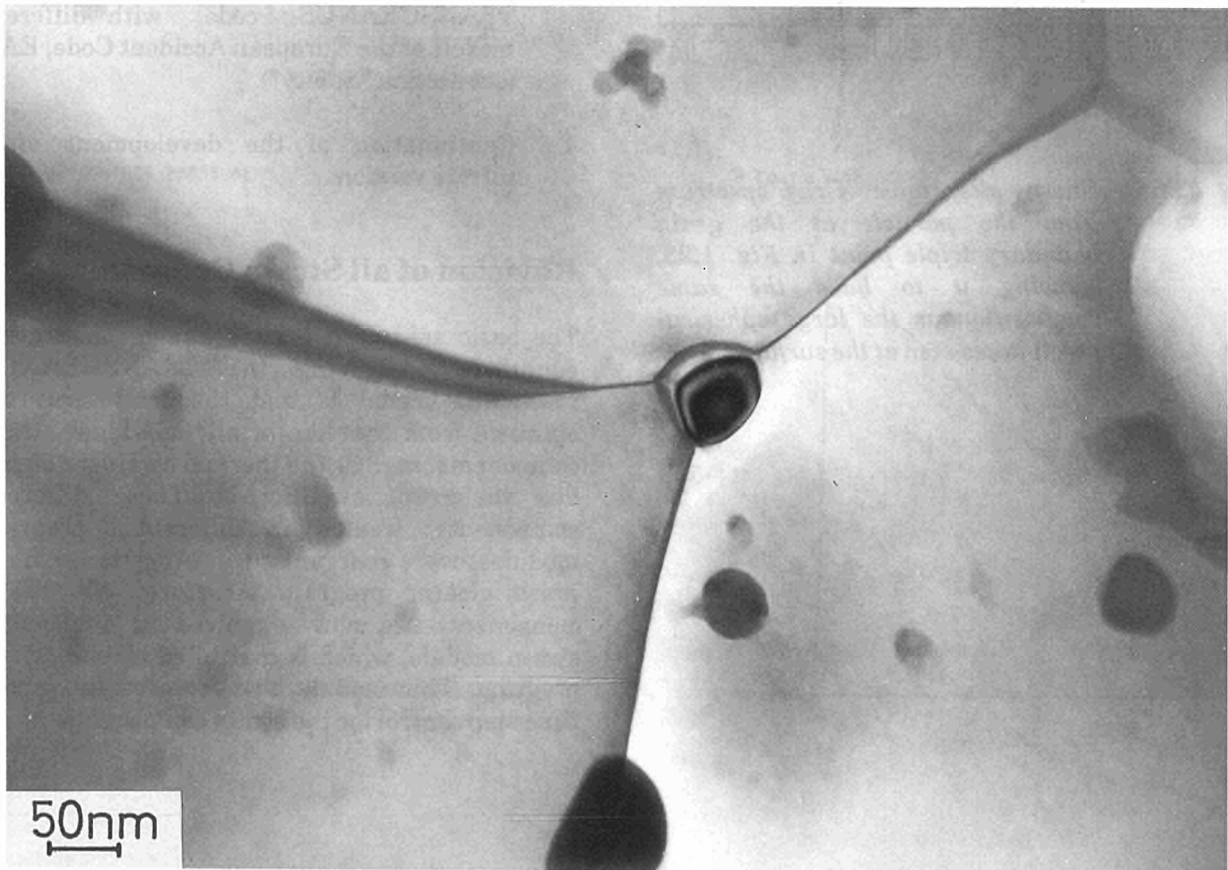


Fig. 1.25 TEM micrograph showing precipitation at a grain boundary triple point.

dispersive X-ray analysis exhibited these precipitates to have the same composition as the larger precipitates seen on the grain boundaries by scanning electron microscopy. Thus these precipitates range in size in the samples examined from 40nm to over 1.2 μm . Fig. 1.26 shows the energy dispersive X-ray spectrum from the particle at the grain boundary triple point in Fig. 1.25.

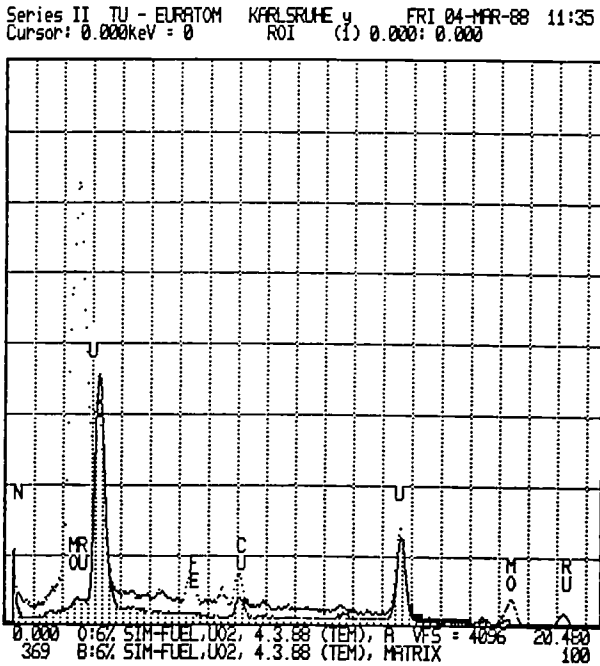


Fig. 1.26 Energy dispersive X-ray spectrum from the particle at the grain boundary triple point in Fig. 1.25, showing it to have the same composition as the large spherical precipitates seen at the surface.

TRANSURANUS Code: Development and Applications

General Results and Code Improvements

The general concept and the most recent status of the TRANSURANUS code has been previously reported [1]. The TRANSURANUS system is continually being improved (reliability of numerics, structure of code components, incorporation of new models and numerical techniques). All changes are documented in the TRANSURANUS-Aenderungsprotokoll [2]. Basically, the improvements were made in the following areas:

1. General revision of all strain components; modification of the programme structure to allow for the calculation of strains in the innermost programme loop (see section "Revision of all Strain Components").
2. Continuation of the general revision of the Fast Breeder Reactor version, see section "Safety".
3. Incorporation of interfaces to couple the TRANSURANUS code with different models of the European Accident Code, EAC (see section "Safety").
4. Continuation of the development of a nitride version.

Revision of all Strain Components

The basic assumption made in the constitutive equations underlying the TRANSURANUS mechanics model is that the total strain is obtained from the sum of all individual strain components, such as the thermal strain, or strain due to creep, swelling etc.. These different components, treated in different program modules, were reorganised in order to obtain a much clearer program structure. All strain components are now organized in one single strain module, which is controlled by one driver program. This module also contains the whole time step control for the strain components.

Up to now, some of the strain components were treated outside the temperature-mechanics loops ("explicit" models), while some of them were included in this innermost loop ("implicit" models). In order to remove this restriction, all subroutines were rewritten to enable the user to apply both techniques for any of the strain components. Since it is well known that explicit techniques may cause instabilities or numerical "noise", an implicit technique may result in a much better numerical performance at the expense of increased computing costs. As an example, an explicitly formulated gaseous swelling correlation was compared with the corresponding implicit treatment. Since the numerical performance of a local swelling correlation can best be seen by an integral effect, the resulting contact pressure was chosen to demonstrate that effect. The comparison between Figs. 1.27a) and b) clearly demonstrates the improvements obtained.

The subroutine which calculates the thermal strains had to be entirely rewritten. The possibility of a difference between solidus and liquidus temperature is now considered. For the new version an incremental algorithm had to be adopted because the assumption is made that part of the volume increase due to melting is compensated for by the existing porosity, i.e. the

remaining porosity is filled up to a certain extent by molten fuel. Due to the discontinuity at the melting temperature (see Fig. 1.28) the incremental formulation is rather complicated. However, by a special test program the correct functioning of this strain component has been proven.

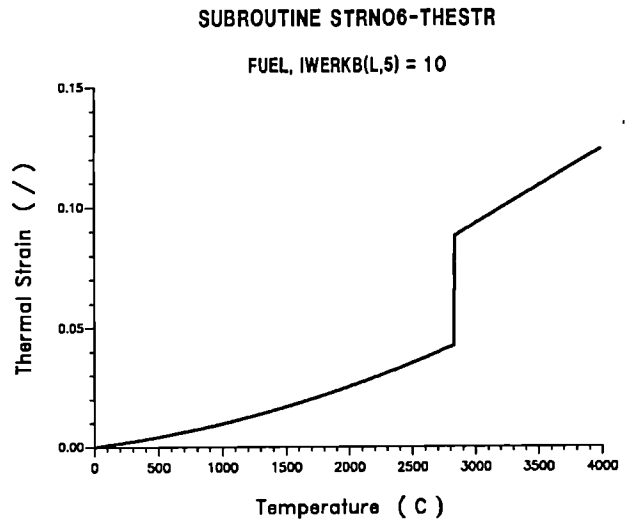


Fig. 1.28 Thermal strain as a function of temperature: the discontinuity at the melting temperature requires a special incremental algorithm.

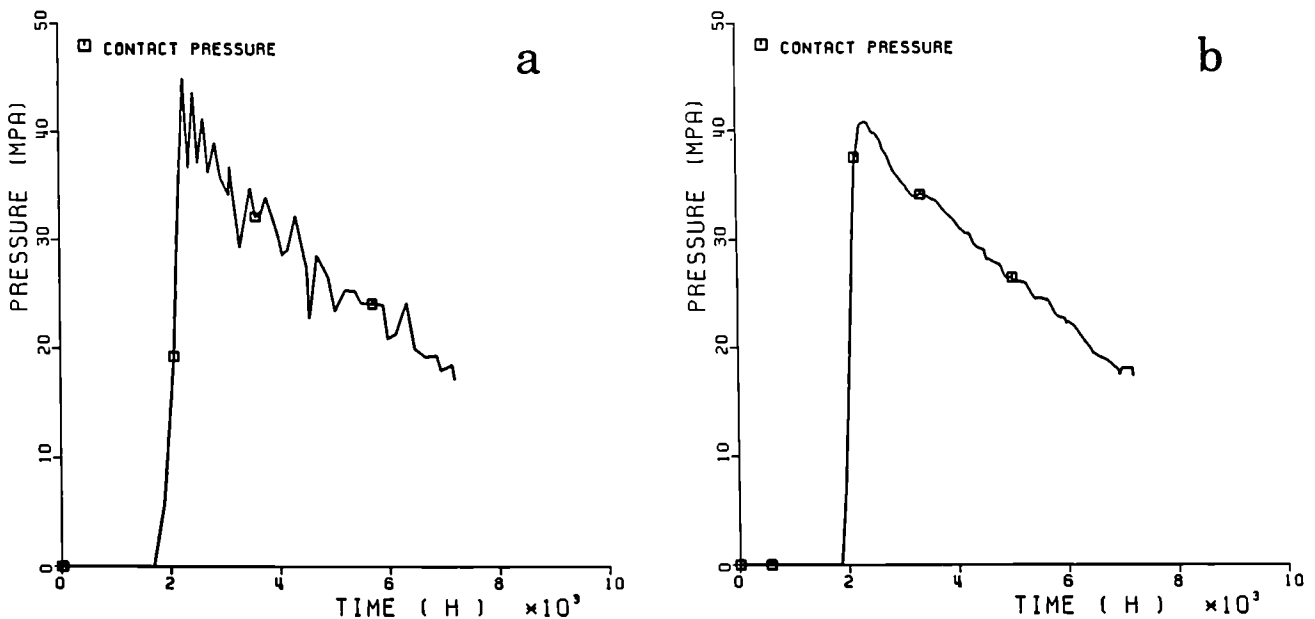


Fig. 1.27 Contact pressure due to gaseous swelling as a function of time: a) explicit treatment, b) implicit algorithm; the results refer to a typical PWR fuel rod.

Influence of a Non-Uniform Power Density on the Radial Temperature Profile in a LWR Rod

In the fuel of a light water reactor a flux depression exists which results in a lower power density at the centre of the fuel than near the fuel pellet surface. This non-uniform radial power density distribution causes a somewhat lower centre-line temperature than that obtained by the assumption of a constant power density at the same linear rating. The effect can be explained quite easily. Since in both cases the heat flux at the surface of the fuel is identical, the temperature gradient at the surface must be the same; however, since in the case of a non-uniform power density the power density decreases towards the centre of the fuel, the temperature gradient must also decrease more than in the case of a constant power density.

During the 6th International Seminar on Mathematical/Mechanical Modeling of Reactor Fuel Elements, Kippel, Switzerland, August 24-25 (1987), the influence of this effect on the radial temperature distribution was vigorously discussed and the purpose of the investigation presented here was to present a quantitative analysis and to establish whether this effect is significant or not. Details of the analysis are being published [3]; two typical results are shown in Figs. 1.29 and 1.30.

The following conclusions are drawn:

- The rather low flux depression at the start of the irradiation has only a minor influence on the centre-line temperature.
- The influence of the radial power density profile at high burn-up must be taken into consideration. This does not raise difficulties if numerical techniques are applied to calculate the radial temperature profile. Nevertheless, it is somewhat difficult to include this effect in a simple analytical solution but at least an approximate correction should be applied in these cases.

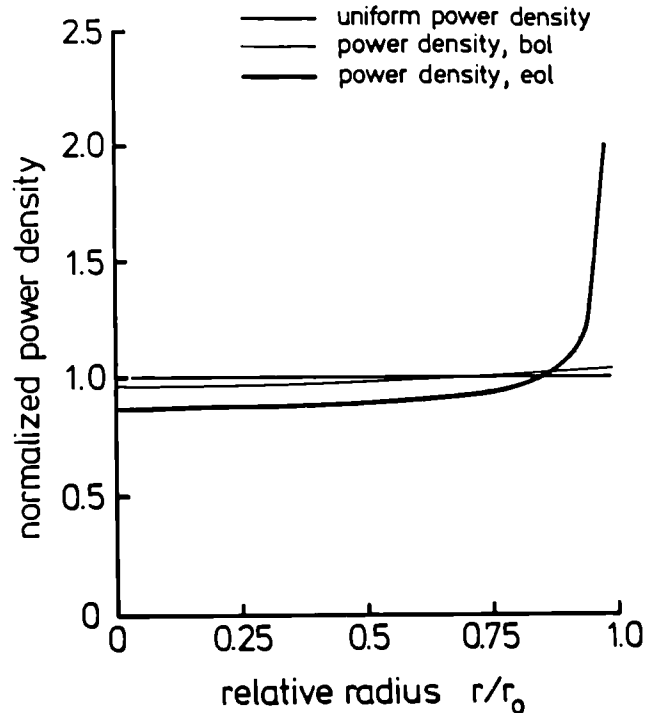


Fig. 1.29 Normalized power density as a function of the relative radius at different burn-up levels: the results refer to a typical PWR fuel rod (BOL \equiv 0 at.%, EOL \equiv 3 at.%).

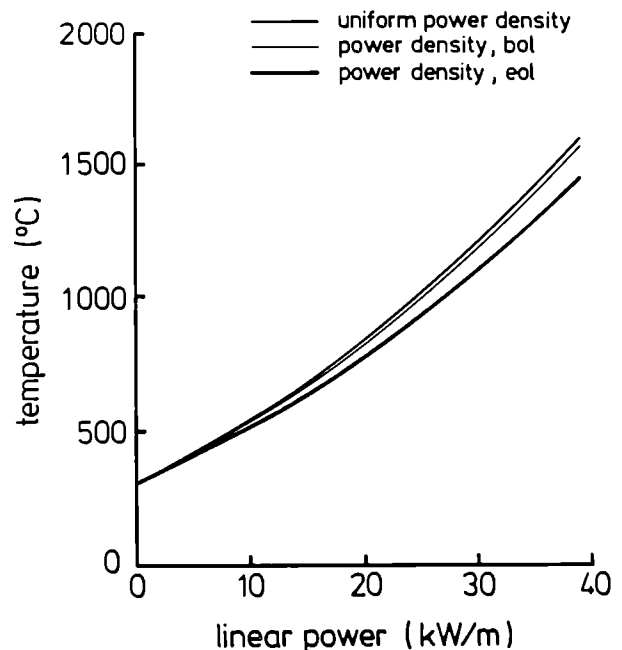


Fig. 1.30 Centre-line temperature as a function of the linear power; parameter is the power density distribution (BOL \equiv 0 at.%, EOL \equiv 3 at.% for a typical PWR fuel rod)

Comparison between the Fuel-to-Cladding Gap Conductance Models URGAP and GTEMP With Out-of-Pile Experiments

An accurate determination of the fuel-to-cladding gap conductance (heat transfer coefficient) in the fuel rods of a nuclear reactor is of extreme importance for assessing the thermal behaviour of fuel rods under both normal and off-normal conditions. Consequently, the model for the gap conductance should provide a reasonable description for all reactor conditions, i.e. for different gap widths, gas compositions, contact pressures and the surface characteristics of the fuel and the cladding. Two gap conductance models which fulfill these requirements, the URGAP model [4] and the GTEMP model [5], were compared with the out-of-pile data of Garnier and Begej [6,7]. Because of the large variety of conditions covered, these data furnish a good experimental data base for theoretical model benchmarking. Both models have been used successfully in many fuel rod analyses. Although the two gap conductance models URGAP and GTEMP differ in some distinct model assumptions, they have many similarities. Both models show the same prediction capability. The discrepancies between the predictions and the experimental data can be understood on the basis of a statistical analysis which takes the indeterminate errors into account. Thus, the indeterminate errors preclude justifying specific model assumptions and therefore both models adequately describe the data. The detailed analyses performed are described in [8]; all predicted and measured results under "light" contact are compared in Fig. 1.31.

Transfer of the Code TRANSURANUS to the Technischer Überwachungs-Verein Baden e.V.

In the frame of a contract between the Institute and the Technischer Ueberwachungs-Verein (TÜV) Baden e.V., concerning transfer of knowledge in the area of fuel rod behaviour modelling, several analyses for typical LWR conditions (PWR and BWR) were performed in order to demonstrate the capabilities of the TRANSURANUS code (e.g. [9]). For the BWR analysis an extremely complicated power history was deliberately selected and examples are given

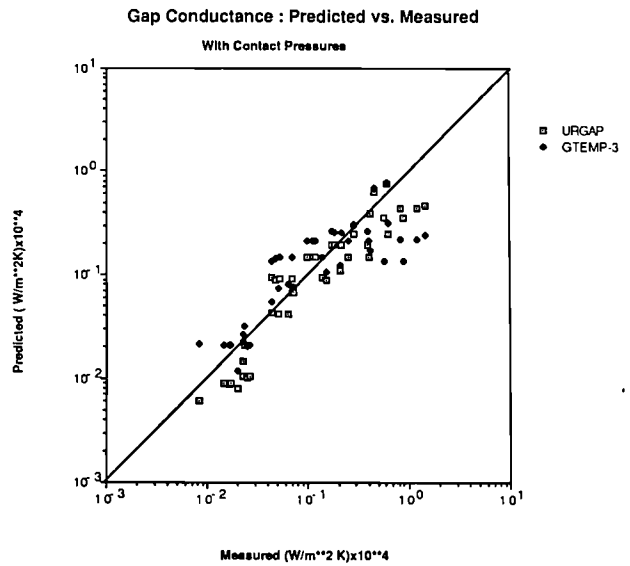


Fig. 1.31 Comparison between the predicted gap conductance according to the URGAP and GTEMP models with the experimental data of Garnier and Begej [6] and [7].

in the following figures: Fig. 1.32 shows the variation of the power as a function of time,

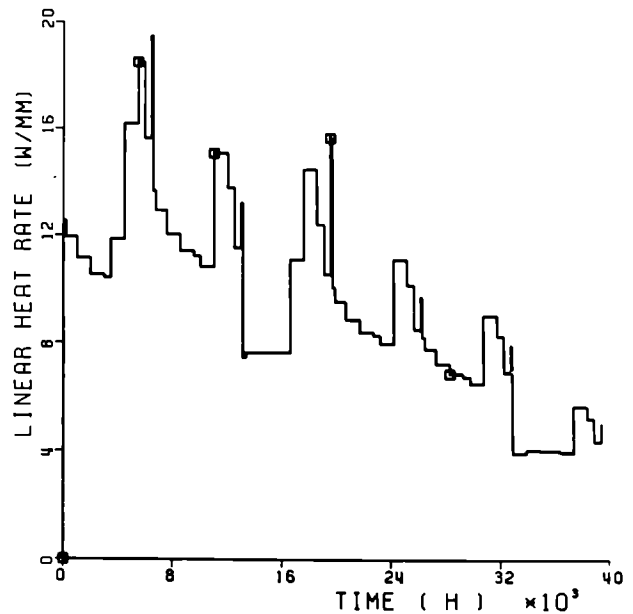


Fig. 1.32 Linear rating as a function of time for the BWR data case analyzed: the curve corresponds to a lower fuel rod section.

Uranium Dioxide: Zircaloy-4 Interfaces, Stage I: Low Gas Pressure', NUREG/CR-0330 (1979) 1, R3.

- [7] J. E. Garnier, S. Begej, 'Ex-Reactor Determination of Thermal Gap and Contact Conductance Between Uranium Dioxide: Zircaloy-4 Interfaces, Stage II: High Gas Pressure', NUREG/CR-0330 (1980) 2, R3.
- [8] R. Jansson, K. Lassmann, A. Massih, 'Comparison between the Fuel-to-Cladding Gap Conductance Models URGAP and GTEMP with Out-of-Pile Experiments' (Oct. 1988), to be submitted.
- [9] K. Lassmann, 'Analyse eines BWR-Brennstabs mit dem TRANSURANUS Rechenprogramm', Technical Note K0288111 (Jan 1988)

Program FUTURE - Fuel Transient Ultimate Response - Status of the Code and Test Calculations

Introduction

The code FUTURE has been developed at the Joint Research Centre in Karlsruhe over several years. Its aim is to calculate some important physical effects of the fuel (swelling, cladding deformation, gas distribution and release) under transient irradiation conditions.

FUTURE was not conceived as a comprehensive code at the outset. It has evolved as a collection of models and sub-models, new ones being added to improve the results or to replace obsolete ones.

This has resulted in:

- A code that is rather heterogeneous and difficult to handle for anyone not familiar with it.
- Cases in which the code has had numerical troubles that prevented it from finishing the calculation correctly.
- Computing costs which were judged to be too high for convenient, extensive use of the code (about 1.1 to 2.6 CPU seconds (IBM 3090) for each time step and each fuel zone in a pin section, that is about 30-60 seconds for a typical case).

It was therefore decided to revise the code before releasing it for external use.

Present State of Future

Present situation

The code is still in the revision and validation phase. This is being achieved by simulating several in pile and out of pile experiments, and comparing the results with the available experimental data. Usually the code finishes the run without errors, but sometimes problems arise from a lack of convergence of a numerical integration algorithm.

Documentation

Documentation on the program is now available. Its aims are twofold:

- To give clear and well defined instructions to the end user on how to use the code correctly (this has been achieved).
- To establish the cross references for all the models contained in the code (this is far from complete).

This documentation is being updated as new models are introduced, or modified.

Input / Output

The input of the program is now completely compatible with the output of TEMPGAP, an auxiliary program that calculates the temperature profile in the pin.

The output has been completely rewritten in a clear and compact form. The units used in the code (especially for input-output) are gradually being converted to SI (International System). SI units are inserted in every revised part.

Computing Costs

These have been slightly reduced relative to the

prototype version (about 0.8 to 1.1 seconds for each time step and each fuel zone). This was achieved by formal modification to the structure of the code (the modified parts have been rewritten following the rules of "Structured Programming"), without affecting the substance of the algorithms.

Application

Two groups of experiments have been simulated so far using the code FUTURE: those performed at KWU and the Institute, and those performed more recently at Harwell [1].

The comparison between the results of one of the KWU experiments and the corresponding FUTURE calculations are presented here. The experiment consisted of a pre-irradiation of about 38 months and a transient of 12 hours, with power ratings of 21410 and 40350 W/m, on uranium dioxide pellets with Zircaloy cladding.

Some of the fuel characteristics are listed below:

- Pin radius = 4.6mm.
- Inner cladding radius = 4.67mm.
- Outer cladding radius = 5.375mm.
- Initial grain diameter = 5.5µm.
- Initial fuel porosity = 5.5%.
- Coolant pressure = 15MPa.

Temperature Profile : These values were calculated with the auxiliary program TEMPGAP. No experimental data are available for comparison. In Fig.1.36, the temperature

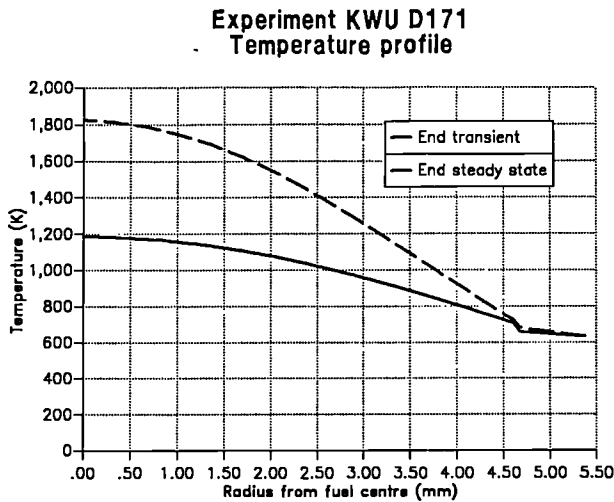


Fig. 1.36 Temperature versus the pin radius at the end of the steady state and transient.

versus, the pin radius at the end of the steady state and the transient is shown.

Grain Diameter : The predicted distribution of mean grain diameter as a function of pellet radius in the ramped fuel is compared with the experimental data obtained at JRC Karlsruhe (Fig. 1.37). It is clear that the code has failed to

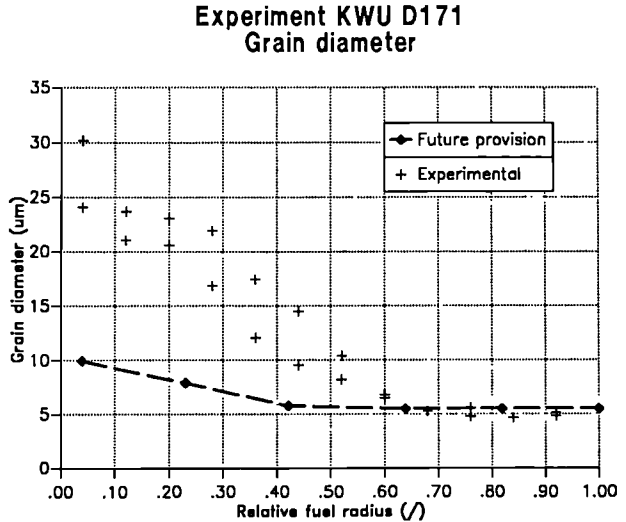


Fig. 1.37 Grain diameter (µm) versus the pellet relative radius at the end of the transient.

predict the substantial grain growth observed in the hotter, central region. However a slight over-prediction of the grain growth was obtained for another fuel cross section that had been ramped to a higher temperature. This seems to indicate that perhaps the FUTURE model for grain growth overestimates the effect of temperature.

Optically Visible Porosity : The data predicted by FUTURE are compared with the experimental data obtained at JRC Karlsruhe (Fig. 1.38). Agreements satisfactory for all the data.

Radial Xenon Profile : The distribution predicted by FUTURE is compared with the experimental data obtained at JRC Karlsruhe (Fig. 1.39). Only xenon retained within the grains is considered here, because a part escapes during the measuring process, when big bubbles are cut. The xenon concentration at the perimeter of the pin is more than 100 % because data have been normalized to the average xenon produced. This accumulation at the edge of the pin is due to the so called "skin effect" (a higher Pu concentration

Experiment KWU D171
Optically visible porosity

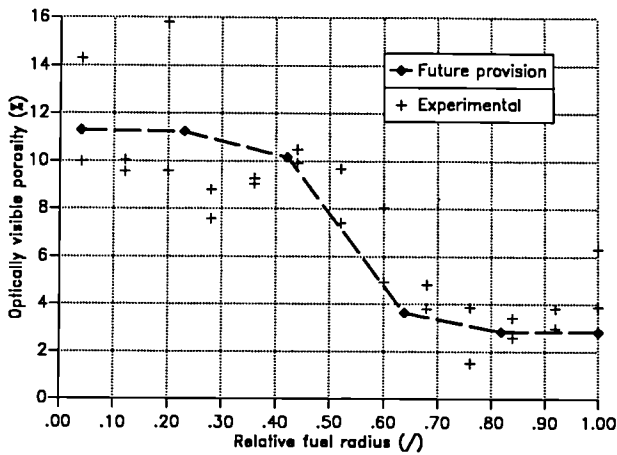


Fig. 1.38 Optically visible porosity versus the pellet relative radius at the end of the transient.

Experiment KWU D171
Fractional gas release

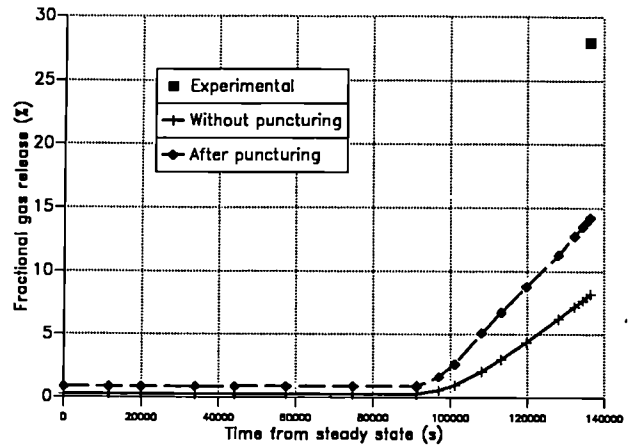


Fig. 1.40 Fractional gas release versus the irradiation time during the transient.

Experiment KWU D171
Xenon profile

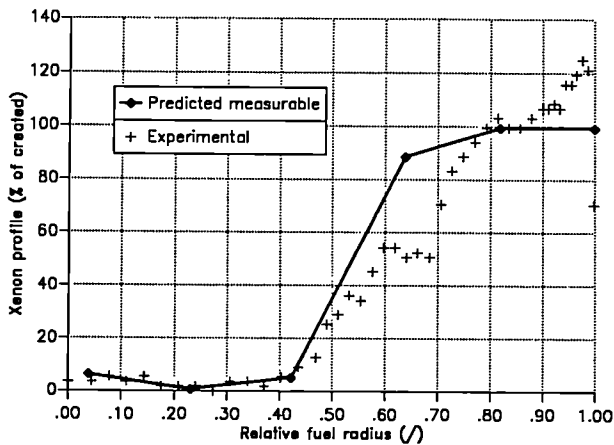


Fig. 1.39 Xenon profile versus the pellet relative radius at the end of the transient.

Conclusions

The code FUTURE has yielded a large amount of relevant physical predictions in previous years. Its basic validity has been confirmed by numerically simulating actual experiments.

It has been found that sometimes FUTURE does not converge to a sensible result for a particular physical variable, without affecting the validity of other ones. Even in this case it is possible to obtain useful information.

This fact, together with some unsatisfactory results, leads us to conclude that the process of validation for the whole program is not yet finished, and that the code is not yet ready for general release.

Reference

[1] G.J.Small, Proc. IAEA Specialists' Meeting on LWR Fuel Performance Modelling, Preston, England (1988).

induces a higher Xenon production rate), that was not considered in our calculations.

Fractional Gas Release : The FUTURE predictions are compared with the experimental data in Fig. 1.40. Two curves are presented in the figure. The curve marked "after puncturing" is

that calculated without external pressure on the pin while the other is calculated for the case when the pin is closed and fission gas cannot escape. Measured values in this experiment must be compared with the "after puncturing" curve. For other experiments, with a very low gas release, FUTURE gives a value greater than the measured one.

Comparison of "Future" with Recent Transient Fission Gas Release Data

Predictions of the mechanistic fuel performance model FUTURE have been compared with recently published fission gas release data [1]. In these experiments small samples of UO_2 which had been irradiated to 1.9 % burn up at low temperature (with negligible gas release) were heated at ramp rates of 1.0, 12.5 and 50.0 $\text{K}\cdot\text{s}^{-1}$ to temperatures in the range 1773 - 2273 K. The release of fission gases during these post-irradiation transients was characterized in all cases by a pronounced burst (up to 50 % of the initial inventory) on heating followed by slower but finite release during subsequent periods at high temperature. Significant release was always accompanied by the appearance of interlinked grain boundary porosity and the population of intragranular bubbles was found to coarsen with increasing annealing time and/or temperature.

These experiments represent the worst case conditions proposed for thermal reactor power/coolant mis-match faults and the release rates are greater than those previously recorded in experiments employing slower ramp rates. Thus they also provide an exacting test for the FUTURE code which until now has been evaluated against the slower transients.

The basic mechanisms for fission gas release considered within FUTURE are

1. The diffusion of gas atoms to the grain boundaries.
2. The simultaneous precipitation of gas into intragranular bubbles which subsequently coarsen and inhibit diffusion.
3. The development of porosity on the grain faces.
4. Venting of the grain face pores via interconnected grain edge porosity, leading to release from the macroscopic confines of the fuel pellet.

The grain boundaries can also collect gas by a grain boundary sweeping mechanism. Thus the release (and swelling) kinetics are controlled almost entirely by these microstructural processes.

The version of FUTURE available at present is still being checked for programming and

calculational errors. However this checking is sufficiently advanced for the evaluation exercise to proceed. FUTURE was used to simulate the condition of the fuel samples during the base irradiation and for a selected number of transients. After the base irradiation with maximum temperatures falling from 1300 to 1100 K the predicted fission gas release was low (2.3 %), in agreement with post-irradiation examination [2]. However the calculated porosity of 7.3 % at the pellet centre does not agree with metallographic observations which showed no grain boundary bubbles.

The calculated fission gas release is compared with data from six of the transient experiments in Tab. 1.6. No attempt has been made at this stage to alter the models to improve agreement. Agreement is in general adequate although the predicted transition between the rapid release during the ramp and the relatively slow release under isothermal conditions was not as sharp as that observed in the laboratory. This is illustrated by Fig 1.41 in which the predicted and measured release rates are compared for a transient at 12.5 K/s to 1973 K.

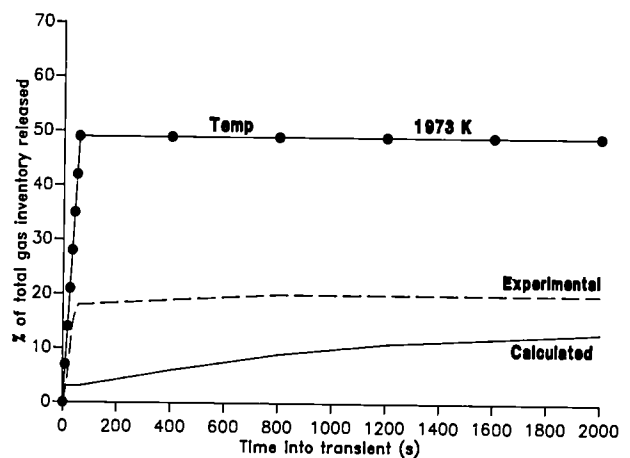


Fig. 1.41 Experimental and calculated fission gas release on rampling at 12.5 K/s to 1973 K

These initial FUTURE calculations indicate that after the base irradiation the majority of the gas was in solid solution within the grains. The intragranular bubbles were very small (0.27 nm radius) and had reached their maximum permissible concentration of 10^{17} per cm^3 . Local concentrations on the grain boundaries ranged from 30 % of the total inventory in the hotter regions of the sample to only 0.5 % in the colder zone. During the transients the intragranular

Tab. 1.6. *Transient Fission Gas Release: Comparison between experimental data [1] and predictions using the code FUTURE. * estimated.*

Expt.	Burn-up (GWd/tU)	Ramp Rate (K/s)	Final. Temp. (K)	Dwell Time (s)	Gas Release	
					Ramp expt / calc	Total expt / calc
A3	18	1.0	1700	180	2.0 / 3.2	3.1 / 4.5
A6	18	1.0	2000	180	8.6 / 16.0	11.1 / 17.4
B3	18	12.5	1700	1800	16.1 / 2.8	20.3 / 13.2
B6	18	12.5	2000	1800	53.4 / 17.0	62.8 / 18.1
D1	18	50.0	1700	180	4* / 2.5	9.6 / 3.5
D4	18	50,0	2000	180	13.7 / 3.1	25* / 15.9

bubbles coarsened to varying extents, for example reaching a mean radius of 68 nm after 30 min at 2273 K. This was accompanied by only limited transfer of additional gas to the grain boundaries. Significantly, the total retained gas within the grains after the transients was almost identical in every case and independent of the transient conditions, which determined only the extent of intragranular bubble coarsening. As the grain face capacity reached a saturation level of about 10 % at an early stage the overall release level was controlled largely by the behaviour of the grain edge bubbles. The close relationship noted between the predicted grain growth and the predicted release may be relevant in this context. Although it has not yet been possible to carry out a detailed comparison between the observed and predicted microstructures, initial indications are that the degree of grain growth is slightly over-predicted as is the amount of swelling due to grain boundary porosity (up to 15%, compared with measured values of the order of 5%).

In summary, FUTURE has been shown to reproduce the observed fission gas release data with reasonable success for the slow (1 K.s⁻¹) ramps but the bursts associated with higher heating rates were under-predicted. These data appear [3] to be consistent with intragranular diffusion with no trapping [4] and no hold-up on the grain boundaries. They have also defied other transient gas release models.

References

- [1] G.J. Small - IAEA Technical Committee Meeting on Water Reactor Fuel Element Computer Modelling in Steady-state, Transient and Accident Conditions, T1-TC-659, Preston, England (Sept. 1988), paper 4.3
- [2] G.J. Small - Harwell Report AERE R11773 (1987).
- [3] G.J. Small & D.A. MacInnes - Harwell Report AERE R12803(1988).
- [4] Hj. Matzke - Rad. Eff. 53 (1980) 219.

References (to Introduction)

- [1] H. Blank, Hj. Matzke, R. Manzel, M. Coquerelle, I.L.F. Ray, C.T. Walker, K. Lassmann and C. Ronchi, "Behavior of UO₂ in Pressurized Light Water Reactors up to High Burn-up in Steady State and in Transient Operation", Jahrestagung Kerntechnik, Lübeck (1988), German Atomforum, Bonn, p. 433
- [2] Hj. Matzke, H. Blank, M. Coquerelle, I.L.F. Ray, C. Ronchi and C.T. Walker, "Oxide Fuel Transients", Proc. Int. Symp. Transuranium Elements Today and Tomorrow, Karlsruhe (1988), J. Nucl. Mater. 160 (1989) in print
- [3] Hj. Matzke and H. Blank: Fuel Research and Basic Aspects of Fuel In-Pile Performance", *ibid.*, J. Nucl. Mater. 160 (1989) in print

2 High Burn-up Chemistry

Progress of work in this field will be described in the 1989 Annual Report

3 Optimisation of Dense Fuels

Introduction

Mixed nitride (U,Pu)N is the reference fuel for a fast reactor cycle with a denser, optimised fuel than the currently used mixed oxide.

The project "Optimisation of Dense Fuels" was started in 1985 with a programme to fabricate, test and optimise "pure" mixed nitrides, i.e. fuels containing about 500 ppm carbon and oxygen each, for high burn-up in fast reactors. The work is carried out in collaboration with the Département d'études des combustibles à base de Pu, CEN Cadarache.

Since the required burn-up will be beyond 15 a/o the fuel density must be low, between 80 to 85 %, and the fuel structure in the He-bonded pins must nevertheless be sufficiently stable. Such a ceramic fuel had never been specified and tested before. Thus apart from two long term fast flux irradiations NIMPHE 1 and 2 carried out in collaboration with the DECPu, Cadarache, two related short term irradiations NILOC 1 and 2 were prepared and carried out by the Institute in the HFR, Petten, in order to quickly obtain results on the behaviour of these new porous fuels at beginning of life (BOL), when the fuel temperatures are highest in He-bonded pins.

For the fuel fabrication of NILOC 1 and 2 the "green pellets" (before sintering) were prepared by three different methods, i) by the conventional powder technique, ii) by direct pressing of the clinkers resulting from carbo-reduction and iii) by a modification of this method, the direct pressing of granules.

The analysis of the experiments NILOC 1 and 2 revealed an interesting dependence on the three methods of fuel fabrication for the fuel behaviour at BOL. The work carried out in 1988 led to a general understanding of the relations between fabrication, fuel structure after fabrication and in-pile behaviour of porous nitride and carbide fuels at BOL.

Fuel Fabrication, Characterisation and Irradiation

Fabrication and Characterisation of Mixed Nitride and Carbide Fuel Pins for the Irradiation NIMPHE 2

Fabrication

For the irradiation experiment NIMPHE 2, a capsule containing 5 nitride and 2 carbide standard Super-Phenix pins was prepared in collaboration with DECPu, CEN Cadarache. The nitride fuel for 3 pins was fabricated at Cadarache by carbothermic reduction of a ball milled mixture of UO_2 and PuO_2 powders, blended with carbon. The reaction product was consolidated in form of pellets by cold pressing after crushing and ball milling and sintered under a mixture of nitrogen and hydrogen at 2000 °K.

Nitride and carbide fuel pellets for 4 pins were prepared at the Institute. The nitride fuel was specified to have an oxygen and carbon content of less than 1000 ppm, the carbide fuel with less than 1000 ppm oxygen and 800 ppm nitrogen and a pellet density of 82 % TD. The cladding and structural material was prepared and delivered by CEN Cadarache.

Both carbide and nitride fuels were synthesized by carbothermic reduction of a blend of $UO_{2+x} + PuO_2 + C$ powder. The starting carbon powder was "UF2" (18 m²/g), previously investigated (TUAR 86, 26). The PuO_2 (2.5 m²/g) and UO_{2+x} (2.4 m²/g) powders, delivered by CEN Cadarache, were sieved < 63 and < 125 µm respectively in order to diminish the agglomerate size, i.e. the diffusion distances, and improve both the kinetics of the carbothermic reaction and ensure a good microhomogeneity of the reaction

product. For the synthesis of both low oxygen nitride and carbide fuel, an excess of carbon with respect to the theoretically calculated quantity was used in the masterblend in order to assure the specified oxygen content below 1000 ppm. These powders were mechanically blended and pressed into pellets.

The carbothermic reduction for the nitride fuel preparation was carried out at 1900 K under flowing nitrogen for 4 hours for conversion of the oxide to nitride, followed by a thermal treatment under a gas mixture of nitrogen with 8 % hydrogen for 12 hours in order to remove the residual excess oxygen and carbon content.

The conversion of the oxide carbon blend into carbide was done at 1825 K for 6 hours under vacuum (1×10^{-2} torr). The reaction product contained 600 ppm oxygen and 7-12 % sesquicarbide due to the excess carbon in the masterblend.

For both carbide and nitride fuel preparation one part of the reaction product was comminuted in a fast turning hammer mill to particle sizes $< 60 \mu\text{m}$ and pressed into pellets by cold pressing (green density for nitride=75% and for carbide=67.5% TD). Fuel sintered from green pellets prepared by this method is called type C fuel. The other part of the pellets was directly recompacted into pellets with a green density of 73% TD for nitrides and 65% TD for carbides. Pellets sintered from this directly pressed green pellets are called type P fuel.

The carbide pellets were sintered at 2020 K under vacuum for 8 hours and the nitride pellets at 2000 K for 17 h under a nitrogen/hydrogen mixture and cooled from 1725 K to room temperature under vacuum or argon atmosphere.

The pellets were loaded into stainless-steel tubes, filled with helium, and T.I.G. welded. The fuel pins were sent after intermediate and final control to Cadarache for assembling together with the fuel pins fabricated by DECPu. The irradiation in the Phenix fast breeder reactor started in October 1988. Fuel and fuel pin data are reported in Tab. 3.1.

Characterisation of nitride and carbide pellets of Type NIMPHE 2

Fuel pellets of the NIMPHE 2 production were analysed by quantitative ceramography, SEM, mercury porosimetry for open porosity and alpha-

autoradiography for plutonium distribution.

The pellets:

- type P were used for the pins N° 3(MN) and 5 (MC)
- type C were used for the pins N° 2 (MN) and 4 (MC).

Alpha autoradiography of pellet cross-sections (Fig. 3.1), show that plutonium is homogeneously distributed in the nitride fuel type C, whereas plutonium depleted areas (dark spots) were detected in the type P. Plutonium is inhomogeneously distributed in carbide pellets: the white spots in Fig. 3.1 represent plutonium enriched zones.

The open porosity (pores which are connected to the outside of a pellet) was measured by mercury porosimetry. Tab. 3.2 shows that the open porosity represents more than 85% of the total porosity of carbide and 95% of the nitride pellets. Consequently most of the pores are connected to the outside of the pellets and form a network of channels. The average diameter of these channels ranges between 1.5 and 2 μm .

The typical microstructures of carbide and nitride pellets in Fig. 3.2 show the planar sections of pores and grains. The porosity of the carbide type C was found to be homogeneously distributed whereas the type P displays a high concentration of pores in the central part of the pellets (Fig 3.3). The nitride pellets type C are by about 12 % less dense at the periphery than in the centre. In nitride type P the pores are mostly located around zones (about 60 μm size) with very high density. The mean values of the porosity measured at three radial positions in pellet cross-sections of each type of fuel are plotted in Fig.3.3.

SEM micrographs of fracture surfaces from carbide and nitride are represented in Figs. 3.4a and b. Comparison of these structures with those of Fig. 3.2 shows that practically all pores are located on the grain boundaries and have a pseudo-ellipsoidal shape. The planar sections of pores and grains were analysed and the results are collected in Tab. 3.2. and 3.3. The discrepancy between the average values of pore size determined by Hg-porosimetry and light microscopy (Tab. 3.2) is due to the fact that only pores greater than 0.3 μm were measured by light microscopy.

Chemical etching ($\text{CH}_3\text{COOH} + \text{HNO}_3 + \text{H}_2\text{SO}_4$ mixture) revealed a phase of composition M_2C_3

Tab. 3.1 Data For Fuel Pins NIMPHE 2

Fuel data	PIN			
	2	3	4	5
Composition	(U, Pu) N	(U, Pu) N	(U, Pu) C	(U, Pu) C
Fabrication method	C*	P*	C*	P*
Pu/(U + Pu)	20.80	20.89	21.57	22.28
Fissile contents of Pu & U				
Pu-239 (w/o)	74.69	74.69	74.68	74.68
Pu-241 (w/o)	2.573	2.573	2.580	2.580
U-235 (w/o)	0.314	0.314	0.323	0.323
Fuel density (%T.D.)	82.04	81.45	80.16	80.57
Stand. deviation	0.23	0.28	0.29	0.49
XRD Param. Å	4.8911	4.8930	4.9659	4.9682
Second phase (w/o)	nd	nd	M ₂ C ₃ /11	M ₂ C ₃ /7
C (w/o)	0.015	0.056	4.94	5.06
N (w/o)	5.41	5.39	0.060	0.062
O (w/o)	0.065	0.068	0.051	0.037
Mean pellet diam. (mm)	7.122	7.163	7.175	7.108
Stand. deviation	0.006	0.007	0.009	0.008
Bonding	He	He	He	He
Gap (µm)	238	197	185	252

* P: Direct Pressing
C: Conventional

nd = not detected

(where M=U+Pu) dispersed in the carbide pellets. The amount of this phase, measured at three radial positions in pellet cross-sections is shown in Fig. 3.3. Comparison of the autoradiographs with the etched pattern of carbide fuels shows that the plutonium heterogeneities depicted in Fig. 3.1 are due to plutonium enrichment of the M₂C₃ phase.

The main results of this analysis can be summarised as follows:

- the open porosity of carbide and nitride fuels represents more than 85 % of the total porosity. Pores are located on grain boundaries and form a network of channels.
- the average value of the pore and grain size of carbide is lower than that of the nitride fuels
- carbide pellets may contain locally more than 20 % M₂C₃
- plutonium enriched and depleted zones were detected in carbide specimens of type P and depleted zones in nitrides of type P.

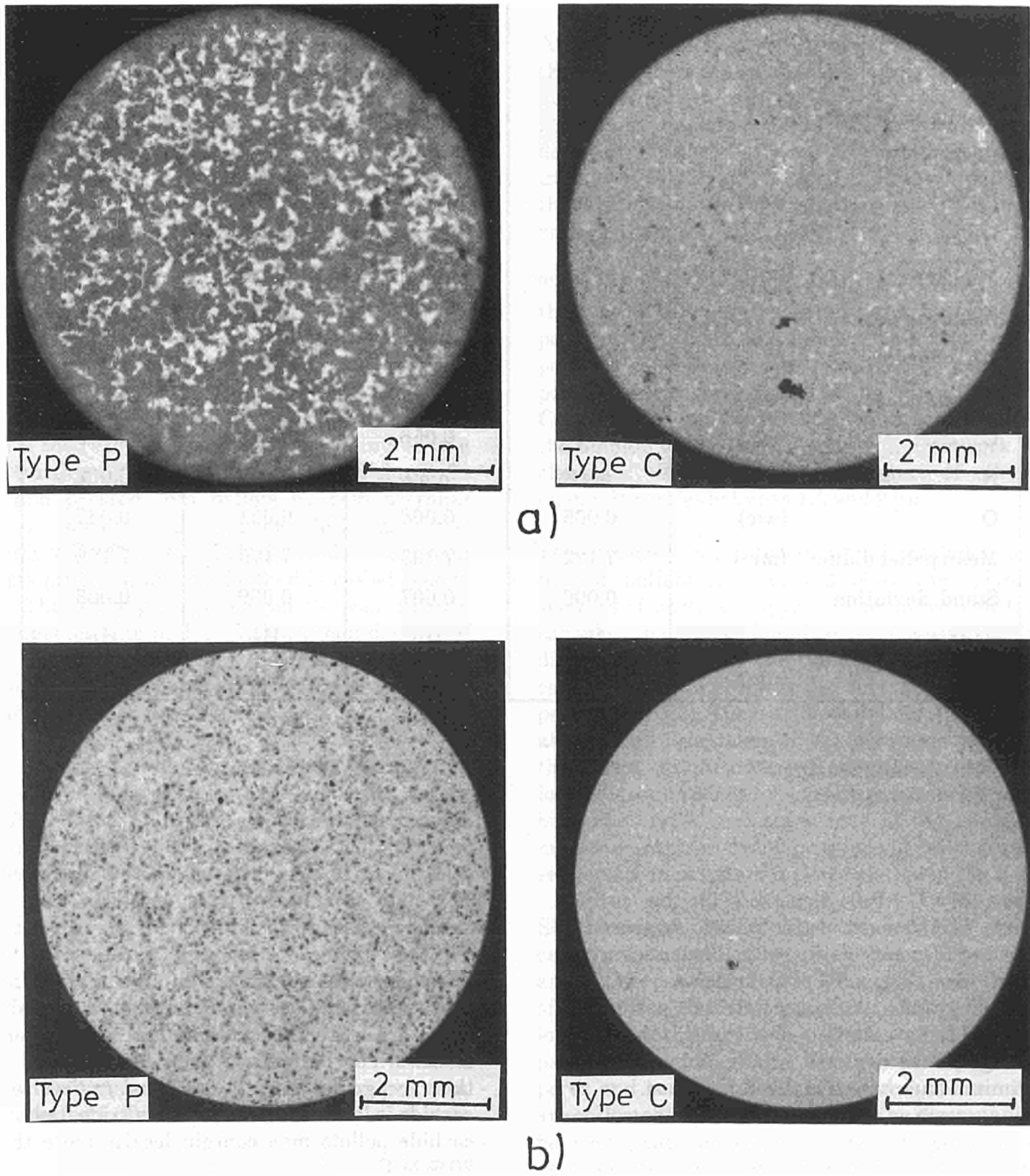


Fig. 3.1 *a*-autoradiographs of radial sections of a) carbide and b) nitride pellets

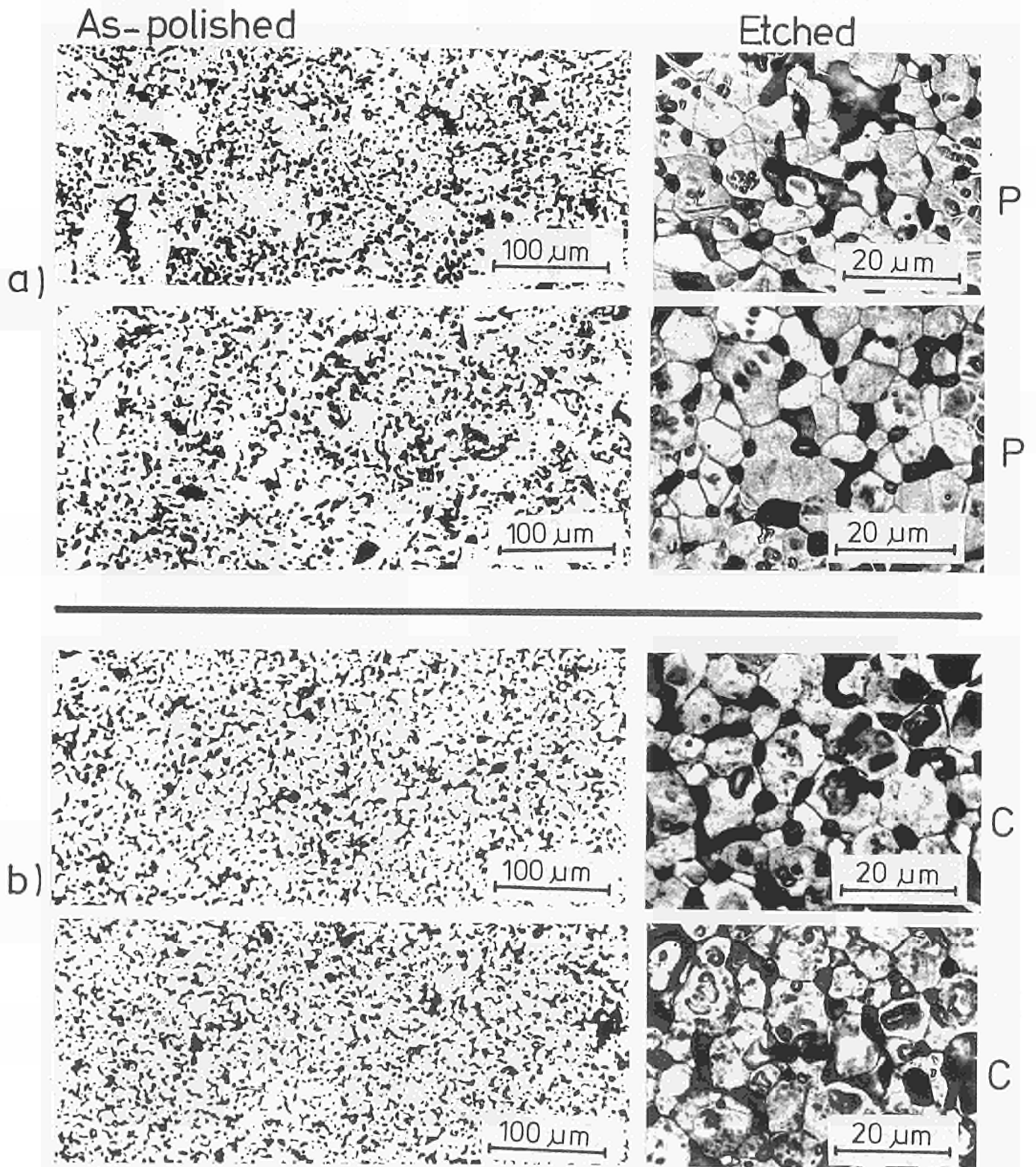


Fig. 3.2a Typical microstructure of carbide pellets

As-polished

Etched

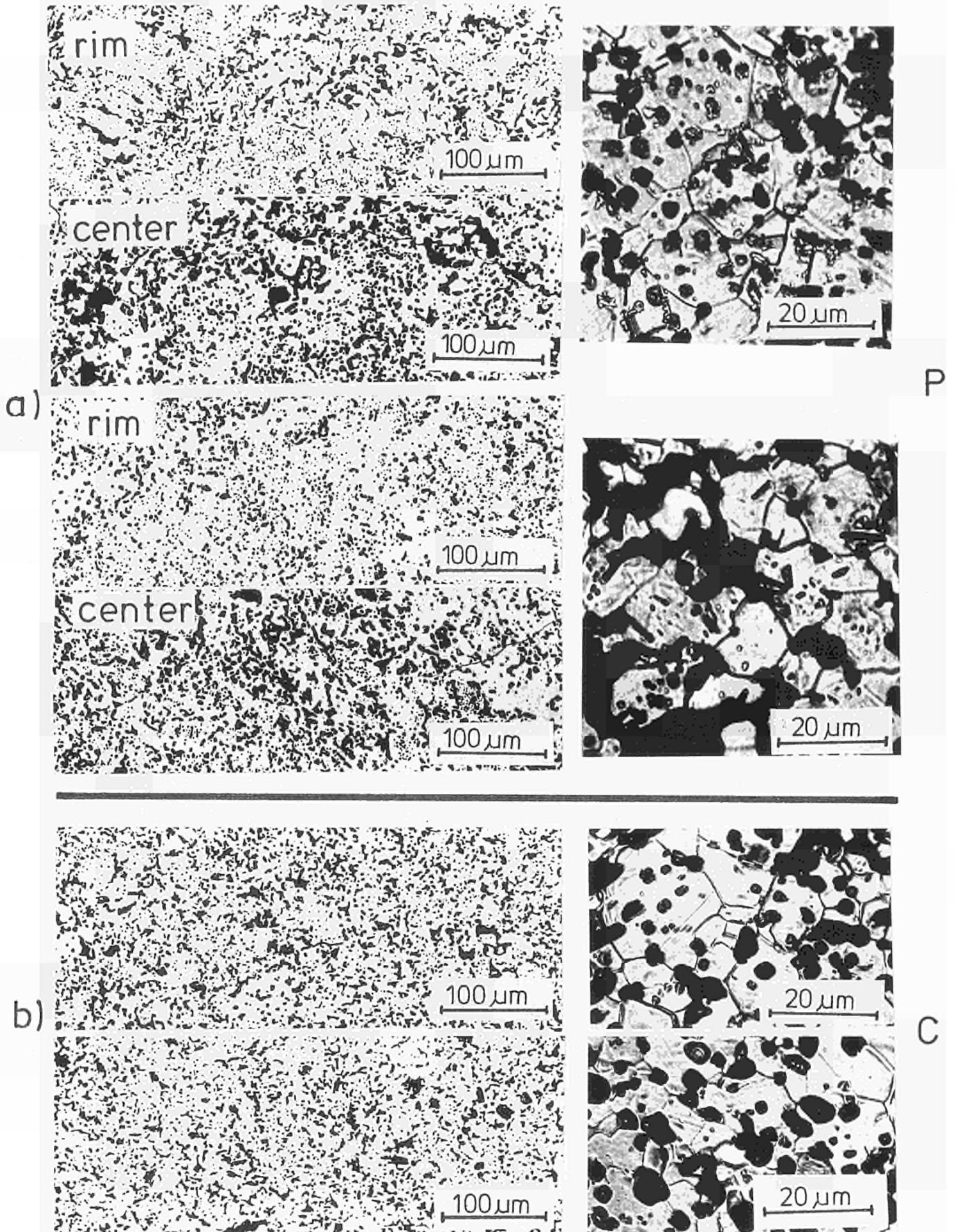


Fig. 3.2b Typical microstructure of nitride pellets

Tab. 3.2 Open porosity and pore (channel) diameter determined by Hg-porosimetry and light microscopy

Spec.	Pin	Pellets		Porosity v%		Mean channel diameter (μm) from:	
		Type	Material	Overall*	Open	Hg-porosi- metry	Light micro- scopy
3238	2	C	MN	18.3	~ 19.0 (12.0) 17.7	1.98	4.1
3239		C	MN	17.8			
3368		C	MN	17.7			
3296	3	P	MN	18.8	18.5	1.95	3.7
3297		P	MN	18.6	17.5	1.95	
3367		P	MN	18.7	17.7	1.95	
3264	4	C	MC	18.9	~ 20.4	1.50	
3265		C	MC	20.0	19.4	1.50	
3266		C	MC	19.6	~ 20.4	1.50	
3310	5	P	MC	16.5	14.7	1.25	3.5
3311		P	MC	19.6	16.9	1.60	
3338		P	MC	20.6	17.0	1.60	

* From fabrication data (geometrical density)

Tab. 3.3 Analysis of the planar sections of ellipsoidal pores and grains

Spec. No.	Mater.	Mean diameter * (μm)	Major axis (μm)	Minor axis (μm)	Mean grain size (μm)	Position (R/Ro)
3292 (P)	MC	2.7±2.3	-	-	-	1
		3.2±2.8	5.9±5.0	3.5±3.5	-	0.5
		3.5±3.0	-	-	-	0
3161 (C)	MC	3.0±2.4	-	-	13.0	1
		2.8±2.5	5.9±5.0	2.8±2.6	-	0.5
		2.9±2.4	-	-	-	0
3238 (C)	MN	3.6±2.6	-	-	8.7	1
		3.9±3.0	7.1±6.0	4.1±3.5	9.8	0.5
		3.9±3.0	-	-	10.0	0
3224 (P)	MN	3.7±3.0	-	-	6.8	1
		3.9±3.0	6.3±5.0	3.7±3.3	7.3	0.5
		4.0±3.0	-	-	6.5	0

* area equivalent diameter $D = 2 \sqrt{(A/\pi)}$ where A = area of pores

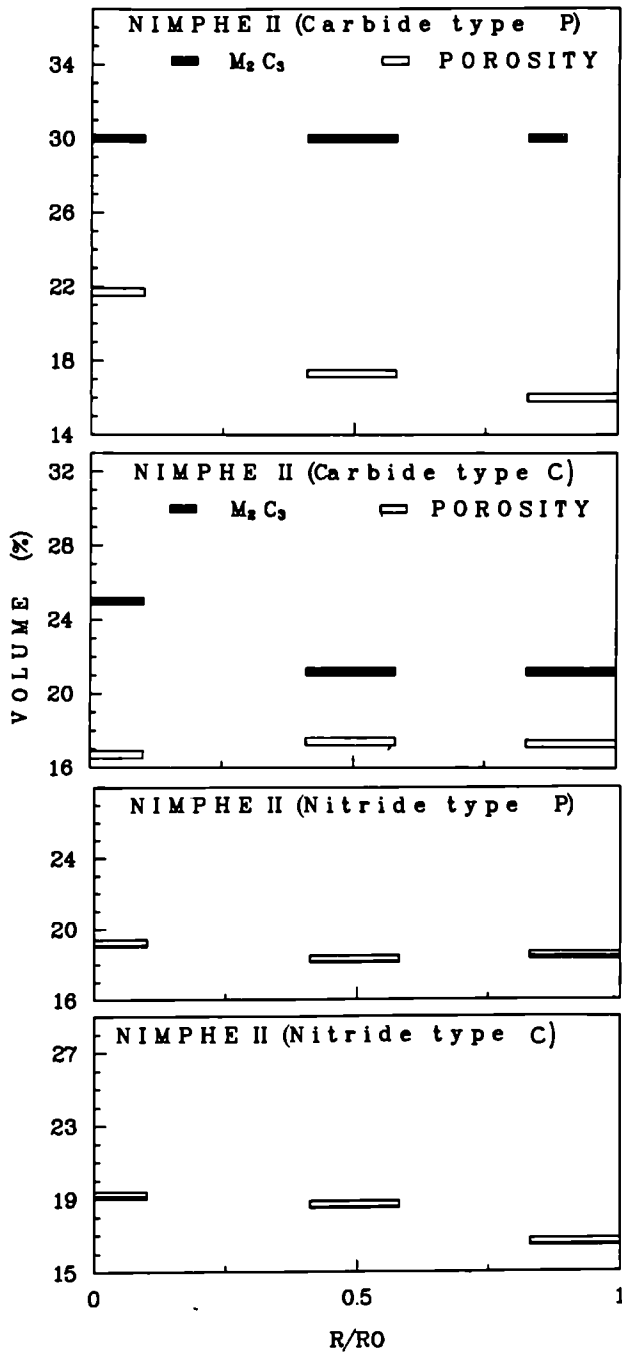


Fig. 3.3 Radial porosity and M_2C_3 ($M = U + Pu$) distribution of carbide fuel

Development of Porous MC and MN Fuels

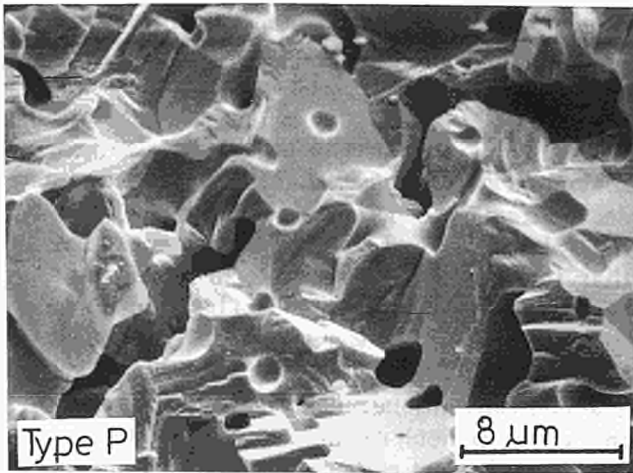
Impact of fuel and fuel pin specification on fabrication

The dense fuel pin concept, with a He-bonded fuel and a smear density of 75 - 80 % TD implies pellet densities of 80 - 85 % TD, in order to accommodate fuel swelling up to a burn-up of more than 15 at.%. The requirement for a fuel with such a high porosity is new and the thermal stability of the fuel structure needs investigation both out-of-pile and at the beginning of irradiation.

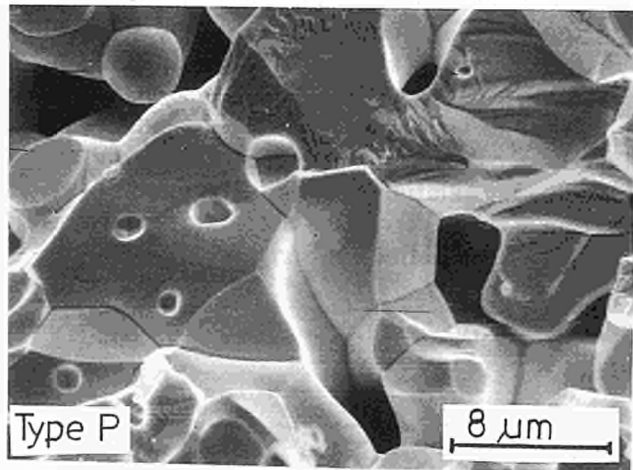
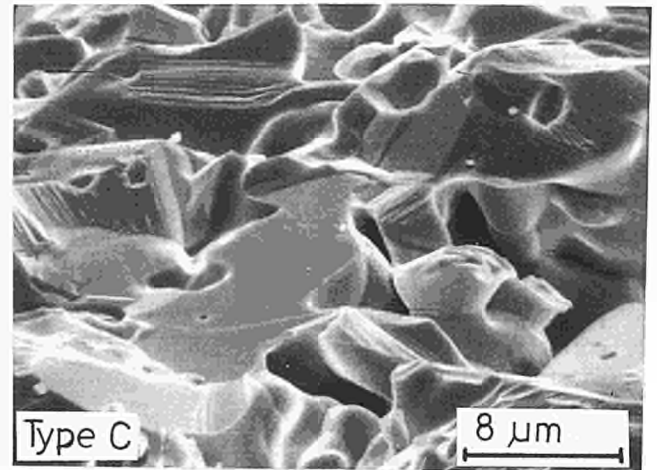
Ceramic fuels, with a porosity of 15 - 20 %, prepared by powder metallurgical processes, represent a material which is thermodynamically unstable and has the potential to densify at begin of life (BOL) when exposed to reactor irradiation. A significant in-service densification, however, is undesirable because it changes important parameters and would lead to inferior fuel performance. A decrease in porosity and hence pellet diameter will decrease both gap conductivity and fission gas release and diminish the overall porosity available for the accommodation of swelling. Furthermore, it raises problems of fuel/clad mechanical interaction (FCMI).

For these reasons the fuel pellet densification kinetics both during pellet fabrication and in the irradiations NILOC 1 and 2 have been investigated extensively. The most important aspect for the choice of the fabrication method and steps was, besides fuel composition and density, the stability of the fuel structure and pellet dimensions at high temperatures. For pellet fabrication a relatively high sintering temperature (2000 K) was chosen. This temperature is a compromise between the fact that an increase in sintering temperature provides pellets, for a given specified density, at reduced sintering time, but increases plutonium depletion during fabrication and decrease the lifetime of the generally used molybdenum heating elements.

The following fabrication parameters proved to contribute to the development of fuels with a better structural and dimensional stability when exposed to high temperatures as compared with previously employed fabrication methods:



a)



b)

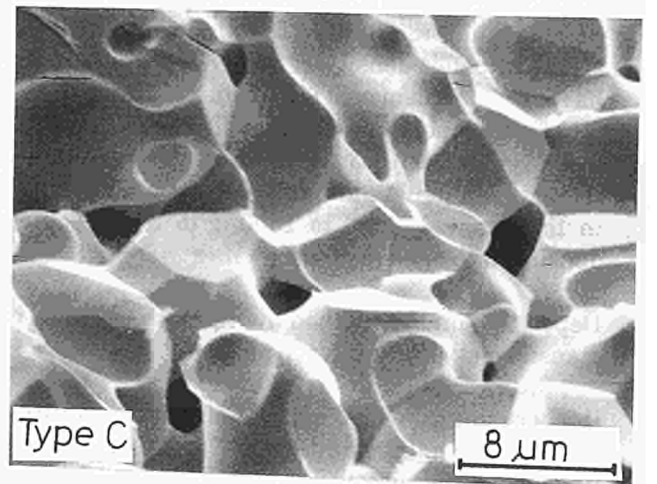


Fig. 3.4 SEM pictures of fracture surfaces of a) carbide and b) nitride fuels

- Crushing of the carbothermic reaction product and subsequent ball milling produces a reactive powder which sinters easily after pressing into green pellets. This is the classical powder route for producing ceramic nuclear fuel pellets. Fuel pellets prepared in this way are called type K fuel and were used as reference material.
- Comminution of the carbothermic reaction product in a fast turning hammer mill provides a coarser and less reactive powder than produced by ball milling, and requires thus the application of higher sintering temperatures (type C fuel).
- Direct pressing of reacted pellets increases thermal stability compared with pellets produced from the same reaction product by the powder-pressing-sinter process. In the direct

pressing procedure i) the starting materials for carbothermic reaction, ii) the reaction temperature and iii) the pressing conditions influence the thermal stability of the pellets fabricated with the specified density (type P fuel).

- Pressing pellets from a granulated reaction product decreases the densification rate under irradiation (see results for short term irradiation NILOC 1 and 2, below). The granulate should, besides its influence on fuel structure, also simulate a nitride feed material prepared by the Sol-Gel technique for pellet pressing.

Densification kinetics of MC and MN in conventionally prepared and directly pressed green pellets

In view of the low thermodynamic stability of a ceramic material with 15 to 20 % porosity a systematic analysis of the fabrication procedure of MC and MN pellets prepared from oxide powders by carbo-thermic reduction was performed. The details of this investigation are collected in a comprehensive report [1]. Here the most important results are outlined.

After an investigation of the carbo-reduction process [2] the first step was to analyse the structure of the reaction product. The reaction product is a "clinker" of 40 to 50 % density with approximately the geometry of the previous powder compact. The analysis of its structure shows that the clinker possesses a very high thermodynamic stability. In order to arrive at the specified pellet density of 80 to 85 % the clinkers have to be transformed into a sinterable state, i.e. into "green pellets" with densities in the range roughly between 63 % to 73 %. Subsequently these green pellets are sintered at temperatures in the range 1720°C to 1800°C to the specified density in the range 80 to 85 %.

Depending on the method by which the clinker is transformed into the green pellet,

- i) crushing with subsequent ball milling (giving a fine powder of MC or MN (K))
- ii) crushing with very short use of a hammer mill (giving very coarse powders) (C)
- iii) direct pressing of the clinker into the geometry of the green pellet (P)
- iv) direct pressing of "clinkers" in the form of granulate particles (G),

the stable structure of the clinker is either completely lost or more or less retained in the green pellet. As a consequence the densification kinetics during sintering and the thermal stability of the final product are strongly affected by the values of the parameters by which the clinker, the transformation into the green pellet and the sintering are characterised.

The next step was to establish a quantitative description of the densification kinetics occurring during the actual conditions of pellet production.

Thus a simple equation was to be selected which can represent the densification-time curves and the rate of densification during second stage sintering with an acceptable approximation from

isothermal sintering experiments. This empirical equation furthermore is required to satisfy the following conditions:

- it should have a reasonable physical basis
- the empirical parameters should be easy to deduce from the experimental results
- the relation should include the physical fact that intermediate stage sintering ends at a certain pellet density, which can be defined as a value somewhere between 5 and 10 % porosity of the material.
- The non-conventional methods used to prepare the green pellets result in green structures which are in part rather far removed from the structures encountered in the usual powder compacts employed in the study of the "classical" sintering and densification models.

The result of an analysis of these requirements is that the densification kinetics can be described by a "recovery type kinetics" [3].

Applying this type of kinetics to the densification of a ceramic during intermediate sintering gives the following relations for the pellet density as a function of time $D(t)$ and for the related change in porosity $P(t)$, as defined in Fig. 3.5:

$$D(t) = D_{II} - P(t) \quad (1)$$

with

$$P(t) = \frac{C'}{(t + t_0)^n} \quad (2)$$

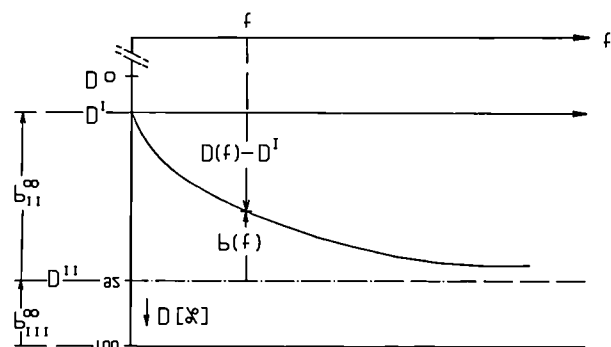


Fig. 3.5 Relations between fuel density and porosity during isothermal intermediate stage sintering. D_0 = green density, D_I = density at start of isothermal sintering, D_{II} = density at the end of the intermediate stage

The quantity D_{II} is the pellet density at the end of the intermediate stage sintering. The three parameters C' , t_0 and n can be determined from three pairs of values $(D_i; t_i)$, e.g. at $t = 0, 3$ h and 17 h, of an isothermal sintering curve. Fig. 3.6 gives as examples the curves $D(t)$ for a type K and a type P carbide. An analogous difference exists also for type K and type P nitride.

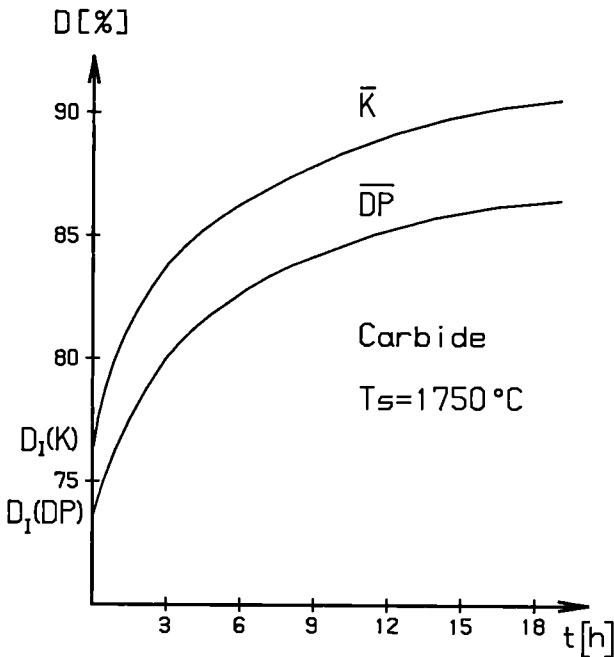


Fig. 3.6 Isothermal density-time curves for a type K and a type P carbide. Analogous differences exist between type C and type P carbides and nitrides

Between the rate of densification $\dot{D}(t)$ and the rate of porosity change $\dot{P}(t)$ the relation is $\dot{D}(t) = -\dot{P}(t)$, hence one has

$$\dot{D}(t) = \frac{C}{(t+t_0)^{1+n}} \quad C = nC' \quad (3)$$

Furthermore one can eliminate the time from equ. (1) and equ. (3) and arrive thus at a relation between the rate of densification \dot{D} and the associated density D .

$$D = f(\dot{D}) \quad (4)$$

Equ. (4) is the most important relation of this analysis since it allows a direct comparison between the densification behaviour and thermal stability of carbide and nitride pellets whose green pellets have been produced according to the different methods K, C, P and G.

In fact, the thermal stability of a pellet with the specified density D_s has to be described by a vector quantity \vec{TS} with three components

$$\vec{TS} = \{\dot{D}_s, D_s, T_s\} \quad (5)$$

where T_s is the isothermal sintering temperature and \dot{D}_s is the rate of densification at the specified pellet density D_s .

In Fig. 3.7 plots of the rate of densification \dot{D} versus density D are shown according to equ. (4) for various nitride fuel fabrications. The designations N71P etc. refer to the number of the fabrication batch and the type of green pellets used. The range for the specified density D_s is indicated. Those pellets possess the highest stability for which \dot{D} is lowest at D_s and for which the sintering temperature is high.

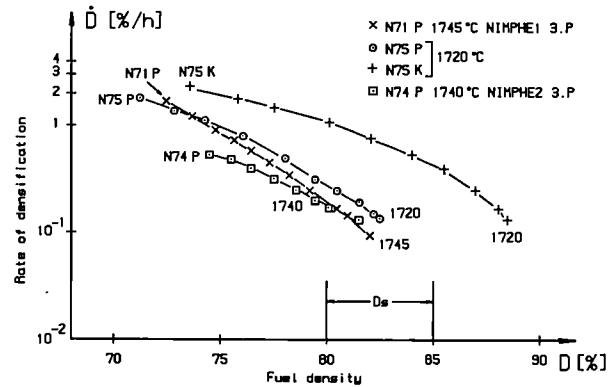


Fig. 3.7 Plot of rate of densification \dot{D} versus density D for various nitride batches. Note the difference between type P and type K fuels

One clearly sees that type K pellets (batch N75K) have a very low stability, but that the pellets of the batches N71P and N74P are much more stable.

These results will be correlated with the in-pile performance of the fuels of NILOC 1 and 2 below.

Post-Irradiation Examination of NILOC 1 and 2

The pin designs, irradiation conditions and the initial fuel temperature have been reported previously (TUAR 87).

In the following, a brief survey about the results of the post-irradiation examination and a comparison with the analogous carbide irradiations CARLO and CARRO are given.

Non destructive examination

Axial γ -scanning revealed a certain mobility of the fission products iodine and ruthenium. The dimensional measurements indicate that the cladding of pin NILOC 2 P showed a certain ovalisation. This FCMI was probably caused by the combination of two facts, small fuel particles which have moved into the fuel/clad gap and a relatively high fuel density, which prevented a relaxation of the corresponding local stresses.

Destructive analysis and fuel behaviour

During the early irradiation period when the fuel temperatures in He-bonded pins are highest, several, mainly temperature dependent, mechanisms operate in any ceramic fuel (oxide, carbide or nitride). In the present case, these mechanisms and their temperature dependence are, however, more or less strongly affected by the method of pellet fabrication, with type K the least and type G the most stable structure.

In the order of increasing temperature the following mechanisms can be deduced from the NILOC 1 and 2 experiments for nitride fuels:

a) *Pellet fracturing*

All pellets fracture during the first temperature rise. However, the number of cracks is clearly less than in the case of carbides. In most NILOC 1 and 2 cross-sections analysed, only one diametral crack was observed with a few small pieces broken off near this crack at the pellet periphery.

b) *Densification of nitrides K, P and G*

As outlined above, fuels with conventional and similar structures containing 15 % to 20

% porosity are not in thermodynamic equilibrium, and the densification mechanisms which were operating during fabrication in each type are reactivated and continue accordingly in-pile. The differences in the densification kinetics during fabrication are thus also valid at the very beginning of the irradiation.

Type K fuel already starts to densify at temperatures $T \sim 1000^\circ\text{C}$ whereas P and G only start densification at 1200°C . Furthermore there appears to be a considerable difference in the temperature dependence of in-pile densification between types P and K on the one hand and type G on the other. Below 1600°C , the temperature dependence for type G is appreciably less than for K and P.

c) *Pu-migration*

Up to about 1500°C , the mixed nitrides of type P and G show only limited Pu migration. For type K this temperature limit may be somewhat lower. Above 1500°C Pu migrates towards the pellet periphery and condenses at crack surfaces and on the inner side of the clad.

d) *Restructuring by vapour transport*

In the temperature range 1550°C to 1700°C , slow restructuring occurs around the pellet centres by which cracks are closed and a hole may be formed in the centre. This mechanism is too slow to lead to a clear central hole in NILOC 2. It has, however, been observed in previous nitride irradiations.

e) *Restructuring at very high temperatures*

Very strong restructuring may occur at temperatures $> 1800^\circ\text{C}$ by the rapid loss of nitrogen and concurrent liquid phase sintering. This leads to a region of very dense fuel in the centre surrounded by a porous zone.

f) *Comparison of fuel restructuring at BOL between carbide [4], [5] and nitride of type K [1].*

The cross sections of a carbide and a nitride both irradiated at about 75 kW/m to 0.5 a/o burn-up are shown in Fig. 3.8. The striking difference is that in the carbide cross-section the initial radial fuel clad gap of 0.1 mm width is closed and all cracks in the pellet centre have been eliminated by fuel swelling, whereas in the nitride cross section the

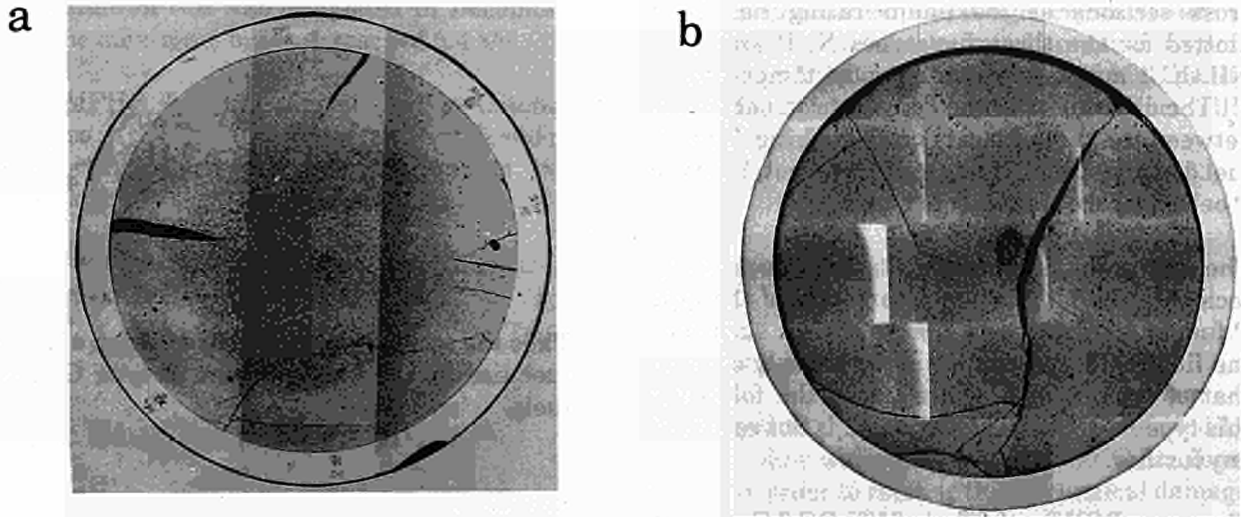


Fig. 3.8 Comparison of He-bonded type K fuel carbide and nitride fuel cross sections after 0.5 a/o burn-up and comparable irradiation conditions.
 a) Carbide cross section CARLO 3.1,
 b) Nitride cross section NILOC 2 K 2.1

originally smaller initial radial gap (of 0.07 mm) and the cracks in the pellet centre are still open because of fuel densification.

This different behaviour can be understood in detail [1]. It depends on a difference in the starting porosities (12.7 % for the carbide and 16.5 % for the nitride), but also on the fact that the kinetics of in-pile densification and of fission gas release to the grain boundaries and into closed porosity differ between carbide and nitride by roughly an order of magnitude.

In fact, in both fuels the same sequence of mechanisms operates but in the carbide it works much faster than in the nitride. A re-evaluation of the previous fast flux nitride irradiations carried out by the Institute between 1971 and 1979 has shown that swelling in nitrides only starts after 2 to 3 % burn-up.

Relation between Out-of-Pile Pellet Stability and Irradiation Performance

One should expect that the stability criterium expressed in equ. (5) of the pellets is also valid for the irradiation behaviour of porous nitride (and carbide) fuels, especially at BOL.

In Fig. 3.9 the relative shrinkage ΔP_A of the fuel

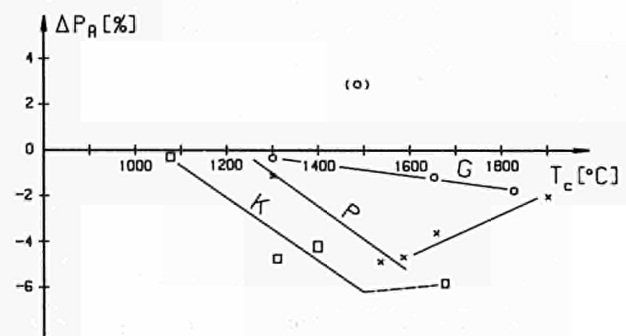


Fig. 3.9 In-pile densification ΔP_A deduced from the shrinkage ΔA of the initial pellet cross sections A_0 of pellet types K, P and G in NILOC 1 and 2. ΔP_A has been plotted versus the calculated fuel centre temperature of each cross section analysed. Note the low densification of type G pellets

cross sections at maximum rating has been plotted for the three fuel types K, P and G of NILOC 1 and 2 versus the centre temperatures T_c . The differences in the densification behaviour between the three fuels is quite striking. Type G fuel densifies least and type K fuel most, but type P behaves here similarly to type K.

The last point is rather particular, because by incidence the fabrication parameters of the type P fuel of NILOC 1 and 2 were chosen such that the final pellet properties are relatively close to that of type K fuel. Therefore in the following this type P fuel of NILOC 1 and 2 is not regarded any further.

The curve D(D) for the fuel of NILOC 2 G was not known before irradiation, but was established afterwards by densification experiments of archive pellets. The result is shown in Fig. 3.10. For comparison, curves for a type K and a "normal" type P nitride are shown as well.

In agreement with the in-pile results, one finds type G to be the most stable fuel; type P obviously can be fabricated with stabilities not too far from type G, but type K cannot be made a stable fuel at all in the porosity range indicated.

Based on the in-pile behaviour of type G nitride pellets as shown in Fig. 3.9 and on the out-of-pile densification behaviour of this fuel in Fig. 3.10 the thermal stability vector, equ. (5), can be quantified tentatively for stable nitride fuel as

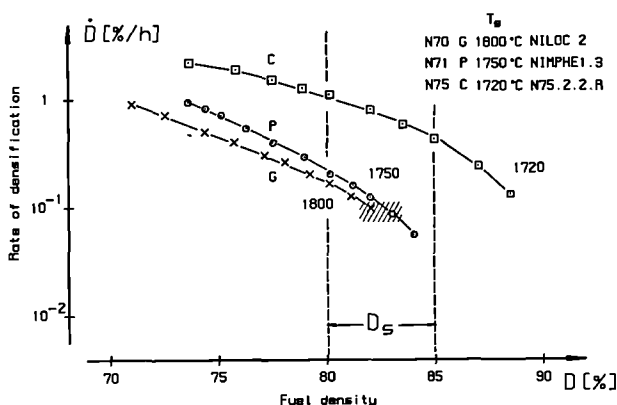


Fig. 3.10 Plot of rate of densification \dot{D} versus D for NILOC 2 G archive pellets. The out-of-pile densification behaviour confirms the high in-pile stability. For comparison curves for a 'good' type P and a type K nitride are shown as well

$$\vec{TS} = \begin{pmatrix} T_s \geq 1750^\circ\text{C} \\ D < 0.11\%/\text{h} \\ D_s = 82.5 \pm 1\% \end{pmatrix}$$

Thus the scope for further optimisation of nitride fuel lies in the improvement of type G and P fuels.

References

- [1] H. Blank, 'Fabrication of carbide and nitride pellets and the nitride irradiations NILOC 1 and NILOC 2', Technical Note K 0288112, Febr. 1989
- [2] G. Pautasso, C. Sari, K. Richter, J. Nucl. Mat. 158 (1988)12
- [3] H. Blank, 'A rate equation for recovery, precipitation, transient creep and sintering', to be published in Mat. Sci. and Technol. (1989)
- [4] H. Blank, M. Campana, M. Coquerelle, K. Richter, IAEA-TECDOC-466, IAEA Vienna 1988, p. 81
- [5] H. Blank et al., Int. Conf. on Reliable Fuels for LMFBR's, ANS, 7.-11.9.1986, Tucson, USA, p. 7-15

Irradiation Experiments

During 1988 the basic studies on mixed nitrides were continued. Out-of-pile tests on fuel densification were performed in order to better understand the fuel behaviour at B.O.L. As a consequence of these the irradiation experiments POMPEI and SWELLAC are being postponed and a new series of NILOC experiments is under preparation. In the irradiations NILOC 3 and NILOC 4 the behaviour of tailored fuel structures will be investigated.

Fast Reactor Experiments NIMPHE (TUAR 86, 20)

The NIMPHE 1 experiment was continued in the Phenix reactor during the reporting period, the

5th irradiation run was completed in December 1988. The maximum burn-up reached 6.4 a/o.

The NIMPHE 2 experiment started in October 1988, also in the Phenix reactor, and at the end of the reporting period after 1 irradiation run, the maximum burn-up was about 1.5 a/o.

The state of experiments under preparation is summarised in Tab. 3.4.

Basic Studies on Uranium Nitride

Uranium Self-Diffusion in UN

No reliable data were so far available on metal atom self-diffusion in UN, although it can be rate-controlling for various important processes (sintering, grain growth, swelling, fission gas bubble behaviour, etc.).

The cation self-diffusion was therefore studied on two batches of UN (sinters and single crystals) and consistent results were found. The influence of the nitrogen potential on the diffusivity has also been investigated.

Experimental

The sintered material used was 84.9 % of theoretical density and contained 1000 ppm

metallic impurities. The single crystals were of high quality, as shown by channeling experiments (see following section) and of high purity (230 ppm C, 100 ppm O and <50 ppm metallic impurities).

Diffusion Procedure

Sample preparation

After polishing the specimens to a mirror-like surface, they were annealed at 1400 °C for about 1 hour in order to recover the mechanical damage introduced by polishing. The radioactive tracer, ²³³U (half life: 162 000 yrs), was deposited by flash evaporation. Two coated samples were placed as a "sandwich" in a tungsten crucible in the diffusion furnace. Prior to the diffusion anneal under static nitrogen pressure, the furnace was evacuated 3 times after filling it with N₂. The samples were then heated up to about 1450 °C under vacuum to avoid sesquinitride formation. The temperature was controlled with a calibrated optical pyrometer.

Evaluation of Diffusion Profiles

After the diffusion anneal, tracer concentration profiles were evaluated using the α -energy degradation method [1], which consists of recording high resolution α -spectra evaluating them and converting them into depth profiles (resolution 5 nm/channel) by applying the

Tab. 3.4 Irradiation experiment of the Institute

Experiment	Reactor	Scheduled beginning of irradiation	Aim of experiment
NILOC 3+4	HFR	mid 89	behaviour of tailored fuel structures
POMPEI	HFR	mid 89	fuel behaviour at high burn-up
Swellac	HFR	end 89	swelling accomodation

mathematics given previously [2] for small penetration depths ($< 1 \mu\text{m}$). An energy loss of $450 \text{ keV}/\mu\text{m}$ was used to correlate α -energy and depths. One should note that a very important feature of the α -energy degradation method is the fact that it is non-destructive, thus allowing the time-dependence of tracer penetration to be followed and to check that true volume diffusion is measured. Fig. 3.11 shows a typical mean square penetration plot versus time. It illustrates clearly how a single diffusion measurement necessarily would lead to erroneous high diffusivities. Cation diffusion in UN is very slow, even at high temperatures; therefore, the α -energy degradation method is ideal because of its high sensitivity (lower limit $10^{-18} \text{ cm}^2/\text{s}$).

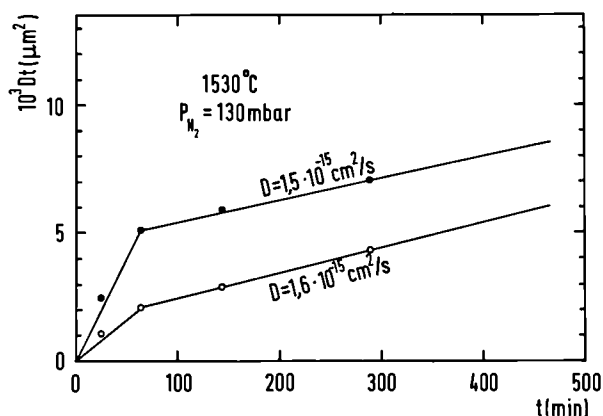


Fig. 3.11 Typical mean square penetration of ^{233}U in UN versus time.

Results

For every temperature and N_2 pressure, tracer penetration was measured for at least four different annealing times. In all experiments, the mean square penetration x^2 was linear with time, as expected for volume diffusion ($x^2 = 2 Dt$). Indeed, artifacts due to short circuiting can be corrected for when analysing the α -spectra. The U self-diffusion was mainly measured at three different pressures: 10, 130 and 1000 mbar. The results are plotted in Arrhenius diagrams in Fig. 3.12 for sinters and in Fig. 3.13 for single crystals. An activation enthalpy of 5.0 eV/atom was calculated from the Arrhenius plots. The diffusivities obtained with single crystals are about 15 times lower than those for sinters. This fact is certainly due to short-circuits and the higher impurity content present in sinters both of which accelerate the diffusivity.

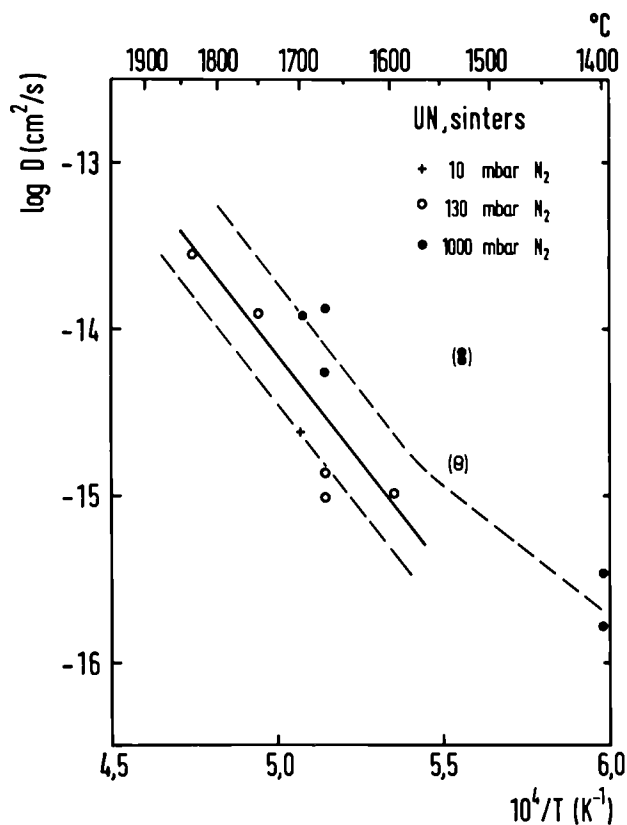


Fig. 3.12 Arrhenius diagram showing U self-diffusion in sintered UN for different N_2 pressures.

Discussion

The diffusion coefficients obtained here for UN are smaller than all previous literature data. This is probably due to higher impurity contents, not up-to-date experimental techniques and short circuiting paths present in previous studies, all causing a too high volume diffusion coefficient. This phenomenon also occurred in the present experiments where sinters give higher diffusivities than single crystals.

Reimann et al. [3] measured diffusion in polycrystals with big grains and obtained the very unplausible result of an almost athermal diffusion process at a given N_2 pressure. Besides this unlikely fact, their reported diffusion coefficients are 2 to 3 orders of magnitude higher than the present values (Fig. 3.13). The few data of Routbort et al. [4] (3 different temperatures) are only about one order of magnitude higher as compared to the present data. These measurements were performed on single crystals similar to those used here. However, only one

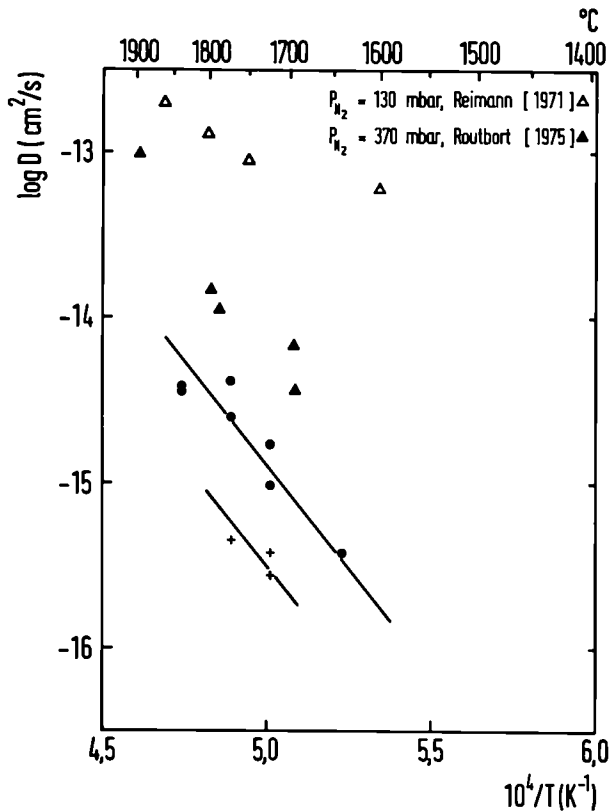


Fig. 3.13 Arrhenius diagram showing U self-diffusion in UN single crystals for 2 nitrogen pressures (+: 10 mbar; ●: 1000 mbar). The triangles represent literature data.

anneal per temperature was made. Any surface effect can therefore not be corrected for, and the quoted D-values are thus expected to be high.

The present data yielding lower mobilities are certainly more reliable for true volume diffusion than the existing literature data.

Let us now consider the diffusion mechanism in UN. Nitrogen is known to diffuse at a much higher rate than uranium [5, 6]. Nitrogen diffusion was observed to increase with increasing nitrogen partial pressure following the dependence $D_{UN}^N \sim p_{N_2}^{1/n}$, with n between 2.0 and 2.8. This effect of p_{N_2} on the diffusion is compatible with an interstitial diffusion. The excess nitrogen is then incorporated as neutral or singly charged interstitials. The expected dependences of diffusion coefficients on nitrogen partial pressure for both the metalloid and metal species are given in Tab. 3.5 Obviously, a vacancy diffusion mechanism on the metal atom sublattice varies in the same way as the nitrogen

interstitial diffusion mechanism. Experimentally, the sinters yield a value of n between 2.0 and 4.0 and the single crystals a value of 3.1. These results are in agreement with a vacancy mechanism for U self-diffusion. It is not possible at the present state of knowledge to discriminate between a neutral vacancy and a singly charged vacancy diffusion mechanism.

Conclusion

The present study fills some important gaps in the knowledge of metal atom self-diffusion in UN. The new reliable cation mobilities are lower than all reported data in the literature. Thus, UN shows the slowest metal atom mobilities in the series carbides - carbonitrides - nitrides. Therefore, metal atom diffusion controlled processes are slowest in UN, confirming the existing picture. The diffusion mechanism was shown to be most likely via a neutral or singly charged vacancy.

Channeling Measurements

As previously reported (TUAR 87, 30 and TUSR 86, 29), Rutherford backscattering (RBS) of ^4He ions combined with the channeling effect was used to investigate radiation damage in UN produced by Kr and Xe ion bombardment. The experiments were performed at the Van de Graaff accelerator and the ion implanter of the "Institut für Nukleare Festkörperphysik", KfK, in cooperation with O. Meyer and A. Turos. In the last report (TUAR 87, 30), the surface preparation was explained and a detailed analysis of the defect structure following implantation was given.

This study was continued with measurements of damage saturation and of the thermal recovery of the disorder in UN.

Kr and Xe were implanted into UN to different doses ranging from 0.4 to $24 \cdot 10^{15}$ ions/cm². The corresponding channeling spectra showed a damage saturation at about $1 \cdot 10^{15}$ ions/cm² for both Kr and Xe implants. Above this dose, important recombination processes take place in the collision cascade. The damage generated was the same for both Kr and Xe. An implantation experiment has also been done with Kr at liquid nitrogen temperature (77 K). The damage saturation level was about twice as high as at

Tab. 3.5 Theoretical dependence of diffusion on nitrogen partial pressure P_{N_2} according to $D \sim P_{N_2}^{1/n}$ [8]

n	2	4	6	-2	-4	-6
U defect	U_v	U_v^-	U_v^{--}	U_i	U_i^+	U_i^{++}
N defect	N_i	N_i^-	N_i^{--}	N_v	N_v^+	N_v^{++}

v = vacancy, i = interstitial

room temperature. This feature illustrates the significant role played by defect mobility in recombination processes. Another important result from this experiment is the observed defect migration below room temperature. Fig.3.14

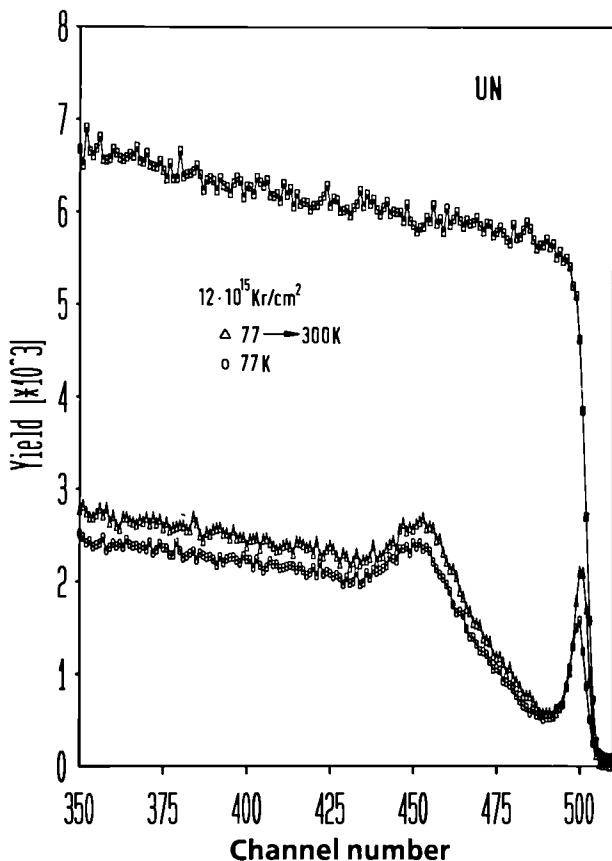


Fig. 3.14 Random and $\langle 100 \rangle$ aligned spectra of UN implanted with 1.2×10^{16} Kr-ions/cm². The figure shows the effect of temperature between liquid nitrogen temperature (77 K) and room temperature (300 K).

shows the increase in dechanneling after heating the Kr implanted crystals to room temperature. One notices the broadening of the surface peak due to migration of U defects. The surface acts as a sink for the defects which are suggested to be uranium interstitials. The interface peak, attributed to the presence of dislocation loops located at the interface between the damaged and the virgin zone, also increases indicating that a defect transformation took place. Its exact nature is difficult to interpret. Nevertheless, this experiment proves the mobility of U defects (probably interstitials) between 77 K and 300 K.

Radiation Damage Recovery

Fig. 3.15 shows the channeling spectra for a UN crystal implanted with $2.3 \cdot 10^{15}$ atoms Xe/cm² subjected to isochronal furnace annealings under high vacuum and at different temperatures. No significant changes occurred after annealing at 480°C, and a small decrease in dechanneling was first observed after annealing at 580°C. Substantial reduction of the interface peak took place after annealing at 700°C. Further annealing does not modify the spectra significantly before 1000°C has been reached. Beyond that temperature, the dechanneling decreases continuously with increasing annealing temperature. At 1400°C, complete damage recovery was attained. The results of annealing experiments for Kr-implanted UN are similar, as shown in Fig. 3.16. This representation exhibits essentially two recovery stages at which important defect transformations take place. The first stage is located at 700°C and the second between 1000 and 1200°C. This behaviour is typical for all samples. For higher doses, as expected, the recovery is retarded.

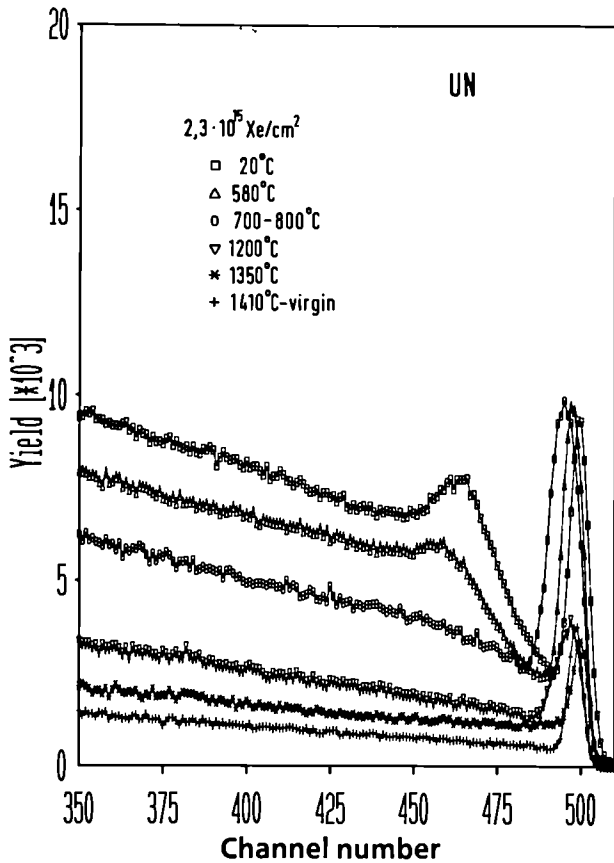


Fig. 3.15 Thermal recovery of damage in a UN specimen implanted with 2.3×10^{15} Xe-ions/cm².

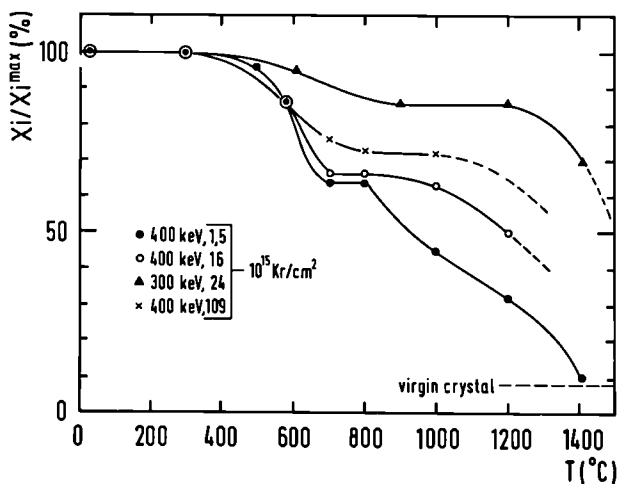


Fig. 3.16 Radiation damage recovery of UN single crystals bombarded with different doses of Kr-ions.

After completion of the first recovery stage (700 °C), a new analysis of the energy dependence of channeling was performed. The investigation proved that the defect structure remained essentially unchanged. Small loops in the interface region grow into bigger ones, and a stable dislocation network is likely to be formed. The further dechanneling decrease observed between 1000 °C and 1200 °C was shown to be due to a transformation in the near surface region. The surface peak (Fig. 3.15) is known to be generated by the presence of U interstitials and small clusters. A thorough analysis of the surface peak showed that it first increases with annealing temperature to reach a maximum in area after an anneal at 800 °C, and then shrinks drastically between 1000 °C and 1200 °C and eventually becomes identical to the normal surface peak of a virgin crystal. This observation suggests that the second recovery stage is due to annihilation of U interstitials with vacancies and/or with small clusters which thus are growing. At 1400 °C the disorder is entirely recovered.

Electron microscopy is the ideal complementary technique to interpret channeling experiments. Therefore, UN samples were prepared for TEM analysis and then ion bombarded with $2 \cdot 10^{15}$ atoms Xe/cm² and $10 \cdot 10^{15}$ atoms Kr/cm². Here again no difference between the two atomic species was observed. The specimens were annealed at 600 °C, 900 °C, 1200 °C and 1500 °C. After implantation, the disorder produced appeared as black dot damage which was not resolved. Only after 1200 °C an important damage transformation (Fig. 3.17) could be seen. A stable dislocation network was formed, together with dislocation loops with an average diameter of 200 Å. Annealing at 1500 °C decreased the dislocation loop densities, respectively by ~ 30% and 60%. The dislocation network grew into a more stable one, the loops attracted defects and grew, with some of them annihilating at the surface.

Conclusion

The radiation damage behaviour of UN is now fairly well understood. Ion bombardment of UN leads to disordered regions which penetrate further into the crystal with increasing dose. An interfacial peak is formed, corresponding to dislocation loops located at the interface of the damaged and the undamaged region. The interface peak is located deeper in the crystal

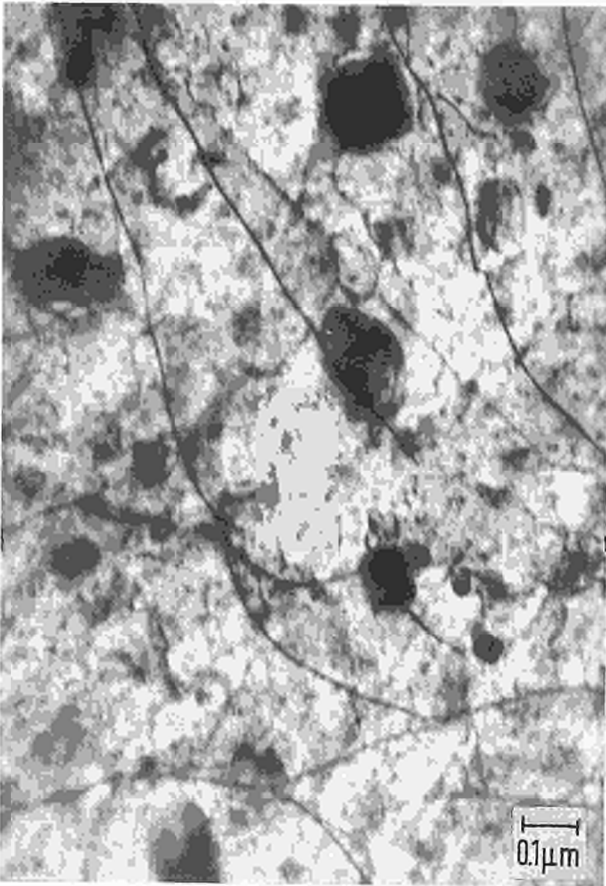


Fig. 3.17 Transmission electron micrograph of a UN specimen implanted with 2×10^{15} Xe-ions/cm² and annealed at 1200 °C.

than the damage-producing ions. U-defects are therefore migrating into the undamaged crystal. The total damage rapidly reaches a saturation value at 10^{15} ions/cm²; this value is twice as high at 77 K than at 300 K. This can be explained by the high recombination rate in the cascades. Low temperature experiments showed the mobility of U-defects (probably U interstitial atoms), which migrate towards the surface, acting as a sink.

Essentially two major types of defects survive the ion bombardment: dislocation loops located at the interface and small clusters. A recovery study with isochronal anneals showed two important stages: the first one at 700 °C, where clusters grow and dislocation loops are restructured but remain essentially unchanged, and a second stage at 1000 - 1200 °C corresponding to the formation of a stable dislocation network and to small clusters agglomerating to form bigger stable loops.

UN shows a typical metallic behaviour. It does not become amorphous even at high doses ($1 \cdot 10^{17}$ ions/cm²). The damage is fully annealed at 1400 °C.

References

- [1] F. Schmitz and R. Lindner, *J. Nucl. Mater.* **17** (1965) 259
- [2] A. Höh and Hj. Matzke, *J. Nucl. Mater.* **45** (1972/73) 29
- [3] D.K. Reimann, D.M. Kroeger and T.S. Lundy, *J. Nucl. Mater.* **38** (1971) 191
- [4] J.L. Routbort and R.N. Singh, *J. Nucl. Mater.* **58** (1975) 78
- [5] J.W. Droege and C.A. Alexander, in: *Progress on Development of Fuels and Technology for Advanced Reactors*, D.L. Keller (ed.) (1971)
- [6] J.B. Holt and M.Y. Almassy, *J. Am. Ceram. Soc.* **52** (1969) 631
- [7] Hj. Matzke, *Science of Advanced LMFBR Fuels*, A Monograph on Solid State Physics, Chemistry and Technology of Carbides, Nitrides and Carbonitrides of Uranium and Plutonium, North-Holland, Amsterdam (1986)
- [8] M.H. Bradbury and Hj. Matzke, *J. Nucl. Mater.* **75** (1978) 68

4 Studies of High-Temperature Properties of Nuclear Materials

Introduction

Several results have been achieved in the Project "High Temperature Properties" during the reporting year.

Particularly important have been the measurements of the **thermal conductivity** in liquid UO_2 . These measurements have been obtained after a lengthy interval of seemingly little advance, spent in consolidation of the measurement techniques and construction of new equipment. The results show that the conductivity λ is not subjected to a large discontinuity in crossing the solid/liquid phase boundary. The direction of this work, whose results substantially confirm those of our past experiments, has been to improve the precision of the temperature measurements and to develop adequate analytical tools. While this may seem at first glance a trivial extension of knowledge, the results obtained have in fact removed a basic uncertainty in the assessment of the thermal conductivity of fuel in the reactor accident analysis. Furthermore, these experiments have led to the development of sophisticated measurement techniques which can be applied to new areas of investigation.

A second problem that had so far resisted complete solution is the high temperature measurement of the **specific heat** of UO_2 . The method developed in our laboratory is based on the analysis of the surface temperature evolution of a spherical sample heated by pulsed lasers. Both, the control of the heating conditions and the theoretical analysis, present serious difficulties which are being solved progressively. Heating experiments have recently been carried out up to temperatures of 4000K; the obtained data are being refined with numerical codes which account for all the existing perturbing effects.

One of our most interesting discoveries concerns the **radiative properties** of metals at high temperature. The so called "grey-point" effect, by

which metals at the melting point exhibit effectively equal spectral emissivities in the wavelength range 500-1000 nm, was first considered as a curious coincidence. Further investigation meanwhile showed that this property is present in all refractory metals and is likely associated with a typical electronic state transition at T_m . The analysis of this phenomenon is in progress.

The **emissivity of oxides** (zirconia, thoria, urania) was measured up to the melting point. Contrary to refractory metals, these materials do not show a grey-point effect at the melting point. But other anomalies were observed during the solid to liquid phase transition.

Experiments were performed aimed at **melting graphite** under controlled conditions. A sphere of 1 mm diameter was partially melted in a 800 bar helium atmosphere for approximately 30 ms. The solidification temperature could be determined from pulse heating experiments up to higher than 8000 K. Though the control of the behavior of graphite at these very high temperatures is entirely not within our grasp, the results obtained represent a further advance in the understanding of its properties.

Finally, a large amount of work was carried out which will not be reported here in detail. This concerns the design and construction of new equipment which is being implemented for new project activities. The scope of this work is dictated by the present needs of the European nuclear safety programmes which are carried out in collaboration with national and international projects. The following actions are in progress:

- The construction of a **laser-flash** apparatus for the measurement of the variation of the thermal diffusivity in irradiated materials. After a preliminary test in our alpha-laboratory, this apparatus will be installed in the hot cells for measurements on high burnup fuels.

- Construction of a high-vacuum furnace with a Knudsen cell for the measurement of the equilibrium partial pressure of mixed U-Pu nitrides up to 3000 K. The work will be carried out in the frame of the cooperation programme with CEA for the development of dense LMFBR fuels.
- Finally, construction of a shielded time-of-flight mass-spectrometer to investigate fission product effusion and transpiration in high burnup LWR fuel. The mass spectrometer will be equipped with a high temperature cell enabling temperatures of up to 2800 K to be reached.

- Data acquisition
- Material characterization
- Temperature measurement at the crater edge
- Data evaluation
- Analysis of the dynamic behaviour of the melt front.

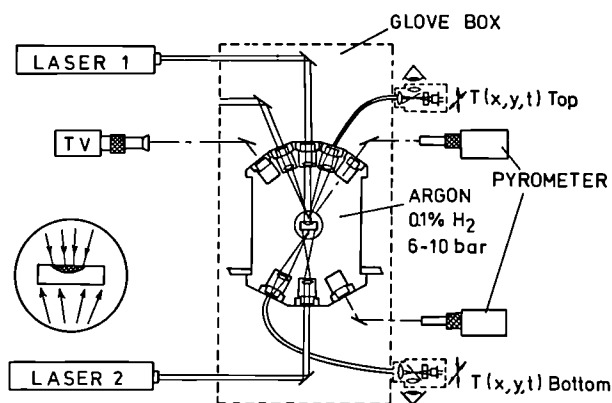


Fig. 4.1 Schematic representation of laser heated furnace for thermophysical measurements on molten UO_2 . A disc shaped sample of UO_2 is heated in a pressurised furnace by two continuous laser beams, whereby the more concentrated upper beam creates a molten pool in the top centre of the sample. Images of the top and bottom surfaces are relayed out of a glove box containment by flexible fibre-optical image guides, and scanned with a small aperture. The light passing through these apertures is measured with band pass filters and photodiodes.

Thermal Conductivity of Liquid UO_2

Introduction

The present activity concerns an attempt to measure the thermal conductivity of a high melting material such as UO_2 on a self-contained partially molten sample. The work described previously (cf. EUR 11783 EN) has been continued. The experimental arrangement is given schematically in Fig. 4.1. A disc-shaped sample of UO_2 is heated in a pressurised furnace by two continuous laser beams, whereby the more concentrated upper beam creates a molten pool in the top centre of the sample. Images of the top and bottom surfaces are relayed out of the glove box containment by flexible fibre-optical image guides, and scanned by small apertures. The light passing through these apertures is measured with band pass filters and photodiodes. The arrangement is operated as separately calibrated monochromatic pyrometers. The experiments gave first, though not quite satisfactory, results on the thermal conductivity of liquid UO_2 , so far confirming the 1982 data [1], which indicated a decrease in conductivity on melting. The results from different samples show an inacceptably large scatter, however, which is tentatively attributed to asymmetric power profiles of the heating laser beams. The following subjects were treated during the reporting period:

Experimental Set-up

Data acquisition

Current-to-voltage converters

The flexible connection of the moving photodiodes to stationary, current-to-voltage converters was found to contribute significantly to the noise. The diode presents a high-impedance current source; its output is thus charge sensitive. Flexing a coaxial cable changes

its capacitance, and easily injects enough charge to drive the subsequent electronics off-scale. This point was readily solved by connecting small current-to-voltage converters rigidly to the diodes. The low-impedance converter outputs are no longer charge sensitive.

2D-Temperature profile scanning

The scanning control device outlined in TUAR-87 has been implemented, and performs correctly. The scanning pattern is down-loaded into a separate buffer memory. The unit is controlled by an independent programmable clock, which triggers two fast analog-to-digital converters (for the top and bottom profiles), and advances the scanning motors if a corresponding bit is set in the scanning pattern. The converted data are stored in an internal buffer, the address counter for buffers and pattern is incremented, and the procedure is repeated at the next clock pulse, until a stop code is encountered in the scanning pattern. The direction of motion is controlled by another set of bits, one for each motor. Acceleration and deceleration is accomplished by omitting some of the advance bits in the pattern at the start and at the end of each line. When the scanning is terminated, the data are read out to the computer by (fast) block transfer. The electronics of the device, allow a scanning interval of 60 μ s. The mechanical inertia of the scanning device, however, limits the minimum clock interval to 1.2 ms, which is sufficient for the present application. This speed is 60% faster than the maximum speed specified by the manufacturer. The buffers used allow a scanning pattern of 8191 points to be applied.

Measurement procedure

After loading the sample, the furnace is evacuated and flushed repeatedly with Ar/0.1% H₂, which is then admitted to ≤ 10 bar. Only the sample itself and its immediate surroundings are heated above ambient temperature. The oxygen content of the furnace atmosphere is monitored continuously by flowing it through an oxygen sensor based on a Ca-doped ZrO₂ tube heated to 1000 K. The sample is heated from top and bottom by two continuous CO₂ laser beams of ≈ 200 W each. The upper beam is focused to a more concentrated spot than the lower one. With the shutter in the upper beam closed, the bottom power is slowly raised, until (at ≈ 1600 K) the UO₂ is sufficiently plastic to avoid thermal stress

cracking. The scanning pattern is centered on the sample, and a 2D profile of the top and bottom temperatures of the surface sample is recorded. Then the upper laser beam is admitted, which rapidly heats the top of the sample, creating local melting. A few seconds are required for the lower surface to attain a stationary temperature distribution. A line scan is recorded over (part of) the diameter of top and bottom during this time, followed by a (partial) 2D scan centered on the line scan. This final 2D scan provides a check on correct beam alignment, and furnishes the main data for the subsequent evaluation. After completion of the final 2D scan, the upper beam shutter is closed, and the lower, defocused, beam is slowly reduced in power, in order to accommodate the thermal stresses caused by the 11% increase in density on resolidification [2]. If the cooling occurs too rapidly, partially molten samples invariably fragment into small pieces, which are difficult to exploit subsequently.

The raw data from a typical run, are represented as isotherm plots in Figs. 4.2-4.4.

Fig.4.5 shows an SEM picture of the sample referred to in Figs.4.2-4.4 after cooling, where an oblique view as in Fig. 4.6 reveals the unevenness of the resolidified surface and a radial crack. Usually, such a crack passes near through the centre of the crater. Only a small mechanical effort suffices to break the sample in two roughly equivalent parts. Fig. 4.7 is a SEM matching of the micrograph cleavage surfaces of these halves. The crevasses are caused by the shrinkage on resolidification. Figs. 4.8 and 4.9 show a diametral cross section of one of the halves. The scale of Figs. 4.2 - 4.9 may be deduced from the original dimensions of the sample 5.0 mm diameter \times 0.93 mm. Fig. 4.9 shows the penetration of the melt as the limit of the region where the original porosity and structure has vanished. The position of this phase boundary is established from photographs as Fig. 4.9, and serves as the second crucial input parameter in the further evaluation.

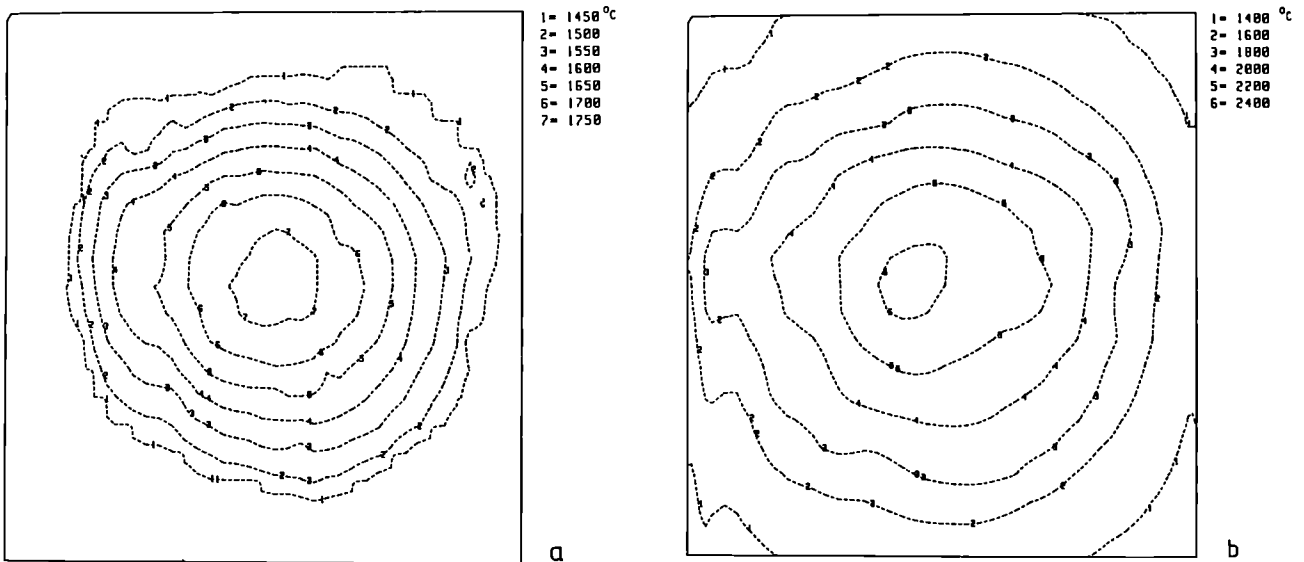


Fig. 4.2 2-D temperature profile representing $5.76 \times 5.76 \text{ mm}^2$ as isotherm plot, heating through bottom beam only, recorded in 40×20 steps in 3.02 s. a: Top surface; b: Bottom surface.

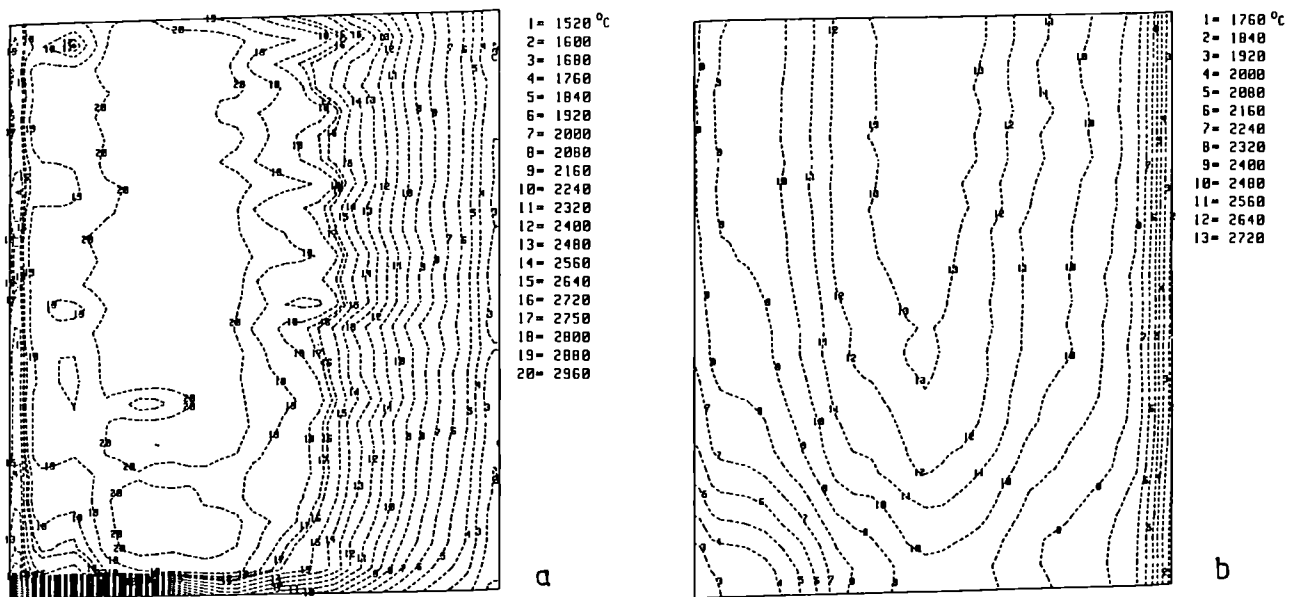


Fig. 4.4. Final 2-D temperature profile of a $4.32 \times 4.32 \text{ mm}^2$ part, with heating through top and bottom laser beams, recorded in 30×15 steps in 1.80 s. The heavy line in Fig. 4.4a corresponds to the edge of the crater seen in Fig. 4.5. a: Top surface; b: Bottom surface.

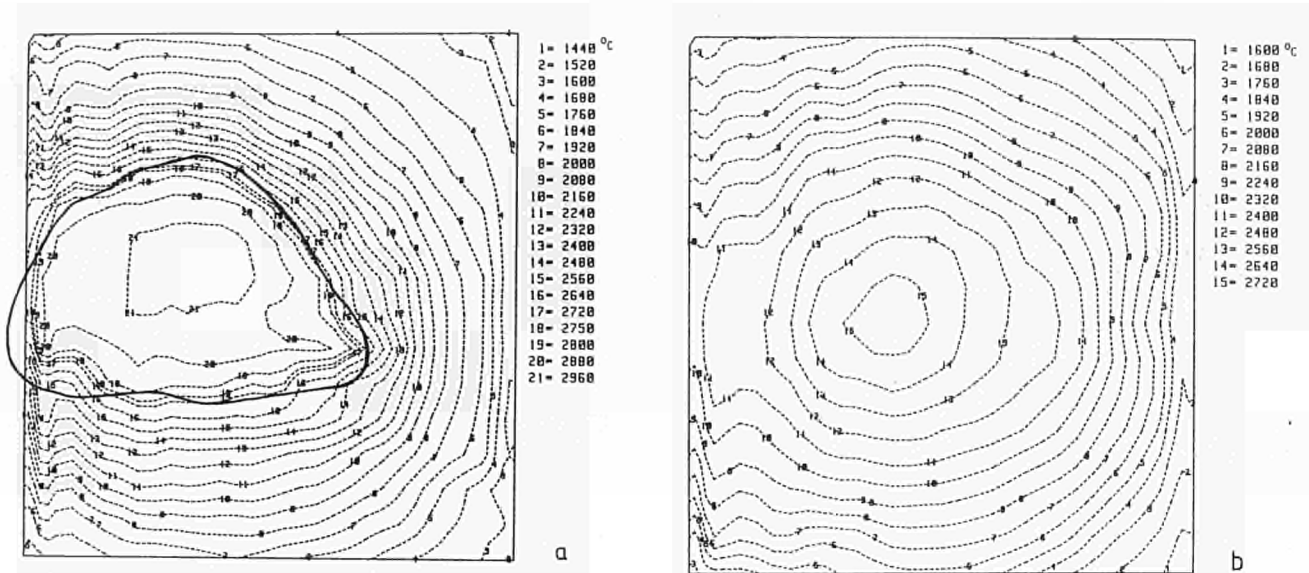


Fig. 4.3 Evolution of the temperature along a 4.32 mm centered part of the diameter after admitting the upper laser beam (abscissa), as a function of time (ordinate). The vertical full scale represents 3.07 s. a: Top surface; b: Bottom surface.

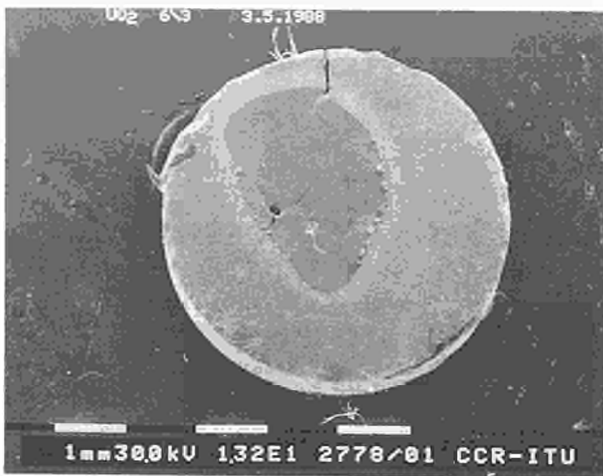


Fig. 4.5 SEM Photograph of the sample of Figs. 4.2-4.4 after resolidification. The markers at the bottom correspond to 1 mm.



Fig. 4.6 SEM Photograph of the sample of Figs. 4.2-4.4 after resolidification, at larger magnification under an oblique angle, showing unevenness of the resolidified surface and a radial crack.



Fig. 4.7 SEM Photograph of the cleaving surfaces along the radial crack, sample of Figs. 4.2-4.4. The crevasses are caused by the 11% reduction in volume on solidification.

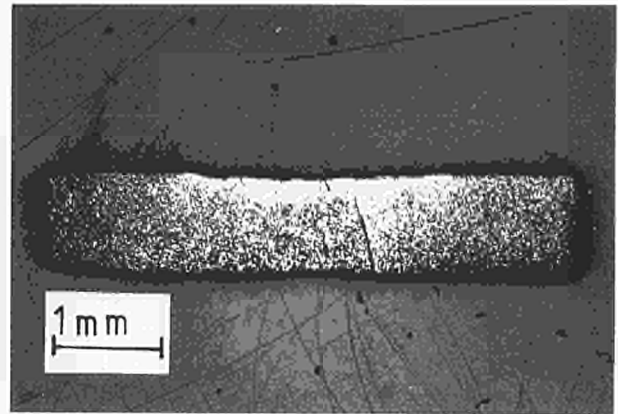


Fig. 4.8 Optical micrograph of the sample of Figs. 4.2-4.4, polished roughly along a sample diameter.

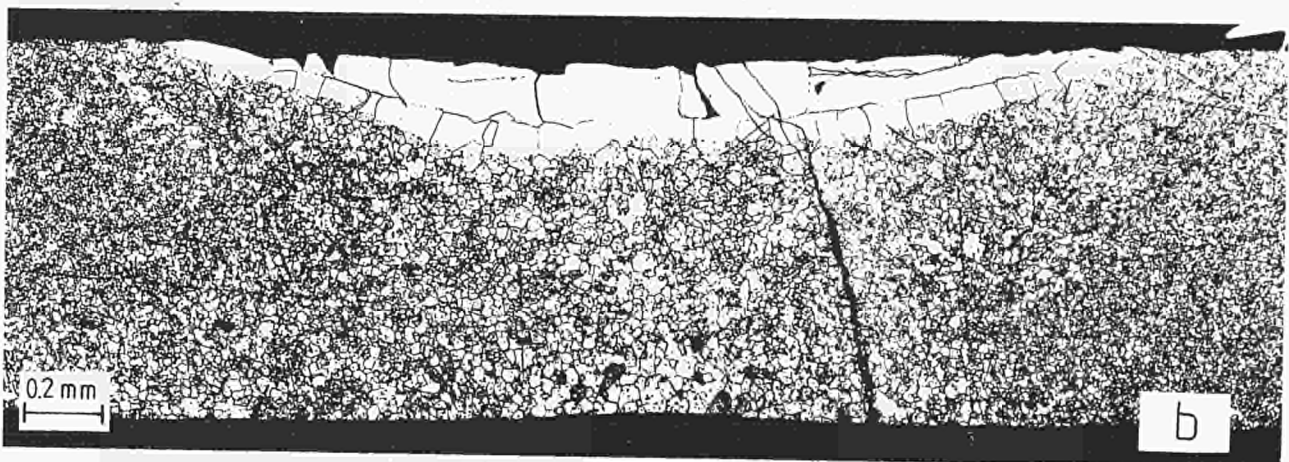
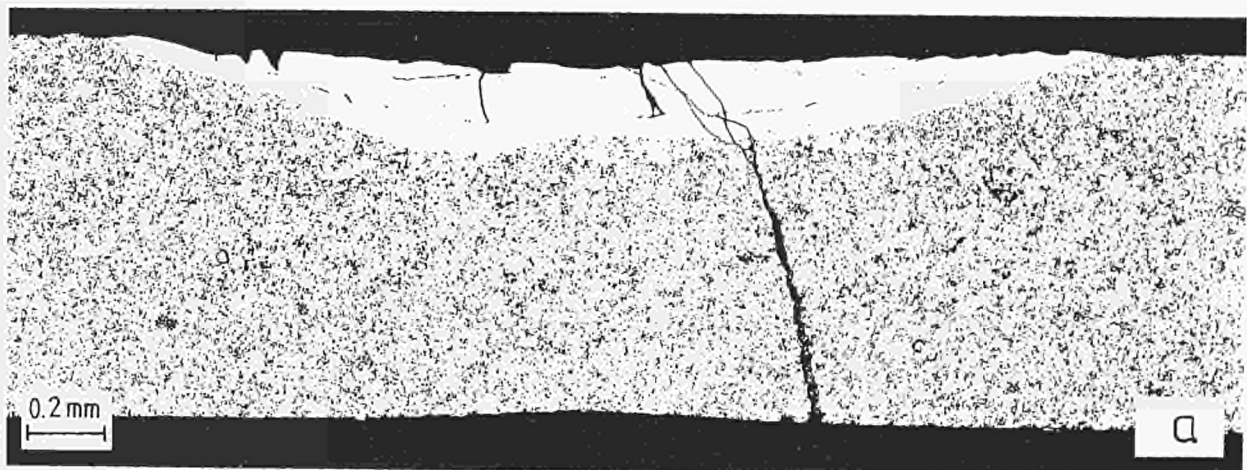


Fig. 4.9 Detail of Fig. 4.8; a: as polished, b: polished and etched.

Materials

Sample purity and stoichiometry

UO₂ samples were used from two different sources. Batch A had natural isotopic composition, 95% of the theoretical density and 6 mm diameter. Batch B was depleted in ²³⁵U, 94% T.D., 5 mm in diameter. The oxygen-to-metal ratio of both batches was confirmed not to differ significantly from 2.00. A spectroscopic analysis revealed the presence of the impurities specified in Tab. 4.1:

The EMF developed on the oxygen sensor corresponded to an O₂ partial pressure of 10⁻²¹ bar. This refers to a probe temperature of 1000 K. The thermodynamic data of H₂, O₂ and H₂O, as tabulated e.g. in [3], show that at 10 bar total pressure with 1000 ppm H₂ the indicated O₂ pressure should correspond to a ratio H₂/H₂O ≈ 2.5. Heating this gas mixture to around the melting point of UO₂ (3150 K) increases to P_{O₂} ≈ 10⁻⁴ bar. This is higher than the P_{O₂} in equilibrium with UO_{2.00} computed by Babelot et al. [4] (Fig.4.10), but should rather correspond to a molten phase with composition UO_{2.01}(l) instead. In spite of the addition of 0.1% H₂ to the otherwise pure argon atmosphere, the molten UO₂ should thus be slightly hyper-stoichiometric.

This statement was confirmed by a solid state EMF technique [5]. A partially molten sample was quenched rapidly. A chip was broken out of the resolidified melt, and measured against an Fe/FeO standard in a Y₂O₃-doped ThO₂ cell at 1000 - 1200 K. The measured EMF corresponded to a nearly temperature independent ΔG(O₂) ≈ -240 kJ/mol, which is in agreement with a composition of UO_{2.01} [6].

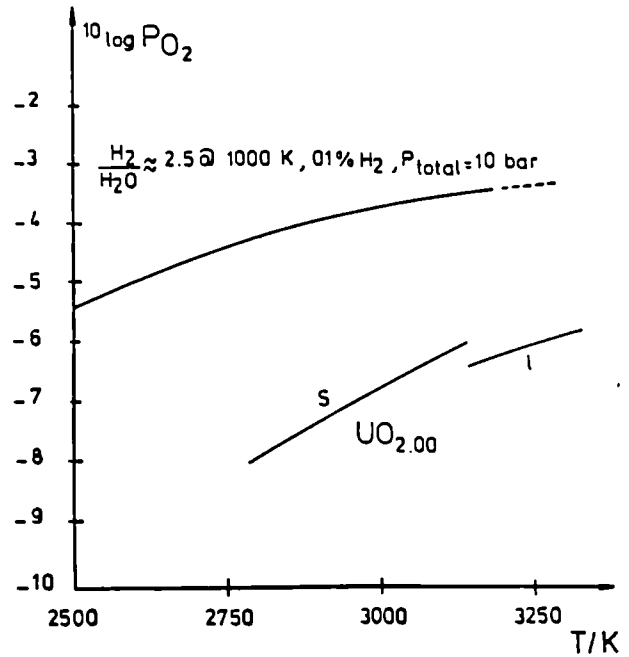


Fig.4.10 Oxygen partial pressure for 10 mbar of H₂ + 4 mbar of H₂O in 10 bar of Argon (upper curve), as well as equilibrium oxygen pressure over solid and liquid stoichiometric UO₂ (curves labeled 's' and 'l' respectively), as a function of temperature in C.

Temperature at the crater edge

UO_{2.01} does not melt congruently, in a temperature range somewhat lower than the melting point of stoichiometric UO_{2.00}. The solidus and liquidus temperatures T_s and T_l, were estimated from the arguments of Babelot et al. [4] as T_s ≈ 3020 K and T_l ≈ 3070 K. The edge of the molten pool as shown in Fig. 4.5 should have been at the 'melting temperature'.

Tab. 4.1: Impurities in UO₂ samples, in ppm

Element	Al	B	Cr	Cu	Fe	Mg	Na	Pb	Si	Zn
Batch A	15	<.05	5	30	0	3	5	5	50	50
Batch B	18	2½	3	30	8	2	<2	1	50	10

The shape and size of the crater was measured with a microscope, and superimposed to scale on the isotherm plot, such as shown by a heavy line in Fig. 4.4a. In all four runs that have been evaluated so far, the pool edge coincides with an isotherm in the range 2870 - 2920 K, which is more than 100 K lower than the 'melting point'. The calibration accuracy of the profile scanning pyrometers is estimated as ± 30 K. Thus a significant discrepancy remains to be explained.

Additional experiments were performed with lower power, that limited the maximum top temperature to 2920 K. Although appreciable densification and grain growth as well as a 'glassy' appearance were observed in the top surface centre, the optical micrograph (Fig. 4.11) does not show signs of melting. Remnants of the original grain structure still persist. In some of the runs with confirmed melting, the lower surface temperature attained values around 2870 - 2920 K. The micrographs of these runs showed grain growth, but no melting in the lower half of the sample.

Attempts to detect a 'melting plateau' were not very successful. The scanning aperture was aligned with the centre of the top surface. A scanning pattern was specified of 8000 points without any movement. When the top power was increased manually from 'just below melting' to 'just above melting' and then back to 'just below melting' after a few seconds, an indication of a 'resolidification plateau' was detected around 3020 - 3070 K. (Fig. 4.12). The high noise level is caused by turbulences in the hot gas over the heated spot.

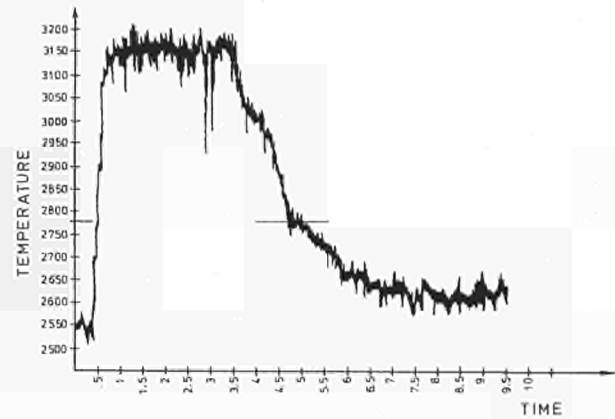


Fig.4.12 Top centre surface temperature of a UO_2 sample against time, with power input manually adjusted to 'just above melting power' for 3 seconds, and then 'just below melting'. A faint indication of a 'resolidification plateau' can be seen around 2780°C.

It thus appears unlikely that the crater edge did not exceed 2920 K. The discrepancy may rather be due to the optical effect of the hot gas column over the molten pool. This hot gas has a lower index of refraction. The pyrometry is done at the sharp angle of 20° . The hot gas acts as a 'negative lens', and reduces the size of the image. The crater edge is located at the maximum radial temperature gradient, where the effect of any distortion is maximum.

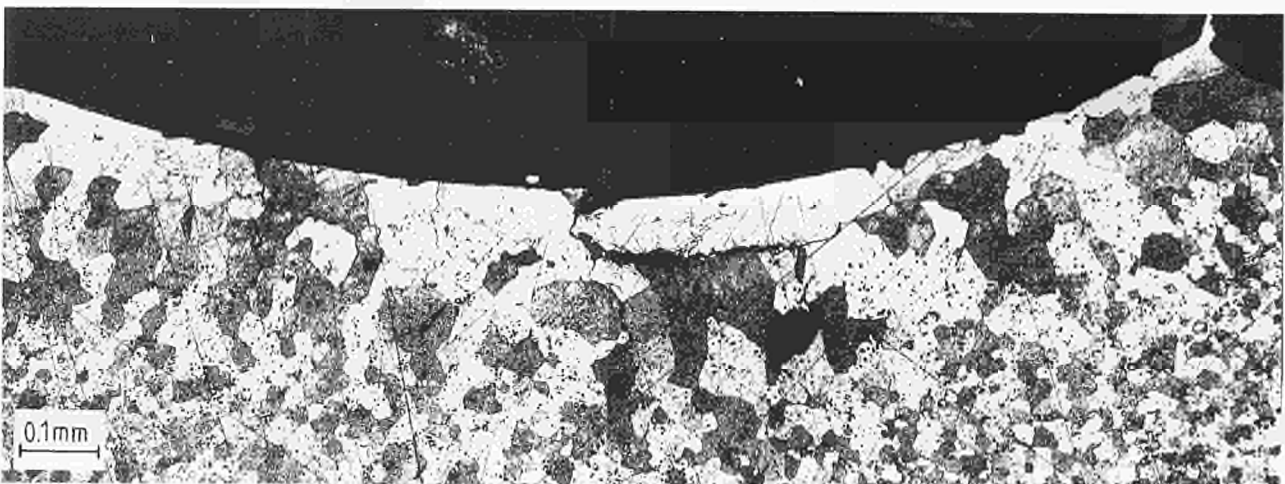


Fig. 4.11 Optical micrograph of a UO_2 sample heated to a maximum top surface temperature of 2650°C, showing grain growth but no signs of melting.

Data Evaluation

At first, the data were evaluated with the assumption that the final square scan as represented in Fig. 4.4 represents stationary conditions, as any further temperature change at this point is masked by the noise.

In the evaluation, cylindrical symmetry is assumed. A 2D grid was placed over (half of) a radial cross section, with a fine subdivision around the phase boundary observed in the micrograph, in order to minimise the effect of a discontinuity of any properties on melting. The experimental data show appreciable deviations from rotational symmetry. Therefore somewhat arbitrary 'average' radial temperature profiles were extracted from data as shown in Fig. 4.4. The axis of the grid refers to the centre of the temperature distribution, rather than to the centre of the sample, so as to minimise the effect of slight beam misalignment.

The experimental temperature profiles on the top and bottom surfaces were used as Dirichlet type boundary conditions in a non-linear stationary two-dimensional Finite Element calculation [7], assuming heat loss by radiation only at the cylindrical side surface. The thermal conductivity of solid UO_2 below the solidus point assumed as $T_s=3020$ K was taken from the expression of Neuer et al. [8,9]. Above the liquidus point $T_l=3070$ K an assumed value for the conductivity of the liquid was used, with a linear transition between T_s and T_l . The temperature dependence of materials properties and the thermal radiation were treated in an iterative process: A starting temperature distribution is assumed, the corresponding properties are computed and used for the next iteration, after which this procedure is repeated until convergence is reached (usually about 8 iterations). Fig. 4.13 shows the result of such a calculation, expressed as an isotherm plot, based on an assumed liquid conductivity of 3.0 W/(m.K) . The temperatures computed along the observed phase boundary for this same run are shown in Fig. 4.14 for several assumed values of the liquid conductivity. Fig. 4.15 shows the assumed value for the liquid conductivity as a function of the calculated temperature at the observed phase boundary at the axis, for four different runs on four samples from the same batch but of different geometry. Evidently, the spread in the results is about a factor three, which is rather larger than expected from the

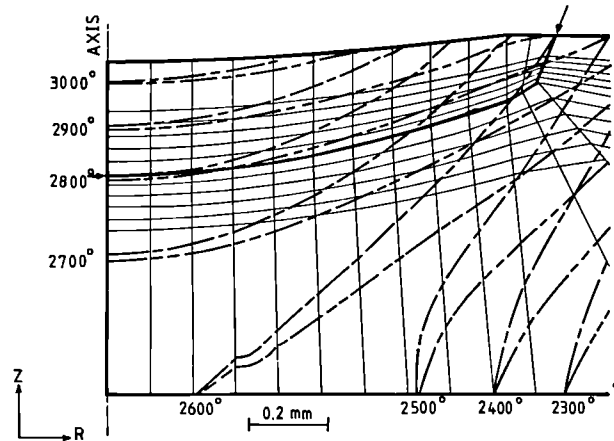


Fig.4.13 Central part of Finite-Element grid with calculated temperature distribution across a longitudinal cross section of run U6-2. The observed position of the melting boundary is indicated by a heavy line marked with arrows. The calculation was performed with fixed surface temperatures, taken from averaged measured surface temperature profiles (Dirichlet boundary conditions). The heat loss at the cylindrical side surface was assumed as radiation only. Two sets of isotherms are shown, in $^{\circ}\text{C}$. The lines $-\cdot-\cdot-$ are based on the temperature profiles as measured, assuming a thermal conductivity of the liquid of 3.0 W/(m.K) . The lines $-\cdot-\cdot-$ refer to a top surface profile 'inflated' to place the crater edge at 2800°C , and a conductivity of 2.5 W/(m.K) .

inherent resolution of the input data (about $\pm 20\%$). Assuming the phase boundary to be at $T_l=3070$ K, the values deduced for the thermal conductivity of liquid UO_2 ranges from 1.0 to 3.0 W/(m.K) .

The two-dimensional evaluation procedure described above is a fairly complicated one. At first glance it looks tempting to deduce a value for the conductivity of the liquid from a simple one-dimensional model, equating the heat flux densities in the liquid and the solid at the phase boundary. In both the solid and the liquid layer the heat flux density equals the conductivity times the temperature difference across the layer

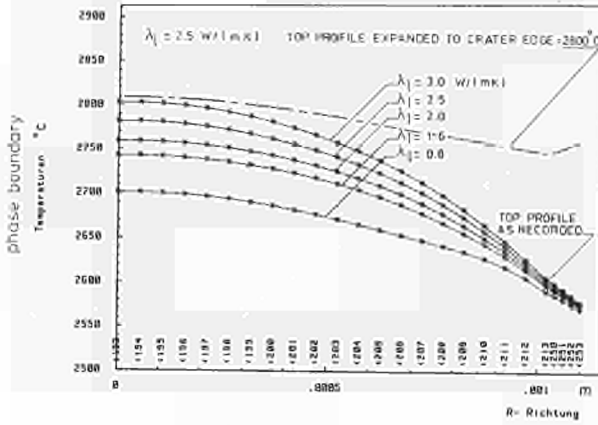


Fig. 4.14 Calculated temperature along the observed phase boundary in run U6-2 for different assumed values of the conductivity of the liquid, based on the temperature profiles as measured. Also indicated is the distribution from the 'inflated' profile, that fixes the crater edge at 2800°C.

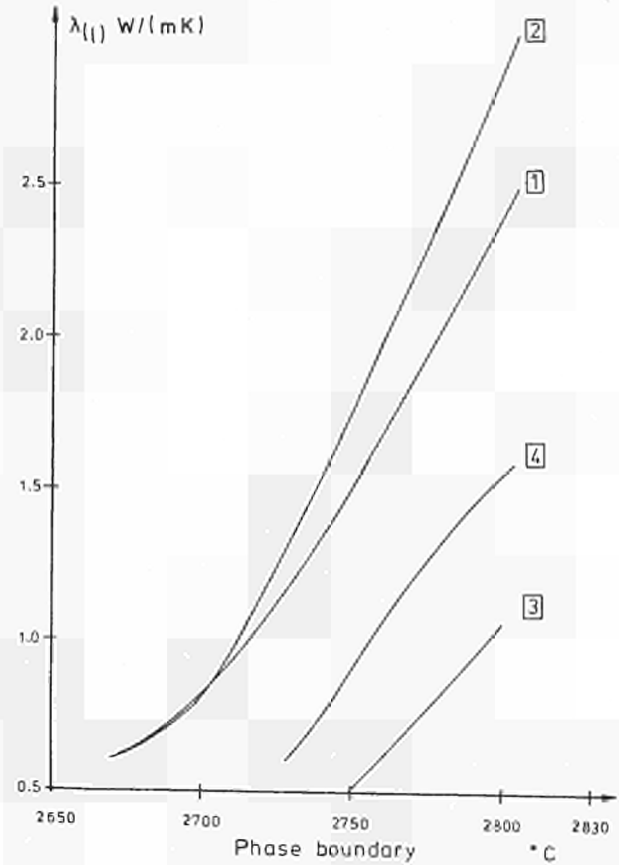


Fig. 4.15 Assumed liquid conductivity as a function of calculated temperature at the observed liquid penetration at the sample axis, from four different runs U6-1 through U6-4, using the temperature profiles as measured, without inflation to set the crater edge at the melting point.

divided by the layer thickness. The phase boundary is at the melting point, whereas the top and bottom surface temperatures have been measured. Unfortunately, this simple approach gives a crude estimate only, as is evident from Fig. 4.16, showing the heat flux density distribution calculated for run U6-4. An adiabatic plane is seen at $\approx 1/5$ of the thickness; heat flows also from the bottom to the side.

Figs. 4.13-4.14 also show the results calculated for the same run with a top surface profile 'inflated' to put the edge of the molten pool at T_1 , and a liquid conductivity of 2.5 W/(m.K). Evidently this results in a better fit. Similar conclusions could be drawn from 'inflated' profiles for other runs, which seems to provide some evidence for the explanation proposed above for the temperature at the crater edge.

Ongoing improvements

A further refinement should consist of the inclusion of convection cooling at the cylindrical side surface. Arguments for the magnitude of convection were obtained from power profile considerations needed in the dynamic treatment discussed below; so far no convection was included in the stationary calculations.

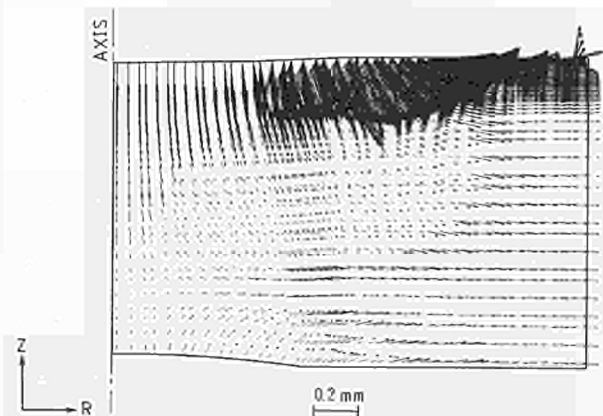


Fig. 4.16 Heat flux density pattern calculated from run U6-4. Only the direction and the relative length of the arrows is relevant. Assumed liquid conductivity: 1.6 W/(m.K). Heat loss at the side is assumed as by radiation only.

One of the major sources of error should be the gross asymmetry in the laser beam profiles, as exemplified most clearly in Fig. 4.4a. Meanwhile it has been demonstrated [15] that the flatness of the Brewster windows in the lasers plays a crucial rôle. The present windows (ZnSe plates) show appreciable deviations from flatness. New windows have now been ordered with strict specifications. Important astigmatic distortion was traced back to the way the rear mirrors in the lasers were mounted. In the original design these mirrors, made from molybdenum discs, were clamped down at the edge of the front surface. This clamping appears to warp the mirror and creates appreciable astigmatism. Consequently, the mirror mount has been modified. The mirrors are now held from the cylindrical side by low tension epoxy resin. This limits the warping to within the inherent inaccuracy of the reflecting surface.

Another source of uncertainty stems from the badly known contribution of forced convection cooling. The computational efforts needed for a better understanding are appreciable, and such efforts will thus be resumed once the laser beam profile quality is considered acceptable.

Dynamic penetration of the melting front

So far, the data evaluation was based on the assumption, that 'stationary' surface temperatures correspond to stationary conditions throughout the sample. As is evident from Figs. 4.3 and 4.12, the turbulences in the hot gas above the sample result in appreciable noise in the raw data. After 3-5 s any further evolution of surface temperatures is masked by the noise and thus no longer detectable. Substantially longer exposures destroy the sample, however.

Fink and Leibowitz [10,11] have analysed the raw data of Tasman et al. [1] by a somewhat different finite-difference calculation. They came to the conclusion, that the stationary assumption put forward in [1] and in the present evaluation was incorrect. These authors suggest that the melting front after 5 s in the data set analysed had attained only 53% of its stationary penetration, and that therefore the deduced conductivity of the liquid could be nearly twice as high as the values reported.

A two-dimensional dynamic analysis of the present data was started. The radial power distributions in the top and bottom beams were

computed from stationary calculations on an extended grid, in which a thin dummy layer with anisotropic (axial only) thermal conduction was added to the top and bottom surfaces. Depending on whether the measured temperature profile was allocated to the outside or to the inside of the dummy layers, the heat flux through the sample towards the surface as well as the net heat loss to the environment could be computed separately. Convection loss was included, at first based on an 'engineering estimate' for natural convection in argon at a pressure of 10 bar. Using data from the first 2D scan (bottom heating only), the requested equality of the heat flux through the sample towards the top and of the loss through radiation and convection, imposed a radius-dependent correction of the convection term, up to a factor 9 in the centre, dropping to a factor 1.4 at the edge. Similar arguments applied to the bottom profiles resulted in even more dramatic corrections of the 'convection' term, which is markedly temperature dependent.

The dynamic behavior of the melting front was now examined with a non-stationary non-linear Finite Element analysis [7]. This requires the use of power profiles rather than temperature profiles as boundary conditions. The power profiles were implemented as heat source distributions in the dummy layers. The heat of fusion and density data were taken from [2] ($H_f = 74.9 \text{ kJ/Mol}$, $\rho(s) = 9.71 \text{ g/cm}^3$, $\rho(l) = 8.64 \text{ g/cm}^3$), the specific heat data were from Hyland and Ohse [12] ($C_p(s) = 161 \text{ J/(Mol.K)}$, $C_p(l) = 138 \text{ J/(Mol.K)}$). The grid subdivision was modified, according to suggestions of Pammer [13] and Stelzer [14]. The elements at the top surface were chosen very thin, increasing in thickness upon penetration in the sample. This precaution accommodates the 'infinite' rate of temperature rise at the top surface in the very first moment after admission of the top beam.

The stationary distribution computed from the bottom power profile only was taken as starting condition. Then the top power was added, and the temperature evolution was calculated as a function of time. The first time steps were taken very short, shorter than suggested by the Pammer rule [13]. Upon attainment of the melting temperature, it was found necessary to choose the time steps very much shorter so as to avoid melting spreading in axial direction over more than one element. This appears to be a consequence of the inclusion of a phase transition with an appreciable latent heat of fusion. As a consequence of the shortness of the steps, the

number of iterations at each step could be limited to one, i.e. each step was calculated with properties based on temperatures attained in the previous step. The results obtained on a grid of 352 elements were verified to be independent of the limitation of the number of iterations to one, and of the way of time subdivision in the range 92 to 160 progressively increasing time steps.

Results from run U6-4, with a rather thick sample (5 mm diameter x 1.36 mm) with an assumed conductivity of the liquid of 1.6 W/(m.K), show a nearly exponential approach towards stationary conditions computed from the same top and bottom power profiles (Fig. 4.17).

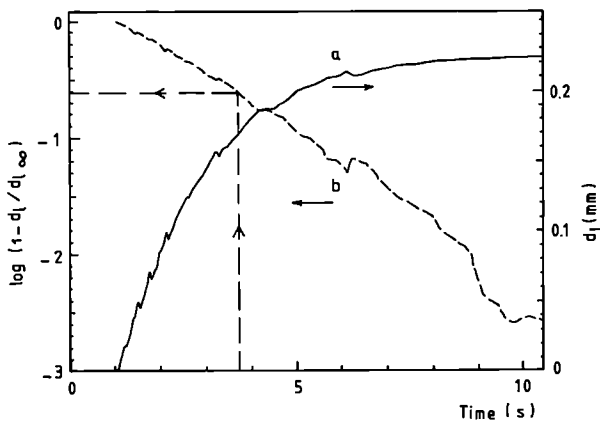


Fig. 4.17 Penetration d_l of the phase boundary as a function of time, run U6-4, assumed liquid conductivity: 1.6 W/(m.K). a: linear scale, b: $10\log(1 - d_l/d_{l\infty})$. The centre of the crater was recorded after an exposure of 3.7 s, for which time the calculated penetration was 75.5% of its stationary value $d_{l\infty}$.

The slight irregularities in the results are caused by numerical instabilities in the calculations that dampen out in subsequent steps. In this particular run, the pool centre was recorded 3.7 s after admission of the top beam. At that time the melt had penetrated only 75.5% of its final depth. The correct thermal conductivity of the melt should thus be around $1.6/0.755 = 2.1$ W/(m.K). A similar analysis of data from run U6-3, taken on a thinner sample (5 mm diameter x 0.96 mm) resulted in a correction of only 2%, raising the result from 1.0 to 1.02 W/(m.K).

The criticism of Fink and Leibowitz [10,11] thus appears to be qualitatively correct, though quantitatively overestimated. Calculations from deduced power profiles with uncertain convection heat losses are less reliable than those from directly measured temperature profiles (Dirichlet conditions). The best approach seems to consist of stationary Dirichlet calculations corrected by means of a dynamic analysis as described above. The dynamic analysis does not suffice to eliminate the unexpectedly large spread in the results. Even with the dynamic correction, the conductivity of the melt still appears to be substantially lower than that of the solid at the melting point. The analysis will be resumed once that better data with more symmetrical laser beams are available.

Conclusion

With the present quality of the input data, any conclusion can only be preliminary. The present status is summarised in Tab. 4.2 and in Fig. 4.18. All evaluations were based on an assumed liquidus temperature $T_l = 3070$ K and on the solid conductivity of reference [8]. In fact the procedure employed here yields results that are (roughly) proportional to the assumed solid conductivity. All results for the liquid conductivity are substantially lower than the solid conductivity of 3.48 W/(m.K) derived from [8] at T_l . A drop in conductivity on melting has so far been observed on all other materials except

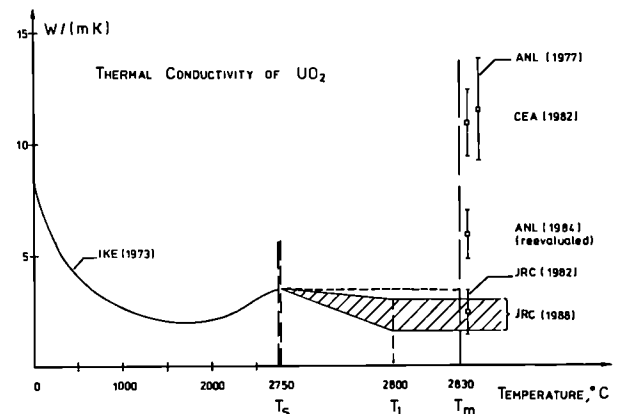


Fig. 4.18 Thermal conductivity of solid and liquid UO_2 . The data labeled 'ANL' and 'CEA', referred to in [11], were obtained on UO_2 encapsulated in tungsten cells. The shaded area shows the present work.

Tab. 4. 2: Thermal conductivity of liquid UO_2 , preliminary results

Run	U6-1	U6-2	U6-3	U6-4	U5-1
Reference in Fig. 4.15:	1	2	3	4	-
Sample batch	B	B	B	B	A
Sample size, mm	$\varnothing 5 \times 1.38$	$\varnothing 5 \times 0.90$	$\varnothing 5 \times 0.93$	$\varnothing 5 \times 1.64$	$\varnothing 6 \times 1.02$
Density, % T.D.	94	94	94	94	95
Max.Temp., °C	3025	3050	3000	3045	2650
Shown in Figs.:	--	4.13,4.14	4.2-4.9	4.16-4.17	4.11
$\lambda_1, W/(m.K)$ (Notes 1,3)	2.5	3.0	1.0	1.6	--
$\lambda_1, W/(m.K)$ (Notes 2,3)	--	2.5	--	--	--
$\lambda_1, W/(m.K)$ (Notes 1,4)	--	--	1.02	2.12	--

Note 1: Top temperature profile taken as measured.

Note 2: Top temperature profile inflated to set crater edge at T_1 .

Note 3: Stationary non-linear calculation.

Note 4: Corrected for dynamic penetration of melting front, non-stationary non-linear calculation.

for a few exceptional cases such as bismuth and silicon. The discrepancy with the results of other authors [11], obtained on molten UO_2 contained in tungsten capsules, remains as before. It could be that the difference is due, at least in part, to the dissolution of W (up to 20%) in the UO_2 matrix at the melting point of the latter. Meanwhile, UO_2 samples with advertent addition of W have been prepared that may help to clarify this point.

References

- [1] H.A.Tasman, D.Pel, J.Richter, H.-E.Schmidt: High Temp.-High Pressures 15 (1983) 419
- [2] J.K.Fink, M.G.Chasanov, L.Leibowitz: ANL-CEN-RSD-77-1 (1977)
- [3] I.Barin, O.Knacke: Thermochemical properties of inorganic substances (Springer Verlag, Berlin/Heidelberg/New York, 1973)
- [4] J.-F.Babelot, R.W.Ohse, M.Hoch: J.Nucl.Mater. 137 (1986) 144
- [5] Hj.Matzke, J.Ottaviani, D.Pellotiero, J.Rouault: J.Nucl.Mater. 160 (1988) 142
- [6] A.Nakamura, T.Fujino: J.Nucl.Mater. 149 (1987) 80
- [7] FEMFAM-T, originally designed by J.F.Stelzer, KFA-Jülich, FRG.
- [8] G.Neuer, R.Brandt, G.Haufler: IKT Report SB3; IKE, University of Stuttgart, F.R.Germany (1973)
- [9] G.Neuer, R.Brandt, G.Haufler: J.Non-Equilibrium Thermodyn. 1 (1976) 3
- [10] J.K.Fink: Thermophysical Properties of Fast Reactor Fuel, CONF-840440-4 (1984)
- [11] J.K.Fink, L.Leibowitz: High Temp.-High Pressures 17 (1985) 17
- [12] G.J.Hyland, R.W.Ohse: J.Nucl.Mater. 140 (1986) 149
- [13] Z.Pammer: Int.J.Numer.Meth.Eng. 15 (1980) 495
- [14] J.F.Stelzer in: "Numerical Method in Thermal Problems" Vol.III (Ed. R.W.Lewis) Morgan & Schreffler, Pineridge Press, Swansea (1981) 636
- [15] H.A.Tasman: unpublished.

Measurements of Specific Heat in High-Temperature Heating Experiments with Pulsed Lasers

A method for the direct measurement of the specific heat of solids and liquids at very high temperatures has been applied to refractory metals. The experimental setup consists of a high-pressure autoclave where the sample levitates in an acoustic field. Heating is produced by four tetrahedrally-oriented laser beams; the surface temperature during the pulse is sufficiently homogeneous. C_p is deduced from the analysis of the measured surface-temperature variation during the heating and cooling phases.

The experimental conditions and the various heat losses which have to be taken into account in order to formulate a precise heat-rate balance and deduce the specific heat of the sample are briefly discussed in the following section. The calibration procedure is examined and the experimental errors are evaluated. Measurements of C_p in tungsten up to 3800 K are presented.

In the preceding report (TUAR 87) the problems concerning the definition of the experimental conditions and the interpretation of the physical processes were discussed. The determination of C_p from laser pulse experiments is based on the accurate measurement of the surface-temperature history and on the definition of the effective heat losses. The expression relating C_p to the total heat loss rate is trivial in cases where the sample has a regular shape and has a virtually homogeneous temperature. Analytical difficulties are encountered if significant internal gradients are present. Since the surface temperature is measured on a limited area of the sample, it is obvious that the analysis is only viable if at least this temperature can be considered as reasonably homogeneous and the internal temperature field as spherically symmetric. Therefore, only an accurate numerical analysis of the heat transport equation in the sample can discern to what extent situations with considerable radial temperature gradients are manageable.

A further important question concerns the evaluation of the surface heat losses. In the given experimental context, only radiative losses (based on distinct physical laws) can be precisely expressed, apart from the determination of the

emissivity, whose measurement has been discussed elsewhere [1]. Other heat losses are in this case due to heat conduction and convection in the buffer gas. These losses can only be formulated on the basis of the phenomenological equations of fluid dynamics and expressed as functions of semi-empirical parameters.

In order to avoid facing these two problems simultaneously, in the first experiments refractory metals were investigated whose thermal conductivity was sufficiently high to ensure fairly homogeneous heating of the spherical samples. The analysis could therefore be concentrated on the operating heat losses.

The prior analysis indicated that in an acoustic levitation field the convective losses may become dominant over radiation losses even at very high temperatures. These undesired effects had therefore to be suitably quantified and introduced in the energy balance equation. A rigorous physical treatment of convection under the given conditions is impracticable. However, the geometry of the system and the homogeneity of the heating conditions showed that this effect is fairly well reproducible and a formulation of the convective losses could be attempted. The experimental evaluations of these losses have been carried out by analyzing the cooling curves of a variety of samples of known emissivity and heat capacity in different gases and under pressures ranging from 0.01 up to 500 bar, with and without acoustic levitation field. The data have been compared with the theoretical curves and the unknown parameters were obtained by numerical fitting. The question whether convection is established rapidly enough to be described by formulae which have only been tested under near-stationary conditions was answered positively in the case of natural convection, by observing the hot gas plume with a refracted light beam: the thickness of the hot convection layer was consistent with the predictions. This is presumably also true for sonic convection where the turbulent flow appears to be much faster than the natural convection flow.

Fig. 4.19 shows the measured natural convection coefficient in He at various pressures as well as the losses due to heat conduction though the support, measured in vacuo. The radiation losses are also plotted. It can be seen that at high pressures convection becomes negligible at temperatures above 4000 K. In fact, whereas the radiative term strongly increases with temperature, the convection coefficient decreases almost linearly with T.

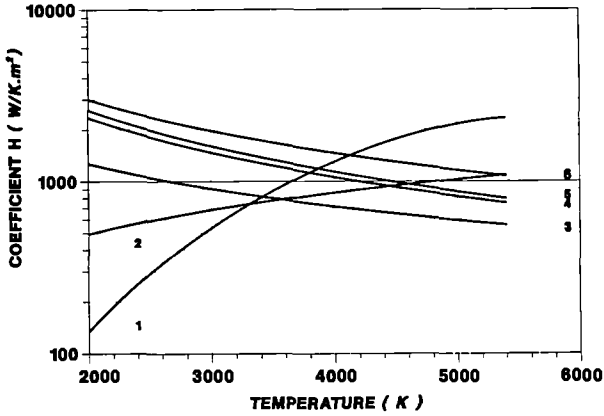


Fig. 4.19 Natural convective heat-loss coefficients in a pulse-heated tungsten sphere in helium as a function of temperature at various pressures: 9.7 bar (3); 74 bar (4); 110 bar (5); 260 bar (6); radiation loss (1); conductive loss through the support (2).

The heat losses under levitation conditions in 70-kHz standing waves are much higher. They present a similar marked dependence on temperature (Fig. 4.20), but the mechanisms are different: A turbulent flow is established involving a much larger gas volume than in the case of natural convection. Four major vortices are formed at the top and the bottom of the sphere with sizes comparable with the sample diameter. The upward motion of the gas produced by buoyancy forces is much slower than the

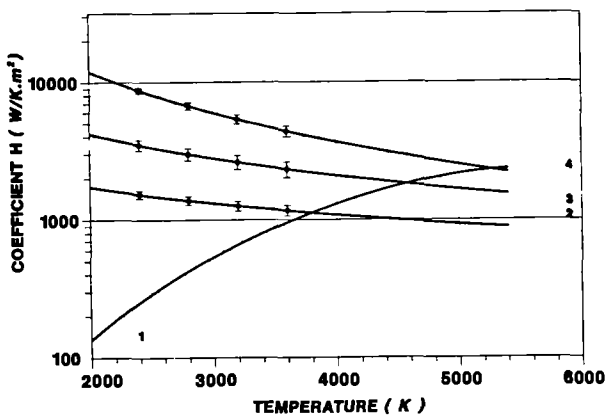


Fig. 4.20 Convective heat losses in an acoustic levitation field of 150dB and 70 kHz frequency in helium at various pressures: 2) 4.7 bar; 3) 45 bar; 4) 260 bar; 1) radiation losses.

motion of the gas in the vortices. At sonic energies of the order of 150 dB in He at 250 bar, the convective losses are larger than the radiative losses up to 5000 K.

An analysis of the experimental measurements was made by comparing the dependence of the heat loss coefficient on the sample temperature (the most important dependence in our context) with the theoretical predictions. Tab. 4.3 shows the experimentally deduced values of the temperature exponents at different pressures. The exponents become more negative with increasing pressure, the effect being more pronounced in the presence of acoustic waves. The observed temperature-exponents are between those predicted by two extreme regimes, showing a regular tendency towards a fast-flow regime as the gas pressure, and hence the heat loss rate, increases. The theoretical exponent -0.7 is actually reached for a gas pressure of 260 bar in an acoustic field.

Tab. 4.3 Temperature exponents for the convection heat losses

p(bar)	Experiment		Theory	
	free	sonic	laminar flow	turbulent
5	-	+0.30	slow flow: +1.2	*1.0
10	+0.20	-		
50	-0.15	-0.01	fast flow:	
80	-0.17	-0.20		
200	-0.19	-	-0.5	-0.7
260	-0.20	-0.70		

Finally, the convective losses, though very complex, can be measured and expressed in terms of functions which have been generally tested and validated.

Preliminary experiments were carried out with the aim of measuring C_p from the analysis of cooling curves starting from the complete heat loss balance equation. Tungsten was chosen for this purpose because its properties are fairly well known up to 3800 K and hence a check could be made on the predicted precision of the method. Fig. 4.21 shows the measured C_p as a function of temperature. The measurements were obtained from five different shots. The continuous line represents the average of the literature data. Inspection of the experimental points shows that the amount of scatter decreases with increasing temperature and above 3300 K the error is less than 10%.

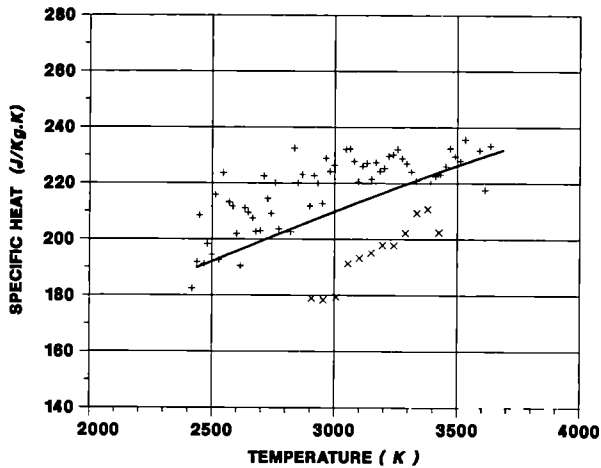


Fig. 4.21 Measurements of the specific heat of tungsten as a function of temperature.

The error sources have different weights in the various temperature ranges (see Tab. 4.4), but those due to the convective losses are predominant up to 4000 K. The other errors are related to the precision of the temperature measurement [1] whose error does strongly affect the evaluation of dT/dt . The errors reported in the table arising from the sample density are of course specific to the metals examined.

Tab. 4.4 Error source in the specific heat evaluation - Fractional Errors

variable: exponent:	C_p -	T 4	dT/dt 1	H 1	p 1/3
2000/3000 K	0.14	0.015	0.05	0.10	0.02
3000/4000 K	0.11	0.005	0.03	0.05	0.10

Conclusion

The work has shown that calorimetric measurements with laser-pulse heating at very high temperatures under acoustic levitation conditions are feasible, however, a complex calibration and analytical procedure is required. The surface heat losses due to convective mechanisms, enhanced by the acoustic levitation field, are predominant up to near 5000 K. They consist of heat abduction processes caused by turbulent gas flow whose extent increases with increasing gas pressure but is little affected by the temperature of the sample.

With the precision achieved in the pyrometric measurements the error in the evaluation of C_p is mainly determined by the reproducibility of the convective heat losses and ranges between 10% and 15% in the temperature range explored.

Reference

- [1] J.P.Hiernaut and C.Ronchi, High Temp.- High Press. (in print)

Deduction of C_p in Pulse Heated Samples under Slow Heat Transport Conditions

Obtaining the specific heat of materials with low heat conductivity from laser pulse experiments requires an accurate analysis of the measured temperature signals. The equation from which C_p is deduced is the balance between the rate of energy stored in the sample and the energy flow through its outer surface. The latter term, discussed in the preceding section, can be calculated from experimental data. The former has to be calculated by solving the heat diffusion equation in the sample, including possibly occurring phase transitions. This is made using an advanced numerical integration method which provides a very precise evaluation of the heat flow in the sample. This calculation is only possible if both thermal diffusivity and specific heat are known at the various temperatures involved in the calculation. Now, the latter represents the unknown of the problem and may therefore be determined by means of an iterating procedure starting from an estimated value. This is formally rather complex because at each time the temperature profile in the sample changes and the volume has to be finely subdivided into nominally isothermal spherical shells; some of these have (low) temperatures at which C_p is known and has to be treated as a constant, and some have temperatures at which C_p is unknown. Thus the energy balance equation contains as many unknowns as shells are present with temperatures belonging to the unexplored range of $C_p(T)$. Under these conditions the analysis of one single temperature profile is not sufficient to solve the equation. Therefore, a number of experimental temperatures (and radial profiles) corresponding to the number of the unknown C_p 's have to be collected to constitute a

determined system of equations. This is obviously possible since several hundreds of profiles are available in each shot. However, in order to avoid solving too large systems a defined analytical sequence is adopted. The method used consists of constructing the function $C_p(T)$ step by step, with the following procedure:

- The existing data of C_p in the T-range already explored are previously assessed.
- Pulse-heating experiments are analysed in a slightly extended temperature range.
- After calculating the internal heat conduction, the internal energy variation rate of the sample is evaluated and, from this, the values of C_p in the incremented temperature interval are deduced.
- The new C_p values are appended to the initial dataset and a following step can be carried out in a further extended temperature interval.

Of course, this procedure implies that the surface heat losses can be calculated with appropriate precision. The error treatment is in this context essential for the significance of the results of the calculation. In fact, several errors arising from different sources have to be accounted for. The analysis of this term reveals that the first-order error in the time derivation of the integral is proportional to the experimental error made in the evaluation of dT_s/dt . Errors of other quantities involved in the evaluations of $\text{grad}(T)$ (i.e. thermal conductivity, deviations from spherical symmetry) and of $\rho(T)$ (density) have a secondary influence on C_p .

A computer program has been written to carry out these calculations. Particular care was devoted to the solution of the heat conduction equation by taking the experimentally measured surface temperature as a boundary condition.

Experiments with pulse heating of UO_2 are in progress where temperatures up to 4000 K have been reached so far. At present the analysis is aimed at separating systematic and stochastic errors in the measured temperatures and emissivities in order to optimise the numerical evaluation of the time derivatives of temperature and stored energy. The temperature evolution in two shots at different powers and deposited energies are shown in Figs. 4.22 and 4.23. The curves of the measured surface temperature and

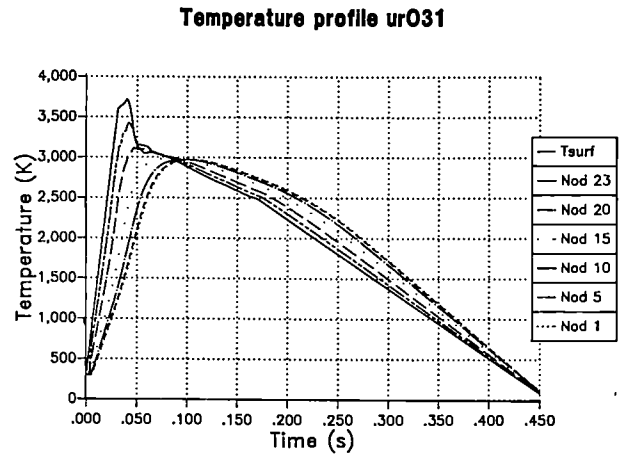


Fig. 4.22 Measured surface temperature pulse in a laser heated UO_2 sphere and temperature propagation in the inner zones as calculated by a computer code. The surface temperature corresponds to the highest curve in the heat-up phase and to the lowest in the cool-down phase. The deposited laser energy was 12 J.

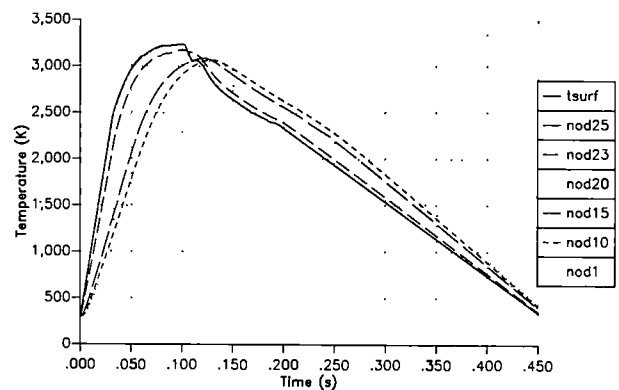


Fig. 4.23 Measured surface temperature pulse in a laser heated UO_2 sphere and temperature propagation in the inner zones as calculated by a computer code. The surface temperature corresponds to the highest curve in the heat-up phase and to the lowest in the cool-down phase. The deposited laser energy was 8 J.

of the calculated temperatures in six inner shells are plotted. The errors are not indicated here, but their order of magnitude can be estimated from the residual fluctuations appearing in some segments of the curves. About 50 similar curves are at present available for the measurement of C_p .

Measurement of the Melting Point and Spectral Emissivity of Refractory Metals

A six-color pyrometer has been used to measure the melting point and the emissivity of nine refractory metals : hafnium, niobium, molybdenum, rhenium, rhodium, tantalum, tungsten, vanadium and zirconium.

In several metals and conductive ceramics the isotherms of emissivity ϵ_λ are found to cross at a particular wave-length, or within a very narrow interval $d\lambda$. This effect holds up to and beyond the melting point: in fact, it was found that the slope of the emissivity against the wavelength changes sign when going from the solid to liquid phase. This inversion occurs at or near the melting point where the investigated metals behave like grey bodies in the interval 500 - 1000 nm.

Though the physical meaning of this property is still unclear, its technological interest for calibration of multi-wavelength pyrometers at high temperature is evident, especially under difficult experimental conditions (typically, when samples are heated in optically absorbing atmospheres). The details of the temperature evaluation method were published elsewhere [1,2,3].

The samples are small spheres of 1 mm diameter, heated in a pure argon atmosphere by 4 pulsed laser-beams disposed in a tetrahedral configuration. Two different sets of 6 interference filters covering the wavelength range between 500 and 1000 nm with a bandwidth of 10 or 40 nm were chosen to measure temperatures above or below 2300 K respectively. A small TV-camera was mounted in the pyrometer to facilitate the alignment and to monitor the sample image during the rapid pulse heating. The pyrometer was slightly improved by inserting a short-pass filter to absorb the reflected laser-light, enabling measurements to be performed during the heating stage. However, due to the better

experimental conditions (thermal homogeneity, slower temperature variation) the cooling curves were preferentially used to measure T_m and ϵ_λ .

a) Radiative properties

A typical temperature signal recorded during the sample cooling- stage is presented in Fig.4.24 for

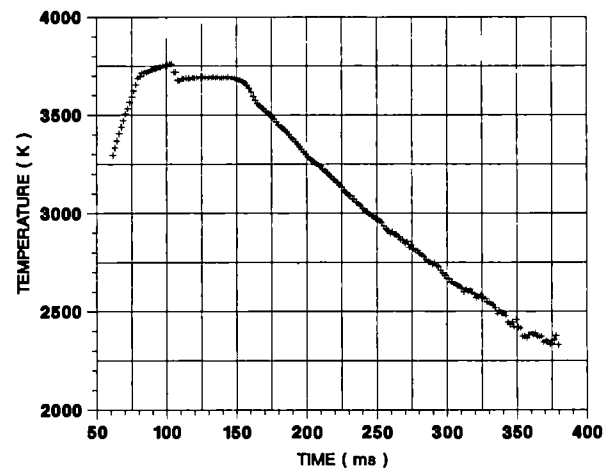


Fig. 4.24 Temperature curve of tungsten showing the heating and cooling periods and the solidification plateau.

tungsten. The spectral emissivities at six wavelengths as functions of temperature for tungsten are shown in Figs. 4.25a,b,c,d,e,f. The points represent results obtained from a number of different temperature pulses. The spline functions drawn in these diagrams are calculated by means of a third-order fitting of the data. Comparison of these data with emissivity data [4,5,6] shows an agreement of better than 5% in the temperature range 2400-2800 K and in the wavelength range 0.5-1.0 μm . One can observe that for the six wavelengths the spectral emissivities vary linearly as a function of temperature up to 3500 K and at higher temperatures they converge to a single value at the melting point. The intersection point, where the emissivity is independent of the wavelength, is called here T_x -point. Furthermore, the plot of the emissivity as a function of the wavelength shows the inversion of the emissivity dependency on λ below and above the melting point as well as the grey-body-like behavior at T_m , and the existence of a particular point, called λ_x -point, at

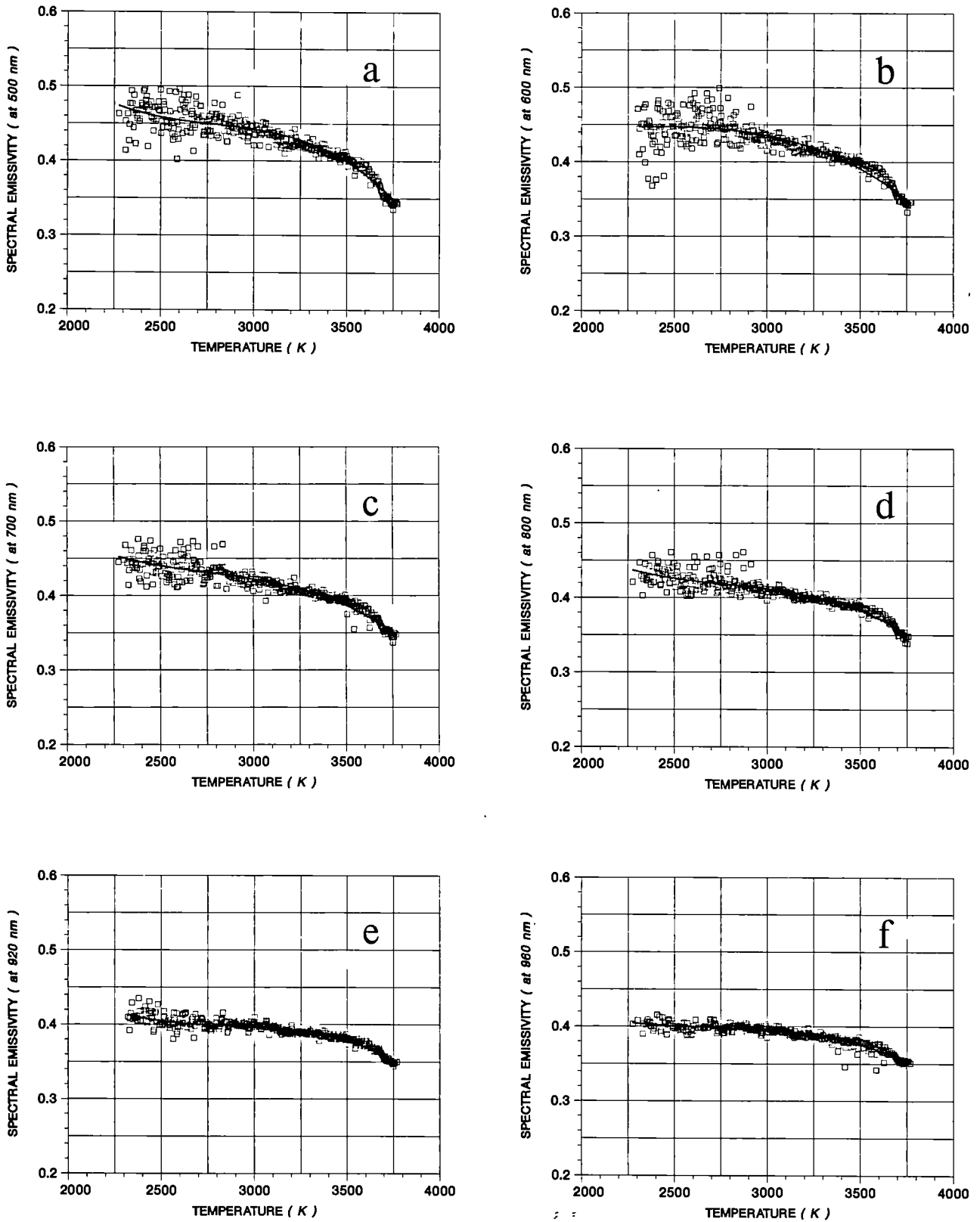


Fig. 4.25 Normal spectral emissivity of tungsten as a function of the temperature a) at 500 nm , b) at 600 nm , c) at 700 nm , d) at 800 nm , e) at 920 nm , f) at 960 nm.

which the emissivity is independent of the temperature (Fig. 4.26). The linear least-square fitting of $\ln(\epsilon)$ vs. λ generally shows good regression coefficients (> 0.995). This confirms the validity of the initial formulation of ϵ_λ . The data plotted in Fig. 4.26 agree very well with the literature results (4), the position of λ_x differing only by 2.4%. All the other examined metals

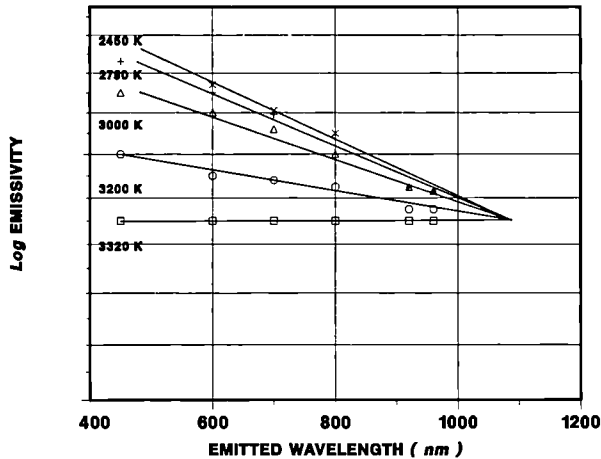


Fig. 4.26 Normal spectral emissivity of tungsten as a function of the wavelength at different temperature.

show an analogous behavior displaying both a T_x - and a λ_x -point. The presentation of the complete database will be the subject of a separate publication. Here the results are only summarised in Tab. 4.5 (extended and improved with respect to that published in TUAR 87) where the melting point, the spectral emissivity at 655 nm at the melting point, the emissivity at the λ_x -point and the value of λ_x are compared with the published literature data.

b) Melting point

The record of temperature pulse versus time provides an accurate method for the determination of the melting point of the sample (Fig. 4.24). In fact, the onset of fusion during heating - and solidification during cooling - results in a clearly detectable change in the temperature slope. During cool-down from temperatures above T_m , a rather long "plateau" can be observed, the extent of which is proportional to molten mass and to the heat of fusion of the metal and inversely proportional to the heat-loss rate of the sample. For highly

conducting metals during cooling from $T > T_m$ the surface temperature remains effectively constant as long as the solidification front proceeds inwards into the sphere and therefore the inflection point and the melting temperature can be established with great accuracy. The measured melting points (underlined in Tab. 4.5) show an agreement better than 0.4 % with the literature values above 2700 K and < 1.5 % for lower melting temperatures.

Discussion

Numerous accurate measurements of the spectral emissivities have been recently carried out. The salient results are summarised as follows:

- At constant temperature, ϵ_λ decreases with increasing λ in the solid state, is independent of l at the melting temperature and increases with l in the liquid state. The isotherms intersect each other at a point λ_x which is typical for the different materials.
- At constant wavelength, the emissivity curve as a function of temperature has a less regular trend, yet the measured isochromates converge to a single point at $T_x = T_m$. The value of the spectral emissivity at T_x is very near to the total emissivity, ϵ_{tot} , indicating that at the melting point the metals are effectively grey-bodies. The existence of a temperature T_x , at which different isochromates intersect each other is implied by the behavior of ϵ_λ as function of λ for different values of T : what is new and remarkable is that T_x corresponds to or is very near to the melting point.

These assessments are obviously only valid within the limits of the experimental errors. Thus, strictly speaking, the X-points should be defined as dX -intervals. In fact, in the vicinity of the melting point the temperature error is of the order of 10 K and the emissivity standard deviation varies between 3 % (W) and 15 % (Zr). Furthermore, the λ_x effect described in a) has been reported by several authors. Inspection of the published data [7] reveals that the effect is displayed by a large number of metals and also conductive ceramics. Most of the published emissivity data pertain to solids and therefore the reversal of the emissivity versus wavelength dependence above T_m cannot be directly

Tab. 4.5 Melting point (m.p.), spectral emissivity (ϵ), emissivity at the X-point (ϵ_x) and X-point (x,nm)

Metal	m.p.	$\epsilon_{m.p.,650\text{ nm}}$	ϵ_x	x(nm)
Mo (99.97)	2892 ^a	0.333 ^e	0.22 ^g	1300 ^g
	2895 ^{b,f}	0.300 ^b	<u>0.31</u>	<u>1100</u>
	2898 ^c	0.306 ^f		
	2883 ^d	0.327 ^c		
	<u>2890</u>	<u>0.310</u>		
Ta (99.95)	3288 ^h	0.350 ^b	0.35 ^m	800 ^m
	3300 ⁱ	0.345 ^e	0.36 ⁿ	720-860 ⁿ
	3256 ^f	0.309 ^f	<u>0.33</u>	<u>840</u>
	3270 ^d	0.375 ^{k,l}		
	3258 ⁱ	<u>0.330</u>		
	<u>3260</u>			
Nb (99.84)	2740 ^o	0.360 ^e	0.32 ^m	950 ^m
	2742 ^c	0.317 ^f	<u>0.30</u>	<u>850</u>
	2750 ^p	0.340 ^q		
	<u>2752</u>	0.360 ^c		
		<u>0.300</u>		
Zr (99.8)	2128 ^{f,r}	0.318 ^f	0.37 ^m	2500 ^m
	2134 ^s	0.367 ^r	<u>0.37</u>	<u>1200</u>
	<u>2140</u>	<u>0.370</u>		
Rh (99.9)	2238 ^t	0.19 ^m	<u>0.206</u>	<u>1450</u>
	<u>2240</u>	<u>0.206</u>		
Hf (99.9)	2495 ^s	0.39 ^u	<u>0.39</u>	
	2471 ^u	<u>0.39</u>		
	<u>2512</u>			
V (99.5)	2193 ^v	0.363 ^w	<u>0.31</u>	<u>1430</u>
	<u>2200</u>	<u>0.31</u>		
Re* (99.5)	3450 ^f	0.34 ^m	0.34 ^x	950 ^x
	<u>3320</u>	<u>0.37</u>	<u>0.37</u>	<u>1100</u>
W (99.96)	3675 ^l	0.378 ^e	0.33 ^{aa}	1280 ^{aa}
	3695 ^y	0.404 ^z	0.31 ^x	<u>1250</u>
	<u>3685</u>	0.360 ^b	<u>0.36</u>	
		<u>0.360</u>		
*0.5% Ni				

a) Barin et al. (1977), b) Allen et al (1960), c) Chekhovskoi and Kats (1981), d) Shaner et al (1977), e) Arpacı et al (1985), f) Bonnel et al. (1972), g) Riethof and DeSantis (1963), h) Worthing (1925), j) Malter and Langmuir (1939), k) Cezairliyan and McClure (1976), l) Worthing (1926), m) Touloukian (1970), n) Lateev et al. (1970), o) Hultgren et al (1973), p) Cezairliyan (1972), q) Cezairliyan (1973), r) Cezairliyan and Righini (1975), s) Ackerman and Rauh (1971), t) Hultgren (1963), u) Cezairliyan and McClure (1976), v) Treverton and Margrave (1971), w) Cezairlyian and Miiller (1979), x) Barnes (1966), y) Cezairliyan (1972), z) Cezairliyan and Miiller (1982), aa) De Vos (1954).

observed; however, extrapolation of the emissivity curves vs. temperature through the melting point show that at $T_m \epsilon_\lambda$ is independent of λ and is equal to ϵ_{tot} . This confirms the occurrence of the T_x effect mentioned in b).

The emissivity X-point phenomena [8] is still not fully interpreted in terms of the reflection or absorption of electromagnetic waves. Even the existence of the emissivity X-point is still a matter of debate both from the theoretical and experimental point of view. For instance, though the X-point of tantalum has been determined in this work, other high-precision measurements have shown that in this material the emissivity isochromates cross each other in a small but distinct wavelength interval between 780 and 820 nm for temperatures varying from 1200 to 2400 K [9]. As shown in Tab. 4.5 our measurements indicate the existence of a single X-point at 840 nm but the different isotherms (drawn through 6 points corresponding to the 6 wavelengths) have a relatively small regression coefficient (.99) and in fact the X-points should be experimentally defined as intervals $d\lambda_x$ and dT_x , where, in the context of the calculation procedures of e and T , these variances have a rather complex significance (however, dT_x is of the same order of magnitude as the absolute temperature error and dx is approximately 10 % of the considered wavelength interval). However, independently of the question whether an X-point or an X-interval exists, the essential result is that T_x coincides with or is very near to the melting point of the metals investigated.

It is intuitively reasonable that a metal at the transition solid/liquid behaves as a grey body if one thinks that by approaching the melting point the electronic states and in particular the Fermi surface, gradually merge into configurations where the interactions with the electromagnetic waves are increasingly affected by the localised electrons. This means that the conductive electrons which interact with the radiation may display a relatively broad spectrum of collision frequencies. Theoretical models may be envisaged, but they are rather difficult to apply [7]. Therefore, a theoretical description of the emissivity behavior was obtained only in particularly simple cases. The difficulty may be realized by the following general considerations.

When an electromagnetic wave propagates into metals its changes are described by the Maxwell equations and the optical properties of the medium permit us to predict its interaction with the conduction electrons. As has been shown

(TUAR 87,61), in the simplest case, where the electrons interacting with the electromagnetic wave are described in terms of simple conduction the theory excludes any inversion of slope in the curves $\epsilon(\lambda)$ and $\epsilon(T)$ and hence the existence of X-points. The comparison of Fig. 4.27a,b giving the calculated emissivity evolution as a function of r and λ with Fig. 4.25 and 4.26 shows the same evolution only for

$$T < T_x \text{ and } \lambda > \lambda_x$$

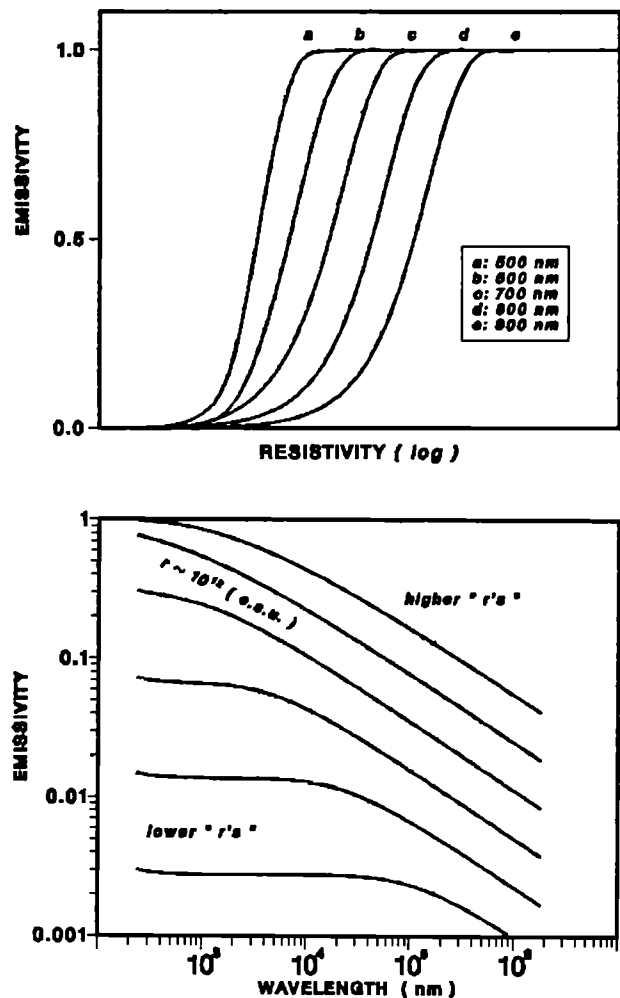


Fig. 4.27 Calculated variation of the spectral emissivity with a simple one-carrier model a) as a function of the electric resistivity (or temperature) at different wavelengths. The abscissa is in arbitrary units. b) as a function of the wavelength at different resistivities. The reference value of 10^{12} esu approximately corresponds to the resistivity of W. The resistivities of two adjacent curves differ by one order of magnitude.

This discrepancy is to be ascribed to the simple dispersion model assumed, by which all electrons have a unified velocity

$$ds/dt = eE/r$$

where s is the electron displacement. If we now suppose that the conductor contains different types of carriers more complex expressions for $v = ds/dt$ and x are obtained.

The emissivity as a function of the resistivity (or temperature) for different wavelengths, as calculated by assuming 3 types of carriers having different collision cross sections and equal densities is shown in Fig. 4.28. The emissivity

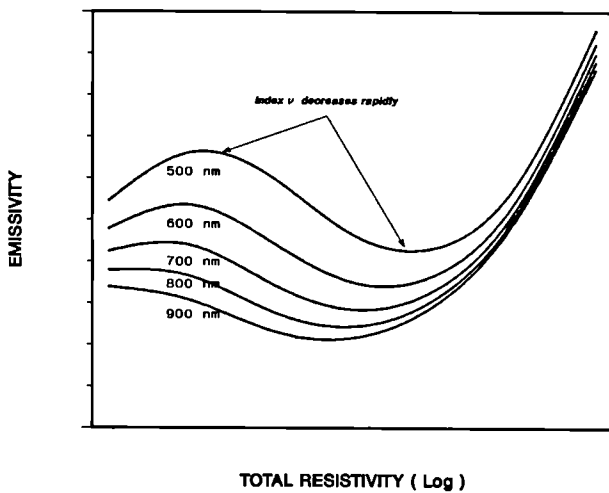


Fig. 4.28 Calculated variation of the spectral emissivity with the electrical resistivity at different wavelengths with a model taking into account of 3 different types of carriers. The coordinates are in arbitrary units. The emissivities exhibit maxima at the left hand side of the flanks of the curves of Fig. 4.27

curve, which for the case of a single carrier has a sigmoidal shape ($\epsilon_\lambda = 0$ for $r = 0$ and $\epsilon_\lambda = 1$ for r) displays a maximum and a minimum at the left hand side of the flank of the sigmoid. The emissivity curves are far apart at low r 's (or T 's) but tend to converge at large r 's after the maxima. This merely illustrative example shows that complex configurations of the conduction band may explain the qualitative dependence of ϵ_λ on λ and T . Experimental observations on the behavior of the resistivity of the refractory metals near the melting point [10,11] emphasize

the cause of the increasing in convergence rate of the ϵ_λ isochromates by approaching T_m . In fact, these metals present a sharp increase in resistivity across the melting point. If the trend of the curves of Fig. 4.28 is considered, a resistivity jump is expected to lead the spectral emissivities to converge more rapidly together when T approaches T_m . It should be noticed however that this is produced by the disappearance or appearance of types of carriers, whose occurrence is revealed by a jump in resistivity, rather than by the (modest) variation of this quantity. In this context, the behavior of the spectral emissivity of hafnium is of particular interest. This metal is subjected to a a/b (cubic-hexagonal) phase transition at $2000 < T < 2270$ K [12, 13, 14]. At this temperature the curve $\epsilon_1(T)$ in the range 500-1000 nm presents a second X-point at 2130 K in addition to that occurring at the melting point (Fig. 4.29): It can be inferred that the electronic state restructuring, revealed also by a resistivity jump [15], is the cause of the appearance of this second X-point.

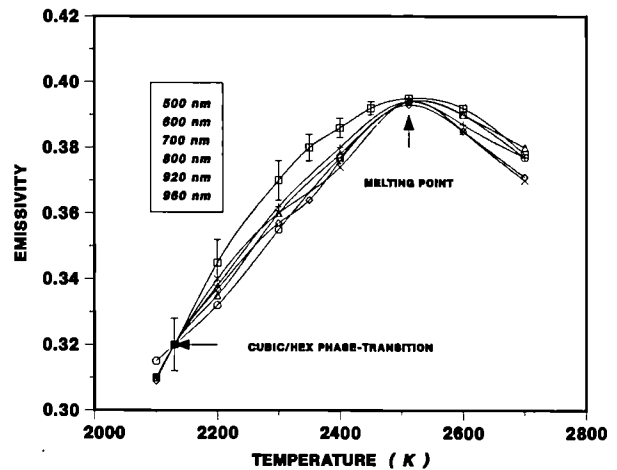


Fig. 4.29 Measured spectral emissivity variation of hafnium as a function of the temperature at 6 wavelengths

References

- [1] Babelot J F, Magill J, Ohse R W, Hoch M, 1982 in Temperature, Its Measurement and Control in Science and Industry volume 5, ed. J F Schooley (New York: American Institute of Physics) pp 439-446
- [2] Hiernaut J P, Beukers R, Heinz W, Selfslag R, Hoch M, Ohse R W, High Temp.-High Pressures 18 (1986) 617

- [3] Hiernaut J P, Beukers R, Hoch M, Matsui T, Ohse R W, *High Temp.-High Pressures* 18(1986)627
- [4] De Vos J C, *Physica* 20(1954)690
- [5] Larrabee R D, *J. Opt. Soc. Am.* 49(1959)619
- [6] Latyev L N, Chekhovskoi V Ya, Shestakov E N, *High Temp.-High Pressures* 2(1970)175
- [7] Touloukian Y. S, DeWitt D P, 1970 *Thermal Radiation Properties: Metallic Element and Alloys*, volume 7 of *Thermophysical properties of Matter* ed. Y S Touloukian, C Y Ho (New York: Plenum)
- [8] Weniger W, Pfund A H, *Phys. Rev.* 14(1919)427
- [9] Latyev L N, Chekhovskoi V Ya, Shestakov E N, *Phys. Stat. Sol.* 38 K(1970)149
- [10] Seydel U, Fucke W, *Metal Phys.* 10L(1980)L203
- [11] Shaner J W, Gather G R, Minichno C, *High Temp.-High Pressures* 9(1977)331
- [12] Cezairliyan A, McClure J L, *High Temp.-High Pressures* 8(1976)461
- [13] Krikorian N H, Wallace T C, *J Electrochemical Soc.* 111(1964)1431
- [14] Ross R G, Hume-Rothery W, *J.Less-Common Met.* 5(1963)461
- [15] Fast J D, *J. Appl. Phys.* 23(1951)350
- [16] Barin I, Knacke O, Kubaschewski O, *Thermophysical Properties of Inorganic Substances (supplement)* (New York: Springer) 1977
- [17] Allen R D, Glasier L F Jr, Jordan P L, *J. Appl. Phys.* 31(1960)1382
- [18] Chekhovskoi V Ya, Kats S A, *High Temp.-High Pressures* 13(1981)611
- [19] Arpacı E, Betz G, Froberg MG, *High Temp.-High Pressures* 17(1985)512
- [20] Bonnel D W, Treverton J A, Valerga A J, Margrave J L, *Temperature, Its Measurement and Control in Science and Industry*, ed H H Plumb (Pittsburgh, PA: Instrument Society of America) 4(1972) 483
- [21] Riethof T R, De Santis V J, report NASA-SP-31 (1963) 565
- [22] Worthing A G, *Phys. Rev.* 25(1925)846
- [23] Malter L, Langmuir D B, *Phys. Rev.* 55(1939)743
- [24] Cezairliyan A, McClure J L, *High Temp.-High Pressures* 8(1976)103
- [25] Worthing A G, *Phys. Rev.* 28(1926)174
- [26] Hultgren R, Desai P D, Hawkins D T, Gleisen M, Kelley K K, Wogman D D, *Selected Values of Thermodynamic Properties of the Elements (Metal Park, OH: American Society for Metals)* 1973
- [27] Cezairliyan A, *High Temp.-High Pressures* 4(1972) 453
- [28] Cezairliyan A, *J. Res. Natl. Bur. Stand.-A Phys. and Chem.* 3(1973)333
- [29] Cezairliyan A, Righini F, *Rev. int. Htes Temp. et Refract.* 12(1975)201
- [30] Ackerman R J, *High Temp. Science* 4(1972)272
- [31] Hultgren R, Orr R L, Anderson P D, Kelley K K, *Selected Values of Thermodynamic Properties of Metal and Alloys* New York ed. John Wiley Sons, Inc. 1963
- [32] Cezairliyan A, McClure J L, *J. Res. Natl. Bur. Stand.-A Phys. and Chem.* 80A(1976)659
- [33] Treverton J A, Margrave J L, *J. Chem. Thermodynamics* 3(1971)473
- [34] Cezairliyan A, Müller A P, Righini F, Rosso A, *High Temperature Sc.* 11(1979)223
- [35] Barnes B T, *J. Opt. Soc. Amer.* 56(1966)1546
- [36] Cezairliyan A, *High Temp. Sc.* 4(1972)248
- [37] Cezairliyan A, Müller A P, *Int. J. of Thermophysics* 3(1982)89

Radiative Properties of UO₂ in Liquid and Solid Phases

The spectral emissivities of UO₂ and other ceramic oxides have been measured up to temperatures above the melting point T_m . The experimental method adopted is based on multiwavelength pyrometric measurements, where the determination of the spectral emissivity is implicitly related to the evaluation of temperature through the radiation emission law and an assumed relationship between the spectral emissivity ϵ and the wavelength λ .

Heating was produced with a pulsed laser in times of the order of 100 ms. The measurements at six different wavelengths were carried out at time intervals of the order of 1.5 ms.

The behavior of the emissivity in ceramic oxides (UO₂, ThO₂, ZrO₂) was studied up to temperatures above the melting point by heating the samples in a high pressure buffer-gas atmosphere in order to minimize vaporisation and stoichiometry variations during the measurements. The spectral emissivities in the examined wavelength interval increase monotonically with temperature up to the melting point. Here a sudden decrease is observed which is immediately recovered within a narrow temperature interval above T_m (Fig. 4.30). This dip in the emissivity curve (Y-point) is observed for all the wavelengths, but its depth decreases with increasing λ : Since the measured emissivities increase with increasing wavelength the isochromates of $\epsilon_\lambda(T)$ do not cross each other and therefore, contrarily to the case of refractory metals, no X-point is observed in the temperature range explored. It is worthwhile noting that the emissivity curves above the melting point appear as a natural extension of the low temperature branch, the Y-point being only related to the liquid-solid transition. The effect was observed

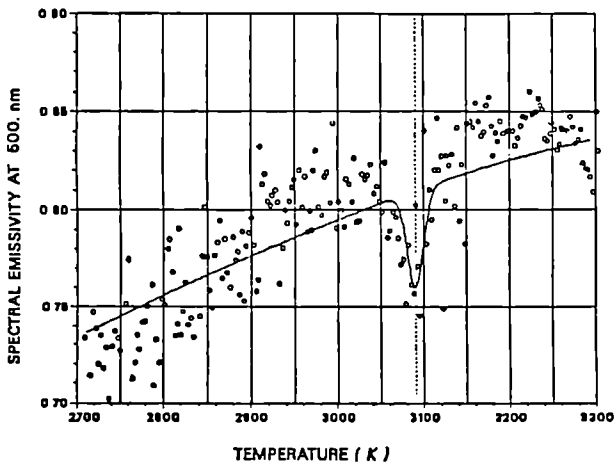


Fig. 4.30 Spectral emissivity of UO_2 as a function of temperature. The solid line represents the spline function fitting the experimental points

with good reproducibility both in the same and in different samples, this would exclude the possibility that it is caused by stoichiometry changes during heating. The interpretation of this effect is being investigated.

Measurement of Thermal Diffusivity by Laser Flash

An apparatus has been designed for the measurement of the thermal diffusivity of radioactive samples by the laser flash method. If the front surface of a sample of thickness d is heated with a short flash, and $t_{1/2}$ is the time required for the temperature rise at the rear surface to attain $1/2$ of its maximum value, then the thermal diffusivity a of the sample may be deduced from the relation

$$a = 0.138 d^2/t_{1/2}.$$

The equipment is shown schematically in Fig. 4.31. The sample S is placed inside a susceptor in a vacuum furnace, and heated to the measurement temperature by a coil HF . Vacuum is provided by a rotary pump RP and a Turbo-Vac pump TV . The furnace is enclosed in a glove box G which can be operated under nitrogen. The laser flash is furnished by a Nd-Glass laser NG , conducted through a glass fiber light guide LG .

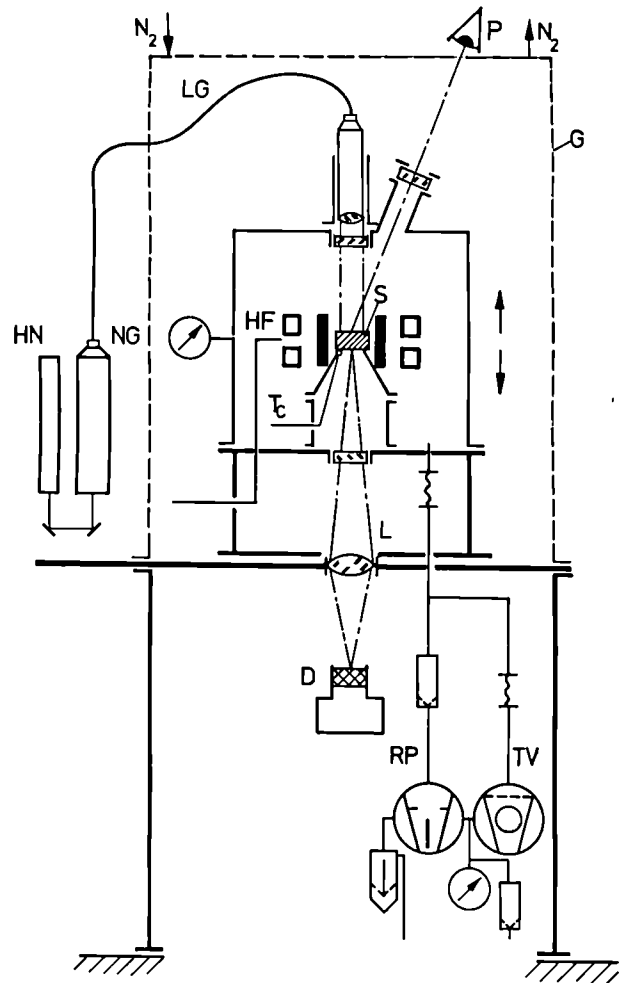


Fig. 4.31 Laser flash furnace for the measurement of thermal diffusivity.

The Nd-Glass laser has a dichroic rear mirror, which allows the introduction of a visible beam of light from a small He-Ne laser HN along the $1.06 \mu\text{m}$ Nd-Glass laser beam for alignment purposes. The sample temperature can be measured in the lower range with a thermocouple T_c or at higher temperatures with an optical pyrometer P . The temperature rise of the rear surface is to be measured by a Peltier cooled infrared detector D operating at $5 \mu\text{m}$ wavelength through a sapphire window and a CaF_2 lens L . This device should operate at sample temperatures $\geq 400 \text{ K}$.

Pyrometry

Classical optical pyrometry requires the knowledge of the spectral emissivity of the material at the wavelength of measurement; but in reality spectral emissivity is not a material property, it depends strongly on the state of the surface, and should be determined for each temperature measurement. Babelot et al. [1] and Hiernaut et al. [2] have proposed a six-color method to solve this problem. The six-color pyrometer uses linear detectors, and relies on a simple expression for the variation law of the spectral emissivity as a function of the wavelength.

The experimental data of De Vos [3], Larrabee [4] and Latyev et al. [5] on tungsten, and the data of Touloukian [6] on NbB₂, TaC, WC, ZrC, HfN, TaN, ZrN, Al₂O₃, Cr₂O₃, MgO and ThO₂ have been analyzed according to the following two-constant expressions for the spectral emissivity ϵ_λ :

$$\ln \epsilon_\lambda = a + b\lambda \quad (1)$$

$$\ln[\epsilon_\lambda/(1-\epsilon_\lambda)] = c + d\lambda \quad (2)$$

$$\epsilon_\lambda = e + f\lambda \quad (3)$$

where a,b,c,d,e and f are constant with respect to wavelength (λ), but can vary with temperature. Fig. 4.32 shows the analysis of the emissivity data of MgO between 1 and 15 μm .

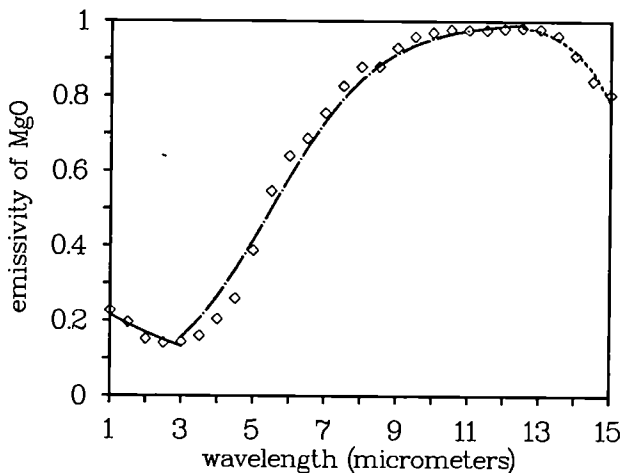


Fig. 4.32 Least squares analysis of the spectral emissivity of MgO (3 different equations of types 1, 2, 2).

It was found [7] that for a wide range of materials, a two-coefficient linear equation represents well the variations of the logarithm of the spectral emissivity with the wavelength in the range 0.4 to 3 μm . The six-color pyrometer can then be used for the determination of the temperature of a surface with unknown emissivity in the temperature range 1000 to 5000 K.

References

- [1] Babelot J.-F., Magill J., Ohse R.W., and Hoch M., in *Temperature, Its Measurement and Control in Science and Industry*, 5 (Am. Inst. of Physics, New York 1982), 429
- [2] J.-P. Hiernaut, R. Beukers, W. Heinz, R. Selfslag, M. Hoch and R.W. Ohse, *High Temp.- High Press.* 18 (1986) 617
- [3] J.C. De Vos, *Physica* 20(1954) 690
- [4] R.D. Larrabee, *JOSA* 49(1959) 619
- [5] L.N. Latyev, V.Ya. Chekhovskoi and E.N. Shestakov, *High Temp.- High Press.* 2(1970) 175
- [6] Y.S. Touloukian, *Thermophysical Properties of Matter*, Vol. 8 (Plenum Press, New York 1972)
- [7] J.-F. Babelot and M. Hoch, to be published in *High Temp.- High Press.*

Thermodynamic Calculations

There is an apparent discrepancy between the experimental values of the constant vaporizing composition (CVC) of UO₂ at 2150 K, as summarised by Ackermann et al.[1], and the CVC found using the Hoch-Arpschhofen model (calculation of Babelot et al.[2]). Babelot et al. found a value very close to O/U = 2.0, while the available experimental data suggest a CVC of O/U = 1.9925.

In order to move the calculated constant vaporizing composition to lower O/U ratio, the Gibbs energies of formation of the molecules present in the gas phase above UO₂ have to be changed. The Gibbs energies of formation of UO₂(g), O(g) and U(g) being well established, the only possibilities are to lower the stability of UO(g), or to increase that of UO₃(g). Both ways have been tried: by completely eliminating UO(g) in the calculation, neither the CVC, nor the total pressure changes much compared to the previous results; to increase the stability of UO₃(g), its enthalpy of formation has to become more

negative, but a large change is needed to approach the experimental CVC at 2150 K. This is shown in Fig.4.33; in addition, the increase in UO_3 pressure increases the total pressure above $\text{UO}_{2.0}$, and decreases the UO_2 fraction in the gas phase, in contradiction to the available experimental data. Similar results were obtained at 2800 K.

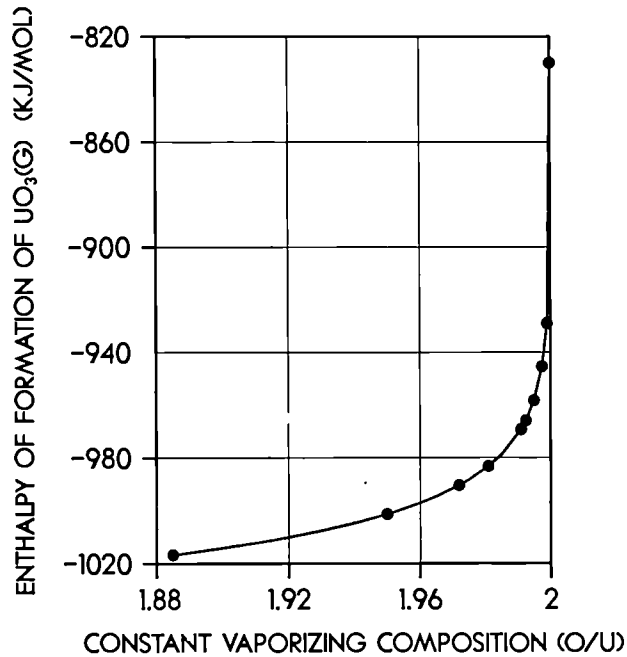


Fig. 4.33 Variation of the enthalpy of formation of $\text{UO}_3(\text{g})$ as a function of CVC

Therefore, the possible variations of the calculated partial pressures and constant vaporizing composition are limited. But on the other hand, because of the possible analytical errors in the experimental CVC measurements, they cannot be used to determine the "correct" value for the enthalpy of formation of $\text{UO}_3(\text{g})$. Thus there is no reason to modify the value given in [2].

References

- [1] R.J. Ackermann, E.G. Rauh, and M.H. Rand, 'The congruently vaporizing compositions of Urania', presented at the Pacific Coast Regional Meeting, Ceramic Technology - Hotter than Energy, San Diego, Oct.25-36,1978
- [2] J.-F. Babelot, R.W. Ohse, M. Hoch, J. Nucl. Mater. 137(1986)144

5 Formation of Actinides

Status of the SUPERFACT Irradiation

The fuel bundle containing the eight fuel pins of the SUPERFACT experiment has been unloaded from the PHENIX reactor and dismantled in an examination hot cell there. The pins appear to be in good condition from visual examination.

The four pins designated for the Institute for examination will be ready for transport in mid 1989 but because of the present unavailability of hot cell facilities can probably be shipped only in January 1990.

Status of Analysis of KNK II b Samples

The goal of this experiment is to check neutron cross-section libraries by measuring and calculating nuclides produced during the irradiation of the KNK II b samples. The irradiation and status of the samples were reported in detail in TUAR 86.

Problems have slowed progress in both the experimental / measurement part and in the calculations. Still to be measured are three main classes of nuclides: elements such as uranium and plutonium where repeat measurements are required; elements such as neptunium and thorium, as major or minor constituents; and certain nuclides such as ^{232}U or ^{236}Pu which require specific techniques.

Flux monitors (see TUAR 86) were irradiated together with the actinide capsules. The capsules have been measured and partly evaluated at CEN, Mol. In order to complete the evaluation to the point of calculating neutron spectra, use and expertise of a program such as SAND-II are required. Once the actual neutron spectra

pertinent to each irradiated sample can be reproduced, the buildup and decay of the components in each capsule can be relatively easily calculated, assuming appropriate cross-sections and knowing the reactor history. Without knowing the actual neutron spectra one can only use assumed or estimated spectra for the calculations. The largest variable in the calculation is then the spectrum and not the cross-sections which are the objects of the comparisons.

Negotiations are being carried out to have the SAND-II calculations done externally. Hopefully they will be completed in 1989 allowing meaningful comparisons with the experimental results to be made.

A first comparison is reported in Tab. 5.1 for sample 7 (Tab. 3.2, TUAR 87, 118). The concentration of each nuclide is given relative to that of ^{238}U to make the comparison easier. The calculated results were based on an estimated neutron spectrum and are exceedingly tentative because the sample was irradiated close to the reflector zone of the core, where the prediction of the neutron energy spectrum is difficult. However it can be seen that the comparison is not bad. Greater deviations are found for the minor isotopes (such as ^{234}U) but for the major isotopes the differences are relative small.

Tab. 5.1 Comparison of preliminary measured and calculated nuclide concentrations, expressed as ratios to ^{238}U .

Nuclide		Measured	Calculated
U	234	2.79 E-4	1.64 E-4
	235	2.00 E-3	2.27 E-3
	236	1.68 E-4	1.10 E-4
Pu	238	9.10 E-3	1.04 E-2
	239	2.94 E-1	3.33 E-1
	240	2.25 E-1	2.72 E-1
	241	6.53 E-2	9.88 E-2
	242	4.22 E-2	

Minor Actinide Recycling Scenario in Europe

Up to the year 2000 more than 35,000 tons of spent nuclear fuel will have accumulated in the countries of the European Community [1]. This fuel will contain several tons of transuranium elements (Tab. 5.2).

After discharge of spent fuel from a nuclear power station the transuranium elements inventory changes due to decay. During the first months the most important changes are the formation of ^{241}Am from ^{241}Pu decay and the decay of the shorter lived nuclides of curium.

The degree of formation of transuranium elements depends on the reactor type (Tab. 5.3) and on the initial fuel composition.

For power stations operating with low enriched or natural uranium the formation of ^{237}Np is less than in plants having a higher initial enrichment of ^{235}U , whereas the formation of the transplutonium elements primarily depends on the fuel exposure i.e. the achieved burn-up. In some countries Pu is separated from the spent fuel and recycled in light water reactors. As indicated in Tab. 5.3 the formation of the higher transuranium nuclides will be more pronounced in this case because the multiple neutron capture reactions start from heavier nuclides e.g. ^{242}Pu instead of ^{238}U . ^{243}Am can be built up to concentrations 20 times higher than normal and ^{244}Cm even higher [2].

If all the actinides are separated from the spent fuel or from the highly active waste from the PUREX reprocessing process, the radiological hazard of the remaining waste is then determined by the fission products which decay relatively quickly (Fig. 5.1).

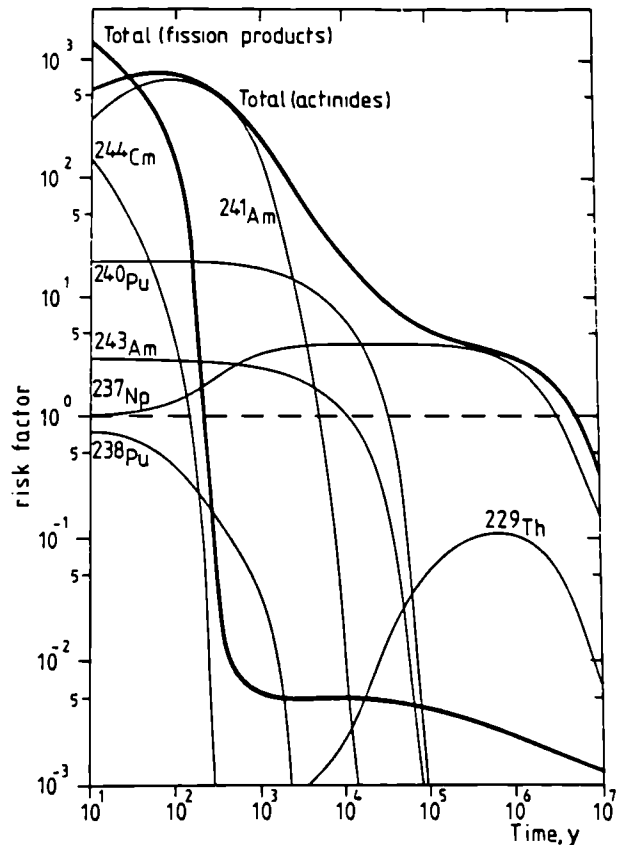


Fig. 5.1 Time dependence of the risk factor for wastes from reprocessed spent fuel (99.5% recovery of U, Pu and MA)

We will consider here the transmutation of actinides in existing nuclear power stations, where the half-life of a transmuted minor actinide differs considerably from the half-life of the natural decay. The transmutation half-life is determined by the neutron flux and the effective neutron cross-sections. The result is transmutation into fission products or another actinide.

Tab. 5.2 Accumulated TU-elements in the year 2000 in the European Community assuming accumulative discharge of 35 000 t spent fuel.

Generating capacity (GWe)	Mass of TU-element (t)			
	Np	Pu	Am	Cm
130	17	300	15	0.8

Tab. 5.3 Minor actinide formation per ton in various thermal reactors [2, 3] (cooling time 150 d)

	Reactor type ^a						
	HWR	GGR	AGR	SGHWR	BWR	PWR	PWR
Initial ²³⁵ U (%) (w/o) ²³⁹⁺²⁴⁰ Pu	1.5 —	0.7 —	2.2 —	2.1 —	2.6 —	3.2 —	0.7 3.2 ^b
Pu and MA content [g/t]							
²³⁷ Np	66	28	171	164	368	426	127
²⁴¹ Am	4.2	6.1	34	25	68	67	690
²⁴³ Am	34	0.12	15	18	45	84	1630
²⁴² Cm	3.9	0.43	1.1	1.9	4.4	6.6	60
²⁴⁴ Cm	1.0	0.018	1.1	2.0	10	24	860
burn-up [GW _{th} d/t]	14	4	18	21	24	33	33

^a HWR, Heavy Water Reactor SGHWR, Steam Generating Heavy Water Reactor
 GGR, Gas-Graphite Reactor BWR, Boiling Water Reactor
 AGR, Advanced Graphite Reactor PWR, Pressurized Water Reactor

^b Equilibrium amount of recycled, self-generated Pu [2]

For existing fast reactor power stations of the 300 MWe class (PHENIX, PFR, SNR-300) as well as for those of the larger 1000 MWe class (SUPER PHENIX, EFR) transmutation into other actinides predominates over fission. Despite this, the overall transmutation half-life is about 3 years i.e. an actinide inserted into such a reactor will be 50% transmuted within this period (Tab.5.4).

The efficiency of transmutation for the two most hazardous nuclides (²³⁷Np and ²⁴¹Am) is acceptable (Figs. 5.2, 5.3). The actinides formed are mainly plutonium nuclides which can be recycled together with the Pu produced in the UO₂ matrix of the fuel. If one wishes to have a more efficient transmutation into fission products then a harder and/or higher neutron flux is needed of the type which is observed in fast reactors with metal, carbide or nitride fuels.

Consequently special minor actinide burner reactors have been conceived (e.g. in Japan [4, 5]) for which metal fuels or nitrides are proposed. If one stays with the technology already developed in the nuclear industry i.e. PWR with Pu recycling and FBR with MOX-fuel, the following options for minor actinide recycling exist:

- recycling in PWR's together with Pu
- recycling in LMFBR's together with Pu
- recycling in LMFBR's without Pu (which is separately recycled in LWR's).

The minor actinides are only suitable as nuclear fuel in a fast neutron spectrum. Their reactivity however is considerably lower than that of Pu.

From Tab. 5.5 the recycling of ²³⁷Np and ²⁴¹Am in LWR's seems feasible, since their composite half-lives (the transmutation into fission products and another actinides) are comparable

Tab. 5.4 Half-lives (years) of minor actinides in a thermal or fast reactor [6]

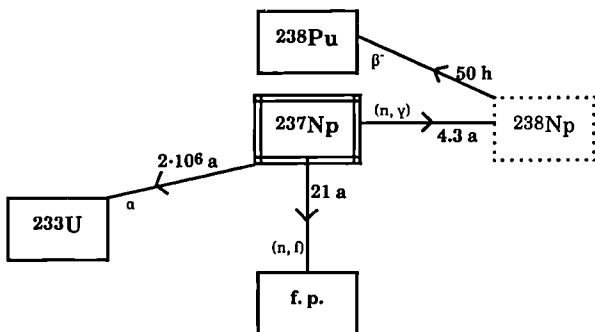
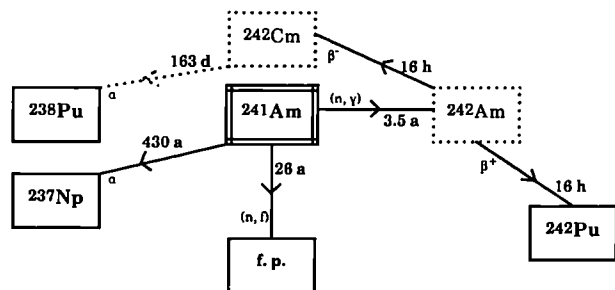
Actinide nuclide	T _{1/2} natural decay [a]	PWR neutron spectrum $\Phi = 3 \cdot 10^{13} \text{ s}^{-1} \text{ cm}^{-2}$			LMFBR neutron spectrum $\Phi = 3.2 \cdot 10^{15} \text{ s}^{-1} \text{ cm}^{-2}$		
		T _{1/2} fission [a]	T _{1/2} capture [a]	T _{1/2} composite [a]	T _{1/2} fission [a]	T _{1/2} capture [a]	T _{1/2} composite [a]
²³⁷ Np	2·10 ⁶	3.8·10 ⁴	4.3	4.3	21	4.3	3.6
²⁴¹ Am	433	230	0.87	0.86	26	3.5	3.0
²⁴³ Am	7·10 ³	>10 ⁴	9.2	9.2	33	4.0	3.6
²⁴² Cm	0.45	>10 ²	46	0.44	12	7.7	0.4
²⁴⁴ Cm	18	610	53	13.1	15	10	4.6

to that in FBR's. However, the transformation rate into fission products in a fast neutron spectrum of present LMFBR design is higher than in LWR's and could be considerably increased if fuels other than oxides were used. More important for the case of ²⁴¹Am is that the ²⁴²Am formed by neutron capture has an extremely high fission cross-section (of the order of 10⁶ barn) which causes strong neutron resonance shielding of the fuel and consequently a pronounced anisotropic burn-up in LWR's. Transmutation of the heavier minor actinides in thermal reactors leads to the build up of considerable amounts of ²⁵²Cf which aggravates the subsequent handling of the fuel.

From these considerations we conclude that the optimal strategies for the transmutation of minor actinides are:

- recycling of MA together with Pu in LMFBR's
- recycling of Pu in PWR and MA in LMFBR's.

Of course, a hybrid strategy of the two may have practical advantages and the technical implications are covered by two scenarios described here. For each of the two options a scenario is developed applicable to the year 2000 in the European Community. At this time the installed nuclear energy generating capacity is taken as 130 GWe for the region, mainly from PWR's. The

Fig. 5.2 Transmutation scheme of ²³⁷Np in a FBR (MOX fuel) ($3.2 \cdot 10^{15} \text{ s}^{-1} \text{ cm}^{-2}$)Fig. 5.3 Transmutation scheme of ²⁴¹Am in a FBR (MOX fuel) ($3.2 \cdot 10^{15} \text{ s}^{-1} \text{ cm}^{-2}$)

Tab. 5.5 Extraction of fission product and light elements by TRPO from 4M HNO₃ (D = Disbtibution Coefficient)

	1 highly extractable	2 partly extracted	3 slightly extracted	4 not extracted
D	> 10	0.1 - 10	0.01 - 0.1	< 0.01
elements	Zr, Tc	Mo, Ru, Pd, Ag	Rh, Fe (Ba, Sr?)	Cr, Ni (Na, Cs)

fuel discharged up to this time amounts to 35,000 t containing 300 t Pu (see Tab.5.2). With the installed reprocessing capacity expected at the time the Pu might be separated off; but it is not foreseen to partition the 35 t of MA from the resulting highly active waste.

If we assume that the partitioning of MA's could also be achieved by that date then the Pu together with MA's could be made into MOX fuel for FBR's, the MA content of which would be only 2%. The resulting scenario is shown in Fig. 5.4.

The Pu from the spent fuel of the thermal reactors together with the MA could fuel fast reactors having a nuclear energy generating capacity of 60 GWe. It is assumed that the highly active waste leaving the reprocessing plant is "alpha-free" and therefore only needs to be stored for about 600 years. For this purpose an engineered storage will be used, so that deep geological disposal is not required.

If however the Pu were recycled in LWR's in the self-generated mode (Fig. 5.5), the amount of

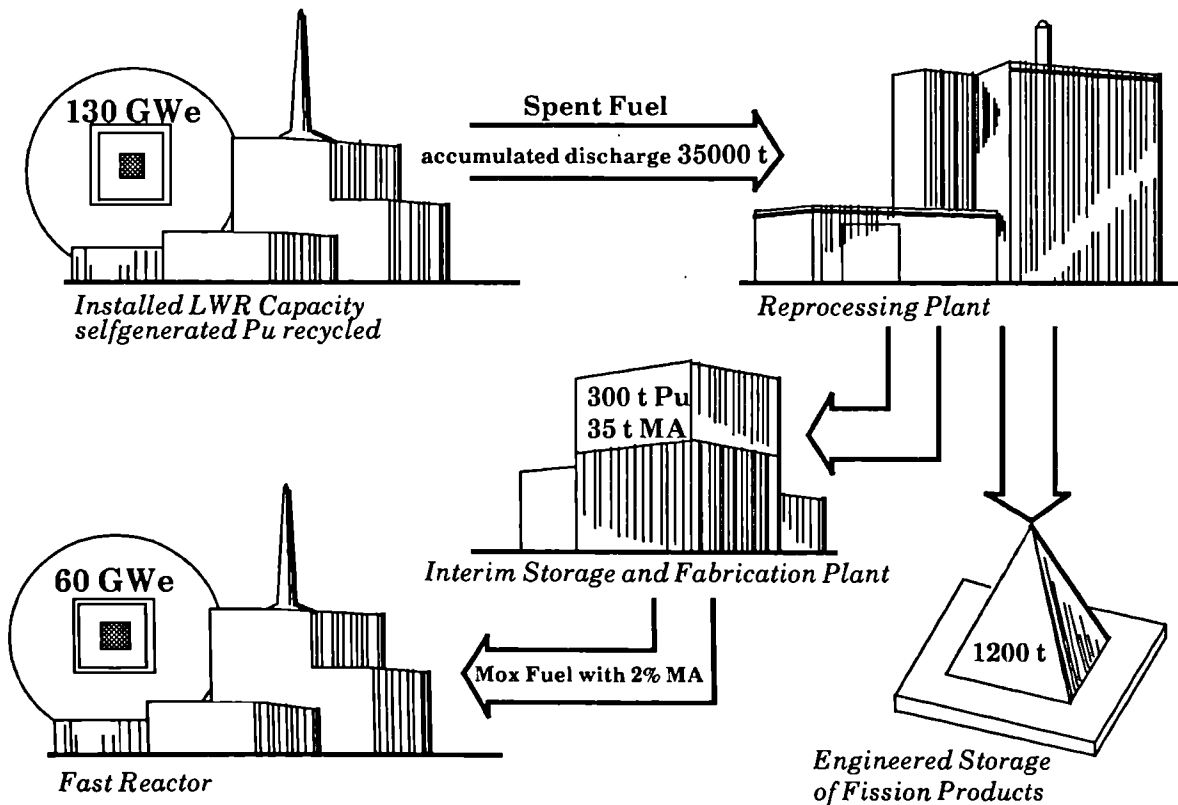


Fig. 5.4 Transmutation of Minor Actinides in FBR (Scenario: Transition from LWR to FBR in the year 2000)

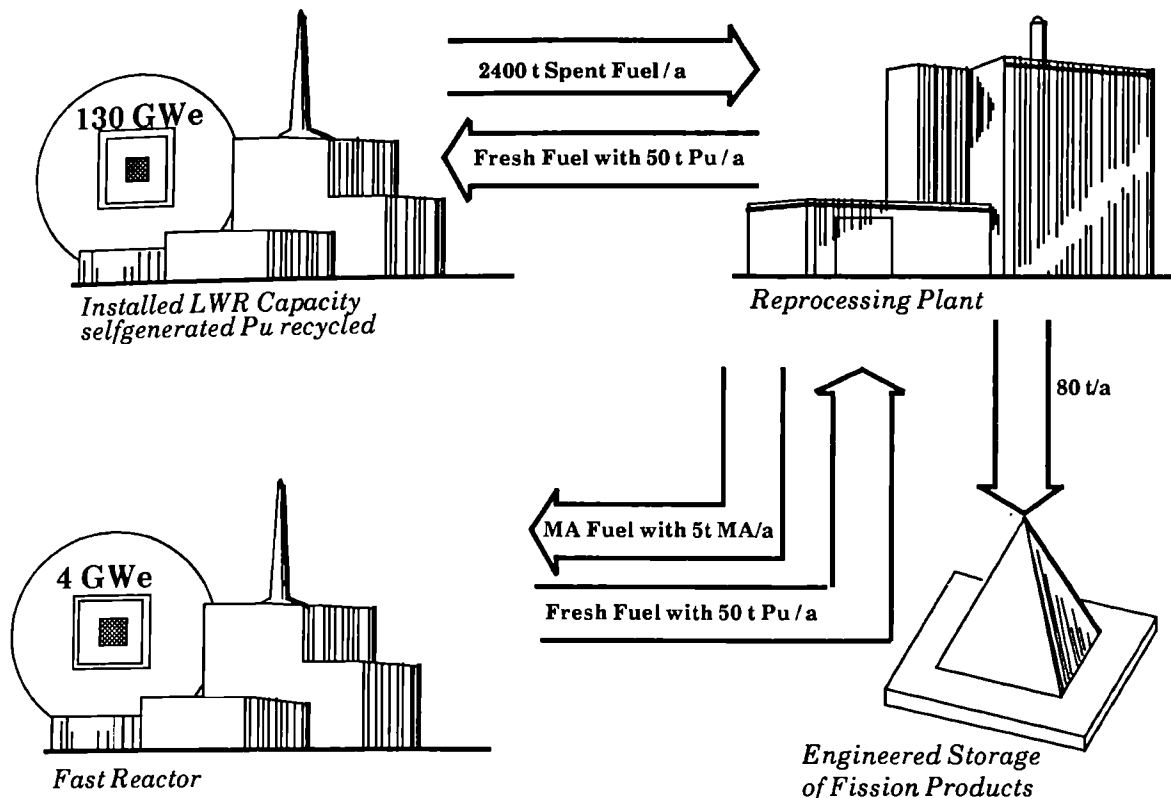


Fig. 5.5 Transmutation of Minor Actinides in LWR- FR symbiosis

spent fuel unloaded per year would be 2,400 t in the year 2000 from which the extracted Pu would be annually 50 t. The assumption underlying the concept here is that the recycling of Pu in LWR's is more cost effective than in FBR's. The MA's, as outlined above, would need a fast neutron energy spectrum for transmutation. But these actinides could also be used as a fuel alone (without Pu) in special minor actinide burner reactors which would have a total nuclear energy generating capacity of about 4 GWe. Depending on the neutronic characteristics, part of the MA's will be transmuted into Pu. If the MA fuel is incorporated into a U matrix, about 3 tons of Pu with a high ^{238}Pu and ^{242}Pu content would be fed back annually to the LWR fuel cycle, with the added advantage that the Pu is further denatured and unsuitable for military use.

References

- [1] "Summary of Nuclear Power and Fuel Cycle Data in OECD Member Countries", Nuclear Energy Agency (1986)
- [2] U. Fischer, H. Küsters, H.W. Wiese, "Validations of Methods and Data for Calculating Nuclear Properties of Irradiated PWR Fuel by Comparison to Experimental Post-irradiation Analyses", Transactions of the American Nuclear Society, 45 (1983) 745
- [3] K. Taska et al., J. Nucl. Sci. Techn., 14 (1977) 519
- [4] T. Mukayama et al., Proc. Int. Conf. Nucl., "Cross-Sections for Technology", Knoxville, 1979 NBX-SP-594 (1980) 552
- [5] H. Murata, T. Mukayama, Atomenergie-Kerntech. 45 (1984) 23
- [6] L. Koch, R. Ernstberger, K. Kammerichs, in: "First Technical Meeting on the Nuclear Transmutation of Actinides", EUR 5897 EN/FR (1978)

Extraction of Actinides from Highly Active Waste (HAW)

The removal of actinides, including the major actinides U and Pu, and especially the minor actinides Am, Cm and Np, from highly active waste (HAW) would reduce the radiological hazard of HAW. In the USA, the application of bifunctional extractants, e.g. octyl(phenyl)-N, N'-diisobutyl carbamoyl methyl phosphine oxide OΦD[iB]CMPO (briefly CMPO) has received much attention in the past decade and a process based on CMPO extraction - the TRUEX Process - has been developed [1]. In the Peoples Republic of China, a mixed phosphine oxide extractant, TRPO has been proposed [2]. At present in the Nuclear Chemistry Service of the Institute the extraction of Am, Cm, U, Pu and Np by TRPO from both a simulated and real HAW is being studied in a cooperative study with visiting scientists from the Institute of Nuclear Energy Technology of the Tsinghua University in Beijing.

The distributions of actinides, fission products and corrosion products between 30 vol% TRPO in dodecane and simulated HAW with HNO₃ concentrations ranging from 0.5 - 5.5 M HNO₃ have been determined. The distribution ratios (D) of U and Pu are very high, of the order of 10³ - 10⁴. The distribution ratios of Am and Cm vary with acidity, with a maximum value of about 10 in 0.3 M HNO₃ (after equilibration) in the aqueous phase, dropping with increased acidity. For an aqueous phase with a nitric acid concentration of about 4 M the distribution ratios are about 0.1. The fission product rare earths behave similarly to Am and Cm. Other elements found in HAW can be divided into four categories according to their distribution behaviour (Tab.5.5).

U and Pu concentrations were determined by isotope dilution mass-spectrometry, Am was determined by γ- and Cm by α-spectrometry. The other elements were determined by ICP - AES (inductive - coupled plasma atomic - emission spectroscopy).

A preliminary extraction and stripping test using real HAW has confirmed the good performance of the TRPO extraction process. In a single stage extraction using 30 vol% TRPO with a volume ratio (O/A) of 1:1, more than 90% of Am and Cm are extracted. U and Pu are extracted from 1.0 M

HNO₃ almost completely. Am and Cm can be stripped into 5.5 M HNO₃, Pu into 0.5 M H₂C₂O₄ and U into 0.5 M Na₂CO₃ yielding different fractions without serious cross-interference. The loading capacity of Am, Cm and rare earths in TRPO were measured using Nd (NO₃)₃. For 30 vol% TRPO in dodecane, no third phase forms even when the Nd (NO₃)₃ concentration in the organic phase reaches the high value of 0.1 M at an aqueous nitric acid concentration of 1.5 M (25°C). The loading capacity of TRPO extractant is thus considerably higher than that of the TRUEX extractant (0.2 M CMPO + 1.2 M TBP in Conacco diluent).

References

- [1] E.P.Horwitz, D.G. Kalina, H. Diamond, G. Vandegrift, W.W. Schultz, *Solvent Extr. Ion. Exch.* **3** (1985) 75
- [2] Zhu Yongjun, Jiao Rongzhou, Wang Shouzhong, Fan Shiguo, Liu Bingren, Zheng Hualing, Zhou Shunli, *Proceedings of the International Solvent Extraction Conference September 1983*

The Potential of Estimating Nuclear Fuel Parameters from Measurements of Rare-Earth Fission Products using ICP-MS

Spent nuclear fuel has an element and isotope composition which is dependent on its irradiation history. Parameters such as burn-up, fuel type, initial enrichment and composition (possible addition of Pu), cooling time after irradiation and the reactor type can be expected to determine the fission product and actinide compositions.

Reversing the argument, one would expect to be able to extract quantitative and qualitative information on the fuel and its irradiation history from measurements of the fission-product distribution and/or actinide isotope distributions.

The installation of an ICP-MS (inductive-coupled plasma mass-spectrometer) capable of analysing active materials has given a new impetus to this so-called 'fingerprinting' method of characterising nuclear fuels. The potentials of the technique when validated could be significant and would have implications in other fields, such as Safeguards.

The rare-earths were selected as a group of elements on which the technique could be brought to bear. They have the following advantages:

- a) they present a chemically homogenous group for analysis
- b) their fission yields, at least up to mass 165 are sufficient for analysis
- c) they lie on the heavy side of the heavy fission yield peak and are thus sensitive to changes in the fissioning compound nuclide

ICP-MS has useful characteristics for this purpose:

- a) a measurement over the complete mass zone of interest can quickly be carried out;
- b) dissolved fuel solutions do not need to be treated before measuring except for acidity and concentration adjustment;
- c) the method is sensitive thus minimizing the amount of active material needed;
- d) the concentrations of nuclides separated by 1 mass unit can be measured.

The technique is not without disadvantages:

- only masses are separated (problem of isobars)
- the instrument is expensive
- many practical problems arise with measuring active solutions.

In order to determine which fission-product masses, or simple combination of mass-yields are suited for determining reactor or irradiation parameters, simulation studies need to be carried out whereby the various parameters of interest can be altered and the effect on the fission-product yields determined. The program KORIGEN [1], in its latest version: KORIG88, will be used for this purpose. Previous versions were limited to a restricted set of fission yields from fissioning actinides but the present version has been considerably extended in this regard.

The calculations using KORIG88 have been started, although it is too early to arrive at conclusions. A series of dissolved fuel solutions are being analysed for their rare-earth concentrations by thermal ionisation mass-spectrometry isotope dilution (IDMS) and ICP-MS. For the measurements by IDMS, isotopic spikes for the rare-earths must be added and the individual rare-earth fractions separated. Preliminary measurements by ICP-MS have demonstrated that the sensitivity of the instrument is entirely adequate for the foreseen measurements.

Reference

- [1] U. Fischer, H.W. Wiese, KfK 3014, 1983

6 Safe Handling of Nuclear Materials

The Resuspension of Uranium-Plutonium Oxide Particles from Burning Substrates

Investigation of the resuspension of (U,Pu)O₂ particles from burning Plexiglas substrate was reported previously (TUAR 87). These investigations have now been extended to substrates of other materials found in contaminated glove boxes. The results on these other materials are reported here. The aim of the experiments, which simulate aspects of a glove box fire, was to quantify the fraction of particles resuspended in a small scale, i.e. non-turbulent, fire and to determine the dependence of the degree of resuspension on particle size.

The following combustible materials were used as substrates for the (U,Pu)O₂ particles: PVC and polycarbonate (both constructional materials), Neoprene and Hypalon (black and white rubber glove materials), Polythene (sack material), and cardboard (tubular waste container material).

The uranium-plutonium oxide particles were irregular particles produced by abrasion of sintered pellets. They were separated into size fractions, according to their aerodynamic diameter, using a cascade impactor. Four size classes were used: 1.3 - 2.2µm, 2.2 - 4.1µm, 4.1 - 6.5µm, and 6.5 - 9.5µm.

The apparatus used was the same chimney combustion chamber as reported previously. The only difference was in the shape of the specimens used. Instead of a vertical hollow cylinder geometry used previously for plexiglas, thin disc shaped specimens were used supported on a fine wire mesh screen. Because of the difficulty of achieving self sustained combustion with some materials, such as polycarbonate, it was necessary to maintain the butane gas flame, normally used for ignition only, for the duration of the experiment. To check on the influence of specimen geometry, a repeat series of fires with plexiglas was made, this time with disc shaped specimens. Each of the 7 materials was

investigated with 4 different particle sizes making a total of 28 fires.

The parameter required from these experiments was the fraction of the initial amount of contaminant released as aerosol and captured on sampling filters. This parameter was established from measurements of the alpha activity of the filters. The results are shown in Fig. 6.1.

Fig. 6.1 shows that the materials can be assigned to a high, medium or low resuspension class. The high resuspension class comprises Plexiglas, neoprene and cardboard, all of which resuspended about 1% of the contaminant. PVC and Hypalon fall in the medium class which resuspend between 0.1 - 0.01%. Polythene and polycarbonate both exhibited almost no resuspension. The limit of detection in these experiments was about 0.001% of the initial amount of material (10⁻⁵ on the scale in Fig 6.1). This is approximately equivalent to a single (U_{0.8},Pu_{0.2})O₂ particle of 1 µm in diameter. The results for polythene and polycarbonate therefore are statistically not very reliable.

Considered were only the materials which showed appreciable resuspension i.e. the high and medium classes. The dependence of the degree of resuspension on particle size seems to fit one of two separate patterns. Plexiglas and PVC both exhibit a minimum for the 4.1 - 6.5 µm fraction. The results for cardboard, neoprene and hypalon, however, zig-zag up and down in a way that might be taken to indicate scatter in the data were it not for the fact that results for 3 separate materials show the same pattern. These results for plexiglas confirm earlier results, using a different specimen geometry (TUSR 87,138), for the dependence of resuspension on particle size.

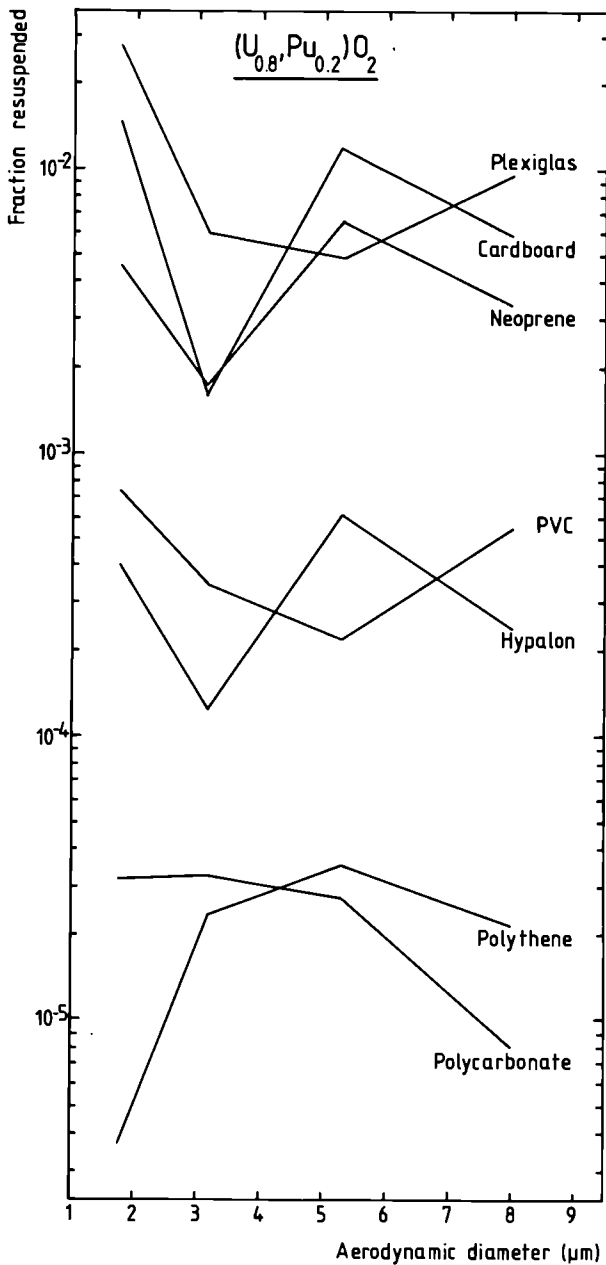


Fig. 6.1: The resuspension of uranium-plutonium oxide particles from various burning substrates

Fire Experiments under Realistic Laboratory Conditions

Introduction

The series of fire experiments, in which contaminated specimens of various materials (both combustible and not combustible) are burned in or exposed to the flames of a standard PMMA-fire, were completed.

It was also investigated as to whether the nature of the heavy metal contamination, powder or residue of evaporation, influences the spread of the heavy metal during a fire.

Other Contaminated Materials Exposed to a Standard Fire

The series of experiments presented previously (TUAR 87, Tab. 3.7) was completed with fires each involving one plate of the following materials:

- stainless steel (2 experiments)
 - unpainted aluminium (1 experiment)
 - painted aluminium (1 experiment)
 - polycarbonate - 0.9 kg - (1 experiment)
- all with contamination levels of 0.5 mg cm^{-2} .

The agreement with the previous measurements is satisfactory, although the results for aluminium may be affected by the premature collapse of the metal plate carrying the contaminant Ce-Eu-oxide powder.

In addition, two experiments were carried out with 0.3 kg of cleaning tissue (Kleenex) contaminated with 0.5 g of Ce-Eu-oxide powder and contained in a cardboard box set on the top of the fuel assembly.

Tab. 6.1 shows data collected from these experiments (including those taken from Tab. 3.7 of TUAR 87). The following observations were made :

- In general, with the exception of neoprene, the percentage of heavy metal transported into the ventilation outlet is never higher than with PMMA. This is an important result for safety analysis applications.

Tab. 6.1 *Transport of heavy metal from fires involving contaminated plates of different materials*

Type of contaminated material	Percent of original cerium contaminant		
	Transported into ventilation exit channel	Left on the surface	Left in the residue
Stainless steel **	1.7	90	*
Stainless steel **	0.2	86	0.3
Stainless steel	0.6	60	2.9
Stainless steel	0.5	58	0.5
Painted stainless steel **	0.3	78	0.3
Painted stainless steel **	2.0	62	0.4
Aluminium	2.8	14	8.9
Painted aluminium**	2.1	*	20
Painted aluminium	2.3	*	29
Polycarbonate (1.5 kg) **	0.5	-	*
Polycarbonate (0.9 kg) **	0.4	-	63
Polycarbonate (0.9 kg)	1.4	-	46
Polyethylène (1 kg) **	1.0	-	23
Polyethylène (1 kg) **	1.3	-	42
Neoprene (87 g) **	5.9	-	13
Neoprene (32 g) **	2.3	-	19
In a cardboard container :			
Kleenex (0.3 kg)	0.7	-	57
Kleenex (0.3 kg)	2.2	-	34

Contamination level 0.5 mg/cm² - For Kleenex, total contamination 500 mg

(*) not measured

(**) already reported in TUAR 87

- The supposition that the spread of contamination is somewhat stronger from painted than from unpainted metal surfaces is not confirmed.

PMMA Fires with Simulated Contamination from Solution Deposition

In glove boxes for the fabrication of nuclear fuels, plutonium and uranium compounds are usually handled (ballmilled, blended, pressed, sintered etc.) in the form of powder or pellets. Thus the inside of these glove boxes and the equipment

they contain become contaminated with airborne particles directly spread from solid material. In the framework of the contaminated smoke studies, the behaviour in fires of this "dry" contamination was studied first, and in the standard PMMA-fires previously reported (TUAR 86 and 87), the contamination was simulated by spreading cerium-europium-oxide powder onto the appropriate glove box construction material.

Another frequent contamination process is the deposition and subsequent drying inside the containment of droplets originating from aqueous, mostly acid, plutonium solutions normally present in "chemical" glove boxes. This contamination from solution deposition can be simulated by evaporating an acid solution of cerium and europium, previously spread out on the fuel plate.

Two test fires with PMMA as a combustible material were carried out, using the standardized five-plate assembly previously described (TUSR 36). The contaminant solution was made by dissolving ammonium cerium (IV) nitrate and europium (III) oxide in nitric acid to a final acidity of 1.1 N and a Eu/Ce ratio of 0.2. Surface concentration of cerium on the PMMA plates is set to 0.08 mg cm⁻².

The data show that the percentage of cerium carried away with the combustion gases into the ventilation outlet amounted to 0.15 (detection limit) and 0.50 respectively and thus was significantly lower than in the case of dry contamination (1 to 2 %). Likewise the percentage of cerium left in the combustion residue amounted to 22 and 4 respectively (against 33 with a standard deviation of 6 in the case of the dry contamination).

These results suggest that the mechanisms determining the heavy metal transport are different for the dry and the solution contamination cases. Not only are we dealing with different chemical compounds, but also the degree of attachment or even penetration may be higher for solution than for dry contamination. Measurements on small scale fires and of particle size distribution in smoke from large scale fires may provide more information.

7 Reprocessing of Nuclear Fuels (Repro)

Introduction

One activity in sub-project REPRO is devoted to the head-end processes for advanced fuels: a feed solution compatible with the requirements of the Purex process is to be obtained. The studies aim at a description of the head-end reactions taking place upon dissolution of nitrides in nitric acid. The composition of the off-gas and particularly the evolution of elemental nitrogen are of interest here. The formation of ammonium ions in the dissolver solution and their subsequent destruction is a further subject of investigation. The exchange reactions taking place between ^{14}N and ^{15}N upon dissolution of MN in nitric acid - for the case where the fuel has been fabricated with nitrogen enriched in ^{15}N - are also being examined; this part of the project was delayed in 1988 because of budgetary constraints.

Another activity is concerned with separation of actinides from fuel or waste solutions. The aim is to recover the actinides before they enter the waste streams. The chemical behaviour of Np, and of colloidal plutonium are of particular interest in these studies.

Fuel Dissolution Studies

The experiments on nitride fuels have been continued in this period. The level of ammonium ions formed in the dissolver solution was further confirmed; experiments to decompose these ions have started.

No decrease in the level of ammonium ions in the solution of dissolved nitrides was observed after about 8 weeks of contact with a strong gamma field from mixed fission products.

A possible way of destroying the ammonium ions could be through their reaction with nitrite ions. Boiling the solution with an excess of nitrite ions under different conditions are being tested; the results will be reported in the next report. The nitrite should provide the additional advantage of stabilising the plutonium in the tetravalent state.

Absorption Spectroscopy of Neptunium

The study of the absorption spectra of the actinides U, Np, Pu, and Am in their various oxidation states in nitric acid (1-14 M) has been completed. The spectra were recorded on the remotely operated Cary 17D spectrometer. The molar absorptivities have been evaluated for some selected peaks in the above mentioned spectra of the actinides.

The dependence of the molar absorptivity for Np(IV), Np(V), and Np(VI) on the nitric acid molarity has been investigated in more depth [1], as such data, measured in strong nitric acid are missing in the literature, whereas the spectra of uranium, plutonium and americium have been published [2,3,4].

Neptunium can be stabilised in concentrated nitric acid in the tetravalent or in the hexavalent oxidation state by the use of an excess of a reduction or an oxidation agent, respectively. In contrast, although Np(V) normally is the most stable oxidation state, pentavalent neptunium disproportionates in strong acid into Np(IV) and Np(VI)

The behaviour of Np(V) has been discussed in the previous report (TUAR 87, 145); here additional data on Np(IV) and Np(VI) will be given. The absorption spectrum of Np(IV) shows very pronounced changes with increasing nitric acid concentration. In contrast, the Np(V) spectrum is very stable, except for the most intense absorption band at 981 nm, the intensity of which decreases in stronger acid.

In the case of Np(VI) the principal absorption band at 1222 nm decreases sharply at acidities above 6 N HNO_3 , in favour of a new peak developing at 1120 nm. These observations are presented in Figs. 7.1 and 7.2 and are assignable to the formation of $\text{NpO}_2(\text{NO}_3)_3^-$ ions.

A decisive factor in the quantitative determination of the concentration of Np is thus the exact knowledge of the acidity prevailing in the solution (see also TUAR 87, Fig. 3.30).

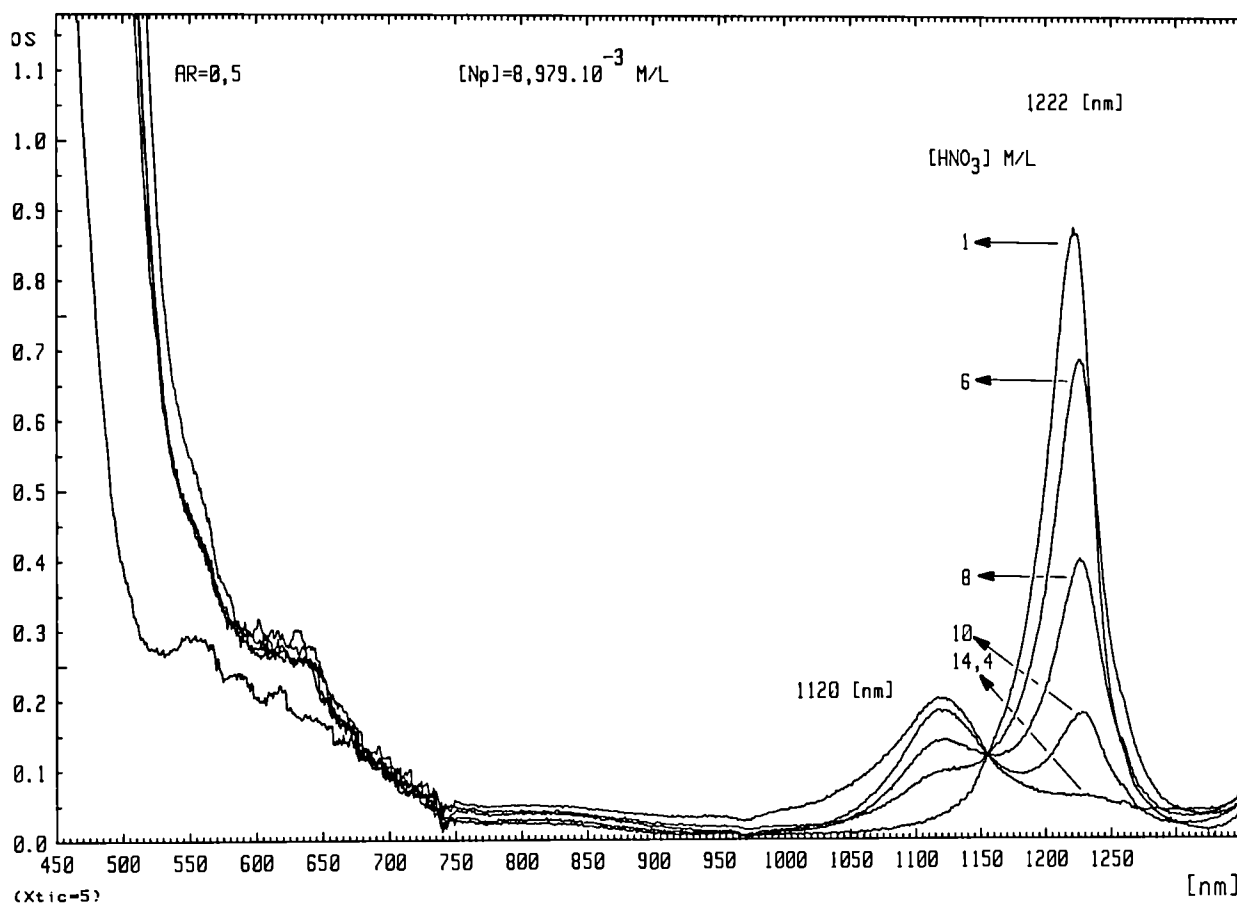


Fig. 7.1 Absorption spectra of Np(VI) as a function of the HNO_3 molarity in the range 1.0 to 14.4 M.

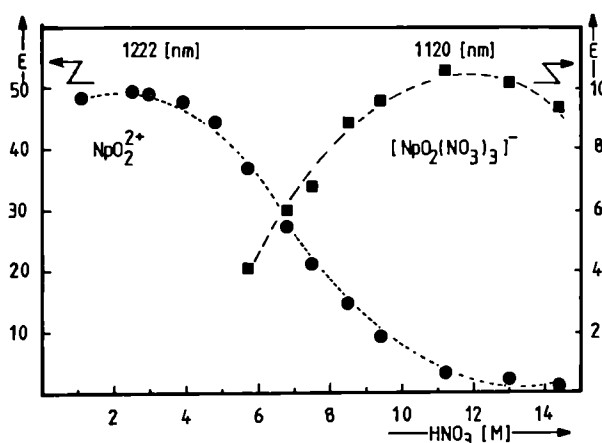


Fig. 7.2 The decrease of the molar absorptivity for Np(VI) at 1222 nm and the increase of the molar absorptivity at 1120 nm as function of the nitric acid molarity.

However, as the molar absorptivities for Np(IV) and Np(VI) are rather small a sensitive Np determination should be based on the higher absorptivity of the Np(V) species at 981 nm in weak acid. In that case a limit of detection of 10^{-6} Mol/l can be achieved in 1 M HNO_3 under stabilisation with H_2O_2 .

Colloidal Plutonium

In the last Annual Report the role of colloidal Pu(IV) in the Sol-Gel process was discussed (TUAR 87, 229), [5]. The autoreduction of Pu(VI) to Pu(IV) was followed by spectroscopic measurements.

A further experiment has been made with twice the concentration of Pu to study the influence of concentration on the autoreduction process. The

dependence is shown in Fig. 7.3: the conversion from Pu(VI) to Pu(IV), taking 50 days at 236 g/l Pu, is accelerated at higher concentrations, i.e.

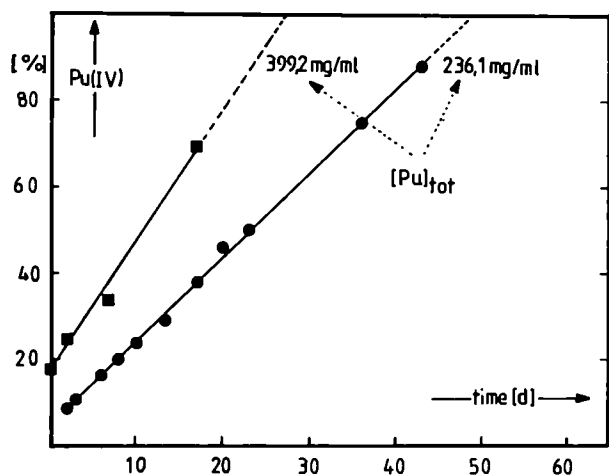


Fig. 7.3 *Autoreduction of Pu(VI) to Pu(IV) with time showing dependence on the total concentration of plutonium.*

about half the time is required at 400 g/l Pu. These rates were found by extrapolation from the experimental curves.

In addition to the described dependence of the autoreduction rate on the concentration of plutonium, these experiments detected the presence of Pu(V) in a measurable and stable concentration, at the prevailing low acidity of 0.6 M HNO₃. Plutonium spectra taken on the solution under these conditions without prior dilution are shown in Fig. 7.4.

Actinide Separation and Recovery

The separation of actinides, from another and from lanthanides, by the HPLC technique described in several previous reports (e.g. TUAR 87, 145) has been continued; a bigger installation on a preparative scale (100 ml/min at 200 bar) has been tested and installed in a glovebox

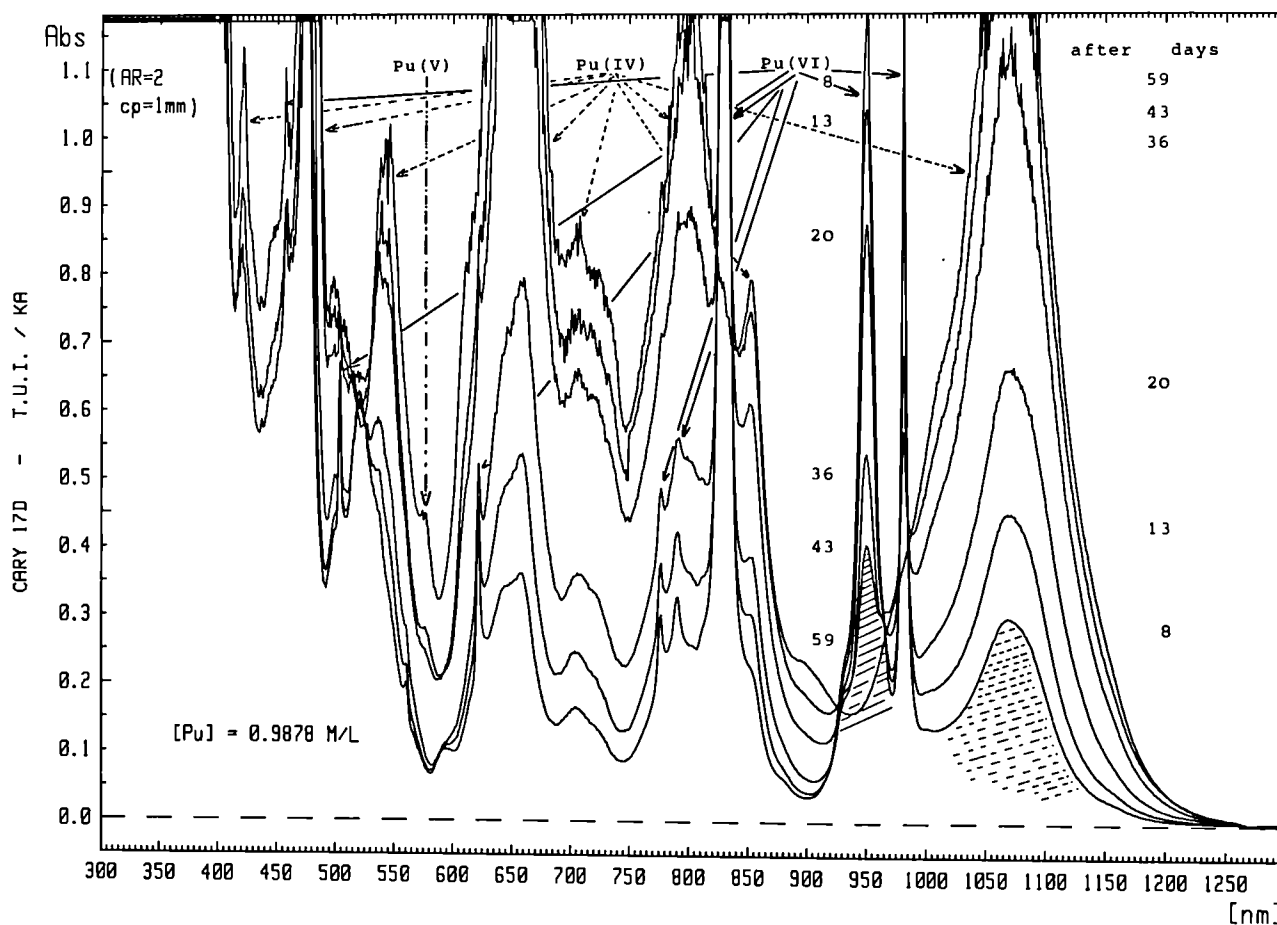


Fig. 7.4 *Absorption spectra showing autoreduction of Pu(VI) to Pu(IV) with time in weak nitric acid. Note the appearance of a peak assignable to Pu(V).*

behind additional neutron- and gamma-shielding. The optical multichannel analyzer OMA-2 has also been connected to the glovebox by an optical fiber system; the instrument will be used in connection with campaigns for the separation and purification of actinides as explained below and for other relevant measurements.

The actinides in fuel and waste solutions from the fabrication of fuels will be recovered by this means. Furthermore, mixtures of actinides containing greater amounts of impurities such as iron and lanthanum are to be treated. A total of about 70 g of Am and 20 g of Np will be involved. This work is a natural extension of the work done earlier on actinide separation from fuel solutions. It will also deal with the final purification of the collected actinide fractions, e.g. the destruction of the complexant and other necessary steps.

Extensive analyses of the content of actinides in these "waste" solutions by spectrophotometry, alpha and gamma spectroscopy have been carried out as a preparation for the recovery. These analytical determinations were often preceded by TBP- or TTA extractions, because of the high concentrations of Am (about 10 g/l), which made the direct determination by gamma and alpha spectroscopy difficult. The spectral absorptions of the various actinides interfere with each other only slightly and advantage could be taken of the recently determined molar absorptivities for the selected peaks in the spectra.

A selected example of a complex spectrum is shown in Fig. 7.5. Clearly seen are the species

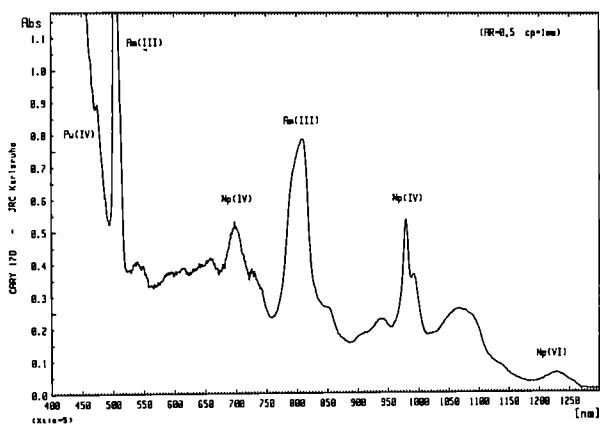


Fig. 7.5 Absorption spectrum of a complex mixture of the actinide species $Np(VI)$, $Np(IV)$, $Am(III)$, and $Pu(IV)$. See the text for a discussion of the possible presence of $U(VI)$.

$Am(III)$, $Pu(IV)$, $Np(IV)$, $Np(VI)$ and possibly, below 450 nm, $U(VI)$; the strong absorption in this spectral range could also contain contributions from $Fe(III)$, colloidal $Pu(IV)$ and from bands due to charge transfer from $Np(VI)$. Only the concentrations of americium and neptunium can be evaluated from this spectrum: $Np(IV)$ contributes 87 % and $Np(VI)$ 13 % to the total Np.

A dilution of 1:10 with 4 M HNO_3 suppresses the charge transfer bands from $Fe(III)$ and $Np(VI)$ and allows the additional determination of the concentration of $Pu(IV)$. However, the oxidation state of Np is changed and $Np(V)$ appears in the spectrum, as is seen in Fig. 7.6.

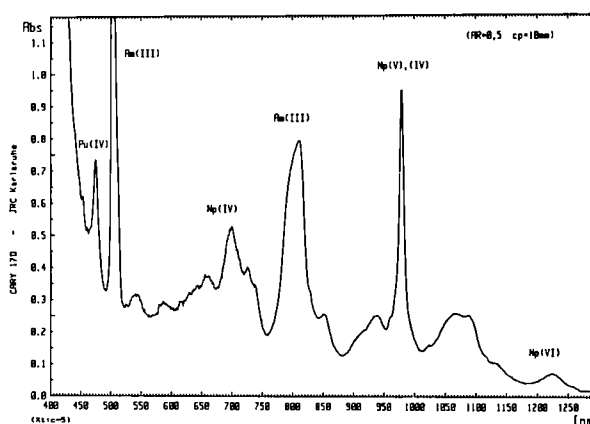


Fig. 7.6 Absorption spectrum of a complex mixture of the actinide species as in Fig. 7.5, but after a 1:10 dilution with 4M HNO_3 . Note the appearance of $Np(V)$ in the spectrum.

Through a direct extraction with 30 % TBP in dodecane, Am and, most importantly, Fe remains in the aqueous phase, whereas the other actinides are extracted; a back-extraction with diluted nitric acid returns the species $U(VI)$, $Pu(IV)$, $Np(V)$ to the aqueous phase, the $Np(V)$ being formed by disproportionation in the weak acid. These species can then be quantified from Fig. 7.7, which shows the appearance of the spectrum after such a extraction/back-extraction cycle.

By the methods described here a complete speciation analysis of the actinides U, Np, Pu, and Am can thus be ascertained. A comparison between the determination of the concentration of Am by optical spectroscopy and by alpha spectroscopy is shown in Tab. 7.1. A statistical

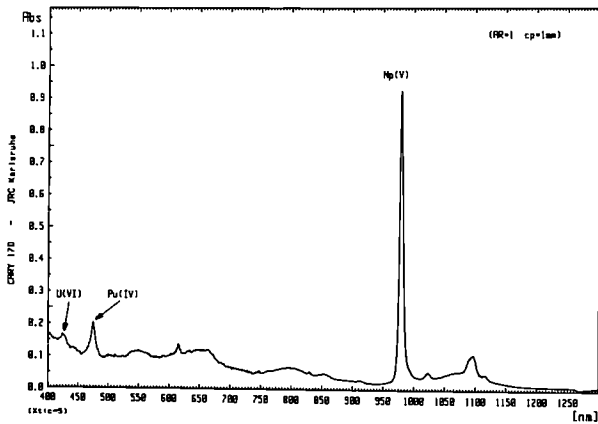


Fig. 7.7 Absorption spectrum of a complex mixture of the actinide species as in Fig.7.5, but after a extraction/stripping cycle with TBP in dodecane. The spectrum shows the stripping solution with the species U(VI) Pu(IV) and Np(V).

evaluation of the few data by a "paired comparison" test gave no statistical significant difference between the methods at the 95 % confidence level and a overall pooled standard deviation of 10 % was found.

References

- [1] C. Apostolidis; H. Bokelund, M. Ougier, 18. Journées des Actinides, Paris, April 1988
- [2] J. L. Ryan, J. Phys. Chem 64 (1960) 1375
- [3] M. Ye Krevinskaia, V. D. Nikolski, B. G. Pozharskii, Radiochem. 1 (1960) 244
- [4] G. N. Yakolev, V. N. Kosyakov, Trans. 2nd Int. Conf. on the Peaceful Uses of Atomic Energy, Geneva 2127 (1958).
- [5] H. G. Schneider TU Technischer Bericht 88/1 1988.

Tab. 7.1 Comparison of two methods for the determination of Am in solutions containing complex mixtures of actinides and lanthanides and macro amounts of impurities.
Method 1: Optical spectroscopy as described in the text
Method 2: Alpha spectroscopy

Concentration of Americium in g/l		Rel. Diff. %	Acidity M HNO ₃	Remarks
Method 1	Method 2			
0,329	0,266	21	4.4	High in U) 4.6 3.8 **)
7,84	14,31	22	2.3	
8,89	9,67	-8	4.3	
1,17	0,843	32	1.1	
6,85	7,02	-2	4.3	
1,05	11,23	2		
5,61	5,28	6		

*) High in U, Np, and Pu

***) Contains halogen ions and CaF₂

8 Actinide Research

Introduction

In Actinide Research the mineralization technique developed for single-crystal growth of uranium and plutonium compounds has been extended to neptunium compounds, and in a new effort involving the miniaturization of this technique, small crystals of AmBi and AmTe were produced. Single crystals of PuFe₂ and UFe₂ were also prepared and studied by neutron diffraction and magnetization; these systems are particularly interesting because they show strong hybridization between the 5f and 3d electrons. This hybridization is also the subject of a considerable theoretical effort involving band-structure calculations.

High-pressure experiments have shown a new phase transition at about 45 GPa in plutonium. X-ray absorption spectroscopy at high pressures has been developed to complement the X-ray investigation of structural phase transitions at high pressure, and the capability to measure optical reflectivity and resistivity under pressure is under development.

Photoelectron spectroscopy techniques were used to study the chemical reactivity of O₂ and CO at the surface of uranium metal. In the case of neptunium metal we have observed by the same technique the formation of Np₂O₃, a compound which is not stable in bulk form.

Objectives

The aim of the project is the understanding of the properties of actinide-containing solids in terms of the electronic structure of their constituents and of the 5f electron contribution to the bond. The objective is attained by the experimental and theoretical investigation of selected properties of, especially, intermetallics and binary actinide compounds, with emphasis on the less known elements Pa, Np, Am, Cm, Bk, and Cf. This requires the availability, hence preparation of well characterized samples (often as single crystals) of known composition, crystal structure and impurity content.

The effectiveness of the actinide project is much enhanced by extensive collaborations throughout Europe and strong connections with a number of US Laboratories. In a real sense the Institute acts as a focal point for actinide research in Europe and most of our research initiatives, such as the preparation of new compounds and materials, comes as the result of extensive discussion with outside collaborators.

In Sub-Project Actinide Chemistry, specific compounds of minor and major actinides with very high purity and reproducible physical and chemical characteristics are prepared by suitable crystallisation methods. This is a necessary condition not only for the Sub-Project Actinide Physics, but also for the combined efforts on actinide research of the Member States of the Community. In addition, basic physico-chemical properties like crystal structure, PVT diagram, and stability regions of these compounds are studied.

Sub-Project Actinide Physics deals with the physical characteristics (thermodynamics, magnetic, electronic properties, also under high pressure) of well defined metals and actinide compounds, representative for certain bonding types. Joint programmes between chemistry and physics involve studies of organometallics and surface properties. These are performed in the double context of understanding the influence of 5f electrons on the chemical bond, but also of producing a basis for a possible catalytic application of actinide compounds.

Preparation and Characterization of Actinides and Actinide Compounds

Introduction

This effort focusses on materials preparation and characterization. Materials preparation includes

the application of a number of established techniques as shown in Tab. 8.1 and the development of new techniques for preparing single crystals of intermetallic compounds. Characterization techniques include X-ray diffraction and electron microscopy. X-ray diffraction studies also include collaborative studies on the structures of organometallic compounds.

Progress in Materials Synthesis and Characterization

Materials preparation comprises:

- the systematic single crystal growth of materials forming large families of isostructural compounds with crystal structure (cubic) to allow a systematic and comparative investigation of the physical properties:
- the preparation of new compounds with properties of interest for fundamental and applied research.

The compounds prepared and encapsulated for physical property measurements during 1988 are listed in Tab. 8.1.

The systematic preparation of single crystals of compounds with NaCl structure type (monopnictides and monochalcogenides) was continued. Single crystals of neptunium and plutonium pseudobinary compounds were prepared and characterized ($\text{NpSb}_{1-x}\text{Te}_x$, $\text{NpAs}_{1-x}\text{Se}_x$, $\text{PuSb}_{1-x}\text{Te}_x$ and $\text{Pu}_x\text{Y}_{1-x}\text{Sb}$).

The samples of $\text{PuSb}_{1-x}\text{Te}_x$ ($x = 0.02, 0.03$ and 0.04) and $\text{NpSb}_{1-x}\text{Te}_x$ ($x = 0.05, 0.1, 0.15, 0.2$ and 0.25) were prepared with the Te metal enriched to 93.45% of ^{125}Te for Mössbauer spectroscopy.

The lattice parameters of the complete system $\text{PuSb}_{1-x}\text{Te}_x$ (NaCl structure type) were determined using X-ray powder diffraction on crushed single crystals. Fig. 8.1 shows the unusual variation of the lattice parameters versus the concentration of tellurium. This behaviour is similar to that reported by Mössbauer spectroscopy for the magnetic hyperfine field in ^{121}Sb .

In search for new materials with interesting magnetic and superconducting properties, the preparation and characterization of ternary and pseudoternary compounds was performed.

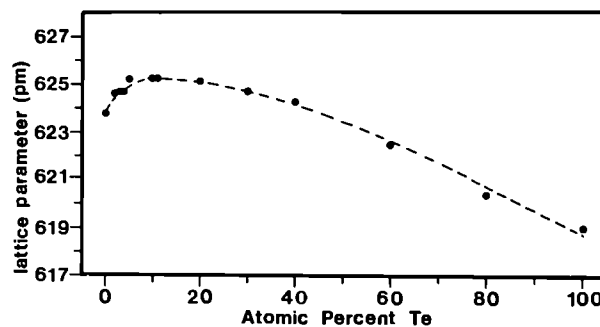


Fig. 8.1 Variation of the lattice parameters for the pseudobinary $\text{PuSb}_{1-x}\text{Te}_x$ (NaCl structure type).

Samples of the systems $(\text{U}_{1-x}\text{Np}_x)\text{Pt}_3$ ($x = 0.04, 0.2, 0.275, 0.5$), $(\text{U}_{0.95}\text{Np}_{0.05})(\text{Pt}_{0.95}\text{Pd}_{0.05})_3$ and $(\text{U}_{1-x}\text{Np}_x)(\text{Pt}_{1-x}\text{Tc}_x)_3$ ($x = 0.075, 0.146$) were prepared. The investigations by X-ray powder diffraction show that the intermetallics are isostructural with the hexagonal UPt_3 compound (SiNi_3 structure type) or NpPt_3 compound (TiNi_3 structure type). The lattice parameters are reported in Tab. 8.2. The powder diffraction pattern of $(\text{U}_{0.5}\text{Np}_{0.5})\text{Pt}_3$ cannot be indexed in hexagonal TiNi_3 structure, but the presence of several weak diffraction lines indicates a superstructure comparable to that observed in $\text{U}(\text{Pt}_{0.5}\text{Pd}_{0.5})_3$. The availability of single crystals is necessary to clarify this problem.

To complete the crystallographic phase diagram and magnetic behaviour of the system $\text{Np}(\text{Ru}_{1-x}\text{Rh}_x)_2\text{Si}_2$, three pseudo-ternary compounds with $x = 0.2, 0.55$ and 0.75 were prepared by arc melting and characterized by X-ray powder diffraction. Fig. 8.2 shows the variation of the lattice parameters and the cell volume versus the content of Rh (in atomic percent).

The study of the Ln-Tc-Si systems led to the discovery of new compounds with the formula $\text{Ln}_2\text{Tc}_3\text{Si}_4$. In the system U-Tc-Si the new compound UTcSi is identified and characterized. $\text{U}_2\text{Tc}_3\text{Si}_5$ and $\text{U}_4\text{Tc}_7\text{Si}_6$ were prepared in pure form.

A large number of compounds were prepared by arc melting of the elements. As shown by X-ray diffraction and metallography, multiphased samples were obtained due to the peritectic decomposition of the compounds. Annealing of the different samples is in progress. By X-ray

Tab. 8.1 Samples prepared, characterized and encapsulated for indicated measurements during 1988

Specific heat	ORNL Oak Ridge	PuS, PuTe NpRu ₂ Si ₂ NpRh ₂ Si ₂ NpTe	M-SC AcM-Poly AcM-Poly M-SC
Magnetization	ETH Zurich	NpSb _{0.95} Te _{0.05} NpCo ₂ NpP PuSb	M-SC Cz-SC M-SC M-SC
Neutron scattering	ILL Grenoble	NpCo ₂	Cz-SC
	CEN Grenoble	NpP, NpAs NpTe NpRh ₂ Si ₂ Np(Ru _{0.45} Rh _{0.55}) ₂ Si ₂ NpSb _{1-x} Te _x (x = 0.05, 0.1, 0.15)	M-SC GSC-Powder AcM-Powder AcM-Powder M-SC
Resistivity	CEN Grenoble	Pu _{1-x} Y _x Sb x = 0.05, 0.1 PuS, PuSe NpAs, NpSb, NpSe NpRh ₂ Si ₂ Np(Ru _{1-x} Rh _x) ₂ Si ₂ (x = 0.2, 0.55, 0.75)	M-SC M-SC M-SC AcM-Poly AcM-Poly
	Uni. Amsterdam	(U _{1-x} Np _x)Pt ₃ (x = 0.04, 0.2, 0.275, 0.5) (U _{0.95} Np _{0.05})(Pt _{0.95} Pd _{0.05}) ₃ (U _{1-x} Np _x)(Pt _{1-x} Tc _x) ₃ (x = 0.075, 0.146)	AcM-Poly AcM-Poly AcM-Poly
Moessbauer Spectroscopy	CNR Strasbourg	NpOBi NpRu ₂ Si ₂ Np(Ru _{1-x} Rh _x) ₂ Si ₂ (x = 0.75, 0.2) NpSb _{1-x} Te _x (x = 0.05, 0.1, 0.15, 0.2, 0.25) PuSb _{1-x} Te _x (x = 0.6, 0.8) (U _{0.50} Np _{0.50})Pt ₃	GSC-Powder AcM-Powder AcM-Powder GSC-Powder GSC-Powder AcM-Powder

M = Mineralisation
Cz = Czochralski
AcM = Arc Melting

GSC = Grinding Single Crystals
SC = Single Crystal
Poly = Polycrystalline Material

Tab. 8.2 Cell dimensions of (U,Np) based ternary and pseudoternary compounds.

compounds	Lattice parameters	
	a in (pm)	c in (pm)
(U _{0.96} Np _{0.04})Pt ₃	576.3(2)	490.0 (2)
(U _{0.80} Np _{0.20})Pt ₃	575.9(1)	488.8(1)
(U _{0.725} Np _{0.275})Pt ₃	576.23(7)	488.34(9)
(U _{0.50} Np _{0.50})Pt ₃	-.-	-.-
(U _{0.95} Np _{0.05})(Pt _{0.95} Pd _{0.05}) ₃	575.67(9)	489.26(4)
Np(Pt _{0.925} Tc _{0.075}) ₃	580.3(2)	955.1(4)
Np(Pt _{0.854} Tc _{0.146}) ₃	580.7(1)	956.1(6)

diffraction on single crystals the new compounds UTcSi, DyTc₂Si₂, Ln₂Tc₃Si₄ with Ln = Dy and Er, U₂Ru₅Sn and U_{4.6}Ru₆Sn_{18.4} were identified and their crystallographic data determined. Physical property measurements will be undertaken on selected single phase systems.

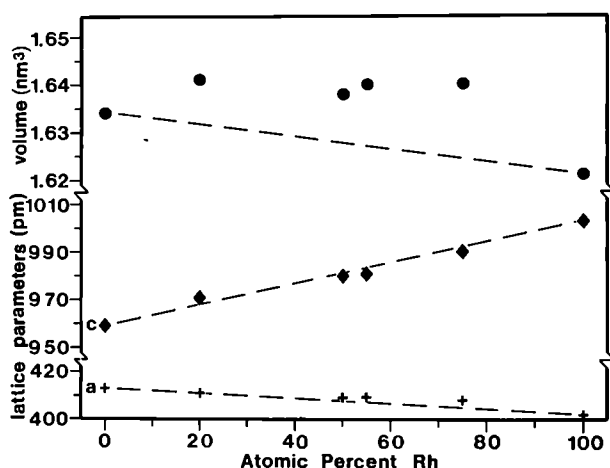


Fig. 8.2 Variation of the lattice parameters and the cell volume for the pseudoternary $Np(Ru_{1-x}Rh_x)_2Si_2$ (ThCr₂Si₂ structure type). The lines here connect end values, which would indicate that Vegard's law was obeyed.

Structure of Organometallic Compounds

The crystal structures of several new organometallic compounds have been determined reported (Tab. 8.3) in order to establish their molecular structure. This work is performed in collaboration with the Institut für Heiße Chemie KfK and the Laboratory of Analytical Chemistry and Radiochemistry, University of Liège, which supply the crystals.

To continue the systematic investigation of the UCp₃X compounds (Cp = C₅H₅), the structure of (Cp₃U)₂O has been determined. The molecular structure consists of two U atoms which are bridged by an oxygen atom located on the inversion centre (0, 0, 1/2). The coordination polyhedron about each U atom can be described as a trigonally compressed tetrahedron along the U-O bond. The bond distance U-O of 208.7 pm is shorter than that observed in Cp₃UO-(C₆H₅).

The investigation of the crystal structure of a new series of compounds of the type AnCp₂X₂ (where Cp stands for pentamethylcyclopentadienyl: C₅-(CH₃)₅) has been started by the determination of the structures of UCp₂X₂, (X = Cl, Br) and ThCp₂Cl₂. The three compounds were isostructural and crystallize in the orthorhombic

Tab. 8.3 Summary of crystal and molecular parameters of organometallics and nitrates complexes.

compounds	Space group	Z	Lattice parameters (pm)	Coordination Number	U-X distances (pm)
U (C ₅ (CH ₃) ₅) ₂ Cl ₂	F m m 2	4	a = 1491.3(3) b = 1734.8(3) c = 816.8(2)	4 tetrahedron	U-Cl = 257.7
U (C ₅ (CH ₃) ₅) ₂ Br ₂	F m m 2	4	a = 1518.8(6) b = 1729.3(6) c = 830.3(3)	4 tetrahedron	U-Br = 274.7
Th(C ₅ (CH ₃) ₅) ₂ Cl ₂	F m m 2	4	a = 1493.9(4) b = 1753.5(5) c = 820.1(2)	4 tetrahedron	Th-Cl = 263.4
[U(C ₅ H ₅) ₃] ₂ O	C 2/c	4	a = 1458.9(2) b = 831.2(2) c = 2200.3(6) β = 111.43 ^o (2)	4 tetrahedron	U-O = 208.7
[UCl ₄ (C ₄ H ₈ O) ₂] ₂	P 2 ₁ /c	2	a = 1075.0(5) b = 1236.2(5) c = 1230.2(6) β = 113.34 ^o (3)	7 bipyramid pentagonal	U-Cl (brid.) = 280.5 U-Cl (av.) = 257.0 U-O (av.) = 240.0
[YbBr(C ₅ H ₅) ₂] ₂	P 2 ₁ /c	6	a = 1388.2(5) b = 1627.2(6) c = 1365.5(5) β = 93.89 ^o (5)	4 tetrahedron	Yb ₁ -Br (av.) = 276.8 Yb ₂ -Br (av.) = 280.2
[U(C ₅ H ₅)(CH ₃ CO ₂) ₂] ₄ O ₂	P -1	2	a = 935.4(4) b = 1298.8(5) c = 1961.3(7) α = 82.74 ^o (3) β = 98.24 ^o (3) γ = 102.89 ^o (4)	7 bipyramid pentagonal	U-O (syn) = 236.1 U-O' = 244.7 U'-O' = 257.2 U'-O'' = 249.2 U-O (oxide) = 205.9
Cis-ZrCl ₄ (NCOCH ₃) ₂	P 2 ₁ /c	4	a = 612.5(2) b = 1374.5(4) c = 1341.9(3) β = 99.38 ^o (2)	6 octahedron	Zr-Cl (av.) = 238.8 Zr-N (av.) = 231.6
[U(NO ₃) ₆][N(C ₂ H ₅) ₄] ₂	C 2/c	4	a = 1832.9(5) b = 1160.3(3) c = 1562.9(5) β = 108.13 ^o (3)	12 icosahedron	U-O = 243.0 to 256.0
[Pu(OH)(NO ₃) ₃ (H ₂ O) ₂] ₂ ·5H ₂ O	F d d d	16	a = 1196.3(8) b = 4524.8(1.1) c = 1851.0(8)	10	Pu-O(NO ₃) = 239.9 to 251.9 Pu-O(OH) = 225.5 to 226.5 Pu-O(OH) = 240.6 to 243.5

space group $Fmm2$, a high symmetry group for the organometallic compounds. The coordination polyhedron of each actinide atom is a symmetrically compressed tetrahedron along the C_2 axis such that the X-An-Cp centroid bond angle is about 105° and the X-An-X angles are about 98° . The An-X bond lengths reported in Tab. 8.3 were shorter than those reported for Cp_3AnX or $(C_9H_7)_3AnX$ compounds.

A dimeric compound of formula $[UCl_4(C_4H_8O)_2]_2$ has been structurally characterized. The molecular structure consists of two U atoms which are asymmetrically bridged by two Cl ions with U-Cl distances of 279.0 pm and 281.9 pm. The U-Cl bond distances for the non-bridging Cl atoms are equal and average to 257.0 pm. The two U-O distances are 238.7 pm and 241.3 pm. Each U atom is seven-coordinated in a pentagonal bipyramidal geometry.

The crystal structure of $[U(C_5H_5)(CH_3CO_2)_2]_4O_2$ consists of two tetranuclear dimers (Fig. 8.3) symmetrically independent, each with an inversion centre located at $(0, 0, 0)$ and $(1/2, 1/2, 1/2)$ respectively. In each dimer, two binuclear

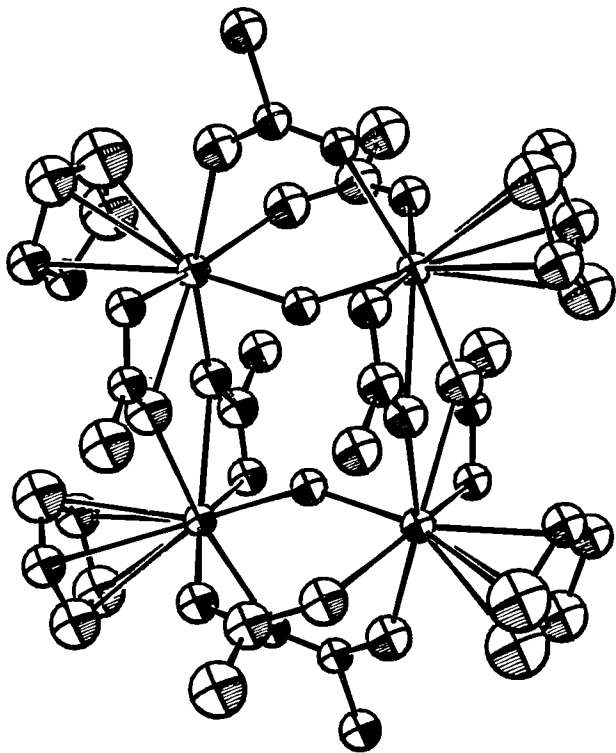


Fig. 8.3 Molecular structure of $UO_2(C_5H_5)_4(CH_3CO_2)_8$

$U_2(C_5H_5)_2(CH_3CO_2)_2$ fragments are connected by chelating carboxylate and oxide bridges. Four acetate groups show the usual bidentate *syn-syn* bridging coordination (O-U) mode between the two binuclear fragments. The two U atoms of each binuclear fragment are bridged by two acetate groups in *trans*-position with the unusual tridentate coordination mode (*syn-syn* and an oxygen acetate as bidentate). Each U atom is seven-coordinated in a distorted pentagonal-bipyramidal geometry with the Cp centroids and the oxygen oxide in the axial positions (Cp-U-O [oxide] averaged to 177.2°) and the carboxyl oxygen atoms in the equatorial plane.

Structure of Actinide (IV) Nitrate Complexes

To understand the separation process of actinides using nitric acid, the determination of the crystal structure of two actinide nitrate complexes is reported (Tab. 8.3). This work is performed in collaboration with the Institut für Heiße Chemie KfK ($U(NO_3)_6(N(C_2H_5)_4)_2$) and with the Institut für anorganische Chemie, Universität München ($[Pu(OH)(NO_3)_3(H_2O)_2]_2 \cdot 5 H_2O$).

In the compound $U(NO_3)_6(N(C_2H_5)_4)_2$, the $[U(NO_3)_6]^{2-}$ anion is twelve-coordinated by oxygen atoms which belong to six bidentate nitrate ligands. All nitrate groups are disordered with two positions for each of the bonding oxygens. The coordination polyhedron around the uranium is an irregular isocahedron, and the tetraethylammonium cation has the expected tetrahedral geometry. The connection between the $[U(NO_3)_6]^{2-}$ anions and the $[N(C_2H_5)_4]^+$ cations is realized through hydrogen bonds between nitrate oxygens and methyl carbons.

In the complex $[Pu(OH)(NO_3)_3(H_2O)_2]_2 \cdot 5 H_2O$, the molecular structure shows a dimeric form (Fig. 8.4). The Pu atoms are linked by two oxygen hydroxy atoms. The bidentate nitrate groups are coordinated to each Pu atom and a coordination number of ten is achieved by coordination of two water molecules. The five crystallisation water molecules form with the water molecules bonded to the Pu atoms and the oxygen nitrates non-bonded to the Pu atoms an infinite tridimensional network, which is held together by hydrogen bonds.

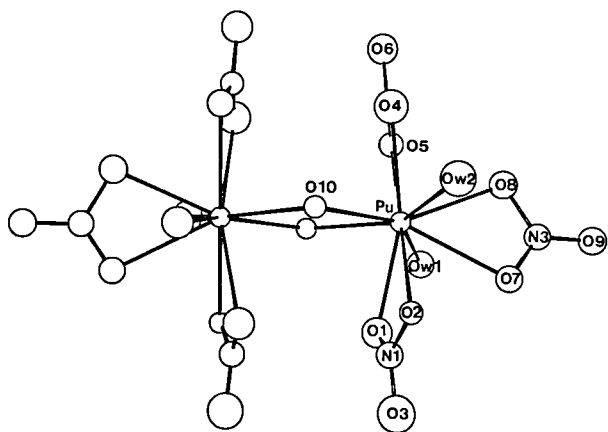


Fig. 8.4 View of the structure of the dimer $Pu_2(OH)_2(NO_3)_6(H_2O)_4$

Catalytic Activity of Ni and UNi_2 in the Hydrogenolysis of Ethane

Actinides and their compounds are considered as well suited model substances to search for basic correlations between electronic structure and catalytic properties because the actinides display a unique electronic structure with a transition from delocalized to localized 5f electrons around Am; they therefore hold a special position in the periodic system of the elements.

To complement surface reactivity studies using electron spectroscopy, reaction rate measurements on the hydrogenolysis of ethane over Ni and UNi_2 catalysts were started in a catalytic flow reactor described previously [1].

The Ni catalyst was obtained from NiO powder by reduction in a hydrogen flow at 400 °C for 72 hours. From the basic powdered UNi_2 material two different catalysts were prepared: a) the so-called UNi_2 prepared in the same way as the Ni catalyst and b) a UO_2 supported Ni catalyst, UO_2/Ni , obtained by an initial oxidation for 2 hours at 300 °C and a subsequent reduction in a hydrogen flow at 400 °C for 84 hours.

The catalytic reaction was performed for different temperatures at a flow rate of 110 ml/min and a partial pressure of 76 torr of

ethane. The reaction mixture and reaction products were analyzed by quadrupole mass spectrometry. The only reaction product found was methane. The results are displayed in Fig. 8.5 (Arrhenius plot) where the logarithm of reaction rate r is plotted against the inverse

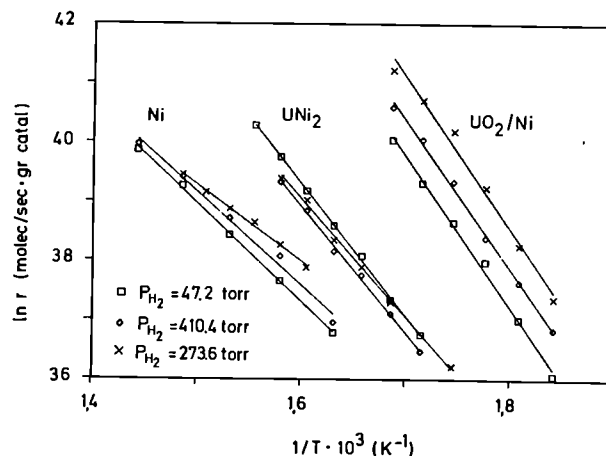


Fig. 8.5 Reaction rates of ethane hydrogenolysis over Ni, UNi_2 and UO_2/Ni catalysts at constant ethane partial pressure $P_E = 76$ torr

temperature T at constant ethane partial pressure and different hydrogen partial pressures. From the slopes of the curves in Fig. 8.5 the apparent activation energies were determined as 32.7, 43.8 and 50.2 kcal/mol for Ni, UNi_2 and UO_2/Ni catalysts, respectively. This increase of the activation energy is somewhat surprising since at the same time the reaction rate is increasing as well. The increase in reaction rates going from Ni to UO_2/Ni may be due to several effects. To get more information on the processes involved further measurements have to be performed, e.g. surface area determination and surface investigations by electron spectroscopy. Of particular interest are possible changes of the chemical composition at the surface induced by the preparation of the catalyst or during the catalytic process itself, as well as the number of active sites and possible changes of the electronic structure of the Ni clusters.

Reference

- [1] TUSR 40 (1985) 89

Electronic Structure Studies on Actinide Systems

Introduction

The effort in actinide physics brings a large number of sophisticated research probes, both in-house and at outside facilities, to bear on problems in actinide materials science. Most of the experiments are performed on the samples prepared by the sub-project "actinide chemistry" and there is thus a close relationship between the efforts in the two sub-projects. As well as containing contributions on the in-house experimental efforts, this report contains sections on work done at large central facilities and a short overview of some of the work performed by our European collaborators on encapsulated samples produced at the ITU. The group's efforts are also strengthened by theory performed in-house and with outside collaborators.

Photoemission Study of 5f-Electron Localization in Am-Pu alloys

5f electrons in light actinides including α -Pu were predicted to be delocalized whereas they are localized in Am and the heavier actinide metals [1]. This has been unambiguously demonstrated by photoelectron spectroscopy [2,3]. The conduction band spectra of α -Pu show the 5f electrons to be at the Fermi-level E_F , thus carrying electric current whereas for Am the 5f electrons are withdrawn from E_F and show the characteristic final state multiplet emission.

To investigate the transition from delocalization to localization of the 5f electrons in more detail, photoemission experiments have been performed on $\text{Am}_x\text{Pu}_{1-x}$ alloys. The Am and Pu 4f core lines were studied by X-ray-induced photoemission spectroscopy (XPS) and the conduction band was investigated by UV-light-induced high-resolution photoemission spectroscopy (UPS).

The starting $\text{Am}_x\text{Pu}_{1-x}$ sample was cleaned "in-situ" by several cycles of annealing and argon ion sputtering until the oxygen contamination was sufficiently small. Due to the extended sputtering the Am/Pu ratio of the sample changed, and enabled the measurement of a Pu-rich and an Am-rich sample for which the exact concentrations cannot be determined at present.

The Am and Pu 4f core level spectra are presented in Fig. 8.6. The shape of the Am 4f emission does not vary with the composition of the sample and resembles that of pure Am-metal. In contrast, the Pu 4f emission does not show the line shape of pure α -Pu (shown as a broken line in Fig. 8.6) but displays, in addition on the high binding energy side of each line, a satellite that becomes dominant for the Am rich sample. In the

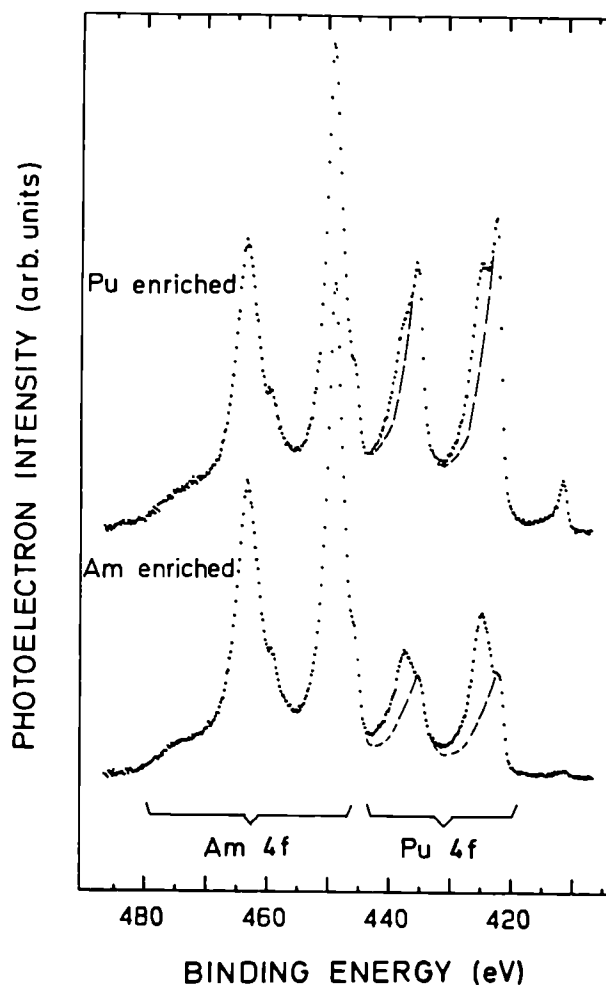


Fig. 8.6 XPS 4f core level spectra of $\text{Am}_x\text{Pu}_{1-x}$ (broken line: pure α -Pu)

latter case the shape of the Pu 4f core line approaches that of the Am line. The high binding energy structure has been shown to indicate the localized character of 5f electrons in Am [2] because of the poor screening efficiency of 6d7s

conduction electrons. Thus, it is clearly demonstrated that, independently of the sample composition, the Am 5f states in $\text{Am}_x\text{Pu}_{1-x}$ are localized as in the case of pure Am metal. The Pu 5f states become the more localized the higher the Am content; in the Am rich sample the Pu 5f electrons have nearly reached the degree of localization which the 5f electrons have in pure Am metal.

This description is confirmed by the conduction band spectra for a Pu rich and an Am rich sample shown in Fig. 8.7. Despite a weak structure around 5.5 eV binding energy which is due to a residual oxygen contamination, the structures A, B, and C are similar to those found in pure Am metal (shown as a broken line in Fig. 8.7) and are

therefore associated with the final state multiplet characteristic for localized Am 5f electrons. The structures D, E, at E_F , and in part also C, are attributed to Pu 5f states. From comparison with spectra for pure α -Pu it is obvious that the emission at E_F represents delocalized Pu 5f electrons whereas the structures D, E and in part C are attributed to a final state multiplet as expected for localized Pu 5f electrons.

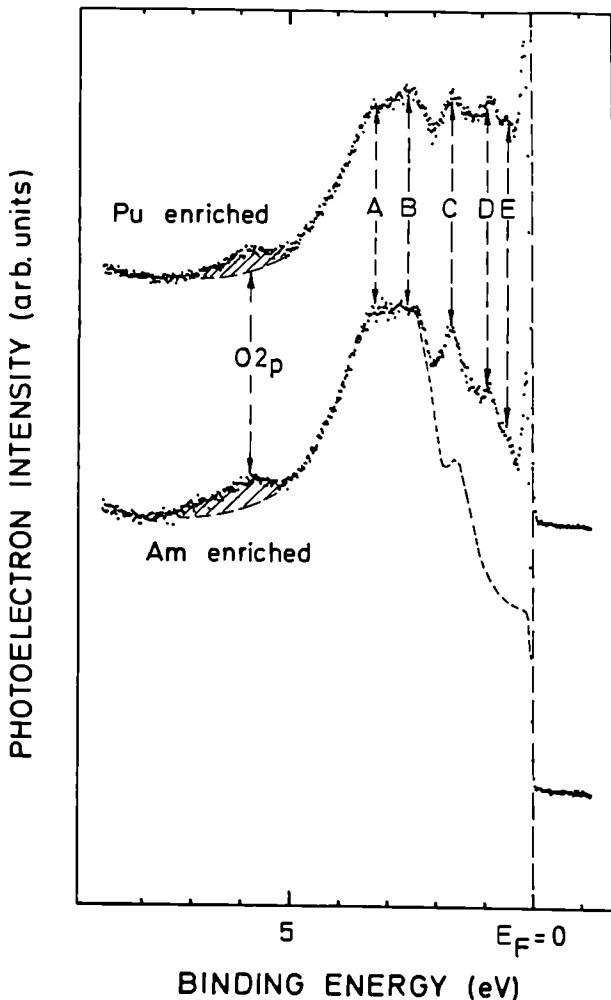


Fig. 8.7 UPS conduction band spectra of $\text{Am}_x\text{Pu}_{1-x}$ for 40.8 eV excitation (broken line: pure Am)

References

- [1] B. Johansson, Phys. Rev. B 11 (1975) 2740
- [2] J.R. Naegele et al., Phys. Rev. Lett. 52 (1984) 1834
- [3] N. Martensson et al., Phys. Rev. B 35 (1987) 1437

Electronic Structure of the Actinide Iridium Laves Phases

The AnIr_2 ($\text{An} = \text{Th}, \text{Pa}, \text{U}, \text{Np}, \text{Pu}, \text{Am}$ and Cm) series of intermetallic compounds exhibits many interesting physical properties [1]. It has been found that ThIr_2 becomes superconducting below 6.5 K. UIr_2 is a nearly temperature independent paramagnet, with a small maximum in the magnetic susceptibility at 60 K. The coefficient of the linear contribution to the specific heat, γ , is high ($62 \text{ mJ/mole} \cdot \text{K}^2$) and the resistivity shows a T^2 dependence at low temperatures. These two latter facts have been taken to be an indication of spin fluctuation effects in UIr_2 . NpIr_2 is the first compound in the AnIr_2 series to order magnetically. Mössbauer experiments indicate that it is an antiferromagnet with an ordering temperature of ~ 6 K and that the measured hyperfine field corresponds to a magnetic moment of $0.6 \mu_B$. The small moment together with a low magnetic entropy of $0.38 R \ln 2$ suggest that NpIr_2 is an itinerant antiferromagnet. The measured coefficient of the linear contribution to the specific heat γ , is very high in the antiferromagnetic phase ($400 \text{ mJ/mole} \cdot \text{K}^2$) and an extrapolation for the paramagnetic phase gives a γ -value of $234 \text{ mJ/mole} \cdot \text{K}^2$. The next compound, PuIr_2 , is a temperature independent paramagnet and the resistivity shows a temperature dependence of the form $\rho = \rho_0 + BT^3$. The T^3 dependence was argued to be characteristic of s-f interband scattering.

Here we report the results of *ab initio* self-consistent energy band calculations of the equation of state and onset of magnetism for $AnIr_2$ compounds. From these we are able to elucidate the nature of the chemical bond in this system of compounds.

According to Vegard's law the volume of the unit cell of the compound is obtained by an appropriate sum of the metal atom volumes. We have plotted these expected compound volumes together with the measured ones in Fig. 8.8. Although Vegard's law is often obeyed, here the disagreement is apparent. The reason for this is two-fold.

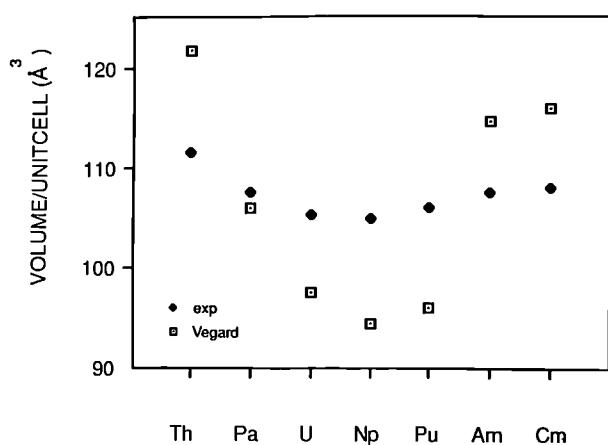


Fig. 8.8 Experimental volumes and volumes calculated from Vegard's law for the $AnIr_2$ systems. (See Ref. 1 for experiments).

(a) It is for the compounds where we expect no or little 5f bonding, i.e. $ThIr_2$, $AmIr_2$ and $CmIr_2$, that the measured volume is lower than predicted by Vegard's law. This reflects the large energy gain due to the formation of the compound. This compound bonding contracts the lattice and the effect is largest for the formation of compounds between late and early transition metals, where the bonding orbitals can be filled and the antibonding orbitals left empty. For $ThIr_2$ this volume contraction is 9.9 \AA^3 and for $AmIr_2$ and $CmIr_2$ it is about 8.0 \AA^3 . The number of d-electrons for Ir is 7.4 and Th, being tetravalent, has 1.9 d-electrons whereas Am and Cm have 1.2 d-electrons each. Hence, upon formation of the compound, $ThIr_2$ with $2 \times 7.4 + 1.9 = 16.7$ d-electrons can nearly fill its

bonding d band (which has the capacity to contain 20 electrons) and in $AmIr_2$ and $CmIr_2$, with 16.0 d-electrons, the bonding d-band is also nearly full. The volume contraction-effect should however here be a little less, as compared to $ThIr_2$, and this is indeed so.

(b) In sharp contrast to this, for the systems with strong indication of having bonding 5f electrons, the experimental volumes exceed the Vegard's law volumes. We explain this apparent paradox by the difference between the 5f bonding in the pure actinide metal and the corresponding 5f bonding in the intermetallic compound.

We calculate the 5f bandwidth in UIr_2 to be 0.2 Ryd whereas it is 0.3 Ryd in uranium metal. There is a significant reduction of the 5f bonding in the compound as compared to the actinide metal, which is due to this band narrowing effect. This volume expansion due to the relative loss of 5f bonding is greater than the volume contraction due to 6d-5f bonding in the compound. Therefore, for systems with itinerant 5f electrons both in the metal and in the intermetallic compound, Vegard's law underestimates the volumes.

A more quantitative theoretical description of the lattice constants requires *ab initio* equation of state calculations. We have made such calculations for paramagnetic and ferromagnetic ground states both with and without relativistic effects. The resulting calculated volumes are shown in Fig. 8.9. The parabolic trend in volume

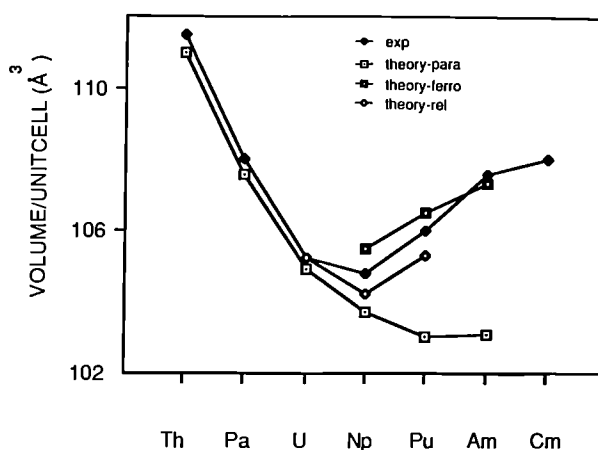


Fig. 8.9 Experimental and theoretical (scalar relativistic, spin polarized scalar relativistic and fully relativistic) volumes for the $AnIr_2$ systems. (See Ref.1 for experiments).

is well reproduced for the early AnIr₂ compounds with paramagnetic ground states whereas relativistic effects become important after NpIr₂. We also find, using a relativistic version of Stoner theory [2] that, for the light actinides up to Am, the inclusion of relativistic effects predicts that only NpIr₂ is magnetic. This is in agreement with experiment.

In conclusion, by using *ab initio* energy band calculations we have obtained a detailed picture of the electronic structure, magnetic properties and equilibrium volumes for the AnIr₂ systems. Good agreement was found both for the occurrence of magnetism and the equilibrium volumes.

References

- [1] See e.g. the collection of articles in "Handbook of Physics and Chemistry of the Actinides", eds. A.J. Freeman and G.H. Lander, North Holland, Vol. 1 and 2
- [2] O. Eriksson, M.S.S. Brooks and B. Johansson, Proceedings of the International Conference on Magnetism, Paris, July 1988, to be published

Studies of Intermetallic Systems

The work described last year in this section has been extended and major progress made in both theory and experiment.

In the theoretical work reported last year on UFe₂ certain specific predictions were made. Briefly, when the actinide ions are non-interacting they can support a spontaneous magnetic moment (in the same way as the lanthanide atoms) by a polarisation of the 5f electrons to give both a spin *S* and orbital *L* moment. When a compound such as UFe₂ is treated by the local spin density approximation in a single-electron band theory we take account of possible interactions between the 5f electrons around the U nucleus and the 3d electrons associated with the iron atom. The result of these band-structure calculations, after the addition of spin-orbit coupling to the Hamiltonian, is that the orbital moment of the f electrons is reduced in magnitude. For the light lanthanide and actinide elements the quantization of *L* and *S* is such that they combine together to give $J = L - S$ and the magnetic moment is proportional to the total quantum number *J*. However, in the band-structure calculations the coupling between *L* and *S* is more complicated and varies across the

Brillouin zone [1]. One may still integrate over the zone, however, to obtain a total moment and the individual (orbital and spin) components. Under these conditions the correct order parameter is the net spin.

The reduction in the effective *L* value implies that the total moment is reduced, since it is the difference between a larger orbital component and a smaller spin component. As proposed by Brooks and Kelly [1] this could be one of the reasons for a reduced moment in many actinide systems. However, a more sensitive test than just the total moment is the measurement of each component separately. In cases where a cancellation between μ_l (orbital moment) and μ_s (spin moment) occurs neutron scattering can provide unique information.

The scattering of neutrons from μ_l and μ_s is not only proportional to their magnitude $\mu = \mu_l + \mu_s$, but it is also sensitive to the spatial extent of μ_l and μ_s , and they are different. This is illustrated in Fig. 8.10. The spin density is more spatially extended than the orbital component. In the

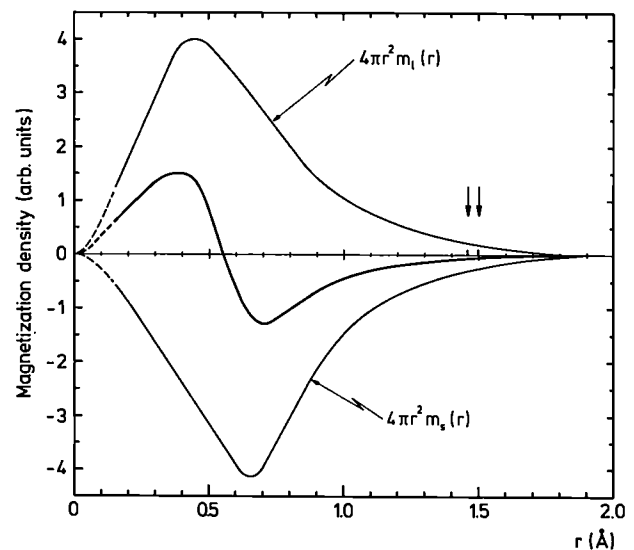


Fig. 8.10 Representation of the orbital ($4\pi r^2 m_l$) and spin ($4\pi r^2 m_s$) components of the magnetisation density as a function of the distance *r* from the nucleus. The difference (heavy line) gives the total magnetization density. The integrated area of this total density is zero.

figure the difference as a function of r is seen to oscillate around zero. In this illustration, which as we shall see closely resembles the true situation at the U site in UFe_2 , the total moment is zero, although both μ_1 and μ_s are finite. The key quantity that represents the spatial extent of the magnetisation density in neutron scattering is the magnetic form factor. We may write this in the dipole approximation as

$$f(Q) = \mu_s \langle j_0 \rangle + \mu_1 (\langle j_0 \rangle + \langle j_2 \rangle) \quad (1)$$

where Q is the momentum transfer, and the $\langle j_i \rangle$ functions are (known and tabulated) averages of spherical Bessel functions over the 5f spin density. We may rewrite this as

$$\begin{aligned} f(Q) &= (\mu_s + \mu_1) \langle j_0 \rangle + \mu_1 \langle j_2 \rangle \\ &= \mu (\langle j_0 \rangle + C_2 \langle j_2 \rangle) \end{aligned} \quad (2)$$

where $\mu = \mu_s + \mu_1$ and $C_2 = \mu_1/\mu$.

We see from Eq. (2) that the signature of a cancellation between S and L is a diminished value of μ (recall that μ_s is negative) and thus a large value of C_2 . For "normal" uranium systems $C_2 \approx 1.5$. This increases for plutonium compounds and can be as high as ~ 4 . For PuFe_2 we found [2] a value of 6.0 ± 0.2 , suggesting significant hybridisation in that compound.

The compound chosen for a close examination [3] was UFe_2 . In this compound a cancellation of μ_1 and μ_s was predicted at the U site and $C_2 \sim 4$. A single crystal was grown at ITU and the experiments performed at both Risø National Laboratory, Denmark, and Saclay, France. The magnetic form factor of the U moment is shown in Fig. 8.11, and is most unusual. A normal form factor falls monotonically from its maximum value at $Q = 0$. The moment on the U site, which is the extrapolated value at $Q = 0$, is clearly almost zero, but the individual $\mu_1 \approx -\mu_s \approx 0.24 \mu_B$ and using Eq. (2) we find $C_2 \sim 23$. In fact, the cancellation is more drastic than predicted [4]. The important point, however, is the experiments confirm that a strong hybridisation does indeed occur in these AnFe_2 compounds. Experiments and further theoretical work are planned on other actinide compounds.

These theoretical ideas have also been recently applied [5] to the cerium compounds with Fe, Co, and Ni. These cubic Laves phases have anomalously small lattice parameters compared with those of the corresponding laves phases of

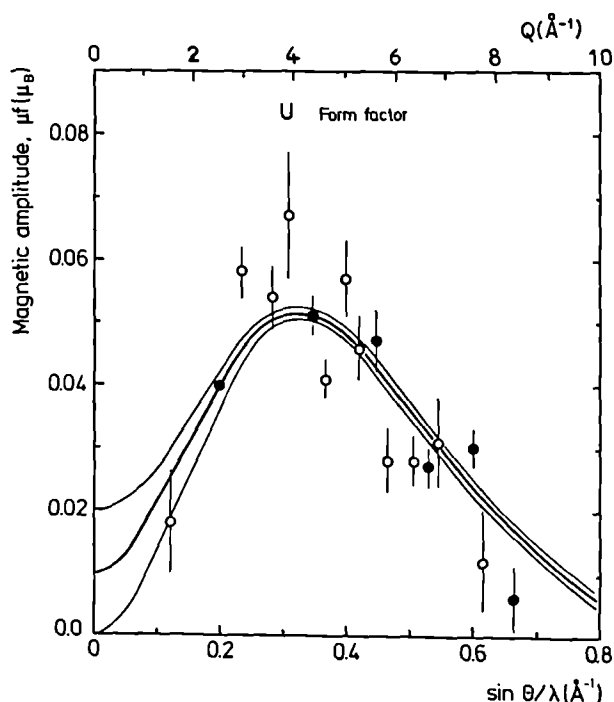


Fig. 8.11 The magnitude of the magnetic scattering on the U sublattice as a function of $\sin\theta/\lambda$ ($= Q/4\pi$). The extrapolation to $Q = 0$ gives μ .

other lanthanides. This is illustrated in Fig. 8.12. The calculated values agree to within 0.5% with the experimental ones. The minimum for CeM_2 at CeCo_2 originates from 3d - 4f hybridisation, which gives rise to an earlier filling of the bonding bands than for a localised 4f compound.

The calculations also give the correct magnetic moment per CeFe_2 molecule and predict that the total Ce moment of $-0.7 \mu_B$ (negative with respect to the iron moment) is made up of $\mu_1 = 0.15 \mu_B$ and $\mu_s = -0.55 \mu_B$. In this compound μ_1 is almost completely quenched and μ_s dominates. Moreover, there is also a calculated contribution ($-0.3 \mu_B$) from the 5d Ce electrons that is comparable to that from the 4f electrons. These predictions of itinerant 4f electrons, as is the case for itinerant 5f electrons in the actinides, may be tested by neutron scattering and spin-polarised photoemission experiments.

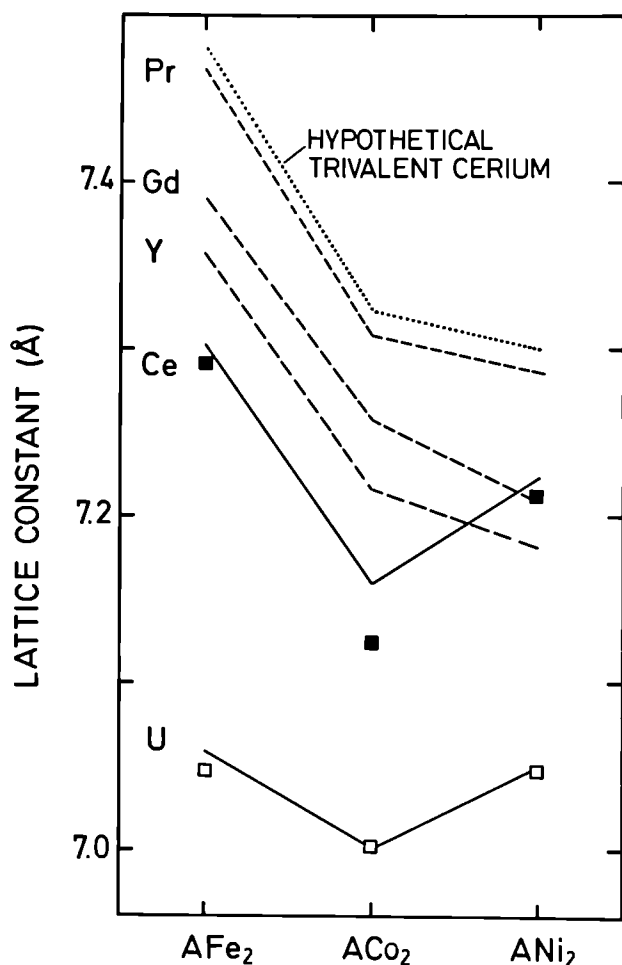


Fig. 8.12 Full and dashed lines connect experimental lattice constants for the AM_2 systems. Filled and open squares are the calculated for Ce and U compounds, respectively. (Taken from Ref. 5)

Actinide Studies at Large Central Facilities

Modern materials science demands a very large and diverse range of experimental probes, and studies in the actinides are no exception. Personnel from the Project, usually working in collaboration with outside staff, make use of the sophisticated instrumentation available at large European or national facilities in their efforts to increase our understanding of actinide materials.

A variety of neutron experiments are performed at CEN, Grenoble, Institut Laue-Langevin, Grenoble, Risø National Laboratory, Denmark, CEN Saclay, Rutherford-Appleton Laboratory, and Argonne National Laboratory. These studies included single-crystal studies of structure (to look for aspects of hydrogen bonding in organometallics), determination of complex magnetic structures, measurement of high-energy crystal-field states at spallation sources and measurements of the excitation spectra in large single crystals.

One of the problems solved this year was the magnetic structure of hexagonal β -Pu₂O₃ at low temperature. Previous experiments [1, 2] had been unable to solve this problem because of lack of experimental resolution. We are particularly interested in the ground state of Pu³⁺ ions because of the unusual hybridization effects that can occur when the Pu 5f electrons interact with neighbouring electron orbitals. In metallic systems such as PuTe [3], PuSb [4], and PuFe [5] these effects are of much current interest; one object of the experiments on Pu³⁺ in the ionic configuration Pu₂O₃ was to examine the ground-state properties in the absence of conduction-electron states.

References

- [1] M.S.S. Brooks and P.J. Kelly, Phys. Rev. Letters 51 (1983) 1708
- [2] M. Wulff et al., Phys. Rev. B 37 (1988) 5577
- [3] M.S.S. Brooks et al., J. Phys. F 18 (1988) L33
- [4] M. Wulff et al., Proceedings Int. Conf. on Neutron Scattering, Grenoble, France, July 1988, to be published in Physica B, also Phys. Rev. (in press)
- [5] O. Eriksson et al., Phys. Rev. Letters 60 (1988) 2523

Neutron experiments were performed on the high-resolution instrument D2B at the Institut Laue Langevin, Grenoble. The sample was 8 g of powder prepared at Argonne National Laboratory with the non-absorbing isotope ²⁴²Pu. The structure is hexagonal and the magnetic configuration of the Pu atoms is shown in Fig. 8.13. Three possible domains are present. The moments of $0.60 \pm 0.02 \mu_B$ per Pu ion are directed along the c-axis. The magnetic propagation vector at T_N is $q_M = 0.5(a, b, c)$ so the unit cell is doubled in all three directions. At ~ 4 K the propagation vector changes to (a, b, c) so that the magnetic and unit cells become identical. The spins remain parallel to the hexagonal c-

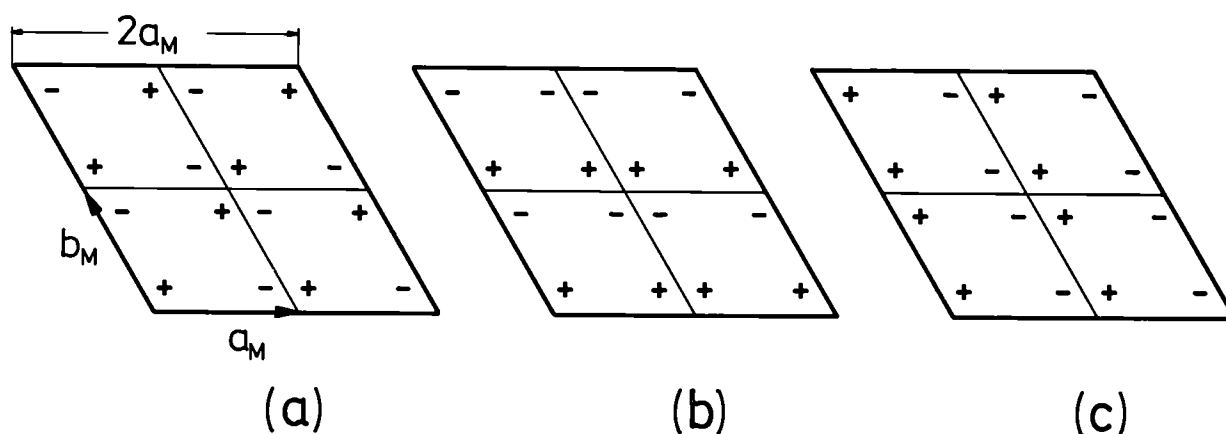


Fig. 8.13 Spin configurations in basal plane of Pu_2O_3 . Each sign represents the direction of the magnetic moment at a Pu ion. The three different designs represent different domains, each with the same energy, that can exist in the material. For a translation of c in the vertical direction the spin of the Pu ion is exactly reversed. The spin direction is parallel to the c -axis.

axis. Because of the high resolution of D2B we were able to extract the intensities of 15 magnetic peaks with enough accuracy to fit a Pu^{3+} form factor. The C_2 coefficient (see earlier section) was derived as 4.5 ± 0.3 . This value, taken together with the spin direction and magnitude, defines uniquely the ground state of the Pu^{3+} ion as the $|\pm 3/2\rangle$ Kramers doublet. The theoretical and experimental situation in this trivalent oxide are thus in good accord. This work has been published [6].

Our work on the trivalent Pu sesquioxide shows that the ground state seems to be readily understood by present theories. A more demanding test for the ionic configuration is to examine the excited states as well. This has not yet been done for Pu_2O_3 , but we have performed measurements to examine these states in the tetravalent oxide PuO_2 .

The compound PuO_2 should be electronically simple. The Pu^{4+} ground state with $J=4$ is split into 4 different states by the electrostatic interaction of the surrounding oxygen charges (the crystal-field potential). The ground state of this multiplet is a Γ_1 singlet with the first excited state a Γ_4 triplet. All low-temperature properties of PuO_2 are consistent with a large separation from the ground state Γ_1 to the excited state Γ_4 . In particular, the susceptibility is independent of

temperature up to 1000 K and the specific heat shows no anomaly up to 1400 K; both measurements being 20 years old. The separation $\Gamma_1 - \Gamma_4$ can be estimated from these results to be greater than 200 meV (2350 K). This energy scale implies a crystal-field potential $V_4 \geq 300$ meV.

Recently, with the advent of spallation neutron sources it has been possible to measure directly these crystal-field splittings. In UO_2 workers [7] first at Argonne National Laboratory and then in more detail Osborn et al [8] at the Rutherford-Appleton Laboratory (UK) have shown that V_4 is about 120 meV. Since these V_4 values should be approximately the same for all tetravalent actinide oxides, we immediately undertook an examination of PuO_2 . The sample, containing 94% ^{242}Pu was made at Los Alamos National Laboratory. The experiments were performed at Argonne and the spectrum is shown in Fig. 8.14. If the V_4 potential is the same as found in UO_2 we expect to find one peak, corresponding to the Γ_1 to Γ_4 transition at 110 meV. Indeed, the center of gravity of the excitation is just about 100 meV, but the spectra consist of at least two peaks, both of which are broadened by the instrumental resolution. This is a totally unexpected result. Unlike in UO_2 the exchange interactions in PuO_2 are negligible, so that the only source of splitting must be a large quadrupolar (or higher order)

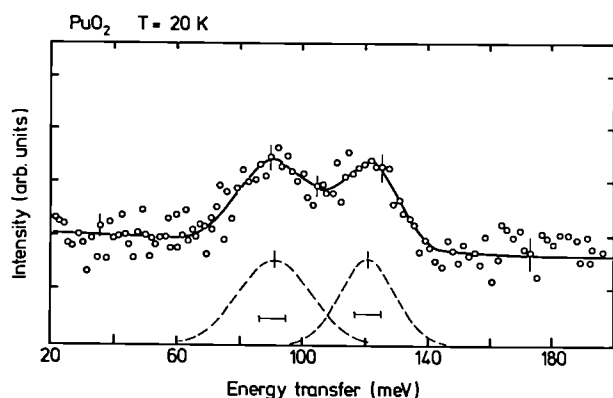


Fig. 8.14 *Inelastic neutron spectra of PuO₂ taken at the IPNS source, Argonne National Laboratory. One peak is expected. Instead two peaks at 91 and 121 meV are seen, with full widths at halfmaximum of ~24 meV. The instrumental resolution ($E_0 = 250$ meV) is ~8 meV.*

one. New experiments to measure this splitting as a function of temperature are in progress at ANL. We are also considering the possibility of other coupling schemes to understand these oxides. The PuO₂ results promise to open much discussion in the actinide community, and hopefully will lead to a better understanding of the oxides in general, e.g. the unusual phase transition [9] in NpO₂.

Both neutron and synchrotron facilities will continue to play a vital role in actinide research efforts in the future. However, because of the excellent penetrating power of the neutrons, encapsulated transuranium samples are routinely examined at neutron facilities but the same is not true for synchrotron facilities. Only in exceptional circumstances, e.g. absorption edges on very thin films, have transuranium samples been examined at synchrotrons. In particular, there seems little hope that such important experiments as high-pressure or photoemission investigations can be carried out at present synchrotron facilities in the near future because of safety requirements. Furthermore, with the increased brightness of new synchrotron machines totally new lines of investigation on very small samples can be envisaged. As a consequence TU, together with a number of collaborators has taken the initiative to promote the development of a "hot" beam line

at a synchrotron facility. A proposal has been made to the European facility in Grenoble and plans are underway to develop some capability at the Daresbury (UK) source.

References

- [1] H.E. Flotow and M. Tetenbaum, *J. Chem. Phys.* **74** (1981) 5269.
- [2] B. McCart et al., *J. Chem. Phys.* **74** (1981) 5263.
- [3] P.G. Therond et al., *J. Mag. and Mag. Mat.* **63-64** (1987) 142.
M.S.S. Brooks, *ibid.* 649; G.H. Lander et al., *Physica* **146 B** (1987) 341.
- [4] G.H. Lander et al., *Phys. Rev. Lett.* **53** (1984) 2262.
G.H. Lander et al., *Physica* **136 B** (1986) 409.
- [5] M. Wulff et al., *Phys. Rev. B* **37** (1988) 5577.
- [6] M. Wulff and G.H. Lander, *J. Chem. Phys.* **89** (1988) 3295.
- [7] S. Kern et al., *Phys. Rev. B* **32** (1985) 3051.
- [8] R. Osborn et al., *J. Phys. C* **21** (1988) L931.
- [9] S. Kern et al., *J. Appl. Physics* **63** (1988) 3598.
J.M. Friedt et al., *Phys. Rev. B* **32** (1985) 257.

Collaborative Research

Over the last decade expensive and complex equipment has been installed at the ITU to produce, characterize, and perform certain physical measurements on transuranium samples, often in the form of single crystals. These facilities are unique in Europe. An obligation, therefore, for the Institute is to assure that the maximum use is made from this considerable investment. This is accomplished by an extensive net of collaborators (see separate list); many of whom bring special techniques to bear on samples produced at the Institute. We give a few examples below.

NpCo₂ has been studied by the Mössbauer technique at CEN, Strasbourg. A narrow single resonance line is observed at 77 K with an isomer shift corresponding to Np⁴⁺. At 13 K NpCo₂ orders magnetically as suggested by the appearance of a hyperfine field splitting; however, the lines are complex and cannot be fitted to any simple model. The moment would appear to be ~ 0.5 μ_B . In separate experiments at Risø National Laboratory no evidence for antiferromagnetic order was found with a single crystal. This apparent discrepancy between Mössbauer and neutron work implies the magnetic ordering to be complex. In an applied field NpCo₂ appears to develop a sizeable

ferromagnetic component; the critical field being about 20 kOe, in agreement with earlier work [1] Further neutron experiments are planned in early 1989 to try to increase our understanding of NpCo_2 .

NpAs has been a compound of interest for some time in actinide research and with the production of sizeable single crystals our understanding of the magnetic phase diagram has been greatly increased. Fig. 8.15 shows the magnetic phase diagram of NpAs as a function of temperature

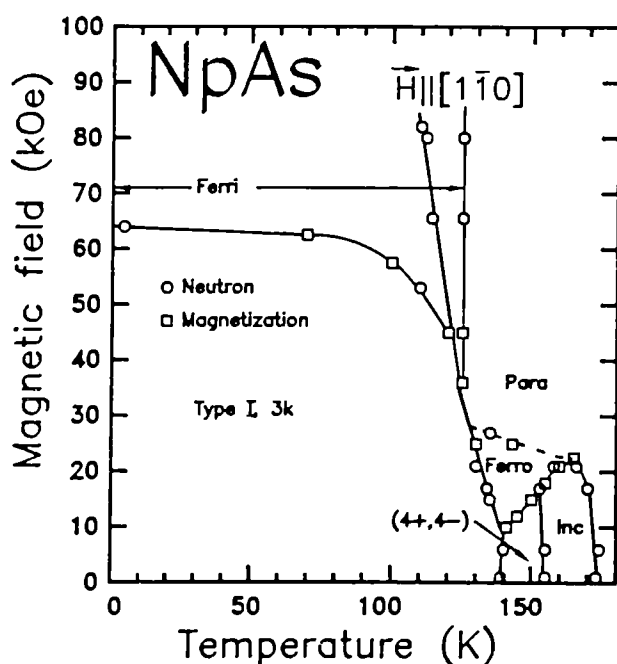


Fig. 8.16 Suggested magnetic phase diagram for NpAs under pressure, as determined by the Mössbauer effect. Work performed at Technical University of Munich.

and applied magnetic field, and represents a collaborative effort [2] between the CEN Grenoble and ETH Zurich, both working on crystals prepared at the ITU. This compound also has been studied by a group in Munich with the Mössbauer technique and both techniques show that important quadrupole and higher-order exchange interactions are important. Pressure experiments have been conducted on NpAs under pressure [3] and the Mössbauer effect shows that a weak delocalisation of the $5f$ electrons, probably as a result of their interaction with the p As valence orbitals, occurs as a function of

pressure. The suggested phase diagram is shown in Fig. 8.16. The Mössbauer hyperfine field patterns suggest that the collinear, single k structure is stabilised at high pressure.

Low-temperature ($T_{\min} \sim 0.6$ K) resistivity measurements are also performed at the CEN

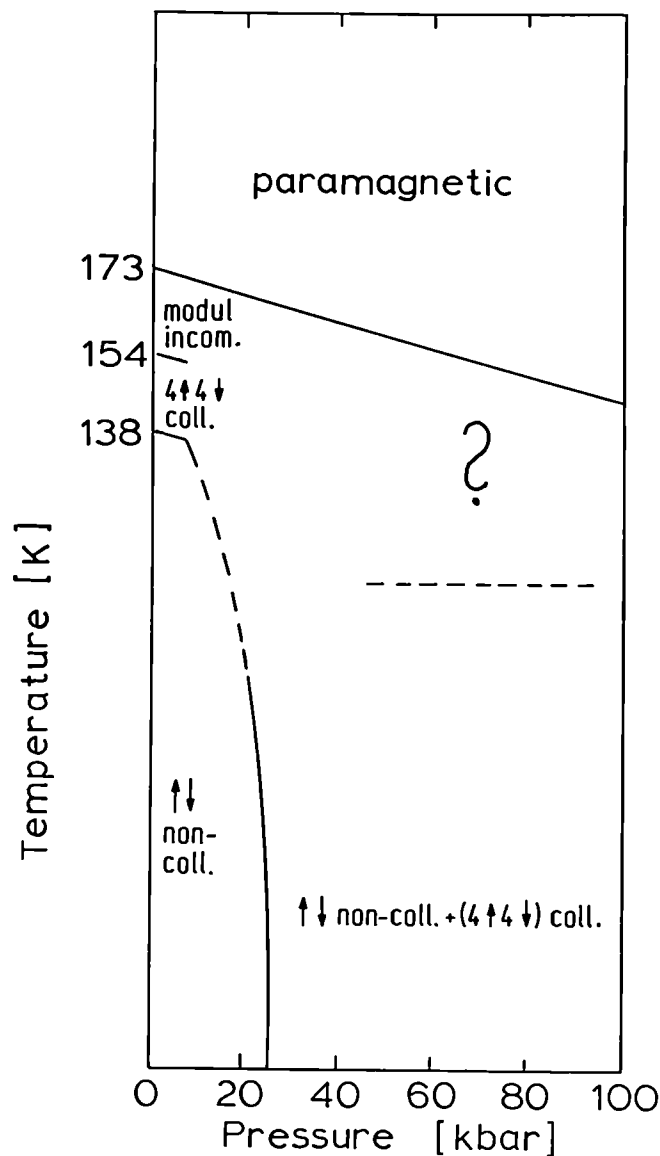


Fig. 8.15 Magnetic phase diagram for NpAs as a function of H (applied along the 110 axis of a single crystal) and temperature. Work performed at the CEN, Grenoble, and ETH, Zurich.

Grenoble, on active samples. Of special interest this year were measurements performed on NpTe [4] and NpRu_2Si_2 [5]. NpTe orders antiferromagnetically with a complex structure

at ~ 30 K and the resistivity is shown in Fig. 8.17, together with that of the other actinide monotellurides. It is interesting to note that the resistivity at 300 K is lower than that at 0 K in both NpTe and PuTe, and this is unusual for metallic compounds. These monotellurides are of much interest as they lie on the border between localised and itinerant behaviour. High-pressure experiments (performed at the Institute) show that all the monotellurides have low bulk moduli.

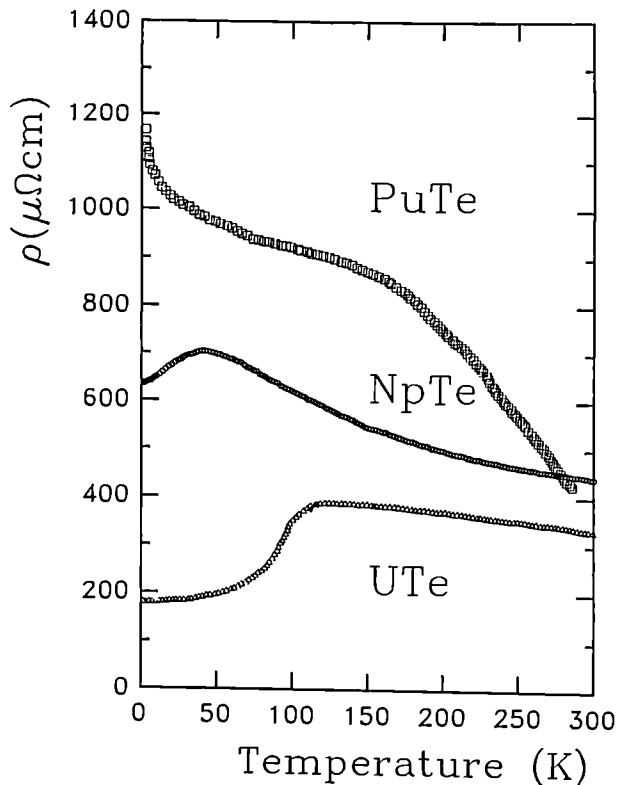


Fig. 8.17 Electrical resistivity of the actinide monotellurides as a function of temperature as measured in the CEN, Grenoble.

In NpRu_2Si_2 , which is isostructural with the heavy-fermion compound URu_2Si_2 , the ordering temperature is 29 K and the resistivity shows a sharp decrease, much as happens in NpTe, at T_N . The resistivity continues to decrease until 1.5 K and plans are in progress to measure below this temperature to determine whether this material becomes superconducting [5]. Many of the properties resemble those of heavy-fermion systems and the specific heat over different ranges of temperature will be measured at both CEN Grenoble, and Oak Ridge National Laboratory.

To extend our measurement capability at the Institute we are installing a low-temperature (1.2 K) high-pressure (300 kbar) instrument for measurements of the electrical resistivity. The equipment has been ordered and should be operational in early 1989. This represents a collaboration between KFA-Jülich (J. Wittig) and the Institute.

References

- [1] A.T. Aldred et al., Phys. Rev. **B11**(1975)530.
- [2] P. Burlet et al., J. of Magn. and Magn. Mater. **63-64** (1987)151
- [3] U. Potzel, Dissertation, Technische Universität München, Fakultät für Physik, 1987
- [4] E. Pleska et al., J. de Physique (in press)
- [5] M. Boge et al., J. Nucl. Mat. (in press)

Actinide Behaviour and Radiation Damage in Oxides

In an extension of the work on the partitioning of Np in the tailor-made complex mixture of oxides called SYNROC B reported in TUAR 87, a Cm-244 containing SYNROC was produced. To this end, a green pellet was soaked with Cm-solution and subsequently sintered under reducing conditions. The final product is a fine-grained mixture of zirconolite $\text{CaZrTi}_2\text{O}_7$, Ba-hollandite $\text{BaAl}_2\text{Ti}_5\text{O}_{14}$, perovskite CaTiO_3 , rutile TiO_2 and hibonite $\text{CaAl}_{12}\text{O}_{17}$. Electron probe micro-analysis indicated that Cm was present in all phases except hibonite, but most Cm was incorporated into zirconolite.

The product accumulated radiation damage by α -decay of Cm-244, and has reached a total dose of $\sim 1.5 \times 10^{19}$ α -events/cm³. X-ray analysis showed a gradual line broadening and a reduction of the diffraction peaks. This is in agreement with the results of ion implantation which was shown in TUAR 87 to amorphize SYNROC. Previous work on Cm-doped Zirconolite [1] has shown that the dose necessary for amorphization of this compound is 2.3×10^{19} α -events/cm³.

Reference

- [1] W.J. Weber and H.J. Matzke, Radiation Effects **98** (1986)93

High Pressure Studies on Actinide Systems

Actinides and actinide compounds were studied under high pressure by X-ray diffraction, X-ray absorption and optical reflectivity. These studies concentrated in 1988 on the actinide mononictides and monochalcogenides.

Nearly all of them exhibit structural phase transitions under pressure. A large group, mainly those with anions of medium atomic mass (As, Se, Te), have a CsCl (B2) type high-pressure structure. Sb as an anion favours a tetragonal high-pressure structure, while several other structures were observed for the high-pressure phases of the compounds with N, P and S. The compressibilities were determined for all of the compounds studied. Fig. 8.18 gives the pressure dependence of the relative volume of PuSb, as an example. This compound under pressure first transforms to the B2 type structure, then to a tetragonal lattice of space group P4/mmm (no. 123).

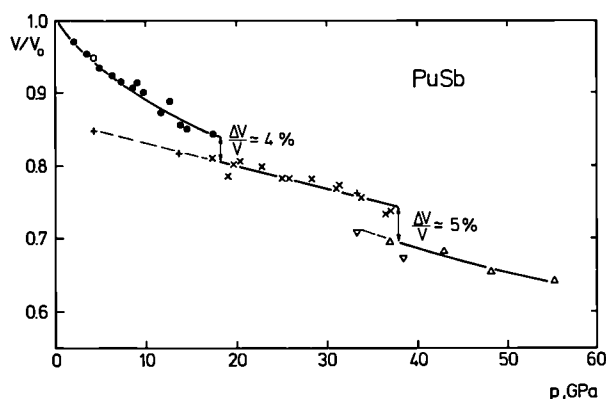


Fig. 8.18 PuSb: Relative volume V/V_0 versus pressure

increas. press.	•	NaCl-type
	x	CsCl-type
	Δ	tetragonal, P4/mmm
decreas. press.	◦	NaCl-type
	+	CsCl-type
	▽	tetragonal, P4/mmm

The high-pressure phase transformation from the NaCl structure (B1) to the CsCl structure (B2) is

well known from studies of the alkali halides [1, 2]. The orientation relationship between the lattices of the B1 and B2 phases has been studied for temperature-induced and pressure-induced transitions [3].

High-pressure structural studies of thorium and uranium NaCl type compounds were performed at HASYLAB-DESY in Hamburg using synchrotron radiation and energy-dispersive powder diffraction [4].

The high-pressure structure of the UX and ThX compounds containing a large anion, i.e. X = As, Sb, Bi, Se and Te, is systematically of the CsCl (B2) type. ThTe and ThBi have this structure already at ambient pressure [5]. The B1-B2 transition of the actinide compounds follows the same general pattern as is known from the alkaline halides. The transformation is sluggish with a strong hysteresis in the compression and decompression curves. In some cases it has been possible to determine structural parameters of the high-pressure phase at ambient pressure.

The unit cell volume as a function of pressure gives information on the bulk modulus and its pressure derivative using an appropriate equation of state. It has been found that a log-log plot of the bulk modulus versus specific volume for the mononictides and the monochalcogenides of uranium and thorium gives a straight line with a slope in the range from -1.6 to -2.

For 10 of these compounds, variation of reflectivity with pressure and with the energy of the incident light was measured. Peaks in the reflection spectrum correspond to resonant electronic processes that are excited in the solid by the incident light. Many of these peaks could be correlated with either the high-pressure or the ambient-pressure phases of the compounds studied, supplying indications on the electronic structures of these phases.

References

- [1] S.N. Vaidya and G.C. Kennedy: *J. Phys. Chem. Solids* **32** (1971) 951
- [2] N. Hamaya and S. Akimoto: *High Temp. - High Pressures* **13** (1981) 347
- [3] B. Okai: *In Solid State Physics under Pressure*, S. Minomura (ed.), p. 177 and references therein. Tokyo: Terra Scientific Publishing Comp. 1985
- [4] J.S. Olsen et al.: *Physica* **144 B** (1986) 56
- [5] U. Benedict: *J. Less-Common Metals* **128** (1987) 7

Collaborations with External Organisations

Germany

Max Planck Institut für Festkörperphysik Stuttgart: Resonant photoelectron spectroscopy and high-pressure reflectivity studies (R.L. Johnson, K. Syassen)

Technische Universität München: Mössbauer and μ SR studies (M. Kalvius, W. Potzel, L. Asch, F. Litterst)

KfK, Karlsruhe, Inst. für Heisse Chemie: Susceptibility and crystal preparation (B. Kanellakopulos)

KfK, Karlsruhe, Inst. für Nukleare Festkörperphysik: Electron spectroscopy (G. Fink)

Freie Universität Berlin: X-ray absorption spectroscopy (G. Kaindl)

KfA Jülich, Inst. für Festkörperforschung: Electrical resistivity under pressure (J. Wittig); Institut für Chemische Technologie: Sample characterization (A. Solomah)

Universität Erlangen: Photoelectron spectroscopy (A. Grassman)

University of Groningen: Resonant photoelectron spectroscopy (J. Ghijsen)

Universität München, Institut für Anorganische Chemie: Single crystal growth and X-ray diffraction (F. Lux, M. Böhme)

Belgium

University of Liège: Single crystal growth, X-ray diffraction, and analysis (J. Goffart, L. Martinot, M.R. Spirlet)

University of Namur: Electron Energy Loss Spectroscopy (P. Thiry, J. Verbist)

Denmark

University of Copenhagen: High pressure X-ray diffraction (J. Staun-Olsen)

Nordita, Copenhagen: Theory (H.L. Skriver)

Risø National Laboratory: Neutron scattering (J. Kjems, B. Lebech)

Technical University Lingby: High-pressure X-ray diffraction (L. Gerward)

France

CEN, Strasbourg: Mössbauer studies, permanent magnet investigations (J. Sanchez)

CEN, Grenoble: Neutron diffraction, magnetic studies, and transport properties (J. Rossat-Mignod, M. Boge, P. Burlet, J.M. Fournier, A. Blaise, M. Wulff, E. Pleska)

ILL, Grenoble: Polarized neutron diffraction and neutron inelastic scattering (P.J. Brown, C. Zeyen)

Inst. Curie, Paris: Mössbauer and high-pressure studies (M. Pagès, A. Tabuteau, S. Dabos-Seignon)

CEN, Saclay: Neutron diffraction (A. Delapalme)

Université Paris VI and LURE, Orsay: High-pressure X-ray absorption (J.P. Itié, A. Fontaine)

Institut de Physique Nucléaire, Orsay: Optical and neutron spectroscopy (P. Delamoye, J.C. Krupa)

CNRS, Grenoble: Crystallography of phase transitions (J.C. Marmeggi)

Netherlands

Philips Eindhoven: Theory (P. Kelly)

University of Amsterdam: Low temperature magnetization and resistivity (J. Franse)

United Kingdom

AERE, Harwell: Low temperature specific heat (R. Hall, M. Mortimer)

University of Birmingham: Preparation of high purity single crystals (D. Fort)

Birkbeck College: neutron and magnetization studies (K. McEwen)

Rutherford-Appleton Laboratory: Neutron spectroscopy (R. Osborn, M. Hagen)

University of Keele: X-ray and neutron scattering (W.G. Stirling, D. Jones)

University of Warwick: X-ray absorption spectroscopy (M.J. Cooper)

Sweden

University of Uppsala: Photoemission and theoretical studies (N. Martensson, B. Johansson, O. Eriksson)

Switzerland

ETH, Zürich: Single crystal growth, magnetic, optical and transport properties (O. Vogt, H. Ott, J. Schoenes, P. Wachter)

Czechoslovakia

University of Prague: Photoelectron Spectroscopy (V. Sechovsky, L. Havela)

USA

Argonne National Laboratory: Neutron scattering (C.K. Loong; L. Morss, S. Kern)

Oak Ridge National Laboratory: Material preparation, high pressure X-ray and optical studies (R.G. Haire, J.R. Peterson)

Los Alamos National Laboratory: Materials preparation and photoemission (B. Cort, J. Ward, L. Cox)

Lawrence Livermore National Laboratory: Surface reactions (C. Colmenares)

University of W. Virginia: Theory (G.J. Hu, B.R. Cooper)

Brookhaven National Laboratory: High-resolution and magnetic X-ray scattering (D. Gibbs, J. Axe, G. Grubel)

9 Fuel Behaviour under Accident Conditions

Introduction

As in previous years, the Institute's activity in the field of reactor safety consisted in support based on the expertise in ultrasonic thermometry, fuel performance modelling and high temperature properties of nuclear fuels. In addition, preparatory work was started for a growing contribution to the Phebus PF project.

Reactor Safety: Study of Fuel Behaviour under Accident Conditions using the TRANSURANUS Code

General Revision of the Fast Breeder Reactor Version of the TRANSURANUS Code

The general revision of the Fast Breeder Reactor version of the TRANSURANUS code [1] has been continued. The revised models, i.e. the models for densification, pore migration, formation and closure of the central void were tested successfully. All changes are continuously documented in the TRANSURANUS-Aenderungsprotokoll [2]. The latest version V1M1J88 was released to the EAC group at JRC Ispra and to KfK-INR.

Contributions to the Development of the European Accident Code (EAC)

Coupling of the code TRANSURANUS with the thermohydraulic model CFEM

The coupling of the TRANSURANUS code with the detailed thermohydraulic model CFEM was

established successfully in cooperation with G. van Goethem, JRC Ispra. The following problems made this coupling an extremely difficult task:

1. A "subcycling technique" (see below) had to be adopted, which means that during one TRANSURANUS time step up to several hundred time steps of the thermohydraulic model CFEM have to be calculated. In mathematical terms this means that the coupling between both codes is weak and stability is therefore not automatically guaranteed. However, by numerous numerical experiments, details of the technique were developed in order to obtain stable results of sufficient accuracy.
2. Both codes have to be applied to the whole core, i.e. for a multi-channel analysis, which of course leads to a very complex data management structure. This problem has been solved and first whole core analyses have been performed successfully. However, after having established the basic algorithms and data structures, a refinement of the techniques is still necessary in order to increase the numerical efficiency.

The coupling algorithm itself is fully described in [3].

Coupling of the code TRANSURANUS with the in-pin fuel motion model CAMDYN

The in-pin fuel motion model CAMDYN (Cavity Material Dynamics) [4] describes the motion of partially and fully molten fuel in the pin of a fast breeder reactor during accident conditions. It is a one-dimensional approach, which treats the molten fuel fission-gas mixture as being compressible and allows variable axial cross sections in a staggered Euler mesh. The mass, energy and momentum equations of both fields are solved explicitly with a finite difference method. The two momentum equations are solved simultaneously.

The partially and fully molten fuel are treated separately. It can move axially into a central hole and reach in certain hollow pellet designs the plenum. Its temperature calculation includes the determination of a radial temperature profile. A simple conduction freezing model is included. At cladding failure, ejection into the coolant channel is modeled where a consistent treatment of the motion in the channel can be performed by the MDYN model.

The CAMDYN model developed at JRC Ispra was coupled successfully to the fuel performance code TRANSURANUS. The latter provides all necessary input data for CAMDYN and receives from it the cavity pressure and the heat flux. These pieces of information are used in TRANSURANUS as the inner boundary conditions for its mechanics and thermal calculations. The difficulties in coupling the models arise from the requirement that during the heat-up phase, where the molten fuel region increases, radial zones have to be decoupled from the TRANSURANUS code whereas during the cooling down phase and the subsequent freezing of the fuel solid fuel regions have to be decoupled from the CAMDYN model. Thus the fuel rod analysis made with the TRANSURANUS code must be based on a time dependent mesh. This problem has been solved and for the first time the coupling between a detailed fluid dynamics model of the cavity and a detailed fuel pin mechanics code has been successfully carried out.

The coupled TRANSURANUS - CAMDYN code system was tested against the CABRI in-pile experiments A1R and A3 and gave good agreement with the experimental data. An example is given in Fig. 9.1. The analyses performed thus far clearly demonstrated the improvements made with this code system to provide more appropriate mechanical loading to the cladding which is the key parameter in all safety considerations concerning the fuel behaviour during a severe accident. It should be noted that the coupling between a detailed fluid dynamics model describing the physical behaviour of molten fuel and a detailed fuel pin mechanics code has been successfully solved for the first time.

Coupling of the code TRANSURANUS with the material motion model MDYN

The Material Dynamics (MDYN) module [7] of the EAC-2 fast reactor accident analysis code simulates the fuel and sodium motion in the

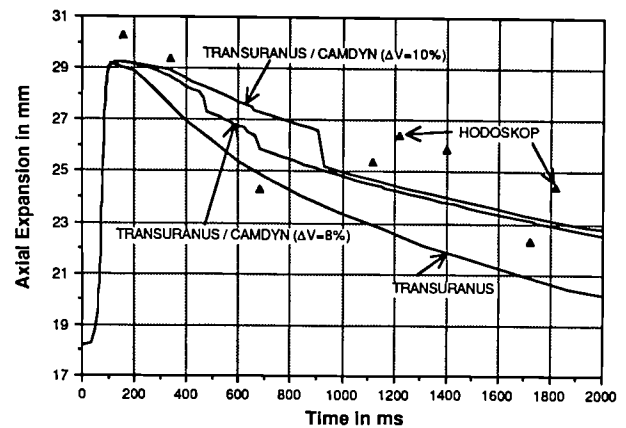


Fig. 9.1 Axial expansion as a function of time in the CABRI-A1R experiment: the results of a stand-alone TRANSURANUS calculation are compared with two calculations of the coupled system TRANSURANUS-CAMDYN. In these two calculations two different numbers for the volume increase during melting $\Delta V = 8$ and 10% were used. The step in the curve using $\Delta V = 10\%$ can be explained by complex axial interaction forces between fuel and cladding which are treated by the TRANSURANUS-URFRIC model [5] and [6].

coolant channels following a local fuel pin rupture. The molten fuel ejection from the pins and the subsequent in-pin fuel motion towards the rupture position is calculated by the CAMDYN model described above. The reactivity effects associated with the in-pin and channel fuel motion as well as the sodium voiding described by the CFEM model (see "Coupling of the Code TRANSURANUS with the Thermo-hydraulic Model CFEM") are of key importance for determining the maximum power level, and thus, pressure that will be reached and the temperature of the core after shutdown has occurred due to fuel dispersal.

The accident progression is strongly influenced by the axial location of the initial pin failure and the subsequent axial pin failure propagation. For the prediction of the failures a good fuel pin behaviour code and an appropriate cladding failure model are necessary. The TRANSURANUS code is therefore being coupled with the MDYN code. Moreover, the Harwell Laboratory, UKAEA, is working under contract

on a mechanistic cladding failure model to be incorporated into the TRANSURANUS code.

The coupling of a detailed fuel motion model such as MDYN with a detailed fuel pin performance code is a novel approach. Since the fluid dynamics model MDYN is based upon an explicit numerical technique, MDYN needs extremely small time steps. It is therefore not possible to couple the codes TRANSURANUS and MDYN directly. Instead, a subcycling technique needs to be established: Within a TRANSURANUS time step, the MDYN model has to be applied up to several thousand times, which of course complicates the coupling considerably. However, in order to achieve a coupling as consistent as possible, the thermal inertia of the fuel pin, and in the case of a single pin experiment that of the surrounding structures have to be taken into account. These effects can be considered as thermal skin effects. Consequently, the subroutine THSKIN which treats these thermal skin effects was developed. Since this subroutine has to be used during the small MDYN time steps, considerable effort was spent in writing an extremely fast calculation. In order to be as flexible as possible, all types of boundary conditions, i.e. Dirichlet and von Neumann conditions, can be applied. The thermal skin subroutine THSKIN was extensively tested in several thousand cases by using a special Monte Carlo technique in which the test cases are generated automatically. This newly developed subroutine is presently being coupled with MDYN through the special adapter program TUMDYN (TRANSURANUS-MDYN) which controls the subcycling algorithm and which takes care of the numerous redefinitions of variables.

Analysis of the pre-transient fuel pin behaviour for the MOL 7C-7 experiment using the TRANSURANUS code

The JRC is supporting the German/Belgian MOL 7C local fault propagation in-pile experiments via a shared cost action. JRC Ispra had agreed to help with the analysis of MOL 7C experiments in order to be more directly involved and also to make up for their limited financial contribution. KfK, who are doing much of the analysis work for the MOL 7C experiments, asked Ispra towards the end of 1987 to perform pre-test fuel behaviour calculations for the forthcoming MOL 7C-7 test using the TRANSURANUS code [1]. This code was developed at JRC Karlsruhe and was used successfully in an older version [8] for the analysis

of other MOL 7C experiments. JRC Karlsruhe agreed to perform these analyses together with JRC Ispra.

The MOL 7C-7 experiment [10] is the seventh in a series of experiments which is now scheduled to take place in mid 1989. It differs from the earlier tests in that it has a wall blockage and uses a small hexcan which is cooled from the outside by a by-pass flow. For this reason only 19 fuel pins can be used, as opposed to the 30 fuel pins of the previous tests. Since MOL7C-7 differs considerably from the earlier tests, major safety margins are required and only a limited burn-up of about 0.3 % is desired. This will be achieved by irradiating the pins for 10-12 days in the BR-2 reactor at Mol. During the pre-transient irradiation, the experiment will be run with a higher mass flow rate than during the transient experiment phase in order to prevent sodium boiling in the blockage. Once the mass flow rate is decreased to the "nominal" value, overheating and melting of the wall blockage will be achieved. The possible molten fuel and pin failure propagation and attack of the hexcan wall are of key interest in this experiment. Because pin failure propagation depends on the state of the fuel pins, these need to be properly characterised.

The main objectives of the precalculations with the TRANSURANUS code are to determine whether, after 10-12 days of irradiation, fuel pin restructuring will be complete. The main considerations are whether a central hole will have formed; how high the central fuel temperatures will be; whether the fuel/cladding gap will be closed at any location and whether the fuel stresses are high enough to lead to significant fuel cracking. The following conclusions are drawn from the analyses performed:

Restructuring

The pin type with the lowest rating is the limiting case and was therefore analysed in detail.

The empirical model of Többe and the best estimate pore migration model predict that the formation of the central void and the restructuring are complete after approximately 1-2 days of full power operation. Both models are in close agreement in predicting the radius of the central void, the radius of the columnar-grain region and the radius of the equiaxed-grain region.

However, the conservative pore migration model predicts that the restructuring of the fuel is not completed, even after 9 days of full power operation. From these results it is evident that for the other pins, which exhibit a higher rating, the best estimate pore migration model predicts a complete restructuring after approximately 1-2 days of full power operation.

The analyses of the lowest rated pin with a 20 % reduction of the linear power are consistent with these statements: according to the model of Többe and the best estimate pore migration model, restructuring is completed. The radius of the central void is of course somewhat smaller than in the case of nominal power. The conservative pore migration model predicts incomplete restructuring.

Temperature

The central fuel temperature Θ_{\max} after restructuring can be approximated by

$$\Theta_{\max} = 775 + 34.2 q', \text{ for } q' > 20 \text{ kW/m}$$

where Θ_{\max} is given in °C.

Gap Size

Gap closure does not occur during the pre-irradiation. Thus, - no strong mechanical interaction between fuel and cladding is anticipated.

Stresses

Cracking of the fuel will occur above approximately 6-8 kW/m. Thus, the fuel will be cracked in all 4 pin types.

Recommendation

Since the different models applied show significant differences a decision concerning the test design should be based upon the conservative pore migration model. This means that a pre-irradiation period of 6 to 9 days at 100 % nominal power should be envisaged.

Examples of these analyses are given in Fig. 9.2 a-c; the detailed results can be found in [11].

References

- [1] K. Lassmann, H. Blank, 'Modelling of Fuel Rod Behaviour and Recent Advances of the TRANSURANUS Code', Nucl. Eng. Design **106** (1988) 291
- [2] K. Lassmann, 'TRANSURANUS Aenderungsprotokoll, Version 1, Modifikation 1, Jahr 1988 ("V1M1J88")', Technical Note K0287109 (December 1988)
- [3] G. van Goethem, K. Lassmann, 'The Coupling Algorithm between Fuel Pin and Coolant Channel in the European Accident Code EAC-2', Nucl. Eng. Design, accepted paper
- [4] G. Peter, CAMDYN: 'Ein neues Brennstoffbewegungsmodell im Brennstoff', PhD-Thesis, Technische Hochschule Darmstadt, to be submitted
- [5] K. Lassmann, 'Assessment of the Axial Friction Force Model URFRIC', TUAR 87 (1988), EUR 11783 EN
- [6] K. Lassmann, 'Treatment of Axial Friction Forces in the TRANSURANUS Code'
 - a. 9th International Conference on Structural Mechanics in Reactor Technology, Lausanne (1987), Post-Conference No. 9 : 6th International Seminar on Mathematical/Mechanical Modeling of Reactor Fuel Elements, Kippel, Switzerland, August 24-25 (1987)
 - b. Nucl. Eng. Design, accepted paper
- [7] J. Devos, H. Nguyen, H.U. Wider, 'Sensitivity of Fuel Relocation due to the Use of Different Flow Regimes in the MDYN Module of the European Accident Code - 2', Proceedings of Liquid Metal Boiling Working Group Meeting (1988) Winfrith, UK
- [8] K. Lassmann, 'URANUS- A Computer Programme for the Thermal and Mechanical Analysis of the Fuel Rods in a Nuclear Reactor', Nucl. Eng. Design **45** (1978) 325
- [9] T. Preusser, K. Lassmann, G. Boecking, 'Ein Kuehlmittel-Blockade modell fuer eine quasi-zweidimensionale Brennstabbeschreibung', Jahrestagung Kerntechnik 1982, Deutsches Atomforum e.V. KTG, Mannheim, Tagungsbericht, 473
- [10] W. Kramer et al., 'Investigation of Local Cooling Disturbances in an In-Pile Sodium Loop in the BR2', Nuclear Technology **46** (1979) 281
- [11] K. Lassmann, G. van Goethem, 'MOL7C/7 Pre-Test Fuel Pin Behaviour Calculations Using the TRANSURANUS code', Technical Note K0288113 (December 1988)

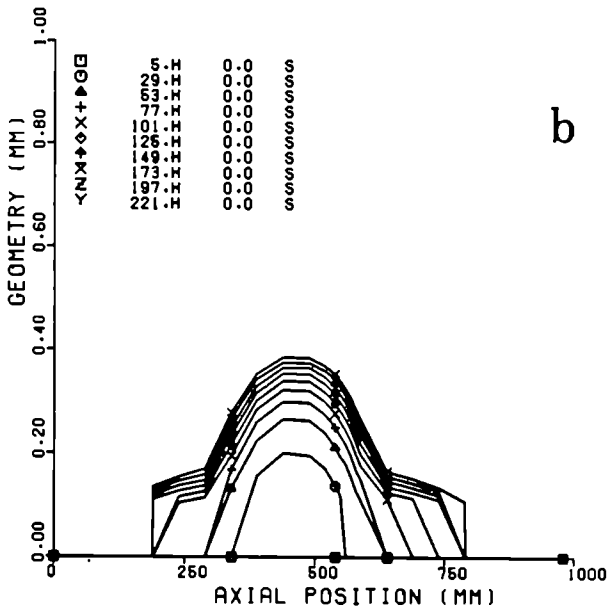
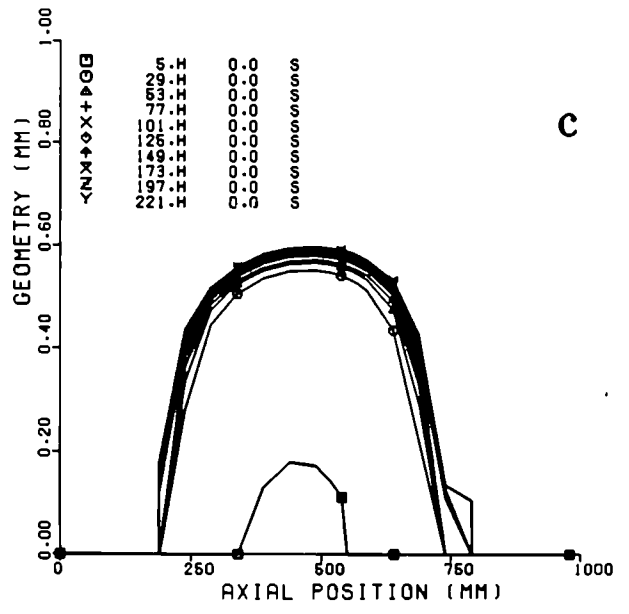
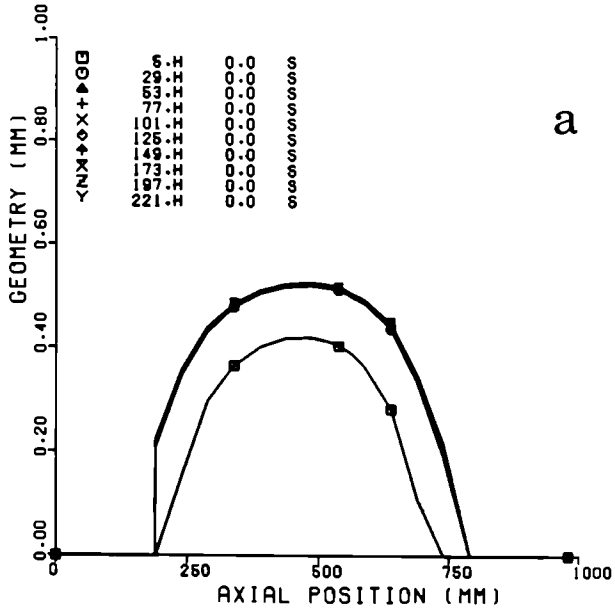


Fig. 9.2 Axial variation of the central void as a function of time for pin 1: a) densification model according to Többe, b) best estimate pore migration model and c) conservative pore migration model. None of these models has been validated in short irradiation tests lasting only a few days.

Ultrasonic Thermometry

Experiment Scarabee BF3

BF3 was the third experiment of the series Bain Fondu (= molten pool), in the Scarabee reactor in Cadarache, aiming at the study of severe core degradation. BF3 ended intentionally as a boiling pool rather than just a molten pool. The goal of the experiment was the study of steel relocation in a boiling bed, as well as of the attack of steel structures at the bottom of a reactor vessel by molten UO_2 at 3000°C .

The rig is shown schematically in Fig.9.3 It contained 6 kg UO_2 , 43.2% enriched in ^{235}U , contained in 35 steel clad fuel pins, arranged in a heavy walled nickel crucible that was externally cooled by rapidly circulating sodium at 245°C .

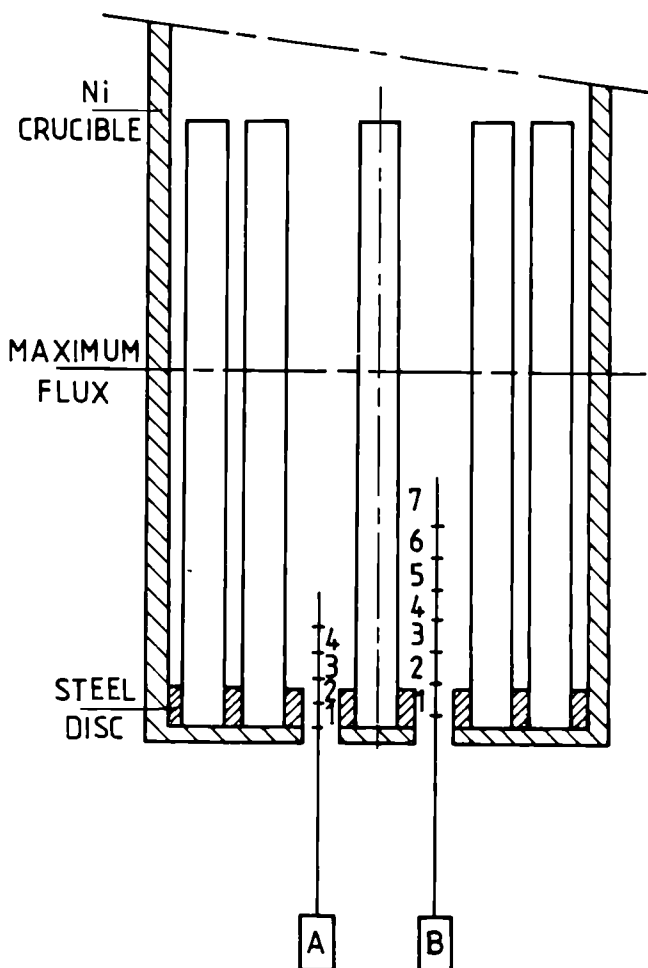


Fig. 9.3 Schematic representation of Scarabee BF3.

The assembly contained 2 kg steel, present as pin claddings and as a 10 mm thick steel disc on the bottom of the crucible. There was no sodium inside the crucible. The rig was placed at the level of maximum flux. Two ultrasonic thermometers (UT's) A and B were installed, protruding through the bottom of the crucible, with 4 and 7 measuring sections, respectively. The UT's were protected by ThO_2 sheaths, ThO_2 being the only material that is compatible both with molten steel and with temperatures above 2500°C .

The actual experiment lasted only 10 minutes. The reactor power was raised to 42 MW over 5 minutes, held at that level for 80 s, increased to 47 MW corresponding to a power rating of 70 W/g, kept at that level for another 80 s, raised to 60 MW = 90 W/g, kept at that level for another 80 s, and then reduced to zero.

Temperature Measurement

ThO_2 is a very fragile material, that cracks easily under mechanical or thermal stress. The choice of ThO_2 sheaths, imposed for reasons of compatibility, meant a risk that was taken in full awareness.

Both UT's performed correctly through the first 260 s of the experiment. They did not quite reach the first power plateau at 42 MW, but failed simultaneously when section B7 had indicated 1880°C , $A4 = 1700^\circ\text{C}$, $B1 = 1360^\circ\text{C}$. After failure the electrical characteristics of the UT coils were normal (ie neither shorting nor open circuit), whereas both echo pictures indicated a mechanical coupling of the sensor wire to a large mass at a level around the bottom of the crucible. The failure occurred when steel melting had penetrated to the bottom plate and the fuel pin arrangement had supposedly collapsed. It looks probable that the UT sheaths were snapped off laterally by an asymmetry in the collapse.

The UT performance was not as outstanding as in the preceding experiment Scarabee BF1 (TUSR 39, 1985, p.27-29). In view of the much severer operating conditions however, it could be judged a success.

10 Characterisation of Nuclear Waste Forms

Radioactive Waste Management and the Fuel Cycle

Radiochemical Separations - Verification of the OXAL-MAW Process

A) The removal of actinides by precipitation with oxalic acid

The verification tests of the OXAL process, [1,2], on genuine intermediate level liquid waste (ILLW) have been finished, [3]. The results showed that it is possible, by optimizing the conditions of the precipitation, to remove the actinides from ILLW to such an extent that the resulting solidified waste can be classified as "alpha free". The details of the experiments have been given in the previous Annual Reports (see e.g. TUAR 87, 200).

In the study on a solution simulating ILLW the following 5 parameters were considered for the oxalate precipitation:

- 1) Element used as carrier (Ba, Ca, Ce and Ni),
- 2) Amount of carrier added (carrier-to-actinide ratios between 8:1 and 400:1),
- 3) pH at the precipitation (0.6, 1.0, and 2.0),
- 4) Temperature of the waste solution (20 °C and 5 °C), and
- 5) Time for digestion of the precipitate (30, 60 and 90 minutes).

The verification experiments on real waste solutions were carried out on a batch scale of 2 litres in a hot cell under precipitation conditions selected according to the results from the simulates. Gamma spectra of the actinide elements and of the fission products were recorded on the feed and on the resulting filtrate, see the Figs. 10.1 and 10.2.

The results for the decontamination factors (DF-values) were treated in an Analysis of Variance, (ANOVA), in a hierarchic classification, giving main effects of the above mentioned parameters and their possible interactions.

From the experiments the following conclusions can be drawn:

- The adjustment of pH with NaOH works satisfactorily, so that a need for a denitration step preceding the oxalate precipitation is not evident. However, it might be of interest to denitrate the solution for other reasons (e.g. salt load).
- Decontamination factors higher than 5000 could be obtained for americium with Ca as carrier; lower DF-values, around 50-80 in the best cases, were consistently found for plutonium. Fig. 10.3 presents as an example the results of the ANOVA on the data for americium with Ca as carrier.
- The carrier Ca gives high DF-factors both for americium and plutonium; with Ba only americium is removed to a high degree, Ce carries plutonium quite well, whereas Ni is inferior as carrier.
- The main effect of "amount of carrier" is highly significant; only the high amounts of carrier provide sufficiently high decontamination factors.
- The pH has an important influence on the DF-value for plutonium in the range of pH 0.6-2.0. The optimum pH is different for the different carriers; plutonium and americium do not respond in the same way to changes in pH, see also Fig. 10.3 for pH related data on americium.
- There seems to be no advantage in a delayed filtration, i.e., after a digestion time (post-precipitation); for americium oxalate a fast phase separation is even beneficial.

FILENAME: W510.DAT
 TIME OF MEAS.: 70000. T.U.I KARLSRUHE
 FILENAME: W511.DAT
 TIME OF MEAS.: 71600. T.U.I KARLSRUHE

DATE OF MEAS.: 10/02/88 12:00
 DATE OF MEAS.: 10/02/88 12:00

RESOLUTION: 8192 SORT FULL-SCALE: 907043.
 PROJECT: REPRO
 RESOLUTION: 8192 SORT FULL-SCALE: 39855.0
 PROJECT: REPRO

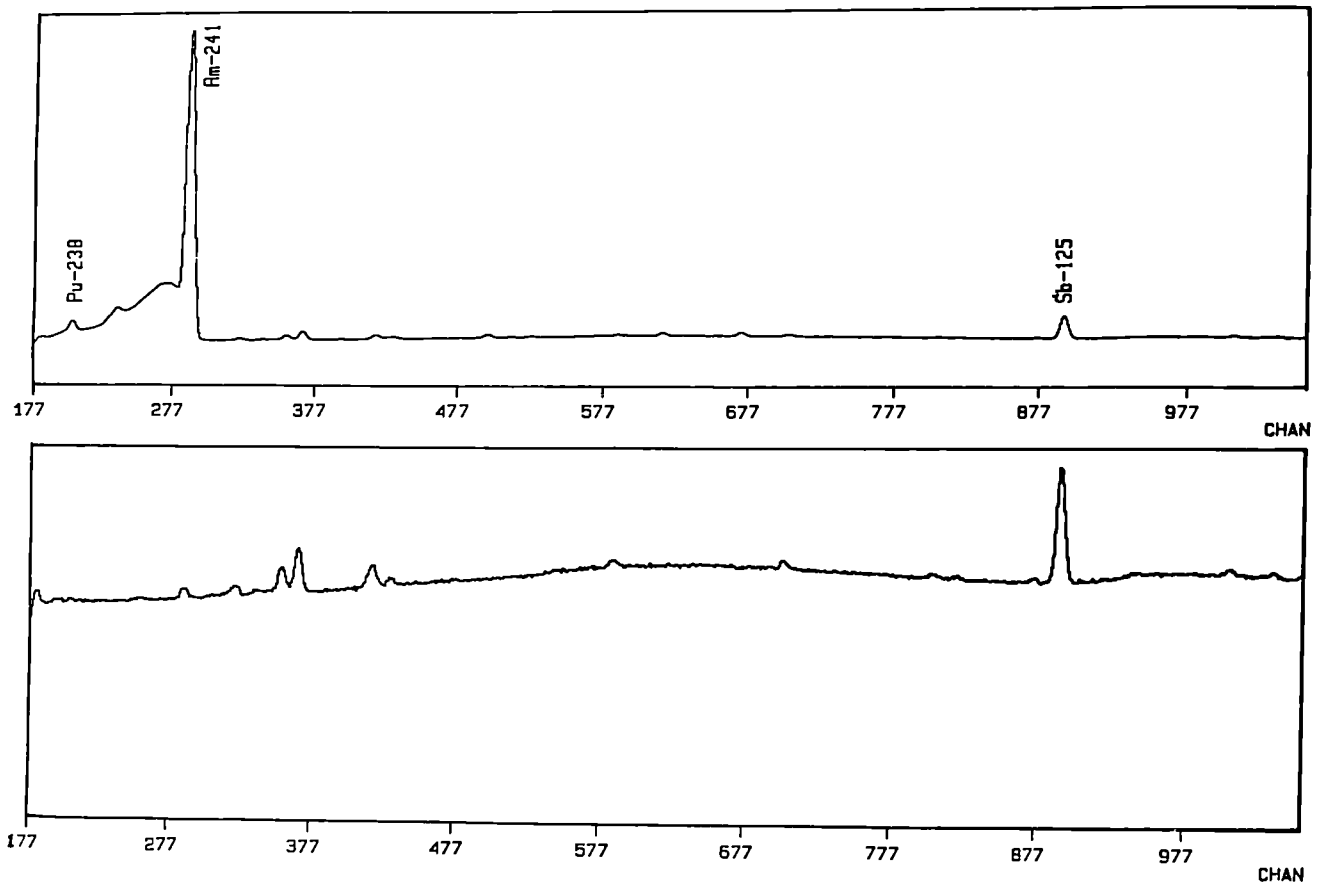


Fig. 10.1 Gamma spectra of feed (top) and filtrate (bottom) in the low energy region showing peaks of plutonium and americium. The ordinate scale of the bottom spectrum has been expanded about 20 times compared to the top spectrum (extensive decontamination).

- The verification of the process with real waste solutions showed DF-values similar to or somewhat lower than those obtained with the simulating solutions, when Ca was used as carrier. Thus, by a careful control of the precipitation conditions, an alpha free final product can be obtained, when the resulting filtrate is solidified, e.g. in a cement matrix.

The results on compressive strength showed no significant difference between the behaviour of cemented simulated ILLW with added oxalic acid and without oxalic acid; both products had lower compressive strength (about 9.3 ± 0.3 MPa) than specimens prepared without simulated waste (about 12.5 ± 0.4 MPa); this fact can be assigned to the effects of the salt content of the waste. These experiments will be repeated under other testing conditions in order to arrive at a certain test optimization.

B) Characterization of the solidified product

The cemented product as produced after OXAL is under investigation; (see also previous report TUAR 87, 201). The main parameters studied are the compressive strength of the cement blocks, the porosity, and the leaching properties. The influence of the excess oxalic on the quality of the product is also being evaluated. Non-active as well as active ILLW-cement specimens are being considered.

The cemented products have been subjected to leaching in demineralized water for up to 24 weeks. In the leachants the elements Al, Si and Ca have been analyzed by spectrophotometry, the

FILENAME: W510.DAT
 TIME OF MEAS.: 70000. T.U.I KARLSRUHE
 FILENAME: W511.DAT
 TIME OF MEAS.: 71600. T.U.I KARLSRUHE

DATE OF MEAS.: 10/02/88 12:00
 DATE OF MEAS.: 10/02/88 12:00

RESOLUTION: 8192 SQRT FULL-SCALE: 307045.
 PROJECT: REPRO
 RESOLUTION: 8192 SQRT FULL-SCALE: 370848.
 PROJECT: REPRO

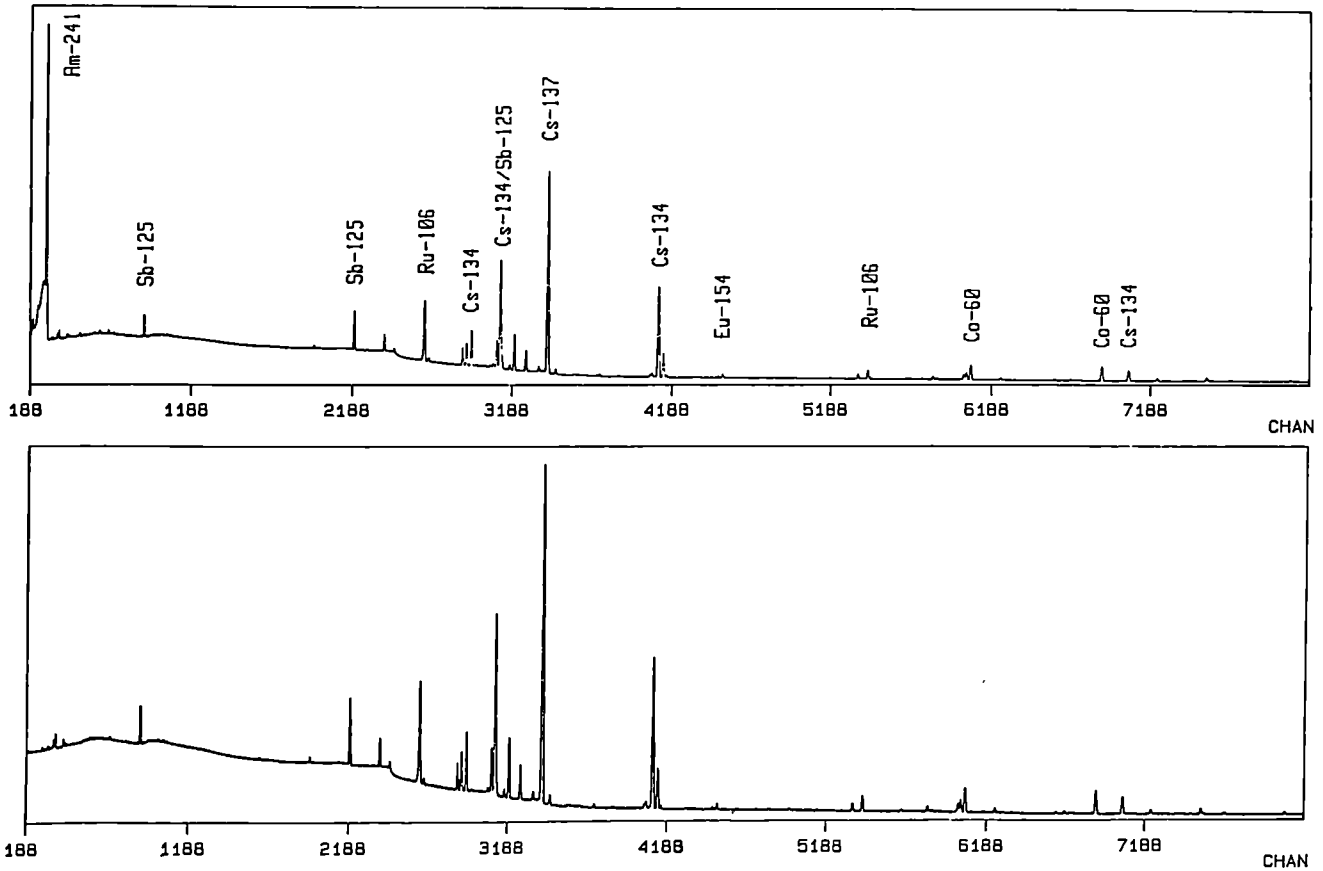


Fig. 10.2 Gamma spectra of feed (top) and filtrate (bottom) in the higher energy region, showing peaks of the principal fission products. The ordinate scale of the bottom spectrum has been expanded about 2.5 times compared to the top spectrum.

pH increases very fast to values above 12. In the case of some specimens 5 % microsilica (SiO_2 particles with a particle size of $0.12 \mu\text{m}$) have been added as an emulsion during the preparation of the cement mixture. This addition is claimed to have a positive influence on the resistance of the cement, in that the pores are being closed to a certain extent. The leaching behaviour is presented in Fig. 10.4, which shows the fraction of calcium leached as function of time; the data are relative to the initial amounts of calcium present. The three lower curves in the diagramme represent the specimens to which microsilica (MS) have been added, the leached amounts of calcium are indeed diminished compared to the specimens without microsilica. Further, it is of interest to note that the samples containing no ILLW, but only water, are being leached somewhat faster than the salt loaded ones; again the influence of oxalic acid (ox) is marginal.

Certain analytical problems with the determination of Si (polymerization and precipitation in the leachant) still have to be overcome.

The above mentioned tests on simulated waste are to be complemented with tests on active samples; these are planned to start in April 1989.

References

- [1] F. Mousty, P. Barbero, G. Tanet, EUR 7975, 1982
- [2] H. Dworschak, B.A. Hunt, F. Mannone, F. Mousty, Transactions p 91, ENC-3 Conference, Brussels, April 1982
- [3] H. Bokelund, M. Ougier, M. Lebrun, International Symposium on Low and Intermediate Level Radioactive Wastes, IAEA-SM-303, Stockholm, May 1988

European Community- Repository System Simulation Test

Introduction

Our Institute has taken part in a Round Robin exercise on the measurement of concentration of matrix constituents and radionuclides released from nuclear waste forms under simulated geologic conditions. This test was organized by the Directorate Science, Research and Development of the Commission of the European Communities (DGXII/D-I) with the participation of a dozen of laboratories in the Community, Switzerland, United States, Canada and Japan. The test duration was one year and the compiled, and critically assessed results will appear as a EUR report.

The most important objective of the Round Robin exercise was to evaluate the relative performances of glass SON68 (or R7T7) (composition shown in Tab. 10.1) in a simulated salt, clay and

granite repository environment. Details of the standardized test procedure provided to all participants can be found elsewhere [1]. We carried out our studies for the salt and granite media. In addition to the compulsory part of the test, i.e. analysis for Si, Mo, B, and Li and pH measurement, a series of additional tests was carried out.

- a) Analyses for Sr, Al, Zn, Fe, Zr, Nd, Eu, Ce and U
- b) Measurement of Eh
- c) Analyses for anions by ion chromatography
- d) Determination of the weight loss of glass coupons
- e) Surface analysis of the glass coupons by Rutherford backscattering (RBS), scanning electron microscopy (SEM) and electron microprobe analysis (EMPA)

The test temperature was 90 °C and the test durations were 14, 28, 56, 91, 182 and 364 days.

Tab 10.1 Composition of the SON68 glass (wt.%)

OXIDE	SON68
SiO ₂	45.5
B ₂ O ₃	14.0
Na ₂ O	9.9
Li ₂ O	2.0
Al ₂ O ₃	4.9
CaO	4.0
ZnO	2.5
Fe ₂ O ₃	2.9
Cr ₂ O ₃	0.5
NiO	0.4
ZrO ₂ (in frit)	1.0
P ₂ O ₅	0.3
Fission Product	
Oxides	11.3
Actinide oxides	0.8
	100.0

Experimental

A scheme of the reaction procedure is given in Fig.10.5 and Fig. 10.6 shows the reaction vessel used for the leaching tests.

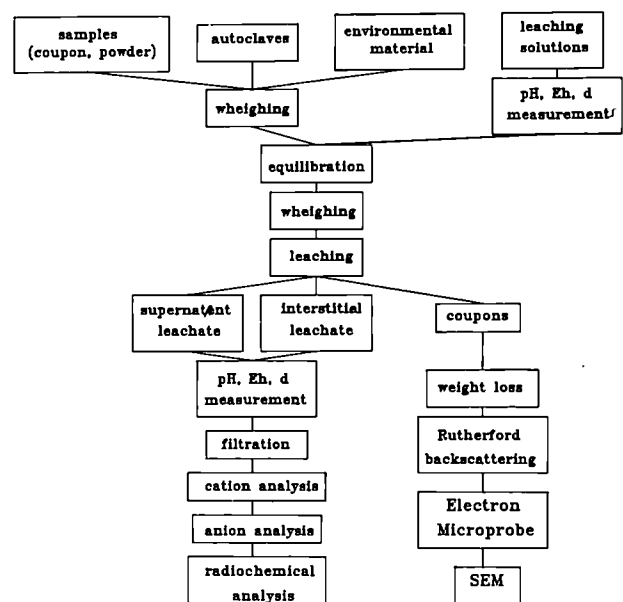


Fig. 10.5 Reaction scheme

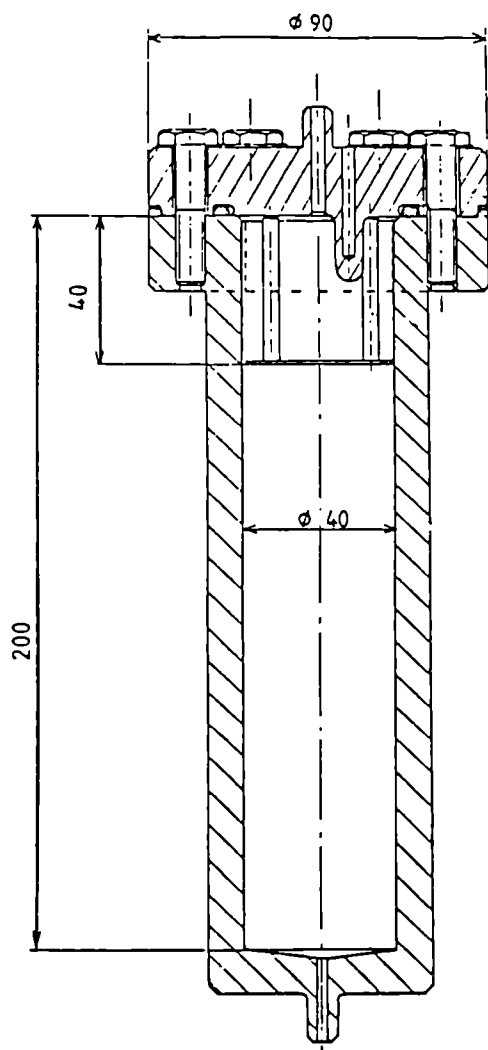


Fig. 10.6 Reaction vessel

The autoclaves are filled with solid host rock material (a mixture of NaCl and $\text{CaSO}_4 \cdot 2\text{H}_2\text{O}$ in one case and a mixture of granite, sand and smectite in the other case) to 4/5 of their volume and for the rest with the corresponding leachant.

After equilibration, the autoclaves are opened and the glass powder (2g), contained in a small nylon (granite) or teflon (salt) bag, is put on the sample holder together with glass coupons.

Finally the containers are returned to the oven for the respective test duration.

Equipment

An overview of the equipment is given in Fig. 10.7. The heating device is an oven and the temperature is controlled by a thermocouple in the well provided in the lid of one of the autoclaves. The filling and emptying of the containers is carried out in a glove box under nitrogen atmosphere (oxygen content at the inlet < 5ppm). They are introduced through a lock.

Analysis

The containers are weighed, opened and the supernatant solution pipetted into nalgene flasks. After pH, Eh and temperature measurements the solution is submitted for cation analysis.

In the case of granite, the host rock materials are then filtered through 0.45 μm filters and washed with a volume of bidistilled water equivalent to the volume of the leachate. This interstitial solution is treated as described above. In the case of salt the host rock material is dissolved in 1 litre of distilled water and submitted to analysis, except for the 28d test, where the procedure was the same as for granite. The cation analysis is carried out by ICP spectrometry and anion analysis by ion chromatography. A radiochemical analysis of U is done by neutron activation with a ^{252}Cf source and measuring the 75 keV line of ^{239}U .

The glass coupons are rinsed with distilled water, the weight losses are determined and the samples prepared for surface analysis.

For RBS analysis the coupons have to be enveloped in a thin Al foil, leaving a hole of 3 mm for the He-beam. EMPA allows secondary electron microscopy and X-ray analysis of solid surfaces to be made. The glass coupons leached and rinsed are cut, embedded in araldite and the cut surface is polished. The sample is covered by a thin layer of Al. An electron beam (up to 50 keV and 1 μA) is focused (500 \AA - 1 μm) on the surface of the bulk glass. By moving the sample it is possible to make a scan through the glass layer.

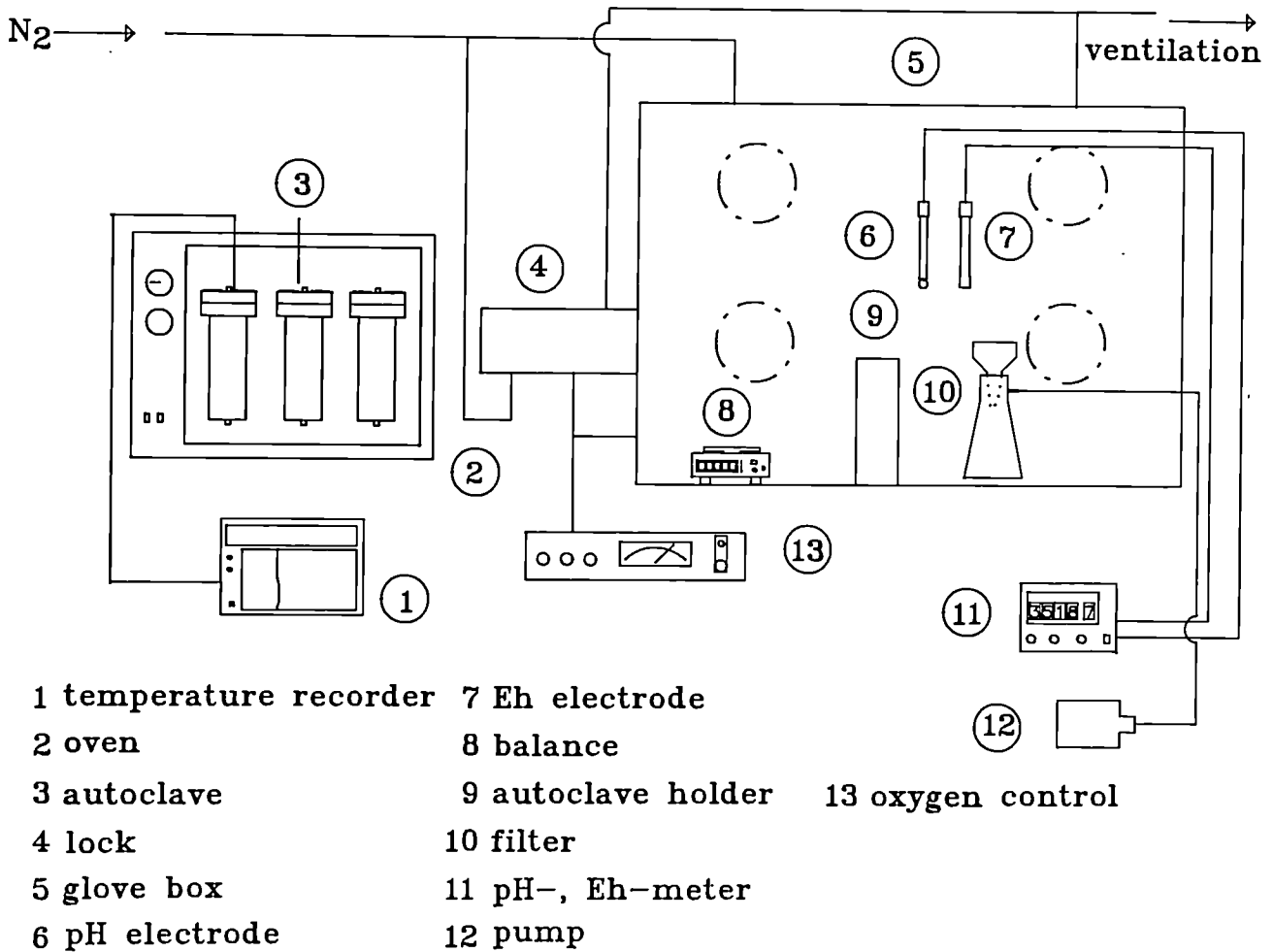


Fig. 10.7 Equipment

Results

pH, Eh and temperature measurement

The density is slightly increased in the supernatant solutions.

The pH increases during the reaction and is higher in the interstitial solution than in the supernatant solution. The Eh decreases during the reaction by about 100 mV to 250 mV, except for the interstitial solution of granite, where a decrease after 14 d is followed by an increase with test duration above the initial value.

All changes are similar for blank and test values.

Compulsory elements

Fig. 10.8 shows the concentrations of the compulsory elements as a function of test duration. The values for the interstitial solutions have been corrected for the dilution factor (see analysis procedure).

The agreement between the test and the replication test values are quite good.

The most significant changes are observed for B. For salt an equilibrium between the supernatant and the interstitial solution is reached, but not in the case of granite.

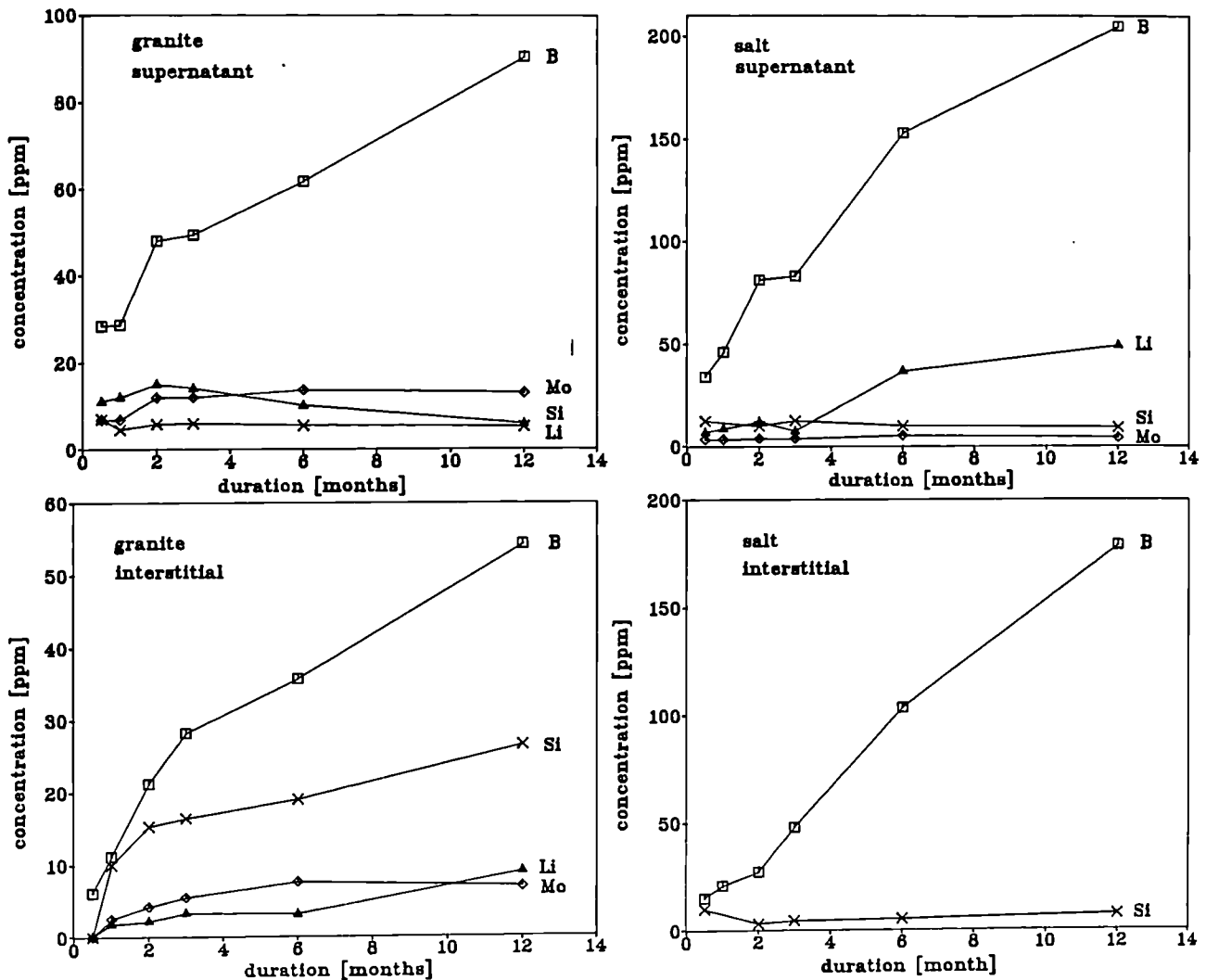


Fig. 10.8 Concentrations of the compulsory elements as a function of test duration

Optional elements

Test concentrations higher than the blank values can only be observed for Zr and Nd in the case of granite and for Zn, Mn and Sr in the case of salt.

Normalised elemental mass loss values have been calculated, assuming a surface area of $110 \mu\text{m}^2$ for spherical glass particles of $187.5 \mu\text{m}$ in diameter.

A graphical presentation of the most important elements is shown in Fig. 10.9. In brine the values are higher except for Mo. For both geological formations the following order of the normalised mass loss is observed

$$B > Li > Si$$

Weight loss of the coupons

The weight loss values of glass coupons are given in Tab. 10.2. The weight losses of coupons leached in granite water are higher than those of coupons leached in a salt environment. On the other hand normalised elemental mass loss values calculated from leachate concentrations for the main constituents of the glass are higher in the brine solution (Tab. 10.3)

RBS-spectra of glass coupons

Rutherford backscattering of 2 - 3 MeV He ions can be used to investigate changes occurring on the glass surface upon leaching. For short leaching periods up to a few days, well separated

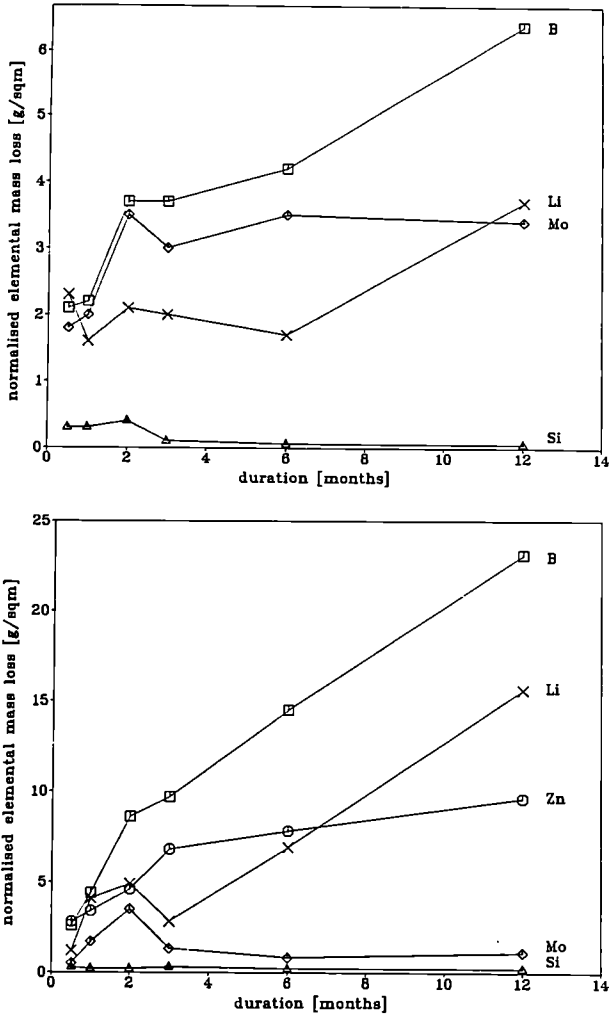


Fig. 10.9 Normalised elemental mass loss values as a function of test duration

peaks are obtained, but the mass resolution of RBS is not good enough to differentiate between the large number of light and heavy fission products present in such a complex matrix as HLW glass. For longer leaching periods leading to thicker layers, the peaks overlap.

Fig. 10.10 shows the RBS-spectra obtained after leaching of glass coupons in brine solution and in volvic water after 28 d of leaching in comparison to an unleached specimen.

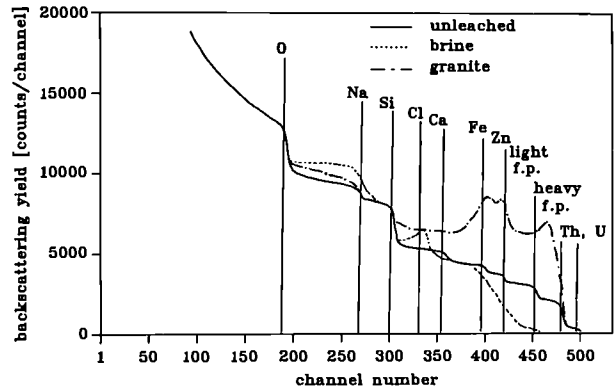


Fig. 10.10 RBS-spectra of glass coupons leached in brine solution and volvic water

For the coupon leached in brine solution a thin NaCl layer has "buried" the other elements. The spectrum of the coupon leached in volvic water shows an enrichment of Fe, Zn, light and heavy fission products on the surface. No Th or U enrichment is observed.

Tab. 10.2 Weight loss values of glass coupons at different test durations

Host rock		granite		salt	
Duration [d]		initial weight [g]	weight loss [g]	initial weight [g]	weight loss [g]
14	test	-	-	4.584	0.002
28	test	4.604	0.006	4.555	0.003
28	repl.	5.606	0.004	5.200	0.004
56	test	5.337	0.009	-	-
182	test	4.879	0.026	5.098	0.010
364	test	5.000	0.035	5.176	0.023
364	repl.	5.663	0.042	5.326	0.014

Tab. 10.3 Normalised elemental mass losses of the compulsory elements (g/m^2) after 1 year

Host rock	granite		salt	
	test	repl.	test	repl.
Si	0.061	0.051	0.247	0.233
B	6.327	6.532	23.085	23.343
Li	3.284	3.981	17.682	13.623
Mo	3.828	2.808	1.228	1.057

SEM Pictures

The scanning electron microscopy picture of a coupon leached 364 days in granite water is shown in Fig. 10.11. The bulk glass is covered by a two gel layers. A small crack between the bulk and the inner layer might be due to the sample preparation procedure. Furthermore an increasing porosity towards the outer surface can be observed. The SEM pictures of glass leached in brine are very similar.

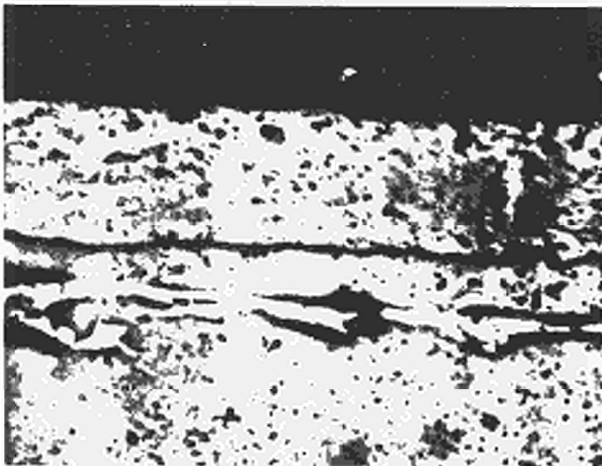


Fig. 10.11 SEM picture of the surface layer on a coupon leached for 1 year in a granite medium (magnification 1200x)

EMPA Spectra

Microprobe analysis was used to make elemental scans through the double layer. Fig. 10.12 shows the spectra of the compulsory elements (Si, B, and Mo) and of Na as another major constituent of the glass.

The spectra confirm the above mentioned observation of a double layer for both leaching media. B and Mo are strongly depleted in the outer layer, Si shows only a slight decrease compared to the bulk glass with maxima in the inner layer and on the outer surface for granite leaching.

Tab. 10.4 shows the behavior of other elements. The main differences between salt and granite are observed for U (in the first case enriched in the second depleted in the outer layer) and for Ca (strongly depleted in salt and enriched in granite).

After 182 d only a single layer is observed on the glass. The thickness of the layer is 16 μm compared to 29 μm after 364 days (9 μm for the inner and 20 μm for the outer layer). The coupon leached in salt has a layer thickness of 26 μm (7 μm for the inner and 19 μm for the outer layer).

Anions

The anion analysis of brine solution is very difficult because of a large excess of NaCl. The large differences of SO_4^{2-} and F^- concentrations for different test durations might be due to varying impurity contents in the salt used as host rock material.

For granite the anion concentrations are much lower, but similar to salt no significant influence of test duration and no difference between the blank and the tests values can be observed.

Conclusions

No major problems occurred during the leaching test except for
- recrystallisation of salt during filtration

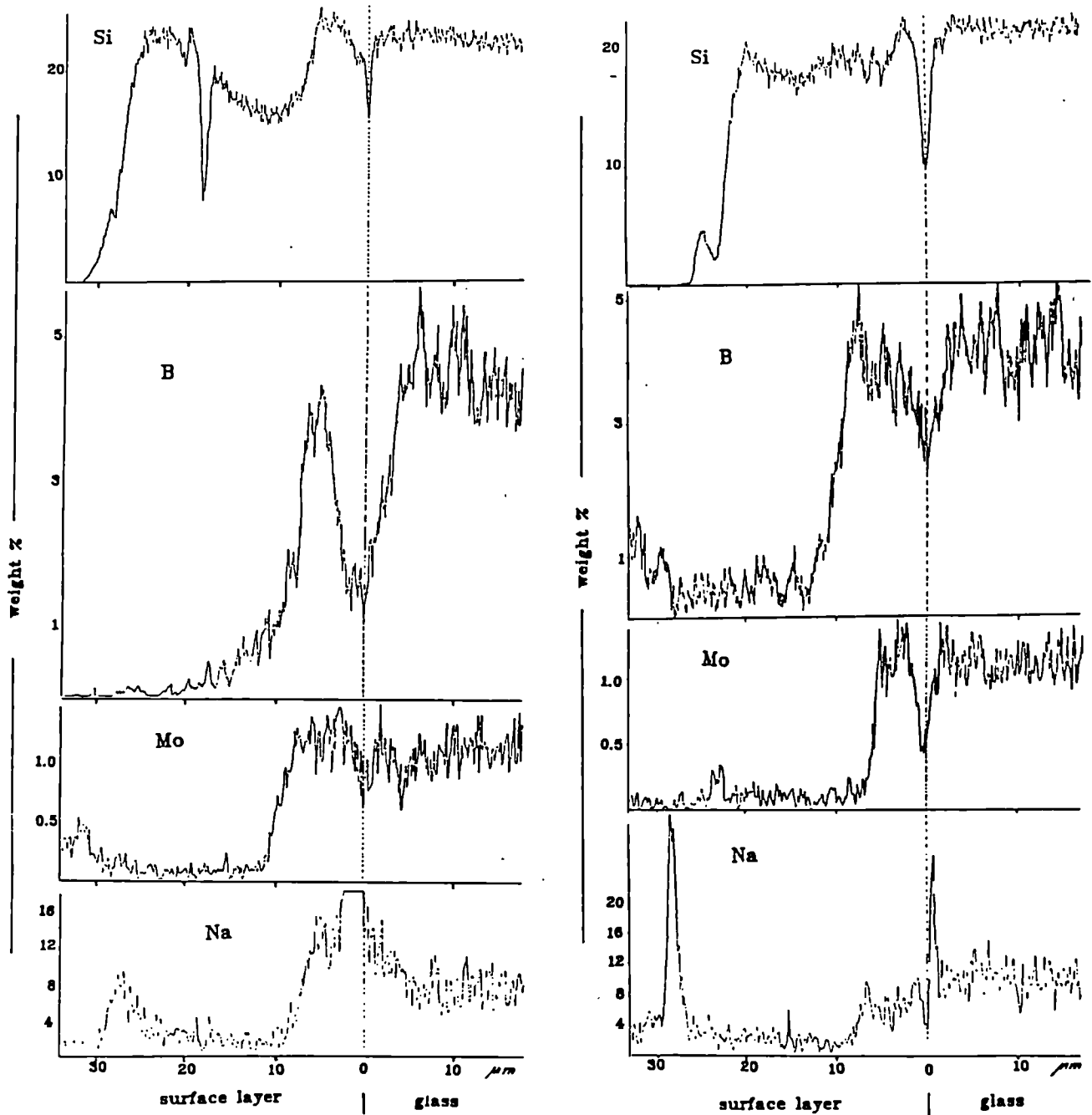


Fig. 10.12 EMPA spectra showing Si, B, Mo and Na distribution in the surface layers and in the bulk glass (right: salt left: granite)

Tab. 10.4 Concentrations of glass constituents in leached glass layers (1 year test duration)

Host rock Element	salt		granite	
	inner layer	outer layer	inner layer	outer layer
Cs	0	-	0	-
Sr	0	-	0	-
Ce	0	- p	-	0 p
Th	0	+	0	+
U	0	+	0	-
Zn	-	--	-	--
Ca	-	--	0	+
Zr	0	+	0	++
Fe	0	++	0	++

0 : unchanged p : peak at the surface
 - : slightly depleted + : slightly enriched
 -- : strongly depleted ++ : strongly enriched

- slight temperature fluctuations ($< \pm 2^\circ$ between day and night)
- corrosion of some autoclaves leading to iron hydroxide precipitation in a few cases.

The compulsory elements have the following decreasing order of leaching (normalised elemental mass loss)



Leaching is higher in the salt medium than in granite, especially at the beginning. Among the optional elements (Na has not been determined) only a few show a significant leaching (e.g., Zn in salt).

RBS shows an enrichment of fission products but not of U in the surface layer.

Surface analysis by EMPA of glass coupons leached in brine and granite water shows a double gel layer after 1 year of leaching. The composition of the inner layer is only slightly changed compared to the bulk glass composition. The outer layer is enriched in Zr, Fe, Ce and Th and depleted in Mo, B, Cs, Sr and Zn. Na and Si show an irregular profile in this layer.

The main differences between samples leached in salt and samples leached in granite are observed for Ca (enriched in granite and depleted in salt) and U (enriched in salt and depleted in granite).

These results confirm fairly well the values for normalised elemental mass losses, but they are in contradiction to the weight loss values. This is probably due to the fact that the corrosion of the glass powder was inhibited.

In a final report results from all the laboratories participating in the test will be compared and evaluated.

References

- [1] EC Test procedure for the 'Repository System Simulation Test', edited by HMI, Berlin, August 1987
- [2] Chu W.K., J.W. Mayer, M. Nicolet Backscattering spectrometry, Academic Press, New York 1969
- [3] Matzke Hj., Fresenius Z. Anal. Chemie (1984), 319, 801

Radiation Damage Studies

Cm-Containing Glass

The work with French, German and US waste glasses doped with ^{244}Cm has been largely terminated. Saturation damage was achieved with many glass specimens. The highest damage level was 18×10^{24} α -decays/ m^3 . The main results reported in TUAR-88 were confirmed: Damage due to α -decay produced

- very small density changes $\leq 0.5\%$; both swelling and densification were observed, possibly due to slight differences in the fabrication procedure;
- no important change in leach rates;
- very significant increases in fracture toughness, as evidenced by largely decreased crack probabilities and crack lengths in Vickers indentations.

This latter effect is positive for the application of waste glasses, since for a given thermal or mechanical shock smaller cracks than in the as produced glass, or no cracks, will be formed in a damaged glass.

Figs. 10.13 - 10.16 show typical results, as function of α -dose, for volume changes, leaching, hardness and fracture behaviour. The three glasses tested, i.e. GP 98/12, SON 681817 L1C2A2Z1 and MCC 76-68 showed a very similar behaviour, with leach rates being highest in the US glass MCC 76-68, as is obvious from α -spectra of leached glasses (150°C , 2 weeks, distilled water).

A final report on this activity will soon be available, giving both more experimental results and a thorough interpretation.

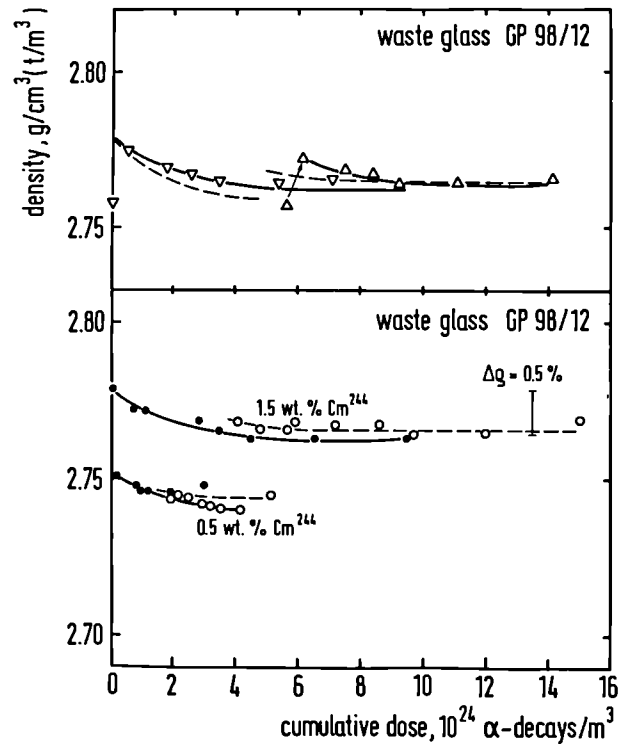


Fig. 10.13 Density changes of the waste glass GP 98/12 containing 0.5 or 1.5 wt. % ^{244}Cm as a function of the α -dose. Similar results (very small volume and density changes) were obtained for the SON and the MCC glasses.

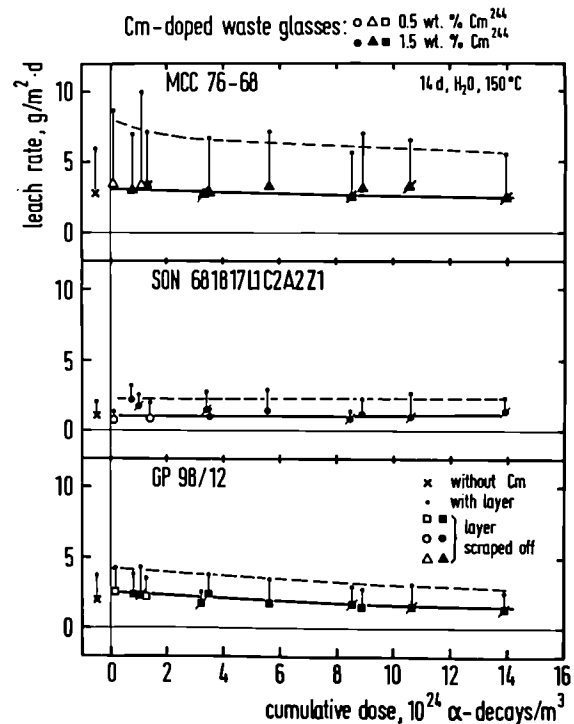


Fig. 10.14 Leach rate (150°C , H_2O) for the three Cm-doped waste glasses as a function of the α -dose.

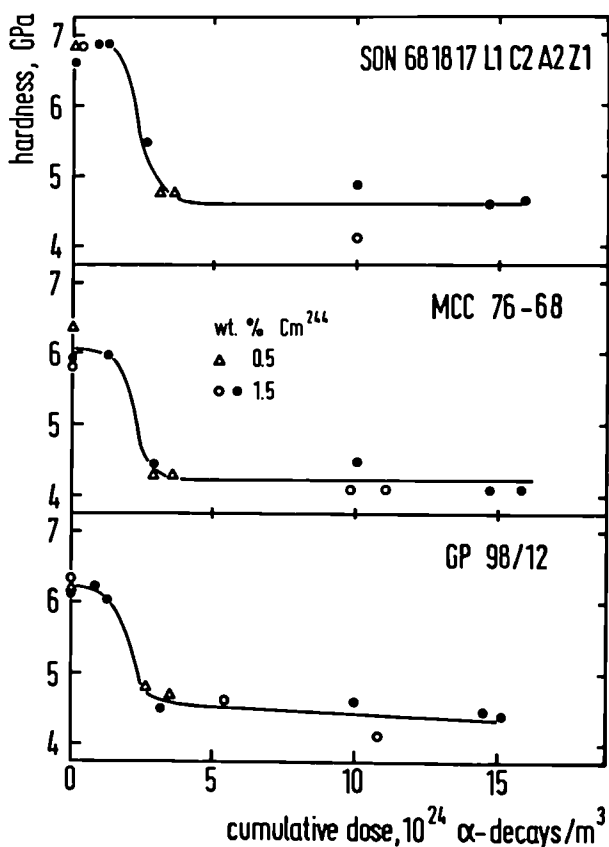


Fig. 10.15 Changes in hardness for the three Cm-doped waste glasses as a function of the α -dose.

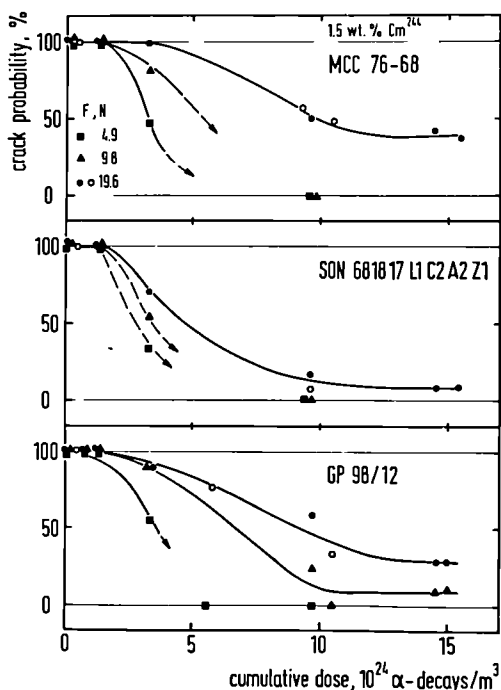


Fig. 10.16 Decrease of crack probability as a function of α -dose for the three Cm-doped waste glasses. Crack probabilities (radial cracks at Vickers indentations) are significantly decreased at higher doses.

Leaching Study of SYNROC

Crystalline Ceramic Waste Forms

(in cooperation with A. Solomah, KFA, G. Linker (KfK) and G. Della Mea (Univ. Padova))

Crystalline ceramics of different compositions are developed on a limited scale as alternative second generation waste forms and for special waste streams (e.g. transuranic wastes). Synroc is one of these waste forms.

SYNROC or SYnthetic ROck as a crystalline ceramic waste form was first proposed by Ringwood [1]. SYNROC-B is based on titanates and zirconate and consists of an assemblage of mineral-like crystalline phases, namely Bahollandite ($Ba_{1.14}(Al,Ti)_{2.28}Ti_{5.72}O_{16}$), zirconolite ($CaZrTi_2O_7$), perovskite ($CaTiO_3$), rutile (TiO_2) and pyrochlore-type structured $CaMTi_2O_7$ where M represents trivalent rare earths and actinide elements which exist in HLW. Such phases have shown their compatibility with one another, their ability to incorporate a wide range of HLW ions in their crystal structure and, most importantly, their naturally occurring analogs have retained uranium, thorium and the daughter products of their radioactive decay chains for up to several hundred million years without any significant release of radioactivity into the biosphere, e.g. [2].

Experimental Procedure

Samples of sintered pure and doped SYNROC (the latter containing 10 or 20 wt% simulated HLW) having dimensions of $10 \times 8 \times 3$ mm³ were cut from pellets of 20 grams sintered under reducing atmosphere at 1220-1240 °C. One side of each sample (10×8 mm²) was polished to a mirror finish. Several samples were ion implanted with Pb⁺⁺-ions of 270 or with Pb³⁺-ions of 570 keV energy or with 40 and 300 keV Bi⁺-ions and doses of 5×10^{15} ions/cm². The implanted samples were analyzed with Rutherford backscattering (RBS) before and after sequential leaching at different temperatures. Unimplanted specimens were leached under similar conditions and the effects of heavy ion implantation were evaluated. The leaching tests were carried out according to the recommendations of the Nuclear Waste Materials Characterization Centre (MCC Leach Test 2). The leached surfaces were characterized using secondary ion mass spectrometry (SIMS) and scanning electron microscopy (SEM). The

formation of hydrated layers on the leached surfaces of SYNROC samples were evaluated using elastic recoil detection analysis (ERDA) with 2 MeV He⁺-ions. RBS analyses were done in cooperation with INFP, KfK (G. Linker), and ERDA analysis was performed at the University of Padova in cooperation with Prof. DellaMea and V. Rigato.

The concentrations of Al, Ba, Ca, Ti, Zr and of simulated HLW elements in the leachants were measured by inductively coupled plasma and atomic absorption spectrometry (ICPS and AAS). Subsequently, the normalized leach rates of specific elements of interest were calculated. The weight losses of the samples during leaching were recorded using a microbalance and, subsequently, the bulk leach rates were determined.

Results and Discussion

Tables 10.5 and 10.6 show some typical leach data from a larger series of experiments, either for undoped SYNROC or for SYNROC doped with 10 at. % simulated HLW, respectively. Both implanted samples and unimplanted SYNROC were leached at 150 °C in deionized water and in Q-brine. Tables 10.5 and 10.6 give data for leaching in H₂O. The data show that the leach rates for Ba and Ca for the undoped Synroc are higher by factors of 2-3 than those for the doped SYNROC. The ratio of the bulk leach rates is still larger. From these data it is obvious that the addition of HLW improves the leach behaviour of SYNROC B. This may be attributed to the improvements in microstructure, most likely to increased density and reduction in open porosity.

Rutherford backscattering spectrometry was used to study the surfaces of unimplanted and of ion implanted SYNROC before and after leaching. Fig. 10.17 shows RBS spectra of as-implanted undoped SYNROC as thick line. The shoulders due to Ba, Zr, Ti, Ca, Al and O are clearly seen and correspond closely to the expected ones (see thin line for a RBS spectrum calculated on basis of the nominal composition of SYNROC). A Pb peak buried at about 0.15 μm depth is also clearly seen. The inset shows the Ba and Zr shoulders following leaching of specimens that were either as-implanted or annealed at 400 °C or 800 °C before leaching. The Pb-peak is still present in the 800 °C specimen, but it is largely gone in the other two specimens which, however, show some remaining Pb at the surface. Obviously, the overlying SYNROC was dissol-

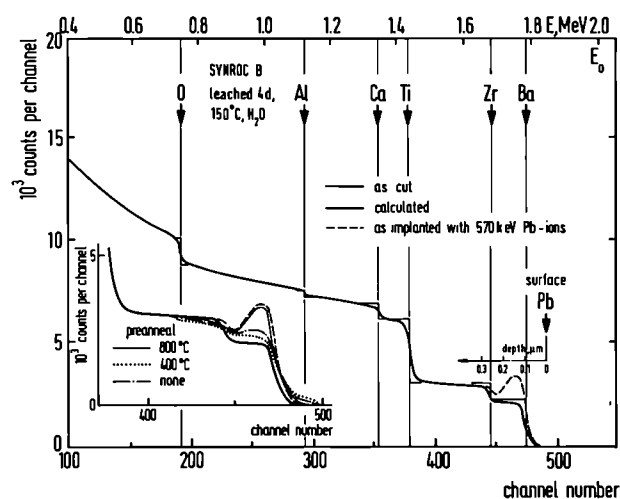


Fig. 10.17 Rutherford backscattering spectra of undoped SYNROC B implanted with Pb-ions, either unannealed or annealed at 400 °C or 800 °C, and leached at 150 °C in H₂O for 4d.

ved, as well as most of the Pb-marker, the rest being located at the surface. Fig. 10.18 shows RBS spectra of the same specimens following continued leaching. Depletion in Ba and Ca is seen; such depletion was also observed in unimplanted undoped SYNROC, and corresponds closely to the leaching data. The 800 °C specimen shows the Pb-peak to persist even after 39 d of leaching. However, the marker peak moves back to the surface indicating a small but measurable dissolution rate of the overlying SYNROC. The indicated rate is of the order of 0.05 μm in 39 d, or about 1.3 nm/d.

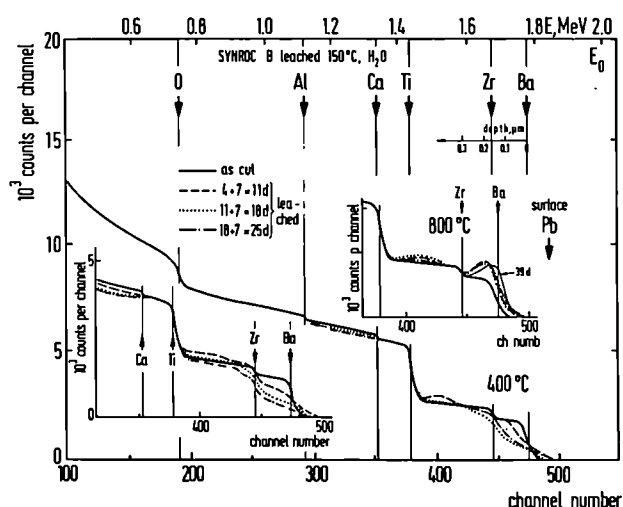


Fig. 10.18 as Fig. 10.17, but with continued sequential leaching of the samples of Fig. 10.17.

Tab. 10.5 Leach data of undoped SYNROC (150 °C, H₂O)

Sequential Leach Period (days)	Normalized Leach Rate (g/(m ² ·d))					Bulk Leach Rate (g/(m ² ·d))
	Al*	Ba	Ca	Ti*	Zr*	
4	<0.05	0.110	0.141	<5x10 ⁻⁴	<5x10 ⁻³	0.123
7	<0.05	0.036	0.062	<5x10 ⁻⁴	<5x10 ⁻³	0.061
7	<0.05	0.032	0.097	<5x10 ⁻⁴	<5x10 ⁻³	0.042
7	<0.05	0.045	0.090	<5x10 ⁻⁴	<5x10 ⁻³	0.056

* Calculated based on the detection limits of ICPS. The normalized leach rate is defined as (elemental conc. x leachant vol.)/(isotop. conc. x surface area x leach period)

Tab. 10.6 Leach data of SYNROC containing 10 wt. % simulated HLW (150 °C, H₂O)

Sequential Leach Period (days)	Normalized Leach Rate (g/(m ² ·d))					Bulk Leach Rate (g/(m ² ·d))
	Al*	Ba	Ca	Ti*	Zr*	
4	<0.05	0.037	0.143	<5x10 ⁻⁴	<5x10 ⁻³	0.01
7	<0.05	0.020	0.024	<5x10 ⁻⁴	<5x10 ⁻³	0.01
7	<0.05	0.020	0.034	<5x10 ⁻⁴	<5x10 ⁻³	0.01

* Calculated based on the detection limits of ICPS.

The experiments with Bi-implanted SYNROC largely confirmed the results on the Pb-implanted specimens.

Analysis of the leach solutions confirmed that annealing the implanted undoped SYNROC at 800 °C for 15 min to recover the damage due to heavy ion bombardment caused the leach rates to approach those measured for unimplanted SYNROC. The enhanced leaching in the as-implanted SYNROC (or the one annealed to only 400 °C) can be related to the amorphization (metamictization) of SYNROC at high doses of heavy ions which was shown previously to occur during Kr- and Xe-implants and was evidenced by the features of the gas release [3]. Amorphization of zirconolite and other ceramic waste forms is expected based on the available knowledge on radiation damage [4] and has been observed before for α -decay damage [5, 6]. Also,

recrystallization temperatures of 600 to 800 °C were found for these materials. Finally, very significantly increased leach rates of these amorphized ceramics were also seen. SYNROC fits thus easily into the existing general picture.

The morphology and the microstructure of the leached surfaces of SYNROC specimens (undoped and doped with simulated HLW, and unimplanted or implanted) were investigated using scanning electron microscopy (SEM) in secondary and backscattered electron imaging modes. The different phases could be qualitatively observed. However, unlike earlier workers, e.g. [7], and unlike investigating borosilicate glasses, where surface alterations can easily be distinguished with SEM, we were unable to observe changes in the surface structure of SYNROC after hydrothermal testing using the secondary electron mode of the SEM.

This may be due to the fact that the alteration products sometimes charge slightly in the electron beam which reduces resolution and obscures precipitates such as TiO_2 [8].

Secondary ion mass spectrometry (SIMS) was utilized to obtain additional information on the compositional changes which occur in the near surface layers of leached SYNROC. Fig. 10.19a shows the depth profiles of Al, Ba, Ca, Ti and Zr in pure SYNROC leached at 150 °C in H_2O for three days. Fig. 10.19b shows the depth profiles of these elements and of some of the waste components (Ce, Cs, Zr and Pd) for the doped SYNROC. These elements were chosen based on their different chemistry and their anticipated leaching behaviour. In both figures, it is evident that depletion in Ba, Ca and, to a lesser extent, Zr, has occurred, while a significant enrichment in Ti, probably as TiO_2 brookite is obvious over the same depth of about 40 nm. Although there is a drastic decrease in the leach rates of Ba, Ca and simulated fission products for periods longer than those used in Fig. 10.19, this is not simply attributable to the TiO_2 behaving as a passivation layer reducing further dissolution.

Rather, the fall-off reflects the removal of near-surface grain boundary phases and the more soluble matrix phases (e.g. perovskite)[9].

It is well known that hydrated gel-type surface layers are formed on leached waste glasses and other silicates, and the mechanism of water attack is understood. Such knowledge does not exist for titanates. However, the formation of hydrated surface layers on leached SYNROC, as a result of water interaction with surface components, could be observed by elastic recoil detection analysis using 2 MeV He-ions. The thickness of the hydrated layers was measured by recording the depth profiles of hydrogen concentration. Fig. 10.20 shows the depth profiles of hydrogen concentration in a borosilicate waste glass leached for only 2 h in H_2O at 150 °C, compared with the hydrogen depth profile in SYNROC leached under the same conditions for a much longer period, i.e. one month. It is evident that a hydrated surface layer in SYNROC exists, but that it is thinner and contains less hydrogen than those on glass. Considering the difference in hydrogen concentration for both depth profiles and the time factor, and using a linear

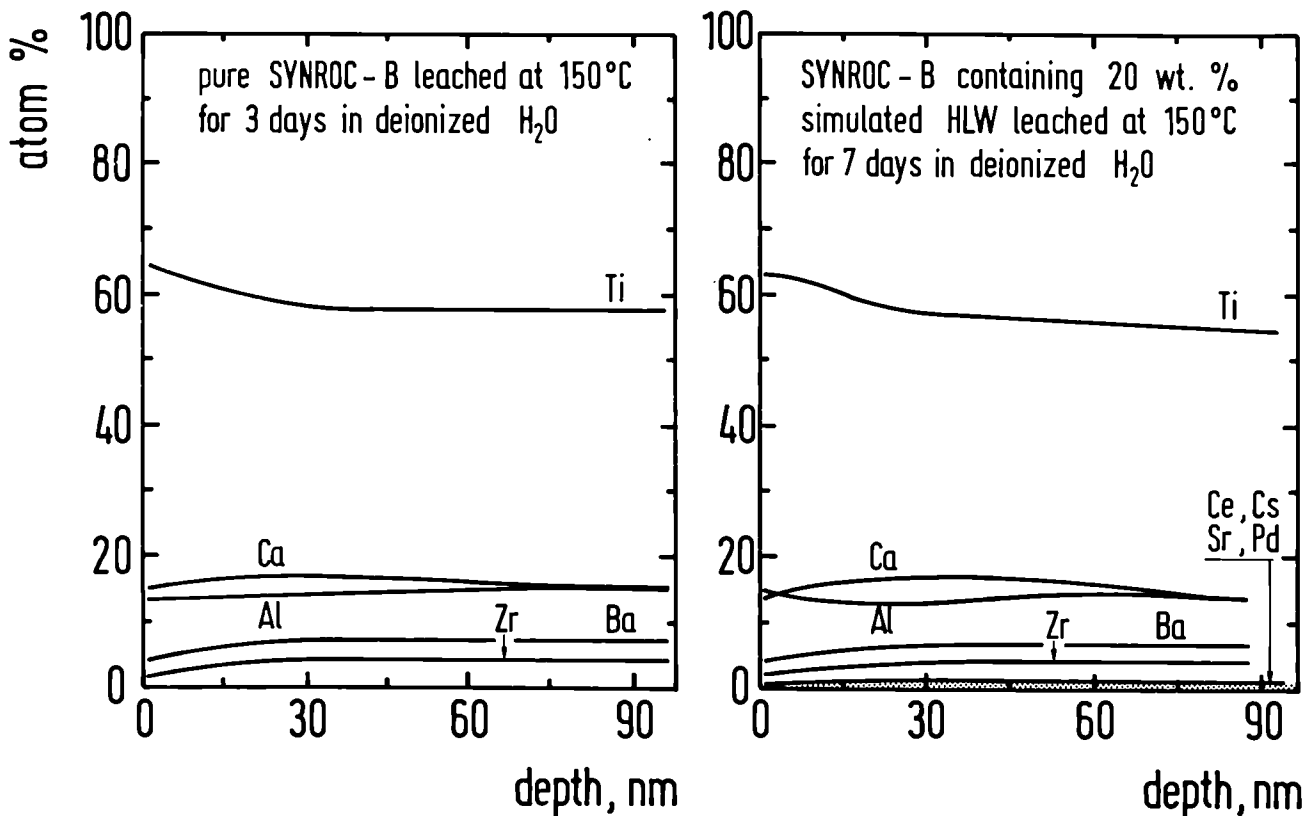


Fig. 10.19 SIMS depth profiles of a) undoped SYNROC and b) SYNROC doped with 20 wt. % simulated HLW, leached at 150 °C in H_2O .

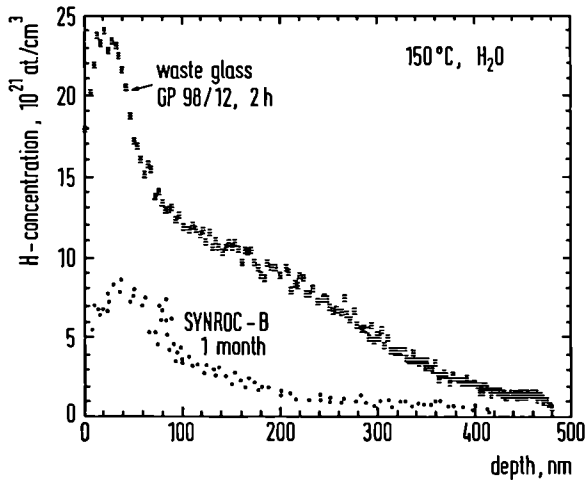


Fig. 10.20 ERDA depth profile of hydrogen in a borosilicate glass leached for 2 h and in SYNROC leached for one month, both in H_2O at $150\text{ }^\circ\text{C}$.

extrapolation one concludes that the rate of formation of hydrated surface layers in glass is higher than in SYNROC by a factor of about 10^3 .

Leach data of SYNROC in simulated brine (Q-brine) at temperatures up to $200\text{ }^\circ\text{C}$ for up to three months showed no significant difference in the leach rates of Ba, Cs, U and other simulated fission products as compared to those measured in water. As an example, for 3 months leaching in Q-brine, significant Ba (and Ca) depletion was seen in RBS, extending to a depth of $\sim 1\text{ }\mu\text{m}$. As with leaching in water, enrichment of both heavy and light fission products in the surface layers was evident in the RBS spectra of the doped SYNROC. A positive temperature effect was observed over the temperature range 90 to $200\text{ }^\circ\text{C}$.

Conclusions

The present study has confirmed the known good leaching properties of sintered SYNROC. Analyses of the leach solution were combined with a number of analytical techniques to characterize the leached surfaces. A very significant radiation-enhanced leaching was observed in SYNROC implanted with heavy ions and was attributed to radiation-induced amorphization (metamictization). A very thin hydrated layer was found on the surface of leached SYNROC which was much thinner than the one found on borosilicate waste glass. No obvious difference between leaching in water and

in simulated brine was observed. The incorporation of HLW into SYNROC lead to a product with further reduced leach rates.

References

- [1] A.E. Ringwood, *Safe Disposal of High-Level Nuclear Reactor Waste: A New Strategy*, (Australian National University Press, Canberra, 1978).
- [2] A.E. Ringwood, S.E. Kesson, N.G. Ware, W.Hibberson and A. Major, *Nature* (London) **278** (1979) 219.
- [3] Hj. Matzke, in *Ion Beam Modifications of Insulators*, eds. P. Mazzoldi and G. Arnold (Elsevier Science Publishers, New York, 1987) pp. 501.
- [4] Hj. Matzke, *Rad. Effects* **64**, (1982) 3
- [5] W.J. Weber, J. W. Wald and Hj. Matzke, *J.Nucl. Mater.* **138** (1986) 196
- [6] W.J. Weber and Hj. Matzke, *Rad. Effects* **98**, (1986) 93
- [7] P.E. Fielding and T.J. White, *J. Mater. Res.* **2**, (1987) 387
- [8] T.J. White, personal communication
- [9] W.J. Buykx, K. Hawkins, D.M. Levins, H.Mitamure, R.St.C. Smart, G.T. Stevens, K.G. Watson, D. Weedon and T.J. White, *J. Amer. Ceram. Soc.* **71**, (1988) 678

A Comparison of Vickers Indentation and Short Rod Fractometry to Determine the Fracture Toughness K_{Ic} of Waste Glasses

The Vickers indentation technique and short rod fractometry were used to determine the critical stress intensity factor (in mode I of fracture) K_{Ic} as a measure of the fracture toughness of the German Nuclear Glass GP 98/12.2 (see Tab 10.7 for composition).

Tab. 10.7 Composition of the German Nuclear Borosilicate Waste Glass GP 98/12.2 and its Precursor VG 98/12.2

Oxide	VG 98/12.2 wt. %	GP 98/12.2 wt. %
SiO ₂	53.20	45.22
B ₂ O ₃	14.80	12.58
Na ₂ O	18.60	15.81
Al ₂ O ₃	2.40	2.04
MgO	2.20	1.87
CaO	4.50	3.83
TiO ₂	4.30	3.65
waste oxides	-	15.00

Vickers indentation technique

This technique, applied already before to waste glasses [1] was used for a detailed study of the effect of residual compressive stresses which arise during the sample preparation. A wide load range was used: at low loads (0.098 - 1.96 N), crack initiation or nucleation was investigated, and at higher loads (1.96 - 42.14 N) crack lengths were measured in the usual way. Residual stresses, e.g. due to polishing, were found to have a large effect, larger than that observed before for noble metal inclusions [2]. The crack lengths at higher loads (≥ 20 N) were insensitive to residual surface stresses whereas at lower loads their influence increased, as indicated in Fig. 10.21.

Two empirical relations suggested and used in the literature were applied to calculate K_{Ic} from the measured crack lengths. Both relations

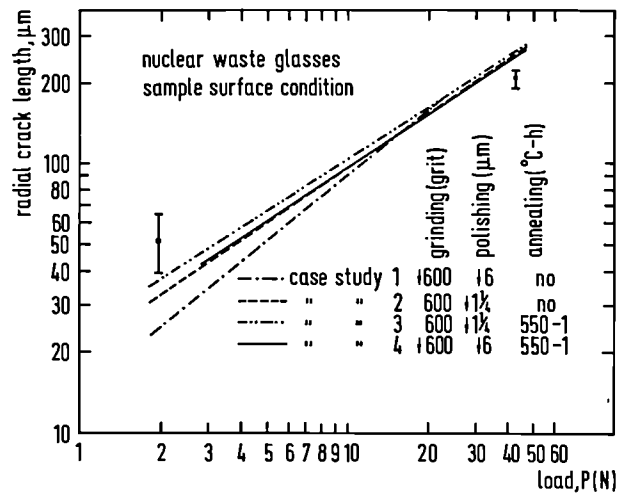


Fig. 10.21 Radial crack length (initial value) versus load, showing the effects of compressive surface stresses, of surface finishing and of preanneals.

contain essentially the same variables but have slight differences, e.g. in the exponent of the ratio of hardness and elasticity modulus. The first relation is due to Evans [3], and was so far mainly used in our previous work.

$$K_{Ic}^E (\text{MPam}^{1/2}) = 0.057 H \sqrt{a} (E/H)^{2/5} (c_0/a)^{-3/2} \quad (1)$$

where

H = Vickers hardness in MPa

E = elasticity or Young's modulus in MPa

a = half diagonal of the Vickers indentation in m

c_0 = length of radial cracks emanating from the corners of the Vickers indentation measured immediately after the indentation, in m.

In addition, K_{Ic} was calculated with the equation proposed by Anstis et al. (4):

$$K_{Ic}^A (\text{MPam}^{1/2}) = (16 \pm 4) (E/H)^{1/2} (P/c_0)^{3/2} \quad (2)$$

where H and E are defined as above:

P = indentation load in N

c_0 = defined as above, but in μm .

When eq. (2) was calibrated against eq. (1) and validated with results from short rod fractometry (see below), the empirical constant (for the waste glasses) had to be increased to the value 20 ± 1 , rather than (16 ± 4) in eq. (2). The revised equation was used for a detailed error analysis

for K_{Ic} . The resulting scatter in K_{Ic} was 10- 15 %. A reduction is possible by improving the surface conditions (polishing, pre-anneal) and the image quality of the microscope. For instance, crack length measurements on near-to-ideal surfaces can be done with a reduction of 20 % in the experimental scatter. The corresponding reduction in the precision index of K_{Ic} is, however, rather small, but it proves that the statistical method of calculating the experimental scatter is adequate. For eq. (1), the same precision index was applied since it depends primarily on errors in the independent variables and is not affected by the way in which they are arranged. Values calculated with both equations with the scatter (precision index) are shown in Tab.10.8.

Crack propagation following the indentation was measured during about two days, i.e. the crack lengths were determined immediately following the indentation (yielding the above value c_0), and after 2, 24, 26, 48 and 50 hours. For GP 98/12.2, c increased to about 1.1 c_0 after 50 hours. The propagation was the same for low and high loads (2.94 and 42.14 N), and the fastest increase (from c_0 to 1.06 c_0) occurred within the first two hours. Whether crack growth stops, or proceeds with a low constant speed, and the influence of humidity will be determined in future.

Short rod fractometry

Short rod fractometry was selected as an independent second means to measure K_{Ic} and to validate the results from Vickers indentation. This method employs chevron-notched specimens of rod shape to determine the plane-strain fracture toughness of small specimens. It is a valuable extension of the Vickers test and is also particularly useful for work with radioactive

specimens since it avoids large specimen sizes and since the rod geometry used (diam. 6.2 mm, length = 1.5 x diam.) can rather easily be produced by drilling cylinders from larger glass blocks. Also, the dimensions needed are very similar to those of fuel pellets thus allowing use of the equipment for testing both fuel and waste matrices.

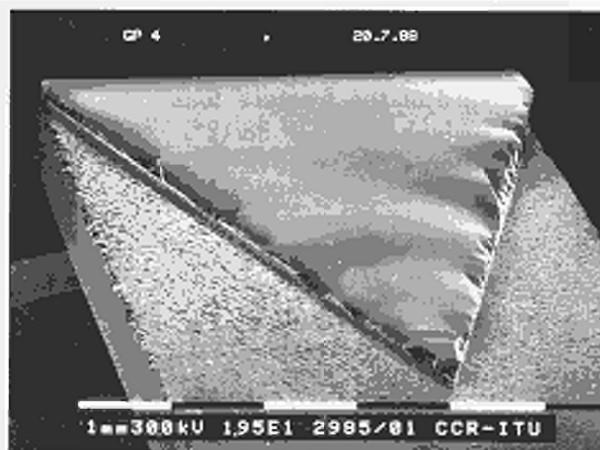


Fig. 10.22 A chevron-notched specimen of the waste glass GP 98/12 following a short rod fracture test.

A fractured specimen is shown in Fig. 10.22 and a sketch of the short rod specimen configuration is inserted in Fig. 10.23. The shaded area denotes the crack. The figure itself shows a measured test of the glass GP 98/12.2 in a plot of applied load F versus crack mouth (or load point) opening x . After producing a thin chevron slot with a

Tab. 10.8 Fracture Toughness K_{Ic} (in $MPam^{1/2}$) for the German Waste Glasses VG 98/12.2 and GP 98/12.2

glass	sample	Vickers indentation		short rod fractometry
		equ. (1)	equ. (2)	
VG 98/12.2	V62	0.60 ± 0.10	0.60 ± 0.10	0.77 ± 0.07
GP 98/12.2	V49	0.76 ± 0.10	0.74 ± 0.09	0.77 ± 0.07
"	V64	0.77 ± 0.10	0.73 ± 0.09	0.73 ± 0.07

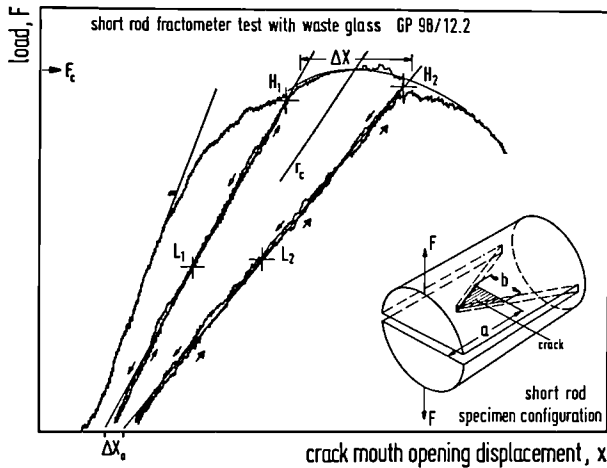


Fig. 10.23 Typical short rod fractometer test of the waste glass GP 98/12.2 showing two loading/unloading cycles. The inset shows the short rod geometry.

thickness $< 0.015 B$ and a groove for a grip system to apply the force and measure the mouth opening, the test is started. The thin chevron slot serves several critical functions: it reduces the size of the non-plane-strain zone at the flank ends of the crack, it forces crack initiation at the point of the "V" during crack initiation, it defines the crack plane and propagation direction and it produces stable crack growth since the crack front widens as the crack advances. Both test equipment and test procedure are described in detail in the literature [5]. The equipment is produced by Terra Tek, Salt Lake City.

The chevron-notched specimens are tested by slowly increasing the load (while elastically deforming the specimen) until a crack initiates at the point of the "V". The subsequent crack growth is stable after reaching steady state such that an ever-increasing load is needed to advance the crack until it reaches a critical length, a_c , at a load F_c . Thereafter, the load decreases with increasing crack length. a_c has been shown to be constant for a given specimen geometry and loading configuration [6]. The theory developed for the short rod geometry and supporting experimental work [5] have yielded the following relation to obtain K_{Ic}^{sr} :

$$K_{Ic}^{sr} = \frac{AF_c}{B^{3/2}(1-\nu^2)^{1/2}} \left(\frac{1+p}{1-p} \right)^{1/2} \sim \frac{AF_c}{B^{3/2}} (1+p) \quad (3)$$

Here, B is the specimen diameter and ν the Poisson's ratio of the specimen. The critical load F_c and the value of p are deduced from loading/unloading cycles. For unloading/loading cycles, a residual crack mouth opening of zero is expected for ideal linear elastic fracture mechanics. An offset Δx_0 , as seen in Fig. 10.23, is either indicative of plastic deformation or of residual stresses causing the specimen to become slightly deformed during the fracture test.

The correction factor p in eq. (3) is defined as $p = \Delta x_0 / \Delta x$ (see Fig. 10.23). Tests with $p > 0.2$ were discarded in the initial work. The calibration constant A has a recommended value of 22. All these tests were performed in laboratory air (21 °C, 50% rel. humidity).

While accumulating the results, significant improvements and extensions in the testing and evaluation procedure of short rod fractometry could be made. These extensions were even necessary due to the characteristics of the load-mouth opening plots obtained with several waste glasses (not only VG and GP 98/12.2). These glasses showed a rather different and more complicated behaviour than the materials used so far [4]. Previously, essentially two cases of mouth crack propagation were defined: the linear elastic fracture case and the elastic-plastic case. The former assumes neither plastic nor residual stress effects, the latter assumes a combined effect of plasticity and residual stresses which is constant during the test. Figs. 10.24 and 10.25 show typical plots with the corresponding

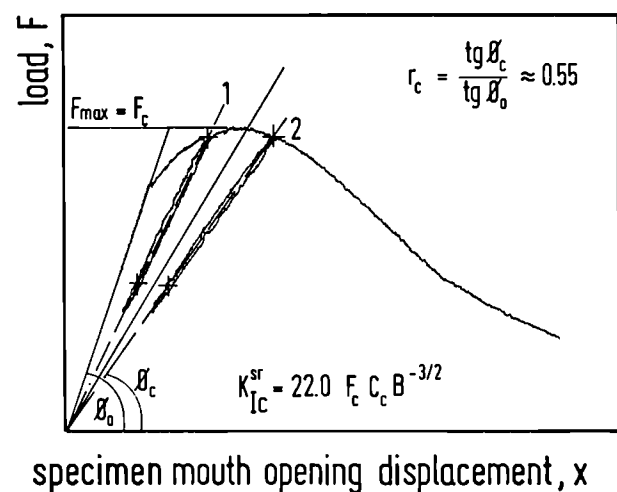


Fig. 10.24 Load-displacement measurement and calculation of K_{Ic}^{sr} for the LEFM case (linear elastic fracture mechanics).

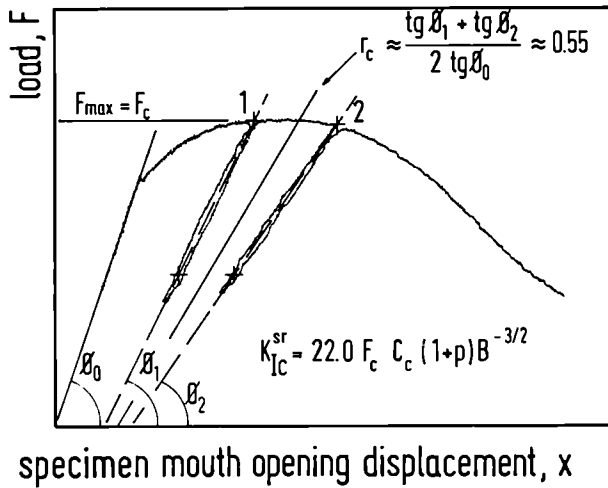


Fig. 10.25 Load-displacement measurement and calculation of K_{Ic}^{sr} for the case of elastic-plastic behaviour.

equations to calculate K_{Ic}^{sr} . The waste glasses, however, showed plasticity-residual stress effects which were variable during the test, a phenomenon not observed in materials investigated previously [4]. The reasons are probably the inhomogeneities such as noble metal fission product inclusions, localized stresses, pores, etc.

Due to the above phenomena, it was necessary to develop a new method of interpreting the load-mouth opening plots and to define the unloading/reloading paths. Also, the number of unloading/reloading cycles was increased (see Fig. 10.26). In this way, either the existing equations (see eq. (3) and Figs. 10.24, 10.25) could be used (K_{Ic}^{sr} evaluated for the "critical" crack length, hence a "slope ratio" $r_c = 0.55$ and a constant $A = 22.0$), or else several K_{Ic} -values could be calculated for the same sample in one test, using all pairs of unloading/reloading paths. This possibility ("multi-cycle-test") had never been used before. It increases the power of short rod fractometry and allows for a statistical analysis of K_{Ic} . The interpretation of variations of K_{Ic} for a given sample during the test (during crack propagation) in relation to microstructural heterogeneities and/or residual stresses is being worked out.

The results obtained up to now show a small improvement in K_{Ic} in waste glasses due to noble metal inclusions, probably due to crack branching at the noble metal particles. The cooling rate of the glasses had no significant effect on K_{Ic} . By and large, the values were all in the scatter range within the experimental

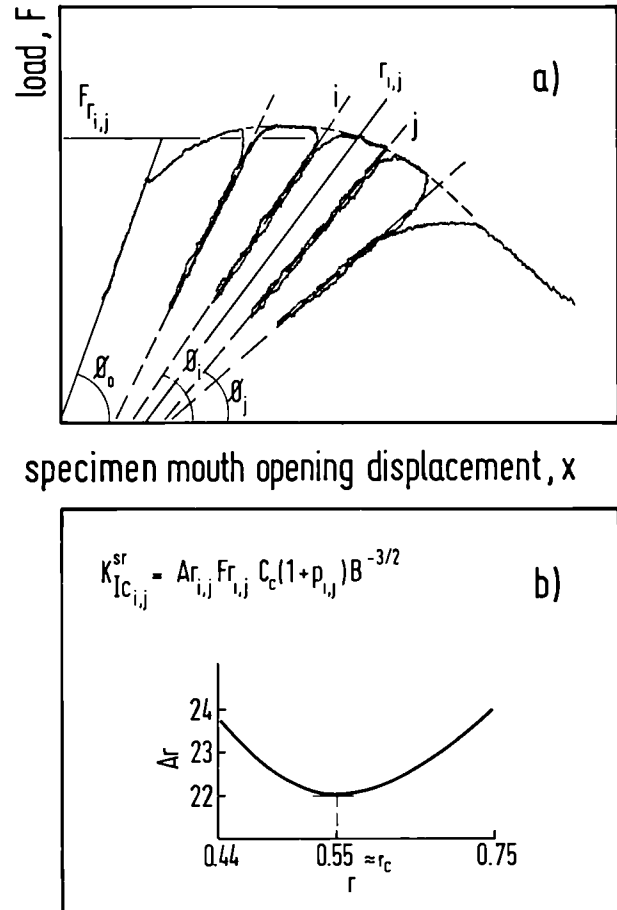


Fig. 10.26 Load-displacement measurement in the newly developed "multi-cycle test" for the waste glasses, and calculation of K_{Ic}^{sr} .

statistical precision index ($\sim 10\%$). This fact is positive for the application of the glasses. The agreement between K_{Ic}^{sr} obtained with short rod fractometry and K_{Ic}^{Vi} obtained with Vickers indentation is very good for GP 98/12.2, though there is a so far unexplained difference for VG 98/12.2. Possibly, effects due to humidity are responsible for the difference. Humidity would be thought to affect Vickers indentation (measured on surfaces exposed to air before the test) more than short rod fractometry (measurements during formation of new surfaces).

References

- [1] Hj. Matzke, Indentation Fracture and Mechanical Properties of Ceramic Fuels and of Waste Ceramics and Glasses, Harwood Acad. Publ., Chur., London, Paris, New York, Melbourne (1987)

- [2] Hj. Matzke, H.G. Scheibel and V. Friehmelt, Proc. Scient. Basis for Nuclear Waste Management, MRS, Berlin (1989) in print
- [3] A.G. Evans, Fracture Mechanics Applied to Brittle materials ASTM STP 768, ed. S.W. Frieman, Amer. Soc. for Testing and Materials, Philadelphia (1979) p. 112
- [4] G. Anstis, P. Chantikul, B.R. Lawn and D.B. Marshall, J. Amer. Ceram. Soc. **64** (1981) 533
- [5] L.M. Baker, Int. J. of Fracture **15** (1979) 515
- [6] L.M. Baker, Engineering Fracture Mechanics **9** (1977) 361

Characterization of Highly Active Glasses

This activity was initiated in 1987 in the framework of a collaboration with ENEA, COMB-SVITE and JRC Ispra. The chemical and radiochemical composition of the ESTER borosilicate glasses under investigation has been described in TUAR-87, together with a number of characterization tests which were pursued during the present year.

Characterization of Glasses

Updating of characterization of glass 4

The first results on the microstructure of the glass 4 and the elemental composition of the secondary phases have already been mentioned in TUAR-87, p. 210.

The EDAX analysis of the phases resulting from the devitrification process has been completed and these phases can be classified according to factors such as crystalline morphology, size and elemental composition as given in the Tab. 10.9.

Additional studies

The distribution of the secondary phases present in the glasses 4 and 8 has been determined at the request of ENEA.

a) Porosity distribution in glass 4

Two-pore populations were found; the first population was composed of pores exceeding 100 μm diameter size which could not be analyzed by means of our image analyzer. However, the second population with pore sizes ranging between 0.4 and 20 μm diameter were analyzed and their distribution in the centre and the outer part of the specimen is given in Figs. 10.27 and 10.28, respectively.

The segment of the latter population with diameters $2 \leq \phi \leq 5 \mu\text{m}$ seems to be the result of a growth mechanism at the expense of the smaller pores.

Tab. 10.9 Classification of secondary phases precipitates in the matrix ENEA - glass 4

	crystalline appearance	size (μm)	elemental composition (major elements)
type 1	tetragonal	1 - 5	Cr, Fe, Co, Ni, Zr
type 2	irregular	10 - 20	Cr, Fe, Co, Ni, Sr, Zr
type 3	hexagonal plates	1 - 5	Cr, Fe, Ni, Gd, Sr, Y, Zr, La, Nd
type 4	needles	10 - 30	Fe, Gd, Nd, Ni, Sr, Y, Zr, Mo
type 4	tetragonal needles	5	La, Pr, Nd, Gd, Fe, Ni, Sr, Zr
	plates	up to 140	
		100	

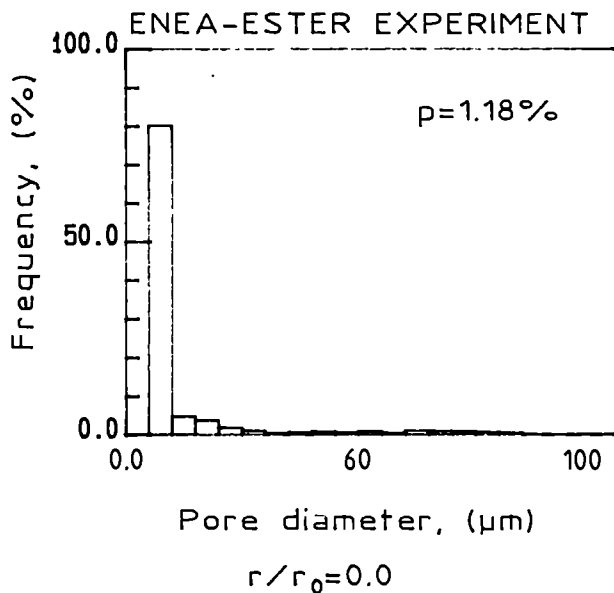


Fig. 10.27 ENEA - glass 4
Pore distribution - centre of the specimen

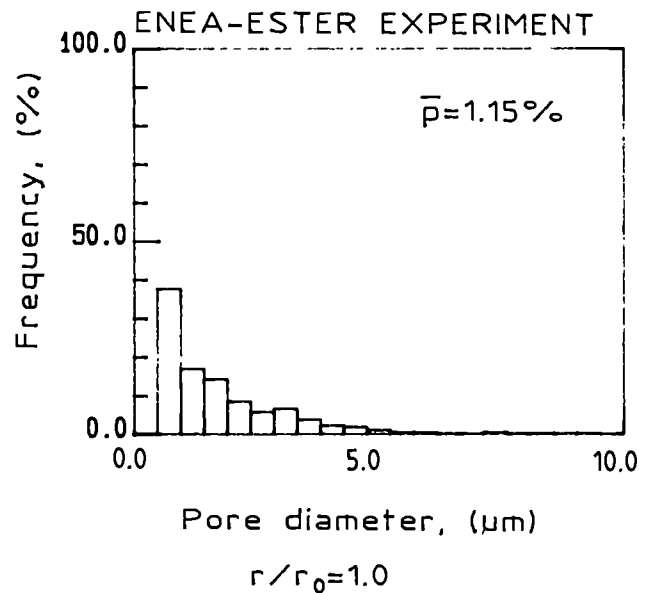


Fig. 10.28 ENEA - glass 4
Pore distribution - outer part of the specimen

b) Distribution of Cr- and Fe-rich precipitates in glass 4

The difference in reflectivity permits the distribution of these two phases to be determined. As indicated by Fig. 10.29, the distribution is independent of the radial position. The elemental composition of crystals growing inside large pores is noteworthy - Ti (Nd, Gd, Fe, Ni, Cr, Zr, Si, Ca, K) - and indicates an enrichment in Ti.

c) Matrix analysis of glass 8

As reported in TUAR-87, Figs. 7 - 11, the matrix of glass 6 appears as a two glass system although the elemental composition is similar in both cases. A possible explanation is the influence of secondary phase and chemical compounds on reflectivity. The light "glass" contains metallic optical precipitates (Fe, Cr, Ni); this phase is absent in the dark "glass". The latter is Al-enriched (24 % Al, 5 % Cr) with regard to the light "glass" (12 % Al).

The distribution of the dark glass within the specimen is given by Fig. 10.30.

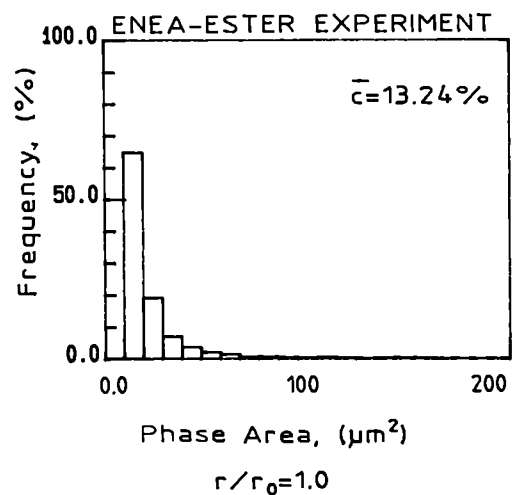
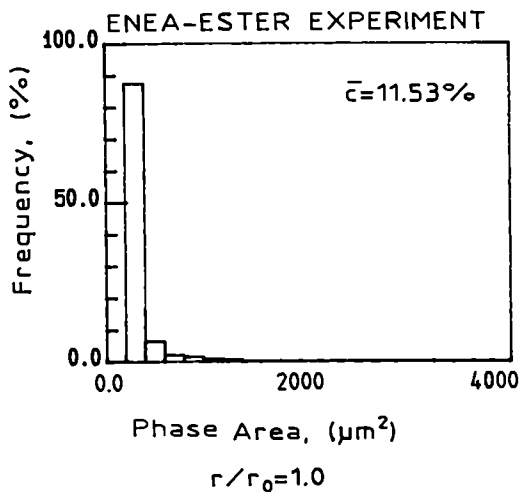
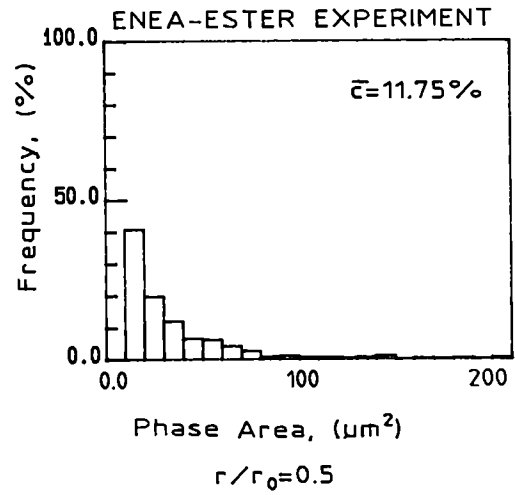
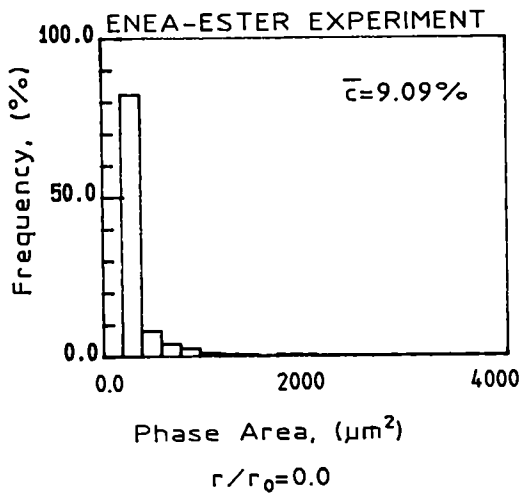
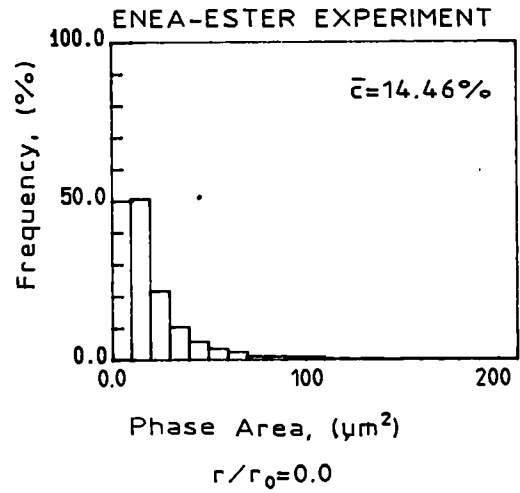
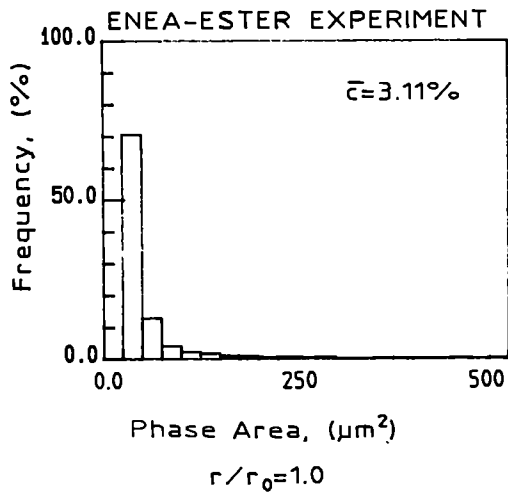


Fig. 10.29 ENEA - glass 4
 a) distribution of Cr-rich precipitates in the centre and outer part of the specimen
 b) distribution of Fe-rich precipitates in the centre and outer part of the specimen

Fig. 10.30 ENEA - glass 8
 Radial distribution of the dark "glass" within the analyzed specimen

Leaching Tests of ENEA Glasses

Leaching tests on glasses 4 and 6 were carried out for 3 days with deionized water by means of Soxhlet extractors.

Experimental

As described in TUAR-87, p.211, three transverse cross-sections were cut through the crucible; from these leaching samples were prepared. Using a diamond borer, cylinders of 8.8 mm in diameter were drilled with one in the centre and a second one in the outer part for each slice. These small cylinders were polished down to about 3 mm in height.

The leaching equipment consists of a series of 5 Soxhlet extractors (Fig. 10.31).

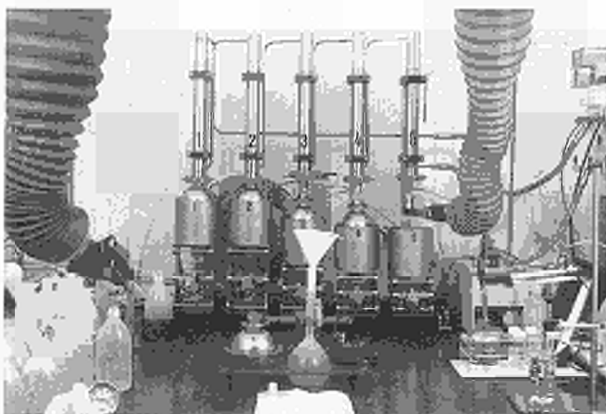


Fig. 10.31 Soxhlet equipment in hot cell

The schematic drawing of a Soxhlet extractor is shown in Fig. 10.32. The apparatus is made of stainless steel and its characteristics are very close to those required for the MCC-55 method, i.e. continuous overflow at a rate of 1 ± 0.2 ml/min with specimen surface area (SA); ~ 200 mm² and $SA/V \approx 0.01$ mm⁻¹.

First chemical analyses

At the end of the reaction the pH of the leachates had increased from about 6.7 to about 8.7. The solutions were analyzed by ICP-OES (a) and ICP-MS (b) techniques. Both results are presented in Tab. 10.10. The denomination of the samples in the Table is as follows: the first number

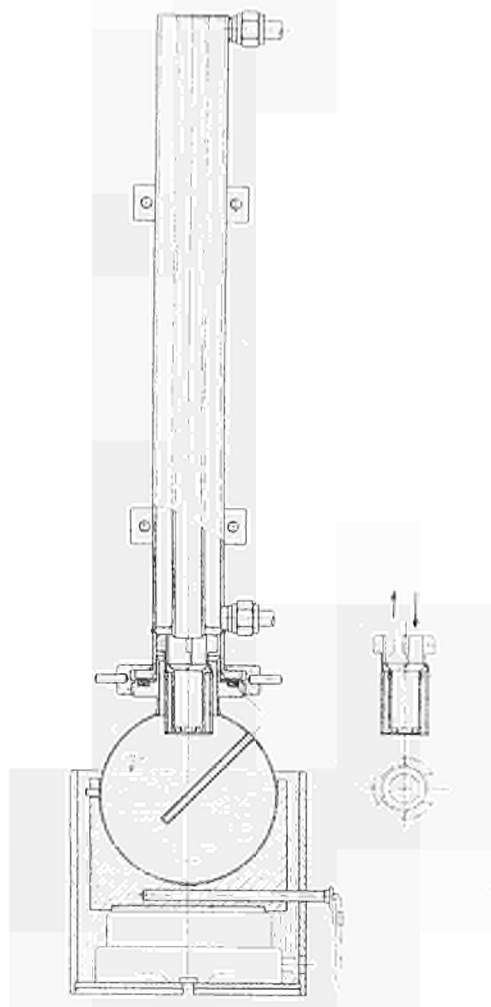


Fig. 10.32 Schematic diagram of a Soxhlet extractor

designates the glass crucible (4 or 6); the second number indicates whether the sample originates from a transverse cross section cut at the bottom (1), the centre (2) or the top (3) of the glass crucible; and finally, the latter shows whether the actual cylindrical (3 mm in diameter) sample submitted to leaching was cut from the periphery (e) or the axis (c) of the above disk.

It is obvious that many elements were below the detection limits of ICP-OES. For the other elements, however, the agreement between the two techniques is encouraging, although it should be stressed that the confidence limits of the various results have not yet been fully assessed. Finally, one should note that in the case of the Si analysis, a second series of measurements by ICP-OES in the same solutions yielded results about 50 % smaller than those listed.

Tab. 10.10 Comparison between the analyzed results from ICP-MS (a) and from ICP-OES (b) for leachates (3 days in Soxhlets - MCC-5S) of ENEA-ESTER glasses (results in ppb)

sample element	4-1 c		4-2 c		4-3 c		4-1 e		4-2 e		4-3 e		6-1 c		6-2 c		6-3 c		6-1 e		6-2 e		6-3 e	
	a	b	a	b	a	b	a	b	a	b	a	b	a	b	a	b	a	b	a	b	a	b	a	b
Li*	52	dl	46	dl	35	dl	90	dl	91	dl	56	dl	20	dl	46	dl	72	dl	112	dl	54	dl	50	dl
Si		1500		2300		1100		2500		2400		1700		2600		1200		1700		2200		1250		800
Mo	48	127	59	160	43	100	102	210	112	230	50	20	74	134	3	dl	2	dl	84	190	3	dl	1	dl
B	170	212	136	165	105	138	229	317	303	353	180	235	337	343	55	88	84	115	318	346	72	94	60	55
Al	10	46	15	dl	50	70	9	dl	12	dl	12	181	12	dl	14	dl	10	28	9	dl	14	dl	18	dl
Mn	7	5	12	12	12	13	4	1	4	dl	14	19	4	dl	20	27	8	14	3	dl	18	25	17	23
Sr	15	36	24	27	14	14	23	25	25	28	21	23	29	36	5	3	6	5	28	33	5	3	6	4
Zr	dl	dl	dl	48	dl	dl	dl	33	3	28	dl	dl	dl	43	dl	37								
Ba	40	43	70	84	35	40	45	61	54	89	54	85	45	73	dl	11	dl	dl	111	82	dl	dl	16	20
Cs	111		134		76		199		209		118		218		5		5		198		5		5	

* dl in ICP-OES = 380 ppb

Metallographic examination of glass 6 after leaching test.

The leached specimen is a small disc and after preparation has two plane polished surfaces and an as-cut (non-polished) cylindrical surface, therefore the influence of the surface finish on the leaching rate can be compared.

a) Surface analysis

As illustrated by Figs. 10.33 and 10.34 the SEM analysis of the leached surfaces indicated an heterogeneous dissolution rate. The leaching proceeds at preferential sites of dissolution located either in the matrix or around precipitates. In the matrix the preferential dissolution sites appear as strings of nodules and when associated with secondary phases as circular microcracks close to the precipitate. A further type of linear microcrack propagation on the glass surface could be seen: in this case, however, no correlation with the presence of secondary phases could be established.

EDAX analysis of the strings of nodules indicates a lower Si content and a higher Fe content, in relation to unleached fracture surfaces and implies a higher Si dissolution rate and a greater Fe retention in comparison with the surrounding phases. The mechanical state of the leached surface determines the amount of preferential

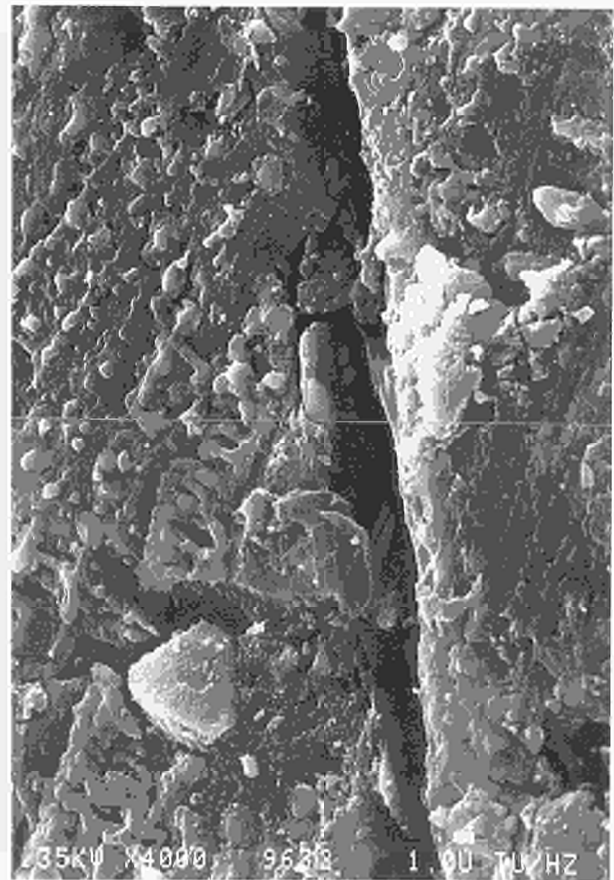


Fig. 10.33 ENEA - glass 6
As-leached surface with features of nodule strings and linear microcracks

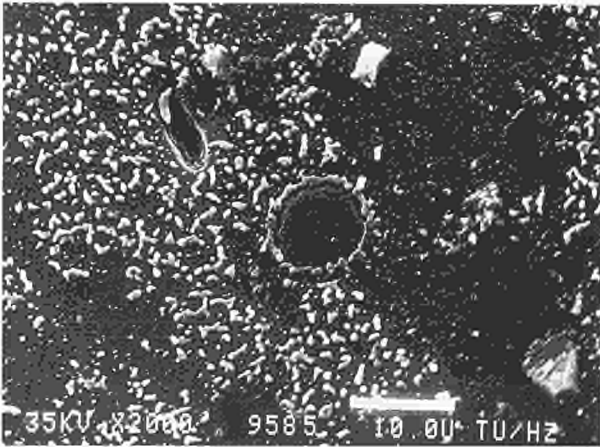


Fig. 10.34 *ENEA - glass 6*
As-leached surface
Formation of circular microcracks
around secondary phase

dissolution sites and linear microcracks formed. Good polishing of the surface appears to reduce the leaching effects by decreasing the formation of linear microcracks.

b) Bulk analysis

The propagation of the preferential sites of dissolution from the glass surface into the glass bulk was studied from polished samples by optical and scanning microscopy. As illustrated by Fig. 10.35 the leaching proceeds from the outer surface at local sites and propagates into

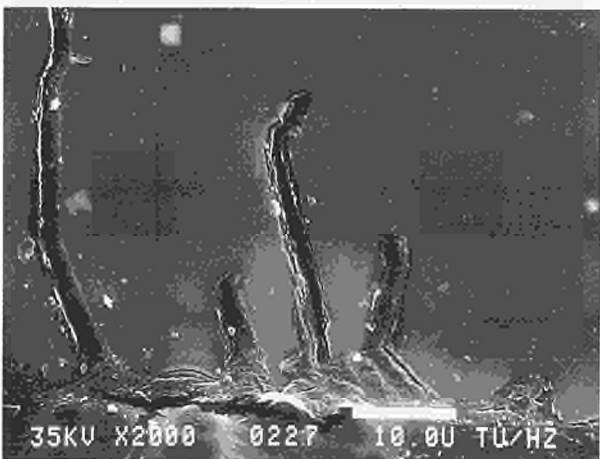


Fig. 10.35 *ENEA - glass 6*
Morphology of as-leached glass
surface
Formation of a "gel" associated with
channels penetrating into the matrix

the glass through channels up to a depth of 50 μm . These channels contain a (gel) phase composed of Si, Fe, Ni, Zr that was depleted in Si and enriched in Fe with regard to the matrix composition; close to the channels and in direct contact with the leachant could be found occasionally a crystalline phase whose composition confirms the preferential dissolution of Si with regard to Fe in the leached surfaces of the specimen.

Spent Fuel Direct Storage

A new activity had been started in 1987 (see TUAR 87, 110) to investigate spent fuel as barrier for long time storage of radioactive fuel elements. Following the development of tracer methods to measure very small leach rates of UO_2 and following an investigation of the effect of radiation damage on UO_2 dissolution, the present contribution deals with a determination of the changes in near-surface layer composition and structure of UO_2 single crystals subjected to leaching at different conditions.

Surface Oxidation to U_3O_7 , and Thickness of U_3O_7 Layers during Leaching of UO_2

The channeling technique and Rutherford backscattering of 2 MeV He-ions of the van de Graaf accelerator of INFP, KfK were used to elucidate the mechanisms of the interaction of UO_2 with water at different temperatures between 100 and 200° C, and as a function of time.

Results:

Leaching at 100 °C even for very long times (i.e. for about 200 h) did not produce any noticeable change in the channeling spectra as compared to that obtained for a virgin, untreated single crystal. Also, no change in weight was observed.

An effect of leaching was first measured after prolonged treatment at 130 °C. The channeling spectrum for a UO_2 single crystal leached at this temperature for 240 h is shown in Fig. 10.36. The spectrum for a crystal leached at 150 °C for 24 h is also shown in Fig. 10.36. Fig. 10.37 shows a time sequence for leaching at 150 °C.

As can be seen in Figs. 10.36 and 10.37, a peak, similar to those which were observed in previous work to be formed due to ion implantation and radiation damage, appears in the aligned spectra. Such peaks reflect the displacements of U-atoms from their regular lattice positions. The prolongation of leaching time results in the broadening of the peak. The characteristic feature of such disorder peaks is also their constant height. One can conclude that the nature of the distortion is

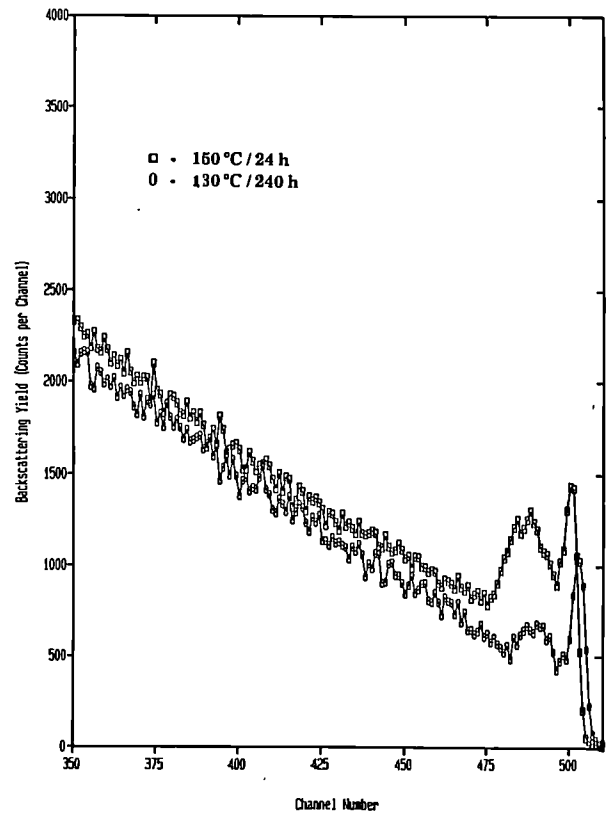


Fig. 10.36 Channeling spectra for aligned UO_2 single crystals leached at 130 and 150° C

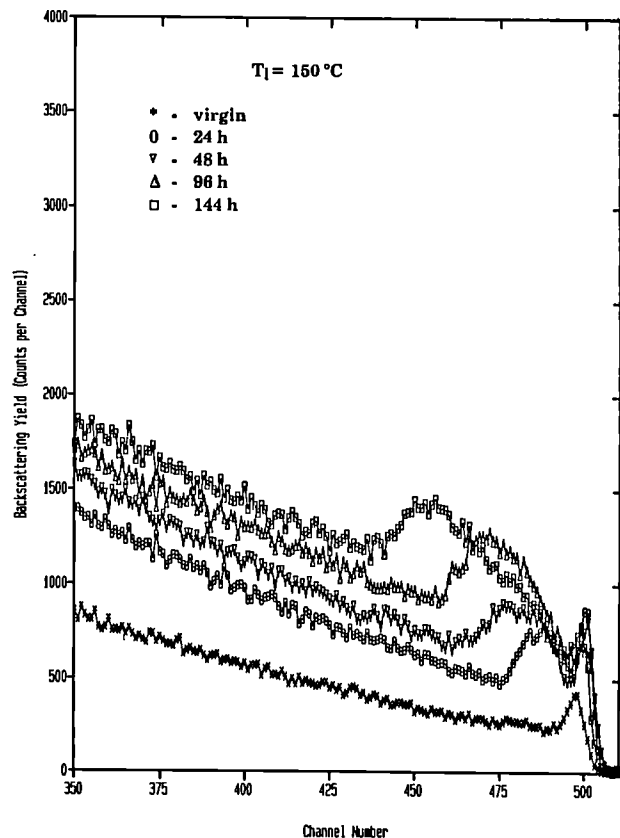


Fig. 10.37 as Fig. 10.36, but time sequence for leaching at 150° C

independent of the leaching time and that it propagates towards greater depths as a function of time.

The same characteristics of channeling spectra were observed after leaching at 175 °C and 200 °C. Figs. 10.38 and 10.39 show the spectra obtained for UO₂ single crystals subjected to leaching at 175 °C for different times. One notes that the disordering of the crystals proceeds faster with increasing temperature.

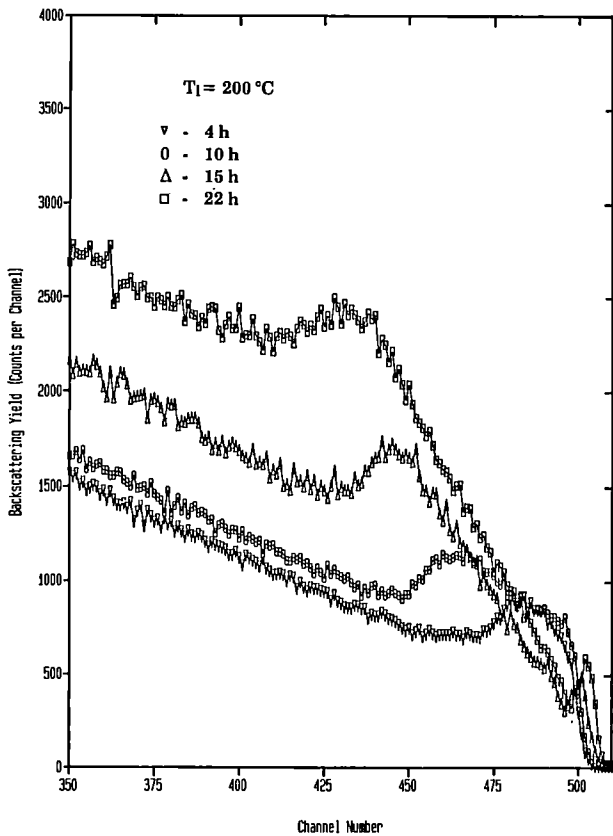


Fig. 10.38 as Fig. 10.36, but for 175 °C

one (\square) was set beneath the distorted region. In both cases the critical angles of the angular scans for the distorted regions are about 0.2° narrower than obtained for the undistorted portion of the crystal. This indicates that U-atoms are slightly displaced from their regular lattice sites. Another interesting effect can be seen in Fig. 10.41 for tilt angles <-1.5 ° and >1.5 °. The scan curve for the distorted region is broader in this part of the scan than that for the undistorted one. The reason for such a behavior may be due to

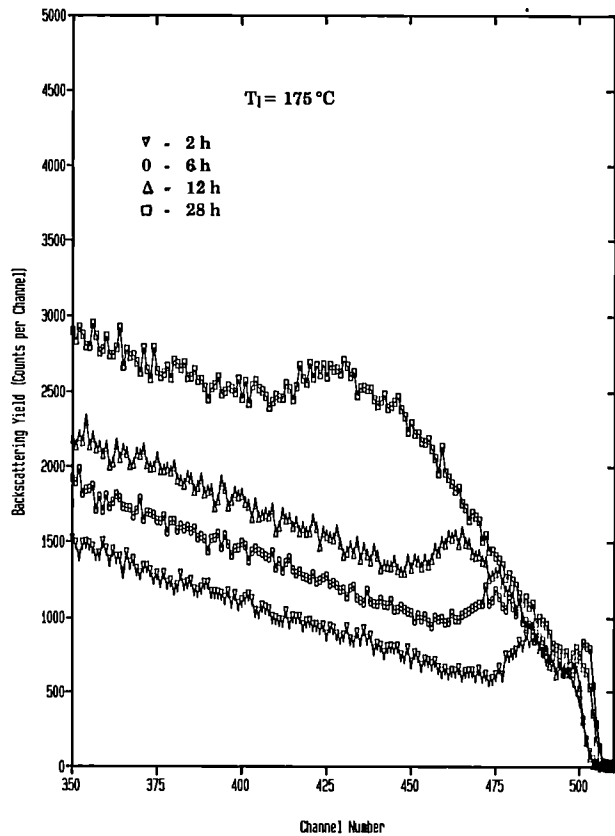


Fig. 10.39 as Fig. 10.36, but for 200 °C

The dependence of the penetration depth of disorder X_p , as a function of the leaching time at 150, 175 and 200 °C is shown in Fig. 10.40. The energy-depth conversion was performed by means of the THICKC computer code. The variation of X_p vs. t is very close to linear. This indicates that the disordering process is most probably reaction controlled.

Angular scans performed with the leached samples provide additional information on the nature of the distortion peak. Fig. 10.41 shows the angular scan measured with the samples leached at 150 °C for 48 h. The first window (O) was set at the distortion peak whereas the second

the squeezing of a part of the U-atoms along the strings in such a way that the distance between the neighbouring atoms becomes smaller. This second component of distortion will result in the increase of the critical angle of the scan.

For the sample leached at 200 °C for 15 h, the distortion of the UO₂ crystal is quite large and this is also reflected in the shape of the angular scan: The χ -min is much larger and the critical angles for the undistorted and distorted regions are equal. This means that displaced U-atoms now occupy positions of low symmetry in the host UO₂ lattice.

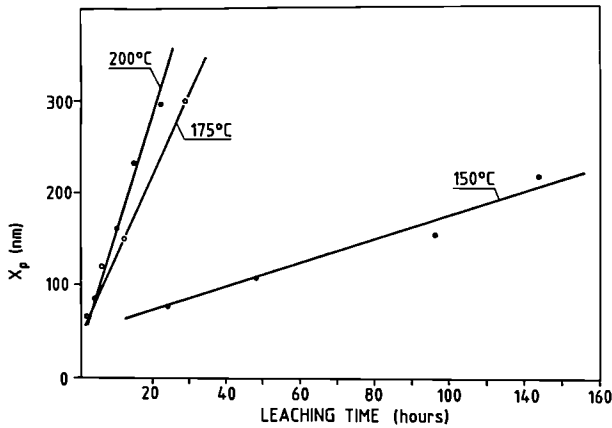


Fig. 10.40 Plot of thickness of U_3O_7 layers versus time for leaching at 150, 175 and 200°C

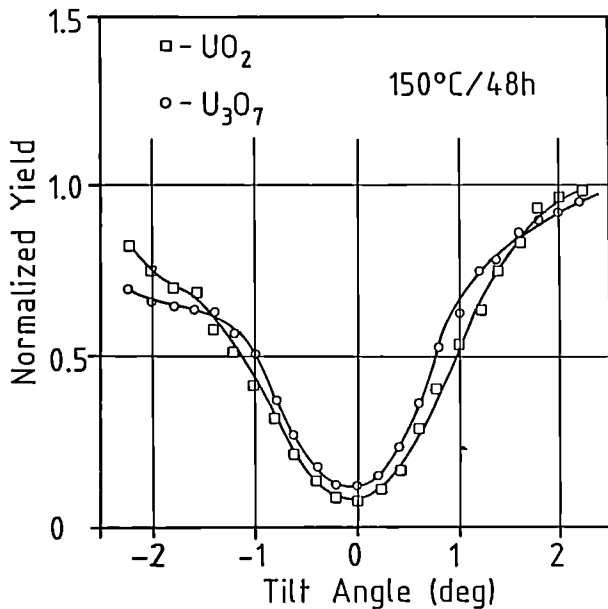


Fig. 10.41 Yield curve for UO_2 crystal and U_3O_7 layers for leaching at 150°C, 24 h

Additional information on the disordering mechanism can be obtained from an analysis of random spectra. Fig. 10.42 shows a set of random spectra with corresponding aligned ones, for the conditions 200 °C/15 h (O) and 200 °C/4h (□). A characteristic step at the depth corresponding to the penetration range of the crystal distortion can be seen in both random spectra. The counting rate deficiency in the channels above that limit can be attributed to the incorporation of impurity atoms during leaching. Assuming that these are

O-atoms one obtains the composition of the near surface layer: this layer is $UO_{2.3}$ instead of the original UO_2 . This corresponds to the formation of U_3O_7 molecules. The possible presence of H atoms was ruled out by separate measurements with elastic recoil detection analysis, ERDA, performed at the Centro di Legnaro, University of Padova.

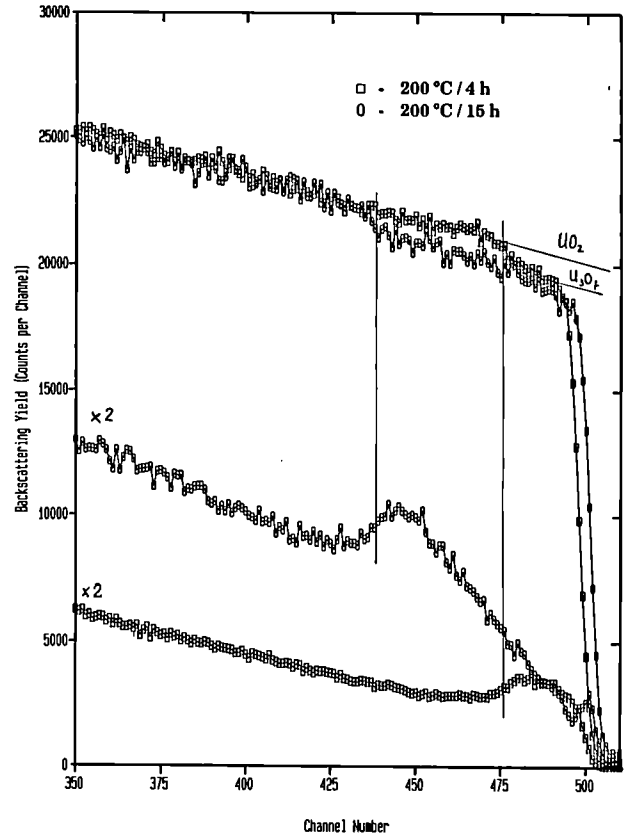


Fig. 10.42 Spectra of random and aligned UO_2 single crystals leached at 200°C for 4 and 15 h, showing the formation of U_3O_7 as surface oxide

Conclusions

The results of the investigation of UO_2 single crystals subjected to leaching at temperatures ranging from 100 °C to 200 °C by means of the channeling technique can be summarised as follows:

1. Leaching at temperatures above 130 °C results in the formation of disorder peaks in the aligned spectra. The peaks have nearly the same height; their width (i.e. the disorder penetration depth) increases with increasing leaching time.

2. Angular scans performed for leached crystals indicate that U-atoms in the distorted regions are slightly displaced from their regular lattice sites. However, with prolonged leaching time these atoms are usually displaced towards lattice sites of lower symmetry.
3. The analysis of random spectra leads to the conclusion that substantial incorporation of O atoms takes place during leaching leading to a change of the near surface layer composition from UO_2 to $\text{UO}_{2.3}$ which corresponds to the formation of U_3O_7 .
4. The kinetics of disordering is linear thus indicating that this process is controlled by the oxidation reaction taking place at the interface between the distorted and the undistorted parts of the crystal. An estimated activation energy is 1.0 eV, very close to that of oxygen diffusion in hyperstoichiometric UO_{2+x} .

11 R&D in Destructive Analysis of Fissile Materials

Conceptual Design of an On-Site Laboratory for Nuclear Material Safeguards

If the larger reprocessing plants which are presently under construction in Europe become operational, the number of verification analyses required would overload the ECSAM laboratory network. Moreover the increased number of samples would mean more transport of nuclear materials to the Institute which already causes problems. The tendency to limit such transports and have them under more stringent control would exacerbate the situation. For this reason we have studied, on request of DCS Luxembourg but also on suggestions made by an advisory committee of the IAEA, the possibility of installing on-site laboratories. They should at least condition the samples at the reprocessing plant so that the subsequent transport would be easier in the sense that only negligible amounts of fissile or radioactive material have to be transported. For this purpose we have developed a mass-spectrometric isotope dilution technique which requires only sub-nanocuries of plutonium and even less for uranium to be loaded on the filament of the mass spectrometer for analysis, and all the analyses, including mass spectrometric measurements, could be done on-site. This has been described previously in TUAR 87, 221. Underlying is the following concept:

It is assumed that the on-site laboratory is located inside the reprocessing plant and is capable of analysing all samples deriving from the open nuclear fuel cycle. In order to operate the laboratory with a minimum of personnel it is to be controlled on-line by a central laboratory.

To achieve this, the hardware on-site consists of automats extended in their functions by robots (Fig. 11.1).

1. Undiluted samples of dissolved spent fuel are treated in a hot cell by a robot which loads them into the cuvettes of a K-edge-XRF [1] spectrometer, and dilutes samples for the subsequent mass-spectrometric isotope dilution analysis of U and Pu

concentrations. The same apparatus would be used for output samples: U and Pu concentrations determined by K-edge densitometry, the plutonium isotopic composition and the Am-241 content determined by gamma-spectrometry using the detector of the densitometer. This set-up is under development.

2. A second robot performs the isotope dilution analyses, including the conditioning, separation, preparation of alpha planchettes and collection of the alpha-spectra, and loading the mass-spectrometer filaments [2].
3. The quantitative analysis of U and Pu by titration is to be carried out by the third robot. Product samples (solid or liquid form) will be handled by this robot which also could be used to aliquot samples for mass-spectrometric isotope dilution analysis or to fill the cuvettes for the K-edge densitometer. This set-up is still to be developed.

The software to operate the automats consists of

1. An expert system. This initiates the analyses by selecting the appropriate analysis type, sample size etc. from which the sequence of operation of the robot is determined. The samples are identified by a barcode label printed by the expert system ensuring that no sample mix-up takes place [3].
2. The programs for the evaluation of the analyses, collecting the already reduced data from the automats and combining them to the final analytical statement.
3. An expert system for the quality control which analyses the measurement data using standard statistical techniques and results of control samples introduced by the first expert system.

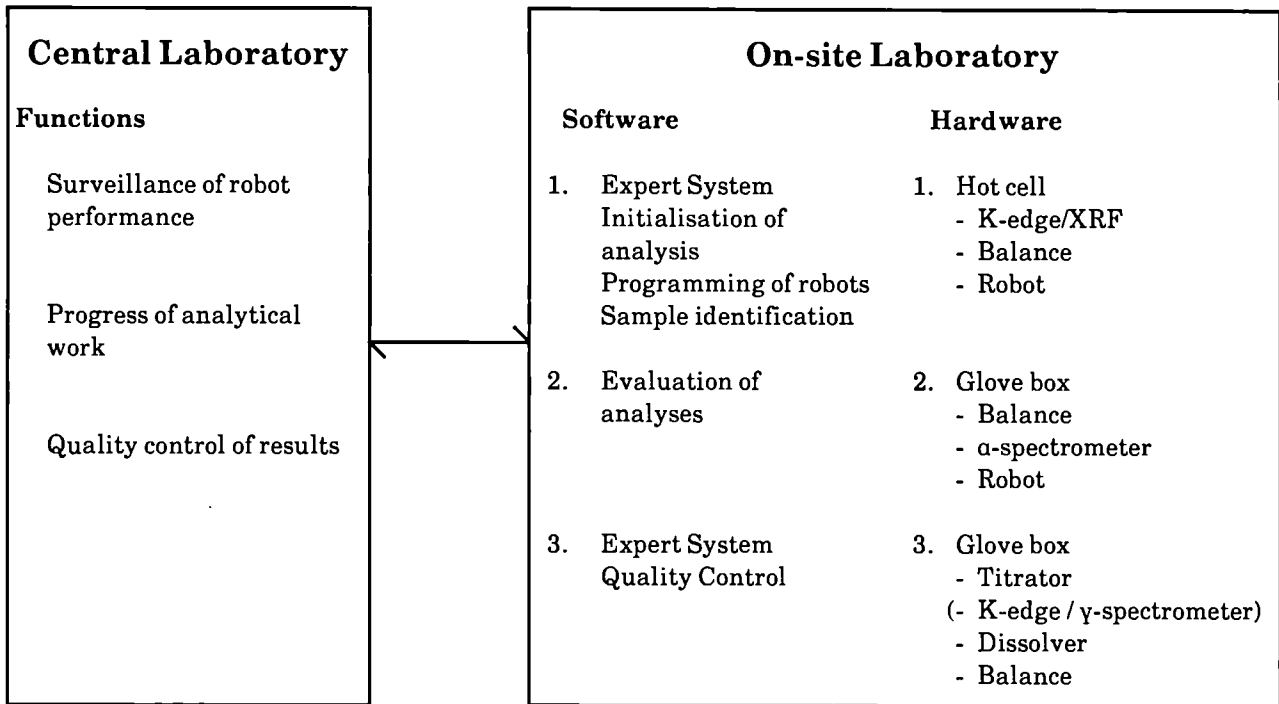


Fig. 11.1 Scheme of on-site laboratory - central laboratory

The performance of the robots as well as the progress of the analyses are monitored on-line from the central laboratory. The results of the quality control and the analyses results are scrutinised at the central laboratory before the results are accepted and transmitted. Duplicate samples are selected on a statistical basis and sent to the central laboratory for performance checking.

References

- [1] H. Ottmar, H. Eberle, L. Koch, R. De Meester, E. Kuhn, "Field Demonstration of an X-Ray Densitometer for Uranium and Plutonium Input Verification in Reprocessing", Inter. Atomic Energy Agency, Vienna, Proceedings of Nuclear Safeguards Technology 1986, Vol. I, IAEA-SM-293/48, (1987) 201
- [2] L. Koch, "New Concept for Reprocessing Input Verification", Proceedings of the 3rd International Conference on Facility Operations Safeguards Interface, San Diego, California, 19.11.1988
- [3] D. Wojnowski, B. Brandalise, M. Merten, L. Koch, "Expert System for Preparation of Safeguards Sample Analyses", Proceedings of the 2nd International Conference on Analytical Chemistry in Nuclear Technology, Karlsruhe, 5th June 1989

12 Support to Community Policies

IAEA Support Programme

Our contribution to the 'Cooperative Support Program in the Field of Research and Development in Safeguards' between the IAEA and the Commission has been budgeted up to now by the Fissile Material Control program. Our laboratory has been involved in three tasks:

MT 14	automatic analysis and data valuation
MT 14a	automatic sample conditioning by robots
MT 14b	cooperative field test for on-site conditioning by robots

The K-edge XRF developed by KfK as part of the first task has been field tested in the Institute. However, due to the long closure of the WAK reprocessing plant the field testing of the K-edge XRF could not be concluded. Several samples have been analysed by this technique and also by routine IDMS. However the results could not be compared since the density measurements of the samples at the reprocessing plant were based on unfiltered solutions.

As part of the second task, the installation of a laboratory robot for the Safeguards Laboratory of the IAEA and the function and the design of a robot glove-box has been defined. In addition to the conditioning of reprocessing input samples for IDMS as performed in our laboratory, provision is made for separation by ion exchange. This method was developed by IAEA and will be installed by us. The components for the construction of the system have been ordered by IAEA. A flow diagram of the system is given in Fig. 12.1.

For the cooperative field test of the on-site conditioning by robot the IAEA has investigated three possibilities: in Japan, in India and in the Soviet Union. At present a test is under consideration at the reprocessing plant in Gatchina (USSR). The field test will consist of three tasks:

- A test of the reliability of the device over a period of up to one year.

- A test of the intrusiveness to inspectors and operators, under the assumption that the instrument is used by the operator under surveillance of the inspector. Here the means to exclude tampering have still to be defined.

- A test of the influence of the instrument on the accuracy of the analyses. This test would be optional, since the accuracy of the analyses is determined by the subsequent measurements provided that cross-contamination during the preparation of the sample can be ruled out.

Transmission of Data to Laboratory Computer and Incorporation of a Bar-Code Reader in the Analytical Robot System

The role of an expert system in the Safeguards analytical flow has been outlined previously (TUAR 87, 225). The instructions from the expert system are coded in an information packet which is sent via a serial line to the laboratory PDP-11 computer (Tab. 12.1). This process has been automated, taking advantage of the characteristics of the TSX-system running on the PDP-11. TSX-Plus handles time-sharing and communication serial lines separately: time-sharing lines are meant for users' terminals and communication lines for connection devices such as printers or instruments and are read and written to under program control.

The line between the personal computer and the PDP-11 is a time sharing line. The Expert System enters the TSX-Plus system as a user on the line and starts an indirect, '.COM' file. This instruction file starts a detached job and logs off the line. The detached job assigns a communication line (CL) to the line and starts the program OLREC as a detached job (a detached job is one which is independent of terminal.).

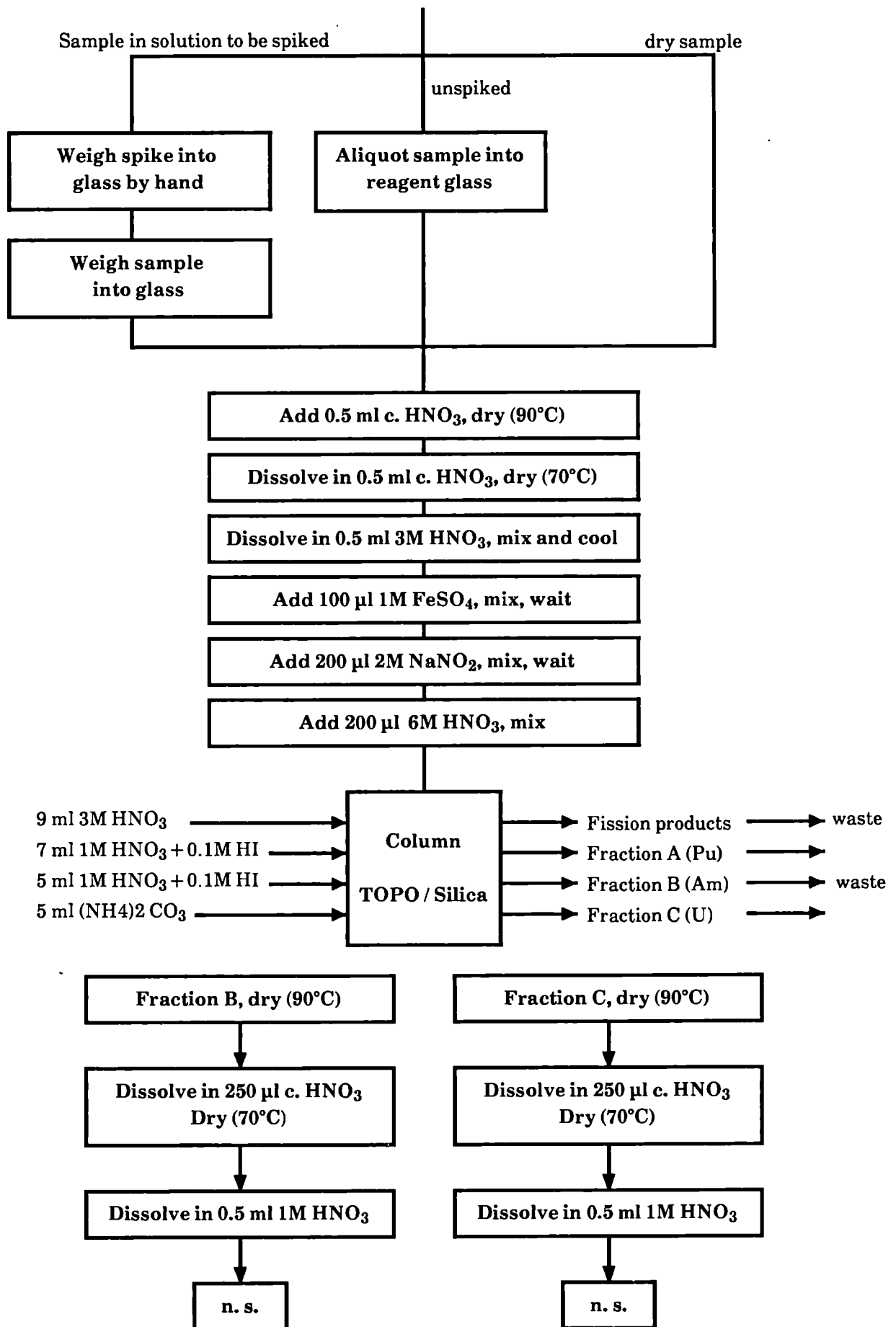


Fig.12.1 Flow diagram of robot separation scheme being implemented for SAL, IAEA

Tab. 12.1 Information packet sent from Expert System to PDP-11

Content	no. of bytes
T	1
message no.	1
sample no.	4
repeats	2
program no.	2
U spike	2
Pu spike	2
3rd spike	2
weight sample	5
weight U spike	5
weight 3rd spike	5
checksum	2
CR / LF	2

OLREC handles the communication from the PDP-11 side and accepts packets of information send from the expert system. When an 'END' packet is received, OLREC is stopped and the line reverts to a time-sharing line ready for the next contact.

The advantage of this procedure is that no operator intervention at the PDP-11 is needed: the only action to be taken is at the personal computer, selecting which data are to be sent and initiating the transfer.

The packet structure is given in Tab. 12.1. Each packet is headed with a 'T' (Transmission) and is followed by a message number between 0-9. This is followed by the sample and repeat number and then a program number which is used to specify options such as label printing, or variables in the chemistry method used by the robot. Details of 3 spikes are sent, although at present the 3rd spike is not routinely used. The checksum is calculated on the ASCII values of the characters, MOD (256), and then MOD (100) to arrive at two digits. Each packet is concluded by a carriage-return / line-feed combination.

On receiving a packet, OLREC tests that the first character is a 'T' and that the checksum is correct. If so, an 'acknowledge' block (Tab. 12.2) is

Tab. 12.2 Acknowledge packet

Content	no. of bytes
A	1
message no.	1
null	2
checksum	2
CR / LF	2

sent back, otherwise a 'negative acknowledge' block (Tab.12.3). A negative acknowledge block causes the last message block to be repeated.

Tab. 12.3 Negative acknowledge packet

Content	no. of bytes
N	1
null	3
2 2	2
CR / LF	2

Blocks are sent until no more data is to be transferred. The last block has a sample number which is predefined as an end of message declaration. The program number sent as part of each message packet defines the subsequent flow of the program OLREC. Printing of bar-code labels is an option, as is sending the data to the robot.

A unique internal number is engendered for the bar-code labels. At present this number is created by the PDP-11 program, but it appears simpler and more logical to let the Expert System do this - especially for the case where more than one robot are connected to the PDP-11. This change is

presently being incorporated. When finished, the message packet format must be extended. The bar-coded labels are stuck to the glass ampoules containing the samples to be analysed before they are inserted into the robot glove-box. Each label has the laboratory designation of the sample in readable form and the internal code as bar-code.

A laser bar-code reader, positioned outside the glove-box is connected to the robot control computer. The robot program has now been amended so that the first step is to take each sample ampoule in turn, bring it to the glove-box wall in front of the laser reader and read the bar-code. Should the robot hand accidentally block the label, the ampoule is replaced in the sample rack, rotated and taken up again to be read again.

At the start of the robot program, the data from the PDP-11 are read. These include the internal number and weight details for sample and spike for each analysis. The bar-codes as read are compared with those expected: should a lack of agreement be found the analysis is immediately stopped and operator intervention is required.

Application of the Radiometer Titralab System to the Measurement of Plutonium and Uranium

An automated titration system has been brought into commission for the routine determination of plutonium and uranium in a variety of materials. The equipment consists of a video titrator, a combination of autoburettes and a sample changer.

After the sample collectors have been manually loaded with a weighed quantity of sample solution, the system analyses each sample in turn automatically.

Uranium is measured by the modified Davies and Gray method [1] whereby the autoburettes deliver the reagents needed for the reduction of the uranium. The timing is preset to allow the various reactions to occur and the potentiometric titration is run in the controlled inflection-point mode.

Plutonium analysis is based upon the AgO-Fe(II)-Cr(VI) method [2]. In the

pretreatment step, plutonium is oxidized to plutonium(VI) by adding a small amount of silver II oxide. Decomposition of the excess silver oxide, reduction of plutonium(VI) and back-titration of the excess iron(II) is done automatically.

The performance of the system has been studied for several months by analysing samples from MOX fuel fabrication and reprocessing output solutions. The accuracy of the set up was tested by NBS uranium and plutonium metal standards in the concentration range for plutonium of 10 mg and for uranium of 40 mg whereby recoveries of $99.98 \pm 0.08\%$ ($n=15$) for Pu and $99.96 \pm 0.14\%$ ($n=50$) for U were found.

References

- [1] W. Davies and W. Gray, *Talanta*, 11 (1964) 1203
- [2] J.L. Drummond and R.A. Grant, *Talanta*, 13 (1966) 477

Establishment of Electronic Mail Service between DCS Luxembourg and the Institute

The reliable transfer of measured results from the Institute to Luxembourg and of analysis input specifications in the opposite direction has always presented problems up to now. Recently, DATEX-P has been employed with personal computers at each end. Difficulties were still experienced and these were normal only solved by telephoning and reCOORDINATING the transmissions.

We have therefore developed a communication program which, installed at each end, carries out the transfer via DATEX-P and which incorporates a password security feature. The program was written and developed in TURBO PROLOG. the modus of operation is as follows:

The programs start automatically at set times (morning and evening) whereby the Karlsruhe program is always contacted by the Luxembourg program. The date and time is sent from Karlsruhe to Luxembourg and a password is returned. This password is unique for each data transfer session. Data, preformatted on disk is sent from Luxembourg to Karlsruhe and vice versa. A protocol is kept at each end of the start, end and possible collapse of each transfer and the protocol is printed out.

Should the printer be out of action for any reason, the protocol is held on a disk file for later printing.

If a false password was received, the session is stopped straightaway and the fact protocolled.

New program releases are sent to Luxembourg by the same mechanism. A code determines that the data is a program source code. The new source code is compiled and replaces the old program.

A version for Safeguards Inspectors in the field has been written and is expected to be released early in 1989. The Inspectors should then be able to collect data on a portable PC and sent them via an acoustic coupler direct to Luxembourg or Karlsruhe.

Software and Hardware Updates for the Laboratory Robot

Software

The Expert System which validates input data from Luxembourg has been extended and improved. The resulting analysis information is sent to the central laboratory PDP-11 computer. The data are reformatted and held in a disk file organised as a silo. Either immediately or at the instigation of the operator, tables are printed containing the internal code for the sample.

The robot is attached to the PDP-11, allowing initial data (spike number, amount of spikes and samples etc.) to be sent to the robot and in return the weights of spike and samples are sent to the PDP-11 immediately they are taken.

The robot software has also been extended to allow this conversational, two-way exchange of data with the computer to take place.

Hardware

The laboratory robot has been equipped with a barcode reader. This serves to check the barcoding which was applied to each sample and spike before introducing them into the roboter glove-box. During the sample conditioning, the barcodes are read by the robot: this prevents samples and/or spikes being inadvertently exchanged.

13 Prospective Studies

Acoustic Scavenging of Hazardous Aerosol and Gas

Introduction

A characteristic of many major accidents is that large amounts of hazardous material can be released into the atmosphere in the form of aerosol and/or gas. The release process can continue for many hours as was the case for example in Bhopal (involving the heavy gas methyl isocyanate) or for many days as was the case at Tschernobyl (where large amounts of radioactive aerosol and gas were emitted). Also characteristic of these accidents is the fact that very little can be done at present to combat the airborne spreading of the hazardous material. As the accident runs its course weather conditions and particularly wind direction determine which towns and countries are to be affected.

In the project 'Acoustic Aerosol Scavenging' the feasibility of the use of high intensity acoustic waves to combat airborne spreading of accidentally released radioactive or toxic material is investigated. The potential areas of application range from small scale laboratory spills and fires to major releases of hazardous material into the atmosphere. During the reporting period, the acoustic agglomeration of a submicron combustion aerosol produced by burning rubber in a 4.5m³ chamber was studied. Of particular interest in these laboratory scale experiments is the rate of decrease of the mass loading and how this scales with acoustic power at a source frequency of 21kHz. Based on these investigations, extrapolations of the results will be made with regard to the problem of large scale 'open-air' scavenging together with a brief discussion of some of the difficulties to be expected.

Background

Aerosol particles with diameter in the range 0.5 - 10 μ can remain airborne for very long periods of time. As can be seen from Fig. 13.1, very small particles, with diameter less than 0.5 μ m, have a

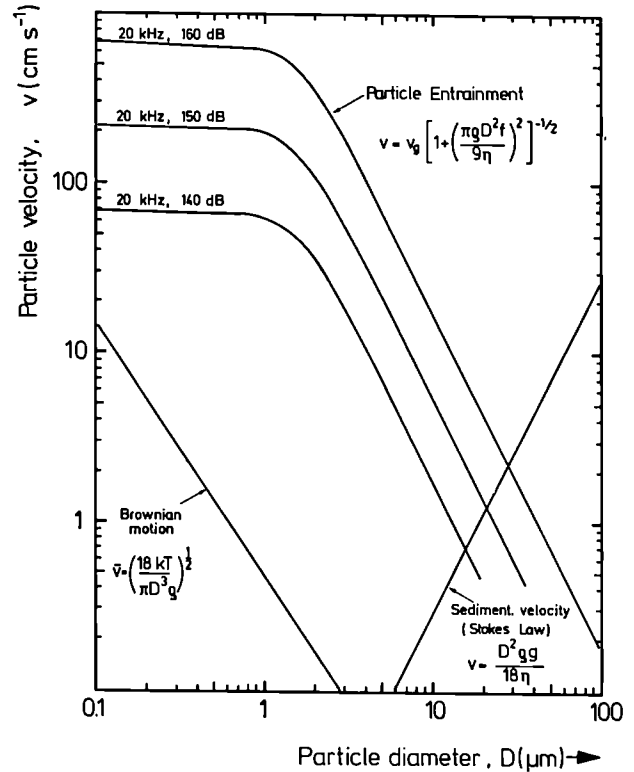


Fig. 13.1 Aerosol particle velocities due to 1. Brownian motion, 2. Sedimentation, and 3. Entrainment in a sound wave. The particles are assumed spherical with unit density.

limited lifetime due to their rapid Brownian diffusion and collision with one another resulting in larger particles. On the other hand, particles with diameter greater than about 10 μ m tend to sediment out by the action of the gravitational field.

One way of reducing the residence time of these intermediate size particles in the atmosphere is to increase the particle mass through agglomeration with other particles. This can be achieved by increasing the particle-particle collision rates through the action of some external field. Of special interest in this investigation is the application of an acoustic field, whereby very high velocities can be imparted to the particles through the viscous coupling of the gas medium to the particle. As

can be seen from Fig. 13.1, because of inertia, large particles are less entrained in the sound wave (in this example a 20kHz progressive wave). The result of this differential entrainment is to enhance the collision cross section as can be seen in Fig. 13.2 for particles with diameter 0.6 and $3\mu\text{m}$ partially entrained in a 20 kHz progressive wave. With respect to the sound wave, the 0.6 and $3\mu\text{m}$ particles have phase lags of 8 and 74 degrees, and entrainment factors of 0.99 and 0.28 respectively. The particles collide within one cycle of the wave motion. Once particles collide they stick together due to short range attractive forces. Thus provided the particle concentration is high enough, this so-called 'orthokinetic' mechanism can lead to very rapid agglomeration. Other agglomeration

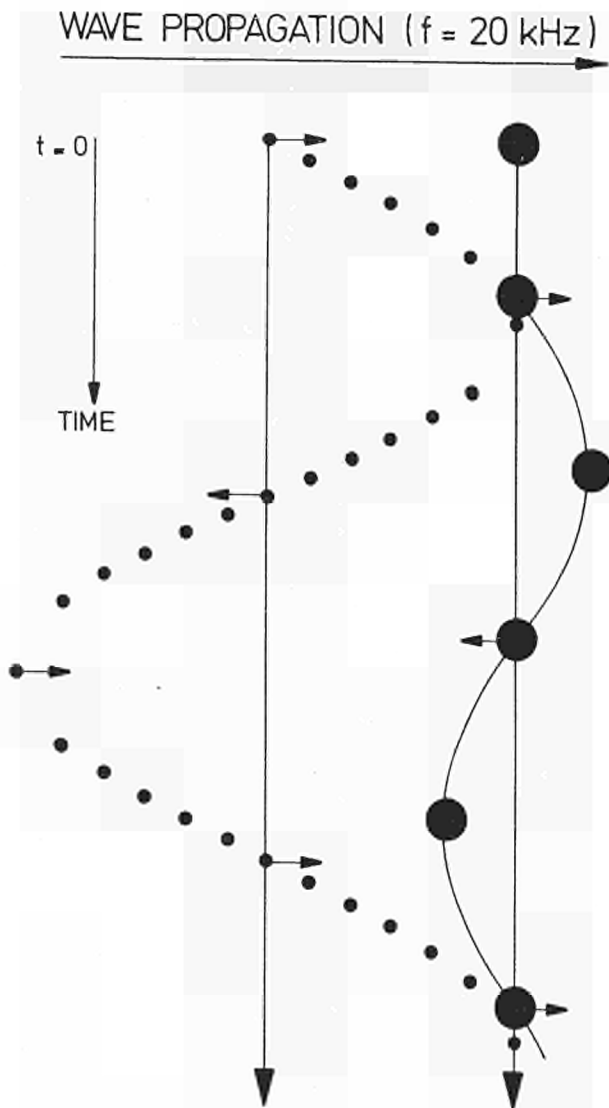


Fig. 13.2 Motion of $0.6\mu\text{m}$ (·) and $3\mu\text{m}$ (●) diameter particles in a 20 kHz progressive sound wave.

mechanisms, in particular those resulting from hydrodynamic and turbulent interactions, have been discussed extensively by Mednikov [1], but for the sound pressure levels of interest in the present experiments (SPL \ll 160 dB), the orthokinetic mechanism is believed to be dominant.

Experimental

The experiments were carried out in a 4.5 m^3 chamber shown in Fig. 13.3a. At the back of the

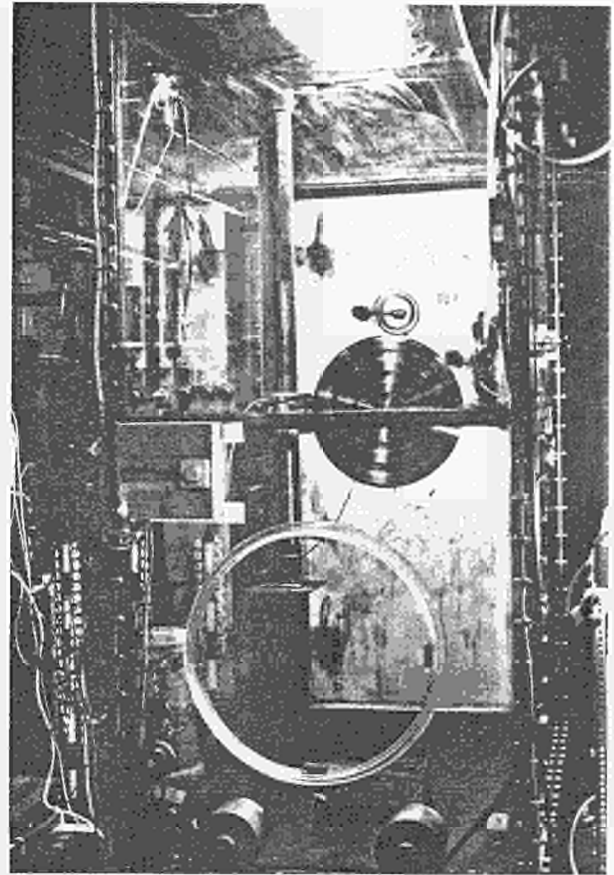


Fig. 13.3a The 4.5 m^3 experimental chamber showing the 400W transducer

chamber a new high power (400 watt), high efficiency (70%), acoustic transducer can be seen. The design and construction of these transducers have been described in detail [2]. The metal rack supporting the rubber to be burned can be seen at the bottom of the chamber. After lighting the rubber (Fig. 13.3b) the chamber quickly fills with a dense black smoke. By the time the fire goes

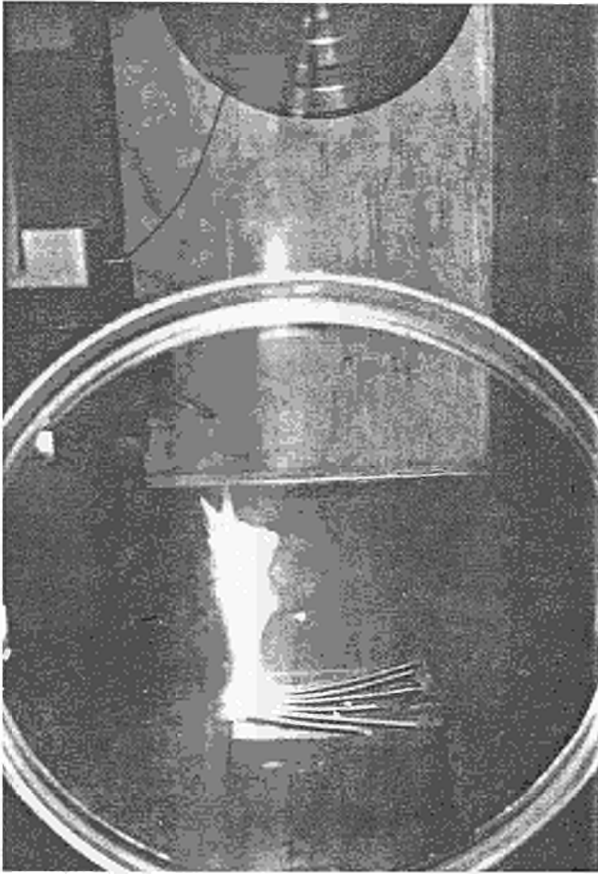


Fig. 13.3b The 4.5m³ experimental chamber showing burning rubber.

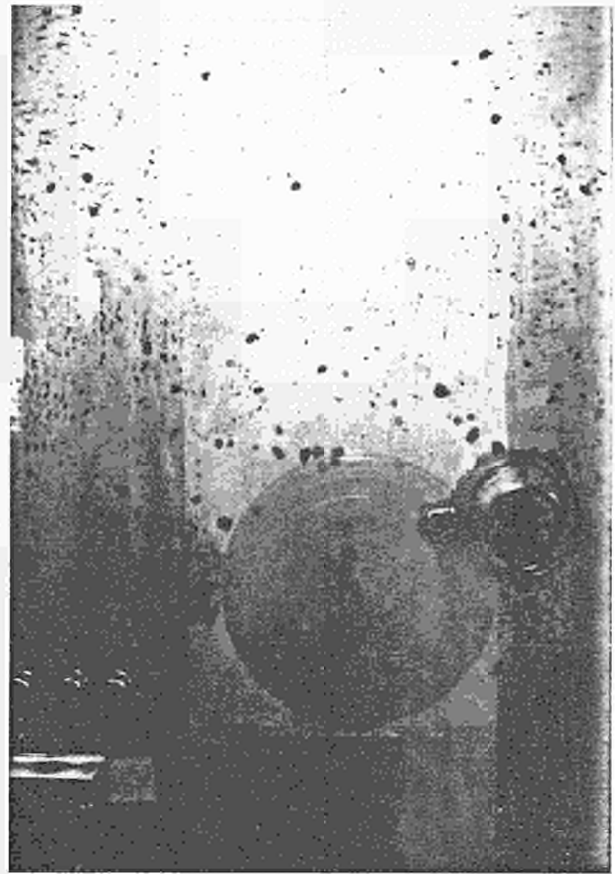


Fig. 13.3c The 4.5m³ experimental chamber showing large agglomerated flakes resulting from the agglomeration of the dense soot aerosol.

out, the chamber is completely opaque due to the soot aerosol in this case with a mass loading of 1 gm^{-3} . The primary aerosol particles, resulting from the condensation of the hot gases, have a diameter of less than 0.1μ but, due to Brownian diffusion, agglomerate on a timescale of about one minute to a 'diameter' of about 0.6μ . Thereafter, the aerosol remains very stable for periods of a few hours (provided no acoustic field is applied). Upon switching on the sound field, the agglomeration process proceeds rapidly. Within a few minutes, one sees the chamber clearing and large black flakes beginning to appear throughout the volume of the chamber, suspended by the action of acoustic radiation pressure forces as can be seen in Fig. 13.3c. These flakes can grow to several centimetres in diameter - a factor of more than 10^4 over the initial diameter. When the sound field is switched off, the flakes fall to the floor of the chamber under the action of gravity at a velocity of about 12 cms^{-1} which is equivalent to an aerodynamic diameter of about 60μ . The time variation of the aerosol mass loading as a

function of the acoustic power and time is given in Fig. 13.4 for a soot aerosol with initial mass loading of 1 gm^{-3} . At maximum transducer power of 400 W (electrical), the mass loading of the aerosol is decreased by a factor ten in about fifteen minutes, at which point the chamber is completely transparent. Full details of these experiments are described elsewhere [3].

'Open-Air' Scavenging

It has recently been proposed to use high intensity sound waves to combat a major release of radioactive or toxic aerosol into the environment [4]. The basic idea is to acoustically agglomerate the hazardous aerosol and then, through the non-linear interaction of the sound wave, force the agglomerates to drift towards the sound source where they are collected. The acoustic generators will be mounted on some type of aircraft and hover above the scene of the

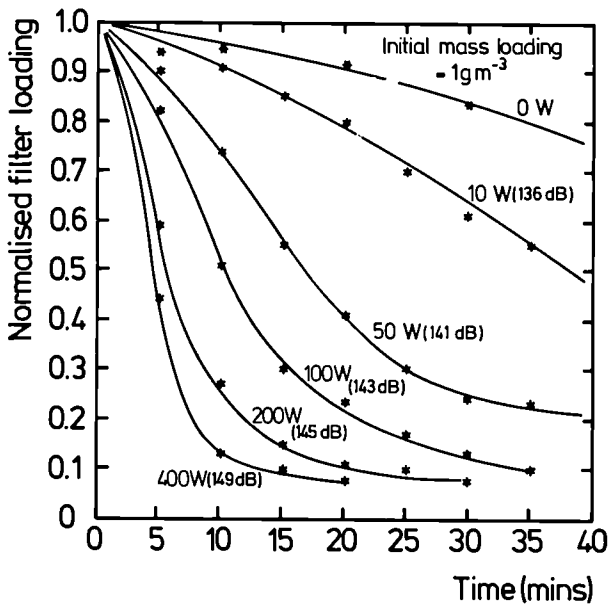


Fig.13.4 The normalised filter loading as a function of time for various transducer (electrical) power levels.

accident to scavenge the hazardous material during the release time. As a first step in considering this two step scavenging procedure (agglomeration and collection), we consider only the agglomeration and sedimentation of the particles in the gravitational field. For the purpose of the present calculations the characteristics of the cloud to be 'scavenged' are given in Tab. 13.1.

Tab. 13.1 Cloud Characteristics

Diameter of the cloud:	100 m
Volume of the cloud:	$5.24 \times 10^5 \text{ m}^3$
Mass loading of the aerosol:	1 g m^{-3}
Mean particle diameter:	$1 \text{ }\mu\text{m}$
Density of particle:	1 g cm^{-3}
Concentration of particles:	$1.9 \times 10^{12} \text{ m}^{-3}$
Distance between the particles:	$100 \text{ }\mu\text{m}$
Total mass of aerosol:	524 kg

Due to the differential motion of the particles and the gas medium through which the sound wave is propagating, energy is lost from the wave through viscous absorption. The power dissipated per unit volume is given by [1] :

$$P = 1/4 \omega U_g^2 M_L \sin 2\Theta \quad (1)$$

where $\omega = 2\pi f$, f is the frequency and U_g the velocity amplitude of wave, M_L is the aerosol

mass loading, and Θ is the phase lag between the particle and wave. When there is no differential motion, the particles are fully entrained in the wave (i.e. $\Theta = 0$) and no energy is dissipated as is the case for gas molecules. In the limit of large particle diameter, the particle remains stationary and the differential motion is a maximum ($\Theta = \pi/2$). Although energy is dissipated in this case, the power absorbed per unit volume given by relation (1) tends to zero since the concentration of the particles, for a fixed mass loading, tends to zero. Strictly, the above relationship is only applicable to a monodisperse aerosol.

From relation (1) it follows that the power dissipated through viscous absorption can be very large - especially at high frequencies. At a frequency of 20kHz and a SPL = 140dB (corresponding to $U_g = 6.6 \cdot 10^{-1} \text{ m/s}$) the power dissipated in an aerosol with mass loading 1 g m^{-3} and particle diameter $1 \text{ }\mu\text{m}$ is $P = 9.2 \text{ W m}^{-3}$. The values used here correspond to the experiments in the chamber described earlier. Extrapolation to large scale, using the cloud characteristics given in Tab. 13.1, yields a total power dissipated of $P_{\text{cloud}} \approx 5 \text{ Megawatt}$.

The very large power required is a direct consequence of relation (1) where it can be seen that the power lost through viscous absorption by the particles increases linearly with frequency. This effect is seen clearly in Fig. 13.5. It also follows from relation (1) that the absorbed power

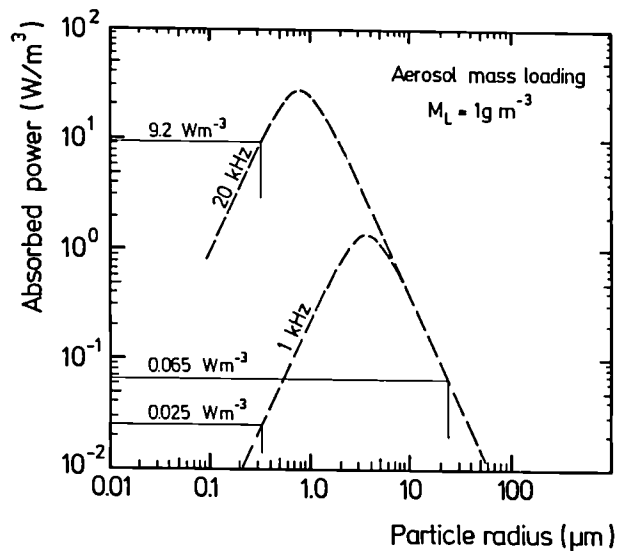


Fig. 13.5 Power lost through viscous sound absorption by aerosol particles of unit density in air.

can be considerably reduced by working at lower frequencies. The problem here, however, is that the fine aerosol particles to be scavenged are now fully entrained in the sound field, i.e. they are all moving backwards and forwards in phase with each other, and no agglomeration should take place. To overcome this difficulty we consider the addition of a 'seed' aerosol with relatively large particle size. These 'seed' particles are much less entrained in the field and can act as scavenging centres. The situation is shown schematically in Fig. 13.6 for a seed aerosol particle diameter of $33\mu\text{m}$ and mass loading of 1 gm^{-3} . In this case the

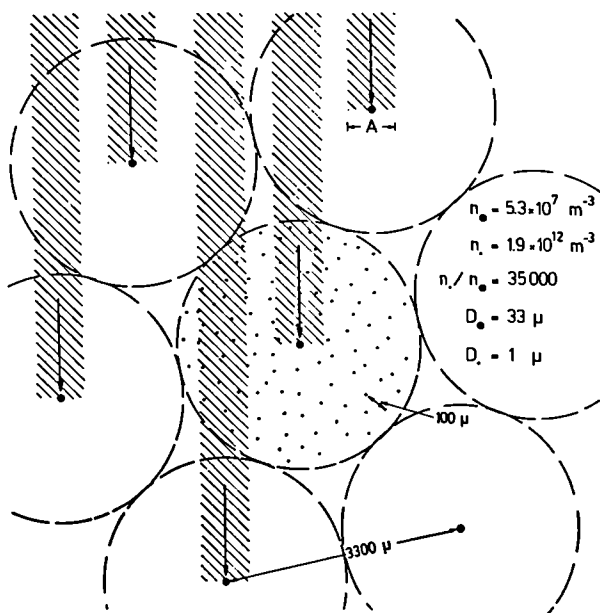


Fig. 13.6 *Acoustically enhanced aerosol scavenging by seed particles falling in a gravitational field.*

power dissipated by the 1 and $33\mu\text{m}$ particles together through viscous absorption at a frequency of 1kHz is now only 0.09 Wm^{-3} (see Fig. 13.5). The volume swept out by the heavy particle per second is $D_0 \cdot A \cdot v_{\text{sed}}$. Here D_0 is the seed particle diameter, A is twice the amplitude of the sound wave displacement, and v_{sed} is the seed particle sedimentation velocity. Since the effective volume 'covered' by each seed particle is given by $1/n_0$ (see Fig. 13.6), the time required to scavenge the fine particles is given by

$$t_{\text{sc}} = 1/(D_0 A v_{\text{sed}}) \cdot (1/n_0)$$

Here it has been assumed that each particle in

the effective volume of the falling seed particle collides and sticks. Due, however, to the tendency of the fine particles to follow the streamlines and thereby flow around the large particle, the number of collisions can be considerably reduced. The magnitude of this effect, for collisions involving spherical particles, is governed by the Stokes number Stk . In the present example $\text{Stk} \approx 0.1$, implying a very low collision efficiency. This collision efficiency is, however, extremely sensitive to the fine particle 'diameter' and requires experimental determination for the chain-like agglomerates resulting from the acoustic agglomeration process (shown in [3]). As a result, the collection efficiency should be considerably larger than that to be expected for low Stokes number spherical particles. In the following calculation we assume a collection efficiency of unity.

Consider a seed particle diameter of $D_0 = 33\mu\text{m}$ and a $\text{SPL} = 140\text{dB}$ at a frequency of 1kHz . The mass loading is assumed to be the same as that of the aerosol to be scavenged. The scavenging time reduces to $t_{\text{sc}} = 1.6$ minutes. In this time the heavy particles fall a distance of about 2.8m . It is, therefore, only necessary to irradiate a narrow section of the cloud of area $2.8\text{m} \times 100\text{m}$ for a period of 1.6 minutes. Thereafter, a different section of the cloud can be irradiated. Notice that the depth of the acoustic irradiation depends only on the absorption length of low frequency sound in air. The power dissipated through viscous absorption by the presence of aerosol particles per unit cross-sectional area amounts to 0.09 Wm^{-1} which is negligible.

The power requirements for each scanning source are determined by the sound pressure level and the area to be irradiated. At a $\text{SPL} = 140\text{dB}$ (corresponding to about 10^2 Wm^{-2}) the scanning power required is $P_{\text{scanning}} = 28\text{kW}$. Total time required to scavenge the cloud is given by the cross sectional area of the cloud divided by the scanning area times the acoustic irradiation time required for each scanning area. Based on the above scenario this time reduces to about 45 minutes. Increasing the number of acoustic power sources available decreases the irradiation time accordingly.

Acoustically Enhanced Toxic Gas Absorption

In these experiments, the time resolution has been increased, and the aerosol injection system has been improved as compared to those described in TUAR-87. A new 400 W transducer has been installed in a 500 l cylinder ; sound pressure levels of 145 to 153 db were measured in the cylinder.

Dynamic Experiment

The dynamic experiment has been described previously (TUAR-87): a short blast of air blows a known mass of aerosol in a cylinder, containing a mixture of air and of the gas to be absorbed. After introduction of the aerosol, the decrease in gas concentration in the cylinder is measured, by analyzing samples taken at various time intervals.

Tests were first done on the absorption of NO_2 by activated carbon particles (Fig. 13.7) ; the total mass of activated carbon injected in the cylinder was 8 g or 1 g. A quick absorption of the "toxic" gas was observed : within the first minute, the gas concentration drops down by a factor of 2, but then stays more or less constant. In spite of the improvement of the measurement accuracy and

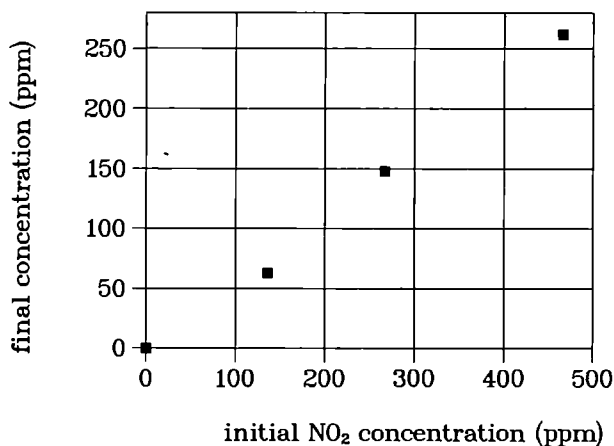


Fig. 13.7 Absorption of NO_2 by an aerosol (8g of activated carbon injected into a 500 litre cylinder) - dynamic experiment.

of the time resolution, an influence of the acoustic field on the absorption could not be confirmed ; any effect would be occulted by the rapidity of the absorption.

Therefore, it was decided to set up a steady state experiment, where the possible effect of an acoustic field could clearly be verified.

Steady State Experiment

For this new experiment, a constant flow (2.5 l/min) of air + toxic gas is passing through the cylinder, and the aerosol is continuously injected into the cylinder at a rate of 1.5 mg/min. (Fig.13.8). The results for the absorption of NO_2

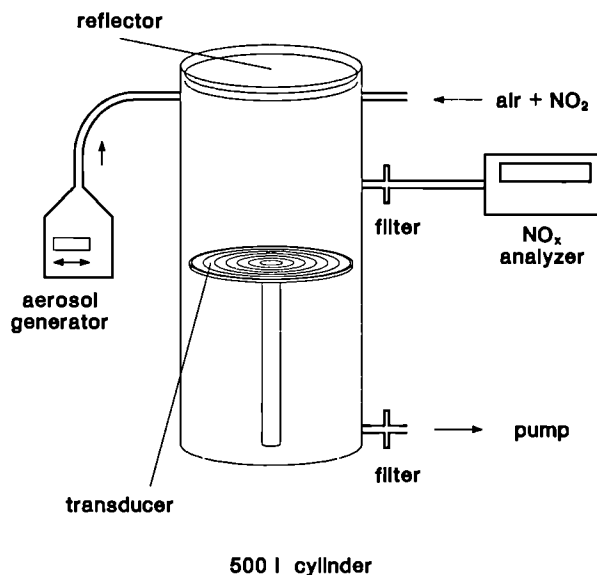


Fig. 13.8 Set-up for the measurement of the effect of an acoustic field on the absorption of NO_2 by an aerosol - steady state experiment.

on activated carbon are shown in Fig. 13.9. After balance has been reached between the incoming flows (gas + air mixture, and clean -no aerosol- aerosol carrier gas), and the outgoing flows (pumps and gas analyzer), the aerosol generator is started ; after 1 hour, new steady state concentrations are reached, due to absorption by the activated carbon aerosol, as can be seen on Fig. 13.9.

Since in the dynamic experiment, the continuous flow of gases allows the utilization of an NO_x analyzer for the determination of the

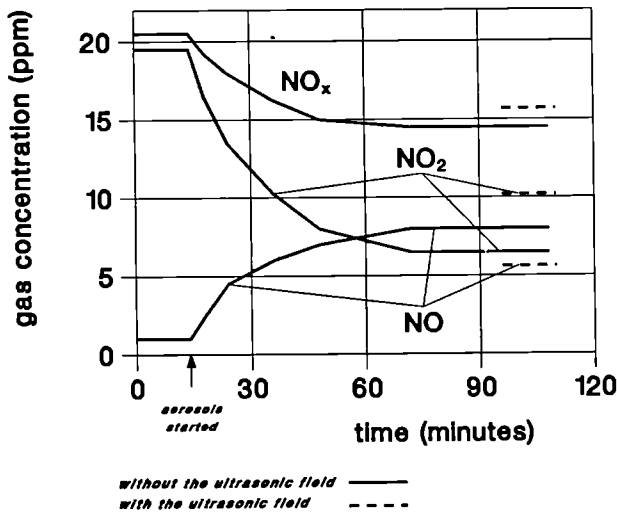


Fig. 13.9 Change of the steady NO_x concentration due to absorption by an activated carbon aerosol, with (---) and without (—) the acoustic field.

concentrations, the NO concentration could be continuously recorded: the decrease in NO_2 concentration, due to absorption by the activated carbon aerosol, corresponds to an increase in NO concentration (by a smaller amount), i.e. the total NO_x concentration goes down, but not as much as expected from the results obtained for NO_2 only during the first (dynamic) experiment. The activated carbon may act as a catalyst for the partial reduction of NO_2 to NO.

Fig. 13.9 shows also the final steady state concentrations obtained, with aerosol injection, in the presence of an acoustic field: the total NO_x absorption remains more or less unaffected by the sound field, but the conversion of NO_2 to NO is restrained. This effect, particular to the very reactive NO and NO_2 , needs further investigation to be completely understood.

Absorption of Butane by Zeolites

In order to avoid such a particular effect, the same experiments were tried again, with absorption of the less reactive butane on an aerosol of tailored zeolites; zeolites of 40 microns diameter have been ordered, but once injected in the cylinder as aerosols, their diameter was only 1 to 10 μm . The concentration measurements were done by gas chromatography.

The dynamic experiment confirmed the rapid absorption of the gas in the aerosol (within 2 minutes), with a final constant concentration of about 2/3 of the initial concentration.

The steady state experiment did not give any exploitable result, mainly because of the difficulty of producing a constant flow of aerosols in the cylinder; the aerosol generator should be adapted to the zeolites.

Summary

Acoustic agglomeration of submicron aerosol particles at relatively low mass loadings and sound pressure levels has been demonstrated in a 4.5m^3 chamber. At maximum transducer power of 400W (electrical) at a frequency of 21kHz, corresponding to a sound pressure level of 150dB, the fine particle mass loading of a dense black soot aerosol decreased by a factor ten in approximately fifteen minutes. Beyond a certain diameter (a few millimetres) the agglomerates no longer participate in the air circulation in the chamber, caused by acoustic streaming, but remain suspended throughout the volume at pressure nodes under the action of acoustic radiation pressure. On switching off the sound field the flakes fall under the action of gravity at speed of about 12cms^{-1} .

Application of acoustic scavenging in 'open-air', to combat a release of hazardous material into the atmosphere, is considered. A method is proposed in which large 'seed' particles are sprayed into the aerosol cloud to act as scavenging centres. The agglomeration of the fine particles to the large particles is enhanced by the action of the sound field. Calculations indicate that acoustic sources capable of delivering 28kW at a frequency of 1kHz and a sound pressure level of 140dB are capable of clearing an area of 280m^2 of the cloud in a time of 1.6 minutes. Future experiments will be directed at testing these ideas and, in particular, the collection efficiency of sub-micron chain agglomerates by large seed particles in the presence of a high intensity sound field. Experiments to acoustically enhance toxic gas absorption to aerosol particles were continued under dynamic as well as under steady-state conditions.

References

- [1] E. P. Mednikov, *Acoustic Coagulation and Precipitation of Aerosols*, Consultants Bureau, New York, 1965
- [2] J. A. Gallego-Juarez, G. Rodriguez-Corral, L. Gaete-Garretón, *Ultrasonics* **16** (1978) 267
- [3] J. Magill, S. Pickering, S. Fourcaudot, J. A. Gallego-Juarez, E. Riera-Franco De Sarabia, G. Rodriguez-Corral, *European Aerosol Conference*, Aug.30-Sept.2, 1988, Lund, Sweden, to be published in *J. Aerosol Sci.*
- [4] J. Magill, "Verfahren und Vorrichtung zum Entfernen einer Aerosolwolke aus der Luft", *European Patent Application EP-A 0292932*, 1988

High T_c Materials Studies

Our research on high T_c materials may be briefly characterised as follows:

- (1) It is basic in nature.
- (2) It is aimed at studying structural and magnetic properties of the superconductors and parent compounds.
- (3) The work is restricted to neutron diffraction and has (so far) used only the facilities of the Institut Laue-Langevin (ILL), Grenoble, France.
- (4) The work is restricted to single-crystal samples, because the information content of neutron diffraction is higher when the samples are in this form.

Work on YBa_2CuO_7

The superconducting compound (oxygen composition > 6.5) has an orthorhombic structure in which the a and b axes have different lengths. This orthorhombicity leads to twins of the compound in which a single crystal has a and b axes superimposed in the diffraction pattern. Our experiments are aimed at studying a possible anharmonic motion of the O atom. This is one of the postulated mechanisms driving superconductivity. In fact, because of the twinning problem, no good single crystal data exists for the compound at low temperature. Our idea is to use a position-sensitive area detector at the D9 4-circle diffractometer to separate the peaks from each twin domain.

Initial experiments demonstrating the technique were performed in April 1988. However, the crystals at that time were too small ($< 1 \text{ mm}^3$). Y. Henry (CEN, Grenoble) now has larger samples ($\sim 4 \text{ mm}^3$) and new experiments will be done in April 1989.

Collaborators are G. McIntyre (ILL) and A. Renault (U. of Grenoble).

Work on La_2NiO_4

The original, and most famous, high T_c -superconductor was Sr doped La_2CuO_4 . This parent compound has been exhaustively studied. It is antiferromagnetic (ordered moment $\sim 0.4 \mu_B$) at $\sim 300 \text{ K}$, but this ordering is rapidly suppressed when doped with Sr and Ba. One intriguing question is how the magnetism is affected so

strongly by holes in the conduction band. To study this, a program to look at the induced spin density in La_2CuO_4 was started at Brookhaven. This relates to the question of which orbitals are populated at the Cu^{2+} site, and what is the extent of hybridisation with the O 2p states. To obtain complementary information we decided to work on La_2NiO_4 .

The crystals (stoichiometric and of excellent quality ($> 20 \text{ mm}^3$)) were obtained from J. Honig (Purdue University, Indiana, USA). Experiments at ILL are performed with P.J. Brown (ILL).

First, we had to understand the structural transitions in La_2NiO_4 . These are not trivial. They go from tetragonal to orthorhombic and then to tetragonal. As a result of a collaboration with the Brookhaven National Laboratory (USA) scientists now understand this. La_2CuO_4 does not have the last orthorhombic to tetragonal transition, but both the Co and Ni compounds do. Doped materials do not revert to tetragonal so there is some (as yet unclear) relationship to superconductivity.

The polarised-neutron studies disclosed a very interesting effect along the long c-axis in La_2NiO_4 . We do not at present understand this. B. Harmon (Iowa State University, USA) is making band-structure calculations that might help. This is the topic of a publication in preparation.

Unfortunately, the BNL work on La_2CuO_4 was not done with enough precision to say if the results are similar to or different from those for La_2NiO_4 . Both the equipment and neutron intensity at ILL are better, and we may repeat these experiments at ILL. Alternatively, since we know that doped Ni compounds are superconducting, one may wish to examine one of these materials.

14 Work for Third Parties

On-line Determination of the Pu-enrichment of MOX-Fuel by Energy-Dispersive X-ray Fluorescence

In recent years, a method had been developed by the Technische Hochschule Darmstadt, using X-ray fluorescence analysis for the on-line determination of actinides in solutions of reprocessing plants [1].

The Alkem/RBU Company decided to check whether this method could be adapted for the on-line determination of the Pu-enrichment of MOX-Pellets or rods and concluded a contract with the T. H. Darmstadt to investigate this matter.

The method chosen was non-dispersive X-ray fluorescence analysis with a radionuclide as excitation source. The excitation and the measurement of the intensity of the K-lines has a number of advantages over that of the L-lines resulting in higher fluorescence yields, better penetration and resolution. In order to reduce the background due to scattering, a radionuclide with a high γ -energy of about 300 keV, i.e. Ir-192, was chosen.

As it was necessary to handle gram quantities of plutonium and an activation source of about 80 Ci, the Institute was asked to contribute to these studies.

Two test rods containing (U,Pu)O₂ pellets with 2.46, 3.01 and 4.20 % Pu were delivered from Alkem. An Ir-192 source of 80 Ci, was available at ITU and installed with the detector inside a lead shielding.

These measurements demonstrated that a non destructive on-line determination of the U- and Pu- concentration of pellets or fuel rods can be carried out with the available equipment.

Nevertheless the arrangement used could be improved as regards the positioning, precision and the optimisation of the performance of the components (probe, source, detector and shielding). Further measurements are planned in the near future.

Reference

- [1] On-line Determination of Actinide by Energy-Dispersive XRF Induced by γ -Emmiting Radionuclides, T.Hofmann, P.Hoffmann, K.H.Lieser, J. Radioanal. and Nucl. Chem., Articles, 109 (1987) 419.

IV. List of Publications

**Scientific - Technical Articles
and Monographs**

- W. Bartscher, J. Rebizant, J.M. Haschke
Equilibria and Thermodynamic Properties of the
ThZr₂ + H System
J. Less-Common Met. 136 (1988) 385-394
- E. Hovestreydt, E. Parthe, U. Benedict
ENDIX - A Computer Program to Simulate
Energy Dispersive X-Ray and Synchrotron
Powder diffraction Diagrams
J. Appl. Crystallogr. 21 (1988) 282
- Hj. Matzke, E. Toscano, C.T. Walker,
A.G. Solomah
Neptunium Doping of the Crystalline Ceramic
Waste Form SYNROC B
Advanced Ceramic Materials 3 (1988) 285-88
- H. Bokelund, K. Deelstra
Statistical Tests Applied as Quality Control
Measures to Leaching of Nuclear Waste Glasses
Radioact. Waste Manage. 11 (1988) 61-75
- J. Staun Olsen, L. Gerward, U. Benedict,
S. Dabos, O. Vogt
High-pressure Phases of Uranium
Monophosphide Studied by Synchrotron X-Ray
Diffraction
Phys. Rev. B 37 (1988) 8713-8718
- M. Hagen, W.G. Stirling, G.H. Lander
The Temperature Dependence of the Low
Frequency Magnetic Excitations in USb
Phys. Rev. B 37 (1988) 1846-1859
- M. Wulff, G.H. Lander, J. Rebizant, J.C. Spirlet
B. Lebeck, C. Broholm, P.J. Brown
Magnetic Moments and Pu form factor in PuFe₂
Phys. Rev. B 37 (1988) 5577-5585
- J. Magill, G.J. Hyland, M.H. Rand
New Ionic Contributions to the Vapour Pressure
of Urania
J. Chem. Phys. 88 (1988) 4101-4102
- R. Osborn, A.D. Taylor, Z.A. Bowden,
M.A. Hackett, W. Hayes, M.T. Hutchings,
G. Amoretti, R. Caciuffo, A. Blaise, J.M. Fournier
High Resolution Neutron Spectroscopy of
Crystal-field Excitations in Uranium Dioxide
J. Phys. C 21 (1988) L931
- O. Eriksson, B. Johansson, M.S.S. Brooks,
H.L. Skriver
Electronic Structure of the Pseudo-binary
U(Rh_{1-y}Pd_y)₃ Alloys
Phys. Rev. B 38 (1988) 12858
- J.P. Sanchez, J. Rebizant, J.C. Spirlet
237Np Mössbauer Study of a Novel Intermetallic
NpRh₂Si₂
Phys. Lett. A 128 (1988) 297
- M.R. Spirlet, J. Rebizant, J. Fuger,
J.P. Schoebrechts
Structure of Dicaesium Sodium Uranium
Hexachloride
Acta Crystallogr. C44 (1988) 1300-1301
- J. Rebizant, C. Apostolidis, M.R. Spirlet,
B. Kanellakopulos
Structure of a New Polymorphic Form of Tris
(Cyclopentadienyl)lanthanum(III)
Acta Crystallogr. C44 Part 4 (1988) 614-616
- M.S.S. Brooks, O. Eriksson, B. Johansson,
J.J.M. Franse, P.H. Frings
Chemical Bonding and Magnetism in 3d-5f
Intermetallics
J. Phys. F: Met. Phys. 18 No. 3 (1988) L33-L39
- R. Caciuffo, R. Coppola, F. Rustichelli, I.L.F. Ray
Investigation on He-Bubble Growth in Alpha
Implanted 1.4914 Steel
J. Nucl. Mater. 155-157 (1988) 916-920
- G. Van den Bossche, J. Rebizant, M.R. Spirlet,
J. Goffart
Structure of Tetrachlorotris(triphenylphosphine
oxide) thorium(IV)
Acta Crystallogr. C44 (1988) 994-996
- S. Dabos, J. Staun Olsen, L. Gerward,
U. Benedict, J.C. Spirlet
Compression of the hexagonal Laves phase UNi₂
to 41 GPa
J. Less-Common Met. 142 (1988) L19-L21
- Wang Xiang-Yun, Jin Tian Zhu, J. Goudiakas,
J. Fuger
Thermodynamics of lanthanide elements
IV: Molar enthalpies of formation of Y₃ + (aq),
YCl₃(cr), YBr₃(cr), and YI₃(cr)
J. Chem. Thermodyn. 20 (1988) 1195-1202
- G. Pautasso, K. Richter, C. Sari
Investigation of the Reaction
UO₂ + x + PuO₂ + C + N₂ by Thermogravimetry
J. Nucl. Mater. 158 (1988) 12-18
- H. Luo, S. Dabos, U. Benedict, J.C. Spirlet
Compression of the Heavy-fermion Compound
URu₂Si₂ to 50 GPa
J. Less-Common Met. 142 (1988) L23-L25

- P. Bailey, S.E. Donnelly, D.G. Armour,
Hj. Matzke
Gas Release from Pressurized Closed Pores in
Nuclear Fuels
J. Nucl. Mater. 158 (1988) 19-24
- C.T. Walker, P. Knappik, M. Mogensen
Concerning the Development of Grain Face
Bubbles and Fission Gas Release in UO₂ Fuel
J. Nucl. Mater. 160 (1988) 10-23
- G.M. Mazzucchelli, A. Milchev
Frenkel-Kontorova Model with Anharmonic
interactions
Phys. Rev. B 38(4) (1988) 2808-2812
- J. Rebizant, C. Apostolidis, M.R. Spirlet,
G.D. Andreotti, B. Kanellakopoulos
Structure of Bis(tetraethylammonium
Hexanitratouranium(IV)
Acta Crystallogr. C C44 (1988) 2098-2101
- M. Wulff, G.H. Lander
Magnetic Structure and Pu ground state in Beta-
Pu₂O₃
J. Chem. Phys. 89(5) (1988) 3295-3299
- Hj. Matzke, J. Ottaviani, D. Pellottiero,
J. Rouault
Oxygen Potential of High Burn-Up Fast Breeder
Oxide Fuel
J. Nucl. Mater. 160 (1988) 142-146
- O. Eriksson, L. Nordström, M.S.S. Brooks,
B. Johansson
4f-Band Magnetism in CeFe₂
Phys. Rev. Lett. 60 (1988) 2523-2526
- L. Gerward, J. Staun Olsen, U. Benedict,
S. Dabos, H. Luo, J.-P. Itie, O. Vogt
Bulk Moduli and High-Pressure Phases of ThX
compounds: I. The Thorium Monopnictides
High Temp. - High Pressures 20 (1988) 545-552
- J. Staun Olsen, L. Gerward, U. Benedict, H. Luo
O. Vogt
Bulk Moduli and High-Pressure Phases of ThX
Compounds: II. The Thorium monochalcogenides
High Temp. - High Pressures 20 (1988) 553-559
- K. Lassmann, H. Blank
Modelling of Fuel Rod Behaviour and Recent
Advances of the TRANSURANUS Code
Nucl. Eng. Des. 106 (1988) 291-313
- A. Cezairliyan, J.F. Babelot, J. Magill,
R.W. Ohse
Fast Radiation Thermometry (book contribution)
chapter 8 Theory and Practice of Radiation
Thermometry
Eds. D.P. DeWitt and G.D. Nutter (Wiley (1988)
529-552
- Hj. Matzke (Ed.)
"Nuclear Waste Materials", Proceedings of a
Workshop on Radiation Damage Effects in
Nuclear Waste Materials,
Lyon 6-10 July 1987
Nucl. Instrum. Methods Phys. Res. Section B B32
(1988) 453-517
- A. Blaise, J.C. Spirlet
The Low Temperature Heat Capacity of
Protactinium Metal
AERE-R 12608 (1988)
- A. Blaise, R.O.A. Hall, J.A. Lee, M.J. Mortimer
J. Rebizant, J.C. Spirlet
Transition Temperatures in PuSb
AERE-R 12609 (1988)
- P. Thevenard, A. Perez, J. Davenas, Hj. Matzke
(eds.)
Radiation Effects in Insulators - Proceedings
Fourth Int. Conf. on Radiation in Insulators -
including the Workshop on Radiation Damage in
Nuclear Waste Materials,
Lyon 6-10.7.1987
North-Holland-Amsterdam (1988) 535 pages
- K. Anderko, C.A. English, H. Kleykamp,
Hj. Matzke, H. Ullmaier, F.W. Wiffen (eds.)
Fusion Reactor Materials - Proceedings of the
Third International Conference on Fusion
Reactor Materials
(ICFRM-3) Karlsruhe, FRG, October 4-8, 1987,
Part A + B
North-Holland-Amsterdam (1988)
- J. Rebizant, M.R. Spirlet, G. van den Bossche,
J. Goffart
Structure of Tris(1-3-n-indenyl)iodouranium
Acta Crystallogr. C44 (1988) 1710-1712
- M. Bailey, W.G. Kreyling, S. Andre, A. Batchelor
A. Black, C.G. Collier, E. Drosselmeyer, G.A.
Ferron, P. Foster et al., S. Pickering et al.
An Interspecies Comparison of the Translocation
of Material from Lung to Blood
Ann. Occup. Hyg. 32 (1988) 975-985

J. Schultz, C.A. Colmenares, J.R. Naegele,
J.C. Spirlet
X-Ray Photoelectron Spectroscopy Study of the
Surface Reactions of UF_6 with O_2 , CO , and CO_2
Surf. Sci. 198 (1988) 301-314

J.P. Sanchez, P. Burllet, S. Quézel, D. Bonnissieu,
J. Rossat-Mignod, J.C. Spirlet, J. Rebizant,
O. Vogt
Mössbauer Spectroscopy and Neutron Diffraction
Studies of Neptunium Antimonide: $NpSb$
Solid State Commun. 67 (1988) 999-1002

M. Bogé, D. Bonnissieu, L. Asch-Kalvius,
G.M. Kalvius, J.C. Spirlet, J. Rebizant
 ^{237}Np Mössbauer Spectroscopy on $NpSe$
Hyperfine Interact. 40 (1988) 377-380

A.C. Lawson, C.E. Olsen, J.W. Richardson,
M.H. Müller, G.H. Lander
Structure of α -uranium
Acta Crystallogr. B44 (1988) 89-96

K. Lassmann
Treatment of the Axial Friction Forces in the
TRANSURANUS Code
Nucl. Eng. Des.

K. Lassmann
Influence of a non-uniform Power Density on the
Radial Temperature Profile in a LWR Rod
Nucl. Eng. Des.

L. Gerward, J. Staun Olsen, U. Benedict, S.
Dabos, H. Luo, J.-P. Itié, O. Vogt
Bulk moduli and high-pressure phases of the
uranium rocksalt structure compounds: I. The
monochalcogenides
High Pressure Research

J. Staun Olsen, L. Gerward, U. Benedict, S.
Dabos, J.P. Itié
Bulk moduli and high-pressure phases of the
uranium rocksalt structure compounds: II. The
monopnictides
High Pressure Research

U. Benedict (ed.)
Proceedings of the Symposium Transuranium
Elements Today and Tomorrow,
October 26-27, 1988, Karlsruhe, FRG
Special Issue J. of Nucl. Mater.

S. Dabos-Seignon, U. Benedict, J.C. Spirlet,
M. Pages
Compression Studies on PuAs up to 45 GPa
J. Less-Common Met.

M.R. Spirlet, J. Rebizant, C. Apostolidis, G.D.
Andreotti, B. Kanellakopulos
Structure of Tricyclopentadienyl Uranium
Bromide
Acta Crystallogr. C 45 (1989) 739-741

O. Eriksson, M.S.S. Brooks, B. Johansson
3d-5d Band Magnetism in Rare Earth Transition
Metal Intermetallics: $LuFe_2$
J. of Physics: Condensed Matter Physics

J. Rebizant, M.R. Spirlet, S. Betonville,
J. Goffart
Structure of Bis (1-5-n-indenyl) Uranium (IV)
Bis (tetrahydroborate)
Acta Crystallogr. C

Hj. Matzke
Nuclear Techniques in Surface Studies of
Ceramics in Nonstoichiometric Compounds,
Surfaces, Grain Boundaries and Structural
Defects
Eds. J. Nowotny and W. Weppner, MPI Stuttgart

Contributions to Conferences

- H. Bokelund, M. Ougier, M. Lebrun
Removal of Actinide Elements from Intermediate Level Liquid Waste by Precipitation with Oxalic Acid
Int. Symposium on the Management of Low and Intermediate Level Radioactive Wastes
IAEA 16.5.-20.5.1988 Stockholm (Sweden)
Proceedings IAEA - SM - 303 (1988)
- O. Eriksson, M.S.S. Brooks, B. Johansson
Magnetism in Actinide Transition Metal Intermetallics
International Conference on Magnetism ICM 88
25.7.-29.7.1988 Paris (France)
J. Phys. Colloque C8 Suppl. au no. 12 Tome 49
(1988) C8-695
- O. Eriksson, L. Norström, M.S.S. Brooks, B. Johansson
Nature of the Magnetism in CeF₂
International Conference on Magnetism ICM 88
25.7.-29.7.1988 Paris (France)
J. Phys. Colloque C8 Suppl. au no 12, Tome 49
(1988)C8-693
- G.H. Lander, W.G. Stirling, J.M. Rossat-Mignot, M. Hagen, O. Vogt
Magnetic Excitations in Monodomain Ferromagnetic UTe
Int. Conf. on Neutron Scattering
12.7.-15.7.1988 Grenoble (France)
Physica B 156 & 157 (1989) 826-828
- K. Richter, H. Blank
Fabrication of Ceramic Nuclear Fuels
CEC Yugoslavia Colloquium on Advanced Materials
12.9.-14.9.1988 Sarajewo (Yugoslavia)
- M. Wulff, B. Lebech, A. Delapalme, G.H. Lander, J. Rebizant, J.C. Spirlet
U Form Factor and 3d-5f Hybridization in UFe
Int. Conf. on Neutron Scattering
12.7.-15.7.1988 Grenoble (France)
Physica B 156 & 157 (1989) 836-838
- K.A. McEwen, W.G. Stirling, C.K. Loong, G.H. Lander, D. Fort
Crystal-Field Excitations in Polycrystalline U(Pd_{1-x}Pt_x)₃
6th Int. Conf. on Crystal Field Effects and Heavy-Fermion Physics
18.7.-21.7.1988 Frankfurt (FRG)
J. Mag. & Magn. Mat. 76 & 77 (1988) 426-428
- P.D.W. Bottomley, M. Coquerelle
Metallurgical Examination of Bore Samples from the TMI-2 Reactor Core
Topical Meeting on the Three Mile Island Accident:
Materials Behaviour, Plant Technology and Recovery
ANS/ENS 30.10.-4.11.1988 Washington, D.C. (USA)
Trans. Am. Nucl. Soc. 57 (1988) 403-404
- G.-J. Hu, B.R. Coper, G.H. Lander
Theory of Hybridization-Broadened Magnetic Response in Uranium Systems
4th International Conference on Neutron Scattering ICNS 88
12.7.-15.7.1988 Grenoble (France)
Physica B 156 & 157 (1989) 822-825
- R. Osborn, M. Hagen, D.L. Jones, W.G. Stirling, G.H. Lander, K. Mattenberger, O. Vogt
High Energy Magnetic Inelastic Neutron Scattering on USb and UTe
6th International Conference on Crystal Field Effects and Heavy-Fermion Physics
18.7.-21.7.1988 Frankfurt (FRG)
J. Mag. & Magn. Mat. 76 & 77 (1988) 429-431
- C.T. Walker, K. Lassmann, M. Coquerelle
The D-COM Blind Problem on Fission Gas Release: Further Experimental Results and Calculations with TRANSURANUS
IAEA Tech. Com. Meeting Water Reactor Fuel Element Computer
Modelling in Steady-State, Transient and Accident Conditions
19.9.-22.9.1988 Preston (UK)
Report IAEA TC-657/31
- Hj. Matzke, E. Toscano
Vickers Indentation on Radiation Damaged Cm-Containing Waste Glasses
2nd International Workshop on Indentation Techniques in connection with 7th SIMCER
13.12.-16.12.1988 Bologna (Italy)
Europ. Appl. Res. Reports
- A. Bevilacqua, Hj. Matzke
A Comparison of KIC Values of Nuclear Waste Glasses Obtained by Vickers Indentations and by Short Rod Fractometry
2nd International Workshop on Indentation Techniques in connection with 7th SIMCER
13.12.-16.12.1988 Bologna (Italy)
Europ. Appl. Res. Reports

R. Dal Maschio, Hj. Matzke, G. Della Mea
Fracture Toughness of Nuclear Waste Glasses
Following Ion Implantation at Different
Temperatures
2nd International Workshop on Indentation
Techniques in connection with 7th SIMCER
13.12.-16.12.1988 Bologna (Italy)
Europ. Appl. Res. Reports

Hj. Matzke
Recent Developments in Indentation Techniques
2nd International Workshop on Indentation
Techniques in connection with 7th SIMCER
13.12.-16.12.1988 Bologna (Italy)
Europ. Appl. Res. Reports

J.-F. Babelot, M. Hoch
The spectral emissivity of metals and nonmetals
in the wavelength range 400-15000 nanometers
and their total emissivity
11th European Conference on Thermophysical
Properties
13.6.-16.6.1988 Umea (Sweden)
Proceedings High Temp. - High Pressures

J.-F. Babelot, M. Hoch
The Constant Vaporizing Composition of UO_2
Seventh International Symposium on
Thermodynamics of Nuclear Materials
American Society for Metals
24.09.-30.09.1988 Chicago (USA)
J. Nucl. Mater.

A.G. Solomah, Hj. Matzke
Leaching Studies of Synroc Crystalline Ceramic
Waste Forms
Twelfth International Symposium on the
Scientific Basis for Nuclear Waste Management
10.10.-13.10.1988 Berlin (FRG)
Mat.Res.Soc.Symp.Proc. 127 (1989) 241-248

Hj. Matzke, H.G. Scheibel, V. Friehmelt
Characterization of Waste Glasses using
Vickers Indentations, Short Rod Fractometry
and Drop Tests
Twelfth International Symposium on the
Scientific Basis for Nuclear Waste Management
10.10.-13.10.1988 Berlin (FRG)
Mat.Res.Soc.Symp.Proc. 127 (1989) 173-180

Hj. Matzke
Fission Gases in Nuclear Fuels
Colloque de Métallurgie - Les Gaz dans les
Matériaux
INSTN, CEA 20.06.-22.06.1988 Saclay (France)
Proceedings Ann. Chim. Fr., 14 (1989) 133-147

J. Magill, S. Pickering, S. Fourcaudot,
J.A. Gallego-Juarez, E. De Sarabia,
G. Rodriguez-Corral
Ultrasonic Aerosol Agglomeration at Low Mass
Loadings
European Aerosol Conference
30.08.-02.09.1988 Lund (Sweden)
J. Aerosol Sci.

J.C. Spirlet
New Techniques in the Preparation Chemistry of
Transuranium Materials
Transuranium Elements Today and Tomorrow
JRC Karlsruhe
26.10.-27.10.1988 Karlsruhe (FRG)
Proceedings J. Nucl. Mater.

U. Benedict, S. Dabos-Seignon, C. Dufour, H. Luo
S. Heathman
Transuranium Materials under Extreme
Pressures
Transuranium Elements Today and Tomorrow
JRC Karlsruhe
26.10.-27.10.1988 Karlsruhe (FRG)
Proceedings J. Nucl. Mater.

J.R. Naegele
Surface Analysis of Actinide Materials
Transuranium Elements Today and Tomorrow
JRC Karlsruhe
26.10.-27.10.1988 Karlsruhe (FRG)
Proceedings J. Nucl. Mater.

H. Blank, K. Richter, M. Coquerelle, Hj. Matzke
M. Campana, C. Sari, I.L.F. Ray
Dense Fuels in Europe
Transuranium Elements Today and Tomorrow
JRC Karlsruhe
26.10.-27.10.1988 Karlsruhe (FRG)
Proceedings J. Nucl. Mater.

K. Lassmann
The Role of Modelling in Fuel Research, Reactor
Operation and Safety
Transuranium Elements Today and Tomorrow
JRC Karlsruhe
26.10.-27.10.1988 Karlsruhe (FRG)
Proceedings J. Nucl. Mater.

Hj. Matzke, H. Blank
Fuel Research and Basic Aspects of Fuel In-Pile
Performance
Transuranium Elements Today and Tomorrow
JRC Karlsruhe
26.10.-27.10.1988 Karlsruhe (FRG)
Proceedings J. Nucl. Mater.

H. Bokelund, C. Apostolidis, J.-P. Glatz
Recovery and Chemical Purification of Actinides
Transuranium Elements Today and Tomorrow
JRC Karlsruhe
26.10.-27.10.1988 Karlsruhe (FRG)
Proceedings J. Nucl. Mater.

S. Pickering, K. Buijs, B. Chavane
The Dispersion of Radioactive Aerosols in Fires
Transuranium Elements Today and Tomorrow
JRC Karlsruhe
26.10.-27.10.1988 Karlsruhe (FRG)
Proceedings J. Nucl. Mater.

J. Magill, S. Fourcaudot, S. Pickering,
J.A. Gallego-Juarez
E. Riera, G. Rodriguez-Corral
Acoustic Aerosol Scavenging
Transuranium Elements Today and Tomorrow
JRC Karlsruhe
26.10.-27.10.1988 Karlsruhe (FRG)
Proceedings J. Nucl. Mater.

M. Boge, D. Bonniseau, P. Burlet, J.M. Fournier
E. Pleska, S. Quezel, J. Rebizant, J. Rossat-
Mignod, J.C. Spirlet, M. Wulff
Magnetic and Electrical Properties of NpRu_2Si_2
Transuranium Elements Today and Tomorrow
JRC Karlsruhe
26.10.-27.10.1988 Karlsruhe (FRG)
Proceedings J. Nucl. Mater.

Hj. Matzke, H. Blank, M. Coquerelle,
K. Lassmann, I.L.F. Ray, C. Ronchi, C.T. Walker
Oxide Fuel Transients
Transuranium Elements Today and Tomorrow
JRC Karlsruhe
26.10.-27.10.1988 Karlsruhe (FRG)
Proceedings J. Nucl. Mater.

H.L. Müller, A. Taya, E. Drosselmeyer, G. Hotz
S. Pickering, I.L.F. Ray, A. Seidel, H. Thiele
Cellular Aspects of Retention and Transport of
Inhaled Soluble and Insoluble Actinide
Compounds in the Rat Lung
Transuranium Elements Today and Tomorrow
JRC Karlsruhe
26.10.-27.10.1988 Karlsruhe (FRG)
Proceedings J. Nucl. Mater.

A. Grassman, J.R. Naegele, K. Söldner,
G. Saemann-Ischenko
Electronic Structure of U_6T (T = Mn, Fe, Co, Ni)
Studied by Photoemission Spectroscopy
6th Int. Conf. on Crystal Field Effects and Heavy-
Fermion Physics
18.7.-21.7.1988 Frankfurt (FRG)
J. Mag. & Magn. Mat. 76 & 77 (1988) 359-360

O. Eriksson, B. Johansson, M.S.S. Brooks
Electronic Structure and Magnetic Properties of
the $\text{Y}(\text{Fe}_{1-x}\text{Co}_x)_2$ alloys
International Conference on Magnetism ICM 88
25.7.-29.7.1988 Paris (France)
J. Phys. Colloque C8 Suppl. au no. 12 Tome 49
(1988) C8-295

S. Blumenröder, H. Brenten, E. Zirngiebl,
R. Mock, G. Güntherodt, J.D. Thompson, Z. Fisk,
J. Naegele
Light Scattering in Heavy Fermion Compounds
6th Int. Conf. on Crystal Field Effects and Heavy-
Fermion Physics
18.7.-21.7.1988 Frankfurt (FRG)
J. Mag. & Magn. Mat. 76 & 77 (1988) 331-334

J.P. Hiernaut, C. Ronchi
Determination of the Melting Point and the
Emissivity of Refractory Metals with a Six-
Wavelength Pyrometer
11th European Conference on Thermophysical
Properties
13.6. - 16.6.1988 Umea (Sweden)
High Temp. - High Pressures Vol. 21 (1989)

J.P. Hiernaut, C. Ronchi
Calorimetric Measurements with Acoustic
Levitation in High-Temperature Heating
Experiments with Pulsed Laser Beams
11th European Conference on Thermophysical
Properties
13.6.-16.6.1988 Umea (Sweden)
High Temp. - High Pressures 21 (1989)

H. Blank, K. Richter
New Concepts for Fast Reactor Fuels
Jahrestagung Kerntechnik '88
Deutsches Atomforum
17.05.-19.05.1988 Travemünde (FRG)

O. Eriksson, B. Johansson, L. Nordström,
M.S.S. Brooks, H.L. Skriver
Electronic Structure of Pseudo-Binary
 $\text{U}(\text{Rh}_{1-y}\text{Pd}_y)_3$ Alloys
8th General Conf. of the Condensed Matter
Division of the European Physical Society
6.4.-9.4.1988 Budapest (Hungary)

L. Koch, S. Franzini, R. De Meester
Quantitative Analysis of Actinides in Highly
Active Waste of Nuclear Fuel Processing
2nd Int. Symposium on Nuclear and
Radiochemistry and Exhibition
11.7.-15.7.1988 Brighton, Sussex (UK)

A.G. Solomah, Hj. Matzke, R. Odoj
 Immobilization of Neptunium in Crystalline
 Ceramic Waste Forms
 90th Annual Meeting of the American Ceramic
 Society
 1.5.-5.5.1988 Cincinnati (USA)

H.A. Tasman
 Thermal conductivity of liquid UO_2
 11th European Conference on Thermophysical
 Properties
 13.6.-16.6.1988 Umea (Sweden)

J. Goudiakas, B. Gilbert, J. Fuger
 Thermodynamics of Some Lanthanide and
 Actinide Complex Oxides
 18e Journées des Actinides
 20.04.-22.04.1988 Paris (France)

C. Apostolidis, B. Kanellakopulos, J. Müller,
 B. Powietzka
 Synthesis and Investigation of Bis
 (Pentamethylcyclopentadienyl) Neptunium (IV)
 Dichloride, $Np((CH_3)_5Cp)_2Cl_2$: Evidence for Np-Np
 Magnetic Interaction
 18e Journées des Actinides
 20.04.-22.04.1988 Paris (France)

C. Apostolidis, H. Bokelund, M. Ougier
 Speciation of Neptunium in Concentrated Nitric
 Acid. Absorption Spectra of Np(IV), Np(V) and
 Np(VI)
 18e Journées des Actinides
 20.04.-22.04.1988 Paris (France)

K. Mayer, L. Koch, J. Naegele, K. Richter
 On the Interaction of Sodium with
 Hypostoichiometric Uranium-50% Americium
 Mixed Oxides
 18e Journées des Actinides
 20.04.-22.04.1988 Paris (France)

J.P. Sanchez, R. Poinso, J. Rebizant, J.C. Spirlet
 ^{237}Np Mössbauer Study of the Intermetallic
 Compound $NpRh_2Si_2$
 18e Journées des Actinides
 20.04.-22.04.1988 Paris (France)

F. Wastin, J. Rebizant, J.C. Spirlet, J. Fuger
 J. Goffart
 Synthesis and Characterisation of New
 Intermetallic Compounds
 18e Journées des Actinides
 20.04.-22.04.1988 Paris (France)

M. Wulff, G.H. Lander, A. Hewat
 Magnetic Structure and Form Factor of Pu^{3+} in
 Pu_2O_3
 18e Journées des Actinides
 20.04.-22.04.1988 Paris (France)

J. Rebizant, C. Apostolidis, M.R. Spirlet, G.D.
 Andreotti, B. Kanellakopulos
 Crystal Structure of Bis(Tetraethylammonium)
 Hexanitrate Uranium: A Twelve Coordinated
 Uranium(IV)Complex
 18e Journées des Actinides
 20.04.-22.04.1988 Paris (France)

J. Naegele, J.C. Spirlet
 Photoemission Investigation of 5f Electron
 Localization in Am-Pu Binary Alloys
 18e Journées des Actinides
 20.04.-22.04.1988 Paris (France)

S. Dabos-Seignon, U. Benedict, S. Heathman,
 J.C. Spirlet
 Phase Transformation of $NpSb$ Under High
 Pressure
 18e Journées des Actinides
 20.04.-22.04.1988 Paris (France)

J.C. Spirlet, J. Rebizant, C. Rijkeboer,
 J. Peterson, O. Vogt
 Single Crystal Growth of Actinide Monopnictides
 and Monochalcogenides
 18e Journées des Actinides
 20.04.-22.04.1988 Paris (France)

H. Luo, K. Syassen, U. Benedict, O. Vogt
 High Pressure Optical Studies of Uranium and
 Thorium Compounds UAs, UP and ThAs
 18e Journées des Actinides
 20.04.-22.04.1988 Paris (France)

U. Benedict
 General Diagram of the Phase Relations of
 Actinide Metals Under Pressure
 18e Journées des Actinides
 20.04.-22.04.1988 Paris (France)
 ORA 33962

G.H. Lander, M. Wulff
 Spin and orbital effects in 5f compounds
 Sagamore IX Conference on Charge and Spin
 Density
 27.6.-30.6.1988 Coimbra (Portugal)

A. Turos, Hj. Matzke, S. Fritz
 Radiation Defect Behavior in UO_2 - A
 Channeling Study
 Int. Conf. on Defects in Insulating Crystals
 29.8.-2.9.1988 Parma (Italy)

H. Blank, Hj. Matzke, R. Manzel, M. Coquerelle
I.L.F. Ray, C.T. Walker, K. Lassmann, C. Ronchi
Verhalten von UO_2 in Druckwasserreaktoren bis
zu hohem Abbrand im stationären Betrieb und
bei Transienten
Jahrestagung Kerntechnik '88
Deutsches Atomforum 1
7.05.-19.05.1988 Travemünde (FRG)

J.A. Fahey, J. Fuger, T. Fujino, L.R. Morss
C.W. Williams
Syntheses and X-Ray Powder Diffraction of
 Rb_2BkCl_6 and $(\text{N}(\text{CH}_3)_4)_2\text{BkCl}_6$
18th Rare Earth Research Conference
11.9.-15.9.1988 Interlaken (Switzerland)

M. Mogensen, C.T. Walker
Concerning the Development of Grain Face
Bubbles and Fission Gas Release in UO_2 Fuel
Enlarged Halden Meeting
8.5.-13.5.1988 Loen (Norway)

L. Koch, R. de Meester, S. Franzini,
H. Wiesmann
Adaptation of ICP-MS to a Glove Box for the
Analysis of Highly Radioactive Samples
The First International Conference of Plasma
Source Mass Spectrometry
12.9.-16.9.1988 Durham (UK)

R.A. Verrall, B.J.F. Palmer, I.J. Hastings,
Hj. Matzke, D.H. Rose, A.Y.H. Gin,
D.M. Schreiter
Gas Release from Oxide SIMFUEL
IAEA Technical Committee Meeting
Water Reactor Fuel Element Computer
Modelling
19.09.-23.09.1988 Preston (UK)

Hj. Matzke
Surface Diffusion and Surface Energies of
Ceramics
Surfaces and Interfaces of Ceramic Materials
NATO Advanced Institute
04.09.-16.09.1988 Oleron (France)

F. Lanza, Hj. Matzke
Surface Modification with Ion and Laser Beams:
Theory and Applications
CEC Yugoslavia Colloquium on Advanced
Materials
12.09.-14.09.1988 Sarajevo (Yugoslavia)

G.H. Lander
The Potential of "large machines" for the Study
of Actinide Materials
Transuranium Elements Today and Tomorrow
JRC Karlsruhe
26.10.-27.10.1988 Karlsruhe (FRG)

R. Caciuffo
A Spectrometer for Laboratory EXAFS Analysis
Congrès sur les techniques utilisées dans
l'analyse des matériaux
Univ. di Camerino September 1988 Camerino
(Italy)

L. Koch
The Possible Role of Nuclear Transmutation of
Minor Actinides in the Fuel Cycle
Transuranium Elements Today and Tomorrow
JRC Karlsruhe
26.10.-27.10.1988 Karlsruhe (FRG)

J.R. Naegele
Characterisation of Actinide Materials by
Surface Spectroscopy (Poster)
Transuranium Elements Today and Tomorrow
JRC Karlsruhe
26.10.-27.10.1988 Karlsruhe (FRG)

U. Benedict, S. Dabos-Seignon, C. Dufour, H. Luo
S. Heathman
Solids under Extreme Pressures (Poster)
Transuranium Elements Today and Tomorrow
JRC Karlsruhe
26.10.-27.10.1988 Karlsruhe (FRG)

J. Fuger
Actinide Research at the European Institute for
Transuranium Elements (Poster)
Transuranium Elements Today and Tomorrow
JRC Karlsruhe
26.10.-27.10.1988 Karlsruhe (FRG)

C.T. Walker, R. Windbiel, W. Ziehl
Hot Electron Probe Microanalysis (Poster)
Transuranium Elements Today and Tomorrow
JRC Karlsruhe
26.10.-27.10.1988 Karlsruhe (FRG)

I.L.F. Ray, H. Thiele, W. Huber
Electron Microscopy of Irradiated Nuclear Fuel
Sample (Poster)
Transuranium Elements Today and Tomorrow
JRC Karlsruhe
26.10.-27.10.1988 Karlsruhe (FRG)

K. Lassmann
 TRANSURANUS - A Computer Program for the
 Thermal and Mechanical Analysis of Fuel Rods
 (Poster)
 Transuranium Elements Today and Tomorrow
 JRC Karlsruhe
 26.10.-27.10.1988 Karlsruhe (FRG)

M. Coquerelle
 The Hot Cell Facility at ITU (Poster)
 Transuranium Elements Today and Tomorrow
 JRC Karlsruhe
 26.10.-27.10.1988 Karlsruhe (FRG)

J.P. Hiernaut, C. Ronchi, H. Tasman, P. Werner
 Laboratory of High Temperatures and
 Thermodynamics (Poster)
 Transuranium Elements Today and Tomorrow
 JRC Karlsruhe
 26.10.-27.10.1988 Karlsruhe (FRG)

H. Blank
 The ITU approach to fuel research (Poster)
 Transuranium Elements Today and Tomorrow
 JRC Karlsruhe
 26.10.-27.10.1988 Karlsruhe (FRG)

M. Coquerelle, C. Sari, H. Blank
 Analysis of Irradiated Fuels (Poster)
 Transuranium Elements Today and Tomorrow
 JRC Karlsruhe
 26.10.-27.10.1988 Karlsruhe (FRG)

H. Bokelund, J.-P. Glatz, C. Apostolidis
 Actinide Chemistry in the Nuclear Fuel Cycle
 (Poster)
 Transuranium Elements Today and Tomorrow
 JRC Karlsruhe
 26.10.-27.10.1988 Karlsruhe (FRG)

K. Richter, J.F. Gueugnon, C. Fuchs, G. Kramer
 Fabrication of Advanced Dense Fuel by the
 Direct Pressing Method (Poster)
 Transuranium Elements Today and Tomorrow
 JRC Karlsruhe
 26.10.-27.10.1988 Karlsruhe (FRG)

K. Richter, J.F. Gueugnon, J. Kalbusch, M.
 Campana
 Fuel Pin Fabrication (Poster)
 Transuranium Elements Today and Tomorrow
 JRC Karlsruhe
 26.10.-27.10.1988 Karlsruhe (FRG)

S. Pickering
 Resuspension of Uranium-Plutonium Oxide
 Particles from Burning Plexiglas (Poster)
 Transuranium Elements Today and Tomorrow
 JRC Karlsruhe
 26.10.-27.10.1988 Karlsruhe (FRG)

S. Pickering
 Particle Distributions in Simulated
 Agglomeration (Poster)
 Transuranium Elements Today and Tomorrow
 JRC Karlsruhe
 26.10.-27.10.1988 Karlsruhe (FRG)

S. Pickering, S. Fourcaudot
 The Penetration of Filters by Alpha-Active
 Aerosols (Poster)
 Transuranium Elements Today and Tomorrow
 JRC Karlsruhe
 26.10.-27.10.1988 Karlsruhe (FRG)

J. Magill, S. Pickering
 Acoustic Aerosol Agglomeration (Poster)
 Transuranium Elements Today and Tomorrow
 JRC Karlsruhe
 26.10.-27.10.1988 Karlsruhe (FRG)

L. Koch
 Potentials of Np and Am Recycling (Poster)
 Transuranium Elements Today and Tomorrow
 JRC Karlsruhe
 26.10.-27.10.1988 Karlsruhe (FRG)

L. Koch
 New Concept for Reprocessing Input Verification
 (Poster)
 Transuranium Elements Today and Tomorrow
 JRC Karlsruhe
 26.10.-27.10.1988 Karlsruhe (FRG)

K. Buijs, B. Chavane
 Contaminated Smoke: A Large Scale Simulation
 of Glove Box Fires (Poster)
 Transuranium Elements Today and Tomorrow
 JRC Karlsruhe
 26.10.-27.10.1988 Karlsruhe (FRG)

K. Buijs, B. Chavane, S. Pickering, V. Prodi
 H.E. Schmidt, A. Seidel
 Aerosol Research at the Transuranium Institute
 (Poster)
 Transuranium Elements Today and Tomorrow
 JRC Karlsruhe
 26.10.-27.10.1988 Karlsruhe (FRG)

- J. van Geel
ITU programme 1988/89 (Poster)
Transuranium Elements Today and Tomorrow
JRC Karlsruhe
26.10.-27.10.1988 Karlsruhe (FRG)
- J. van Geel
For and with whom we work (Poster)
Transuranium Elements Today and Tomorrow
JRC Karlsruhe
26.10.-27.10.1988 Karlsruhe (FRG)
- M. Bailey, W.G. Kreyling, S. Andre, A. Batchelor
A. Black, C.G. Collier, E. Drosselmeyer, G.A.
Ferron, B. Haider et al., S. Pickering et al.
Interspecies Comparison of Lung Clearance of
Inhaled Monodisperse Cobalt Oxide: Particle
Transport from the Lungs to the GI Tract
Congress on Aerosols in Medicine
1988 New York (USA)
- D. Bonniseau, P. Burlet, M. Boge, S. Quézel
J. Rossat-Mignod, J.C. Spirlet, J. Rebizant
Mössbauer and Neutron Diffraction Studies of
NpRu₂Si₂
International Conference on Magnetism ICM 88
25.7.-29.7.1988 Paris (France)
J. Phys. Colloque C8 Suppl. n° 12 Tome 49 (1988)
C8-491-492
- E. Pleska, J.M. Fournier, J. Chiapusio, J. Rossat-
Mignod, J.C. Spirlet, J. Rebizant, O. Vogt
Electrical Resistivity of NpTe
International Conference on Magnetism ICM 88
25.7.-29.7.1988 Paris (France)
- P. Burlet, J.M. Fournier, E. Pleska, S. Quézel
J. Rossat-Mignod, J.C. Spirlet, J. Rebizant, O.
Vogt
Magnetic and Electronic Properties of
Neptunium and Plutonium Compounds
International Conference on Magnetism ICM 88
25.7.-29.7.1988 Paris (France)
- G.M. Kalvius, J. Gal, F.J. Litterst, W. Potzel
U. Potzel, J. Moser, W. Schiessl, S. Zwirner
S. Fredo, S. Tabuchi, J.C. Spirlet
5f Electron Delocalization in Np Intermetallics
International Conference on Magnetism ICM 88
25.7.-29.7.1988 Paris (France)
- M. van Sprang, J.J.M. Franse, J.M. Rossat-
Mignod, J.M. Fournier, J. Chiapusio,
J.C. Spirlet
Experiments on UPt₃ Alloyed with Np
International Conference on Magnetism ICM 88
25.7.-29.7.1988 Paris (France)
- E. Pleska, J.M. Fournier, J. Chiapusio, J. Rossat-
Mignod, J.C. Spirlet, J. Rebizant, O. Vogt
Electrical Resistivity of NpTe
18mes Journées des Actinides
20.04.-22.04.1988 Paris (France)
- O. Eriksson, B. Johansson, M.S.S. Brooks
Metamagnetism in UCoAl
18mes Journées des Actinides
20.04.-22.04.1988 Paris (France)
- R.O.A. Hall, M.J. Mortimer, J.C. Spirlet
Low-temperature Heat Capacity of PuSb
18mes Journées des Actinides
20.04.-22.04.1988 Paris (France)
- K.A. McEwen, W.G. Stirling, C.K. Loong, G.H.
Lander, D. Fort
Magnetic excitations in U(Pd_{1-x}Pt_x)₃
18mes Journées des Actinides
20.04.-22.04.1988 Paris (France)
- M. Bogé, D. Bonniseau, L. Asch, G.M. Kalvius
J.C. Spirlet, J. Rebizant
Magnetic Behaviour of NpSe from Np-Mössbauer
Spectroscopy
18mes Journées des Actinides
20.04.-22.04.1988 Paris (France)
- E. Pleska, J.M. Fournier, J. Rossat-Mignod, J.C.
Spirlet, J. Rebizant
Magnetization Measurements on a NpRu₂Si₂
Single Crystal
18mes Journées des Actinides
20.04.-22.04.1988 Paris (France)
- G. Wagner, D. Tuttas, D. Poesthorst, M.
Romkowski, S. Franzini, L. Koch
Total Evaporation/Integration with Mixed
Multicollection
Modes: New Effective Approaches for Thermal
Ionization MS
36th Conference on Mass-Spectrometry and
Allied Topics
ASMS 5.6.-10.6.1988 San Fransisco, CA (USA)

Reports

C. Ronchi, J. van de Laar
 The Fuel Performance Code FUTURE
 (Description of the Models and Introduction to
 the Program)
 - EUR 11387 EN (1988)

K. Mayer
 Zur Reaktion von oxidischen Uran-Americium
 Kernbrennstoffen mit Natrium
 - EUR 11526 DE (1988)

V. Tebaldi
 Metallographie und Thermoanalyse von
 keramischen Kernbrennstoffen
 - EUR 11716 DE (1988)

K. Buijs, B. Chavane
 Contaminated Smoke: A Simulation of the
 Heavy-Metal
 Containing Aerosols from Fires in Plutonium
 Glove Boxes
 - EUR 11809 EN (1988)

European Institute for Transuranium Elements -
 Expertise and Programmes
 - EUR 11784 EN (1988)

European Institute for Transuranium Elements -
 The Institute at a Glance - Un regard sur
 l'Institut -
 Das Institut auf einen Blick (EN, FR, DE)
 - EUR 11788 (1988)

Das Europäische Institut für Transurane -
 Aus der Geschichte des Instituts
 - EUR 11789 DE (1988)

European Institute für Transuranium Elements -
 Publications 1986/87
 - EUR 11790 EN (1988)

European Institute for Transuranium Elements -
 Annual Report 1987
 - EUR 11783 EN (1988)

K. Lassmann
 TRANSURANUS Änderungsprotokoll
 Version 1 Modifikation 1 Jahr 1988 ('V1M1J88')
 - 1988 - K0288109

M. Campana, J.F. Gueugnon
 Exprience BUMMEL
 - 1988 - K0288110

K. Lassmann
 Analyse eines BWR-Brennstabs mit dem
 TRANSURANUS Rechenprogramm
 - 1988 - K0288111

H. Blank
 The Nitride Irradiations NILOC I and NILOC II
 - 1988 - K0288112

K. Lassmann, G. van Goethem
 MOLC/7 Pre-test Fuel Pin Behaviour
 Calculations Using the TRANSURANUS Code
 - 1988 - K0288113

M. Campana, J.F. Gueugnon, K. Richter
 Exprience NIMPHE 2 - Irradiation de 4 aiguilles
 carbure et nitrure mixtes dans Phénix
 - 1988 - K0288114

V. Glossary

ADC: Analog-Digital Converter
AECL: Atomic Energy of Canada, Ltd.
AERE: Atomic Energy Research Establishment
An: Actinide
ANL: Argonne National Laboratory
ANOVA: Analysis of Variance
ASCII: American Standard Code for Information Exchange
BNL: Battelle Northwest Laboratory
B.O.L.: Beginning of Life (of a fuel pin)
BUMMEL: Irradiation experiment for bubble mobility measurements at HFR
BWR: Boiling Water Reactor
CABRI: CEA test reactor in Cadarache
CAMDYN: Cavity Materials Dynamics
CBNM: Central Bureau for Nuclear Measurements, Geel
CEA: Commissariat à l'Energie Atomique
CEN: Centre d'Etudes Nucléaires
CFEM: Thermohydraulic Model
CMPO: Carbonylmethyl Phosphine Oxide
CNEN: Comitato Nazionale Energia Nucleare
CNRS: Centre National de la Recherche Scientifique
Cp: C₅H₅
CRNL: Chalk River Nuclear Laboratory
CVC: Congruently Vaporizing Composition
DCS: Direction Contrôle de Sécurité (DGXII/F), Luxembourg
DECPU: Département d'Etudes sur les Combustibles au Plutonium et Uranium
DEH: Direct Electrical Heating
DESY: Deutsches Elektronen- Synchrotron (Hamburg)
DF: Decontamination Factor
DLA: Diffusion-Limited Aggregation
EAC: European Accident Code
ECSAM: European Commission Safeguards Analysis Measurements
EDAX: Energy-Dispersive X-Ray Analysis
EDXRD: Energy-Dispersive X-Ray Diffraction
EFR: European Fast Reactor
EMPA: Electron Microprobe Analysis
ENEA: Entente Nazionale dell' Energia Alternativa
EPMA: Electron Probe Micro Analysis
ERDA: Elastic Recoil Detection Analysis
ESTER: Hot vitrification pilot plant (Ispra)
ETH: Eidgenössische Technische Hochschule (Zürich)
EURATOM: European Atomic Energy Community
EXAFS: Extended X-Ray Absorption Fine Structure (measurement)
FACT: Sub-Project Formation of Actinides
FBR: Fast Breeder Reactor
FLAME: Fire Aerosol Monitoring Experiments
FR: Fast Reactor
FUTURE: Code for fuel transient calculations
GC-MS: Gas Chromatography - Mass Spectrometry
GSID: Gamma Spectrometric Isotope Dilution
HASYLAB: Hamburger Synchrotron-Strahlungs-Labor
HAW: Highly Active Waste
HCDA: Hypothetical Core Disruptive Accident
HEPA filter: High Efficiency Particulate Air filter
HFR: High Flux Reactor (Petten)

HPLC: High Performance Liquid Chromatography
HPXRD: High-Pressure X-Ray Diffraction
IAEA: International Atomic Energy Agency (Vienna)
ICP: Inductively Coupled Plasma Emission Spectroscopy
ICP-AES: Inductively Coupled Plasma Atomic Emission Spectroscopy
ICP-MS: Inductively Coupled Plasma Mass Spectrometry
ICP-OES: Inductively Coupled Plasma Optical Emission Spectroscopy
ICRP: International Commission on Radiation Protection
ICT: Isotope Correlation Technique
IDMS: Isotope Dilution Mass Spectrometry
ILL: Institute Laue-Langevin (Grenoble)
ILLW: Intermediate Level Liquid Waste
IMF: Institute für Material- und Festkörperforschung (KfK)
INR: Institut für Neutronenphysik und Reaktorforschung (KfK)
IR: Infra Red
IRCh: Institut für Radio Chemie (KfK)
ITU: Institute for Transuranium Elements
IUPAC: International Union of Pure and Applied Chemistry
IWGFR: International Working Group on Fast Reactors
JRC: Joint Research Centre
KfK: Kernforschungszentrum Karlsruhe
KNK: Kompakte Natrium-gekühlte Kernenergieanlage Karlsruhe
KNK-MTE: Irradiation test at KNK
LANL: Los Alamos National Laboratory
LAT: Laser Autoclave Technique
LMTO: Linear Muffin Tin Orbitals
LLNL: Lawrence Livermore National Laboratory
LMFBR: Liquid Metal (cooled) Fast Breeder Reactor
LWR: Light Water Reactor
M: U_xPu_{1-x}
MA: Minor Actinides (Np, Am, Cm)
MAW: Middle Active Waste
MC: Mixed (Uranium-Plutonium) Carbide fuel
MCN: Mixed Carbo-Nitride fuel
MITRA: Code to calculate the release of radio nuclides
MN: Mixed Nitride fuel
MOX: Mixed Oxide fuel
MSID: Mass Spectrometric Isotope Dilution
MX: U,Pu-fuel containing a combination of the elements C,N,O
NAA: Neutron Activation Analysis
NDA: Non-Destructive Assay
NILOC: Nitride Irradiation with Low Carbon Content
NIMPHE: Nitride Irradiation in the PHENIX reactor
OECD: Organisation for Economic Cooperation and Development
OLREC: Communication Program
O/M: Oxygen-to-Metal ratio
OFT: Oxide Fuel Transients
OPDEF: Sub-Project "Optimisation of Dense Fuels"
ORIGEN: Code to calculate fission yields (Oak Ridge version)
ORNL: Oak Ridge National Laboratory
OXAL: Oxalate Precipitation Process
PAHR: Post Accident Heat removal
PCI: Pellet Cladding Interaction
PFR: Prototype Fast Reactor
PHENIX: French prototype fast reactor
PIE: Post Irradiation Examination
PMMA: Polymethacrylate (Plexiglass)
POMPEI: Irradiation experiment to study the structure of nitride fuel

PPR: Programme Progress Report
PROFI: Irradiation experiment to study fission product release
PSB: Projekt Schneller Brüter (KfK)
PUREX: Plutonium and Uranium Recovery by Extraction
PWR: Pressurized Water Reactor
QIA: Quantitative Image Analysis
QLLR: Quasi-Local Linear Regression
R&D: Research and Development
RBS: Rutherford Backscattering
REM: Replica Electron Microscopy
REPRO: Sub-Project "Reprocessing of Nuclear Fuels"
RLMTO: Relativistic Muffin Tin Orbitals
SAP: Sintered Al Powder
SEM: Scanning Electron Microscopy
SFD: Severe Fuel Damage
SHAPE: Sub-Project "Safe Handling of Nuclear Fuels"
SIMFUEL: Th-based fuel with major non-volatile fission products (simulated)
SNR: German prototype fast reactor
SPAKOR: LWR stress corrosion model
STEM: Scanning Transmission Electron Microscopy
SUPERFACT: Minor Actinide Irradiation in Phenix
SWELAC: Irradiation experiment to study swelling accommodation
SYNROC: Synthetic Rock
TBP: Tributyl Phosphate
TD: Theoretical Density
TEM: Transmission Electron Microscopy
TIW: Tungsten electrode Inert gas Welding
TOP: Transient of Power
TRANSURANUS: Fuel behaviour code
TRPO: Trialkyl Phosphine Oxide
TRUEX: Transuranium Extraction
TTA: Thenoyl Trifluor Acetone
TU: Institute for Transuranium Elements
TUAR: TU Annual Report
TUSR: TU Semiannual Report
UHV: Ultra High Vacuum
UK: United Kingdom
UKAEA: UK Atomic Energy Authority
UPS: Ultraviolet light induced Photoelectron Spectroscopy
URADYN: In-Pile motion model
URANUS: Fuel pin code
URFRIC: Fuel code to calculate friction forces
URGAP: TRANSURANUS subroutine to calculate gap conductance
URGAS: Fuel code to calculate gas diffusion
UT: Ultrasonic Thermometer
VISIR/MITRA: Code for calculating build-up and release of short-lived isotopes
VOLEX: Irradiation experiment to study volume expansion of UO₂ in HFR
WAK: Wiederaufarbeitungsanlage Karlsruhe
XAS: X-Ray Absorption Spectroscopy
XPS: X-Ray induced photoelectron spectroscopy
XRD: X-Ray Diffraction
XRF: X-Ray Fluorescence

List of Authors

Director: J. van Geel

Scientific Coordination: J. Fuger

Programme Management: H.E.Schmidt

1. **Oxide Fuel Transients:** Hj.Matzke, P.Bottomley, M.Campana, M.Coquerelle, K.Lassmann, M.Gardani*, I.Ray, C.Ronchi, G.J.Small*, E.Toscano, C.T.Walker
2. **High Burn-Up Chemistry:** M.Coquerelle, P.Bottomley, E.Toscano
3. **Optimisation of Dense Fuels:** H.Blank, M.Campana, M.Coquerelle, J.-F.Gueugnon, Hj.Matzke, K.Richter, C.Sari, C.T.Walker
4. **High-Temperature Properties of Nuclear Materials:** C.Ronchi, J.F.Babelot, J.-P.Hiernaut, H.A.Tasman, P.Werner
5. **Formation of Actinides:** L.Koch, W.Bartscher, M.Coquerelle, J.-F.Gueugnon, K.Richter, C.Sari, R.Wellum
6. **Safe Handling of Nuclear Materials:** S.Pickering, K.Buijs, B.Chavane de Dalmassy,
7. **Reprocessing of Nuclear Fuels:** H.Bokelund, C.Apostolidis, J.-P.Glatz
8. **Actinide Research:** U.Benedict, W.Bartscher, M.S.S.Brooks, G.H.Lander, Hj.Matzke, H.J.Naegele, J.Rebizant, J.-C.Spirlet
9. **Fuel Behaviour under Accident Conditions:** H.Blank, K.Lassmann, Hj.Matzke, H.A.Tasman
10. **Characterisation of Nuclear Waste Forms:** J.Fuger, H.Bokelund, M.Coquerelle, J.P.Glatz, Hj. Matzke
11. **R&D in Destructive Analysis of Fissile Materials:** L.Koch, S.Franzini, R.Wellum
12. **Support to Community Policies:** L.Koch, S.Franzini, R.Wellum
13. **Prospective Studies:** J.Magill, S.Pickering, J.-F.Babelot, G.H.Lander, S.Pickering
14. **Work for Third Parties:** K.Richter, J.-F.Gueugnon

* visiting scientist

Previous Progress Reports of the Institute for Transuranium Elements

TUSR	Period	COM-Nr	EUR-Nr
1	Jan - Jun 1966	1580	
2	Jul - Dec 1966	1522	
3	Jan - Jun 1967	1745	
4	Jul - Dec 1967	2007	
5	Jan - Jun 1968	2172	
6	Jul - Dec 1968	2300	
7	Jan - Jun 1969	2434	
8	Jul - Dec 1969	2576	
9	Jan - Jun 1970	2664	
10	Jul - Dec 1970	2750	
11	Jan - Jun 1971	2833	
12	Jul - Dec 1971	2874	
13	Jan - Jun 1972	2939	
14	Jul - Dec 1972	3014	
15	Jan - Jun 1973	3050	
16	Jul - Dec 1973	3115	
17	Jan - Jun 1974	3161	
18	Jul - Dec 1974	3204	
19	Jan - Jun 1975	3241	
20	Jul - Dec 1975	3289	
21	Jan - Jun 1976	3358	
22	Jul - Dec 1976	3384	
23	Jan - Jun 1977	3438	6475 E
24	Jul - Dec 1977	3484	7209 E
25	Jan - Jun 1978	3526	7459 E
26	Jul - Dec 1978	3582	7227 E
27	Jan - Jun 1979	3657	7483 E
28	Jul - Dec 1979	3714	7509 E
29	Jan - Jun 1980	3822	7857 E
30	Jul - Dec 1980	3846	8230 E
31	Jan - Jun 1981	3898	8447 E
32	Jul - Dec 1981	3927	8777 E
33	Jan - Jun 1982	3990	9581 E
34	Jul - Dec 1982	4048	10251 E
35	Jan - Jun 1983	4094	10266 E
36	Jul - Dec 1983	4117	10454 E
37	Jan - Jun 1984	4150	10470 E
38	Jul - Dec 1984	4165	11013 E
39	Jan - Jun 1985	4201	11835 E
40	Jul - Dec 1985	4265	11836 E
TUAR			
86	Jan - Dec 1986	4302	12233 E
87	Jan - Dec 1987	-----	11783 E
88	Jan - Dec 1988	-----	12385 E

Previous Programme Progress Reports were confidential for a period of two years. Since 1977 they are made freely accessible after that period as EUR-Reports. They can be ordered from the Office for Official Publications of the European Communities, 2 rue Mercier, L-2985 Luxembourg, Tel. 49 92 81, Telex PUBOF LU 1324 b

This report was compiled and edited by H.E. Schmidt, J. Richter, L. Ruczka and R. Wellum.

For further information concerning JRC programmes please contact the Directorate General Science, Research and Development of the Commission of the European Communities, 200 rue de la Loi, B-1049 Brussels, Belgium.

